Doctoral Programme in Bioengineering

Liquid-crystal modulators in optical phase-shifting interferometry and polarimetric imaging

Esther Nabadda

Director of the thesis

Dr. Ignacio Moreno Soriano

Co-director of the thesis

Dr. María del Mar Sánchez López

Miguel Hernández University of Elche

- 2024 -

This Doctoral Thesis, entitled "**Liquid-crystal modulators in optical phase-shifting interferometry and polarimetric imaging**", is submitted under the format of **thesis by compendium** of the following **publications**:

(a). **E. Nabadda**, G. López-Morales, D. Marco, M. M. Sánchez-López, and I. Moreno, "Mueller matrix polarimetric analysis applied to characterize the physical parameters of a twisted-nematic liquid-crystal modulator", *Optics and Laser Technology* 156(3), 108567 (2022). DOI JCR Index 5.0 (JCR 2022, Optics, Q1)

(b). **E. Nabadda**, N. Bennis, M. Czerwinski, A. Walewska, L. R. Jaroszewicz, M. M. Sánchez-López, and I. Moreno, "Ferroelectric liquid-crystal modulator with large switching rotation angle for polarization-independent binary phase modulation", *Optics and Lasers in Engineering* 159(2), 107204 (2022). DOI JCR Index 4.2 (JCR 2022, Optics, Q1)

(c). **E. Nabadda**, P. García-Martínez, M. M. Sánchez-López, and I. Moreno, "Phase-shifting common-path polarization self-interferometry for evaluating the reconstruction of holograms displayed on a phase-only display", *Frontiers in Physics* 10, 920111 (2022). DOI JCR Index 3.1 (JCR 2022, Physics-Multidisciplinary, Q2)

(d). **E. Nabadda**, M. M. Sánchez-López, P. García-Martínez, and I. Moreno, "Retrieving the phase of diffraction orders generated with tailored gratings", *Optics Letters* 48(2), 267-270 (2023). DOI JCR Index 3.6 (JCR 2022, Optics, Q2) **[selected in Editor's pick]**

(e). **E. Nabadda**, M. M. Sanchez-Lopez, A. Vargas, A. Lizana, J. Campos, and I. Moreno, "Mueller matrix imaging polarimeter with polarization camera self-calibration applied to structured light components", *Journal of the European Optical Society - Rapid Publications* 20(1), 5 (2024). DOI JCR Index 1.5 (JCR 2022, Optics, Q4)

Dr. Ignacio Moreno Soriano, director, and Dr. María del Mar Sánchez López, co-director of the doctoral thesis entitled "**Liquid-crystal modulators in optical phase-shifting interferometry and polarimetric imaging**"

REPORT:

that Esther Nabadda has performed, under our supervision, the work entitled "**Liquid-crystal modulators in optical phase-shifting interferometry and polarimetric imaging**" pursuant to the terms and conditions established in the Research Plan and following the Code of Good Practices of the Miguel Hernández University of Elche, successfully meeting the objectives planned for its public defence as a doctoral thesis.

In witness whereof we sign for all pertinent purposes, in Elche on the 23rd February 2024

Thesis director	Thesis co-director
Dr. Ignacio Moreno Soriano	Dr. María del Mar Sánchez López

Dr. Piedad Nieves De Aza Moya, Coordinator of the Doctoral Programme in Bioengineering.

REPORTS:

that Esther Nabadda has performed, under the supervision of our Doctoral Programme, the work entitled "**Liquid-crystal modulators in optical phase-shifting interferometry and polarimetric imaging**" pursuant to the terms and conditions established in the Research Plan and following the Code of Good Practices of the Miguel Hernández University of Elche, successfully meeting the objectives planned for its public defence as a doctoral thesis.

In witness whereof I sign for all pertinent purposes, in Elche on the 23rd February 2024.

Prof. Piedad Nieves De Aza Moya

Coordinator of the Doctoral Programme in Bioengineering

Acknowledgements

I extend my deepest gratitude to God for granting me the opportunity to complete my doctoral thesis, guided by the unwavering support of Dr. Ignacio Moreno and Dr. María del Mar Sánchez. I am profoundly appreciative of their consistent encouragement and assistance, which has been a cornerstone from the inception of the program to its completion. Their invaluable support during my relocation from Uganda to Spain is something I can never take for granted. Their grace in navigating the complexities of immigration bureaucracy and the warmth of their welcome will forever be etched in my heart, and I am deeply indebted to their kindness. Furthermore, I am sincerely grateful for the wealth of knowledge they have imparted to me and their genuine investment in my current and future professional growth.

I would also like to express my gratitude to Dr. Pascuala García and Dr. Asticio Vargas for their collaborative efforts and the insights they shared during their visits to our laboratory. In particular, I wish to extend special appreciation to Dr. Noureddine Bennis and Dr. Anna Spadlo for affording me the opportunity to undertake a one-month research stay at the Military University of Technology in Warsaw, Poland. Additionally, I am thankful to Dr. Angel Lizana and Dr. Juan Campos for their invaluable contributions to our latest research work.

To my esteemed colleagues, Dr. Guadalupe López, Dr. David Marco, and Shang Gao, with whom I have had the pleasure of sharing a workspace, I extend my heartfelt thanks. I deeply appreciate the conducive working environment we have collectively fostered, and the camaraderie we have shared has been truly enriching. Furthermore, I am grateful to Dr. Tumps Ireeta for the invaluable lessons imparted during my bachelor's and master’s degree studies.

With profound gratitude, I extend my thanks to my parents, Medina Nalwanga and Isaac Kiyimba, and my siblings, Shirah Zalwango, Eric Mulondo, and Isaac Kiyimba Jr., for their unwavering love and prayers. Special mention goes to my nephew, Boseman Mayiga, whose infectious joy has been a constant source of encouragement.

Lastly, I wish to express my gratitude to all those who have supported and loved me throughout this journey of life, even if not explicitly mentioned here, and to you, the reader of this thesis, I extend my heartfelt appreciation.

Funding

This thesis has been conducted under a PhD grant from “Santiago Grisolía” Program of Generalitat Valenciana (GRISOLIAP/2020/004).

The stay at Military University of Technology, Warsaw (Poland) was financed by European Social Fund (NAWA PROM project POWR.03.03.00–00- PN13/18).

The works in this thesis have been conducted under funding from Ministerio de Ciencia e Innovación, Spain (projects PID2021-126509OB-C22, and PDC2022-133332-C22), and from Generalitat Valenciana (ref. CIAICO/2021/276).

Summary

This thesis focuses on the study of the properties of liquid-crystal (LC) optical modulators, the design of novel configurations and methods for characterizing their modulation properties, and their use in two important optical techniques such as interferometry and polarimetry. The work involves three different types of LC modulators: the twisted-nematic LC modulator, the ferroelectric modulator, and the parallel-aligned nematic LC modulator, the latter employed both as ~~in~~ a single cell or as a pixelated spatial light modulator display.

In this work, such LC devices have been applied in the development and implementation of two useful optical systems, namely a common-path phase-shifting interferometer and a Mueller matrix imaging polarimeter. These systems provide quantitative information of the phase and of the state of polarisation respectively, a kind of information that cannot be obtained by simply analysing intensity images on a camera.

The thesis is presented as a compendium of five publications in JCR journals and comprises two main parts. The first part of the thesis is devoted to the study of two LC single-cell modulators: a twisted-nematic LC cell and a ferroelectric LC cell. Like most of LC modulators, their modulation properties are based on the modification of the state of polarisation of the light traversing the LC layer. Therefore, their analysis requires a comprehensive understanding of light polarisation. Both the Jones matrix formalism and the Mueller-Stokes formalism have been applied, this last one facilitating the analysis of the depolarisation properties. Both formalisms, Mueller matrix and Jones matrix have been compared for the different modulation regimes of the twisted-nematic LC modulator. In the case of the ferroelectric LC modulator, a non standard configuration where the in-plane rotation of the LC director is of 90^{o} has been proposed. While this FLC cell is not suitable for standard display purposes, it operates as a pure binary π phase modulation device for all states of polarisation, ideally preserving output polarization in both modulation states. Such a LC cell has been fabricated by a collaborator group at the Military University of Technology, Warsaw (Poland), and the optical properties expected in the design of the device have been verified.

The second part of the thesis is devoted to apply a parallel-aligned LC-SLM for the realisation of a common-path interferometric optical setup, where the device itself acts as an element for the generation of a structured light beam as well as facilitating the implementation of the phase-shifting interferometric (PSI) technique. Phase diffractive optical elements were designed for shaping the input beam and were combined with an encoded diffractive lens to focus the Fourier transform diffracted field in its back focal plane. This standard configuration of Fourier transform holography is transfomed through a simple rotation of a polariser, into a common path interferometer, facilitating phase evaluation of the diffracted beam without any additional element. The PSI technique is demonstrated to characterize the phase spatial pattern of light beams after being diffracted by various customized diffractive elements, including computer-generated holograms for the generation of structured light, or diffraction gratings with continuous phase designs.

Finally, the Mueller matrix imaging polarimeter introduced in the initial part of the thesis has been largely improved by replacing all movable components with computer-programmable LC retarders, ensuring greater precision, and by including a polarisation camera with built-in polarising filters that enables the capture of four linear polarisation images in a single shot. A polarimeter self-calibration method is applied that uses the polarisation camera as a reference, thus eliminating the need of an external calibration equipment, and providing error compensation for the polarisation states effectively generated and detected. Furthermore, a multiwavelength LED source allows to widen the spectral range of the polarimeter and avoids speckle-like noise in the captured images. The accuracy and usefulness of the polarimeter is

tested with different structured elements such as patterned polarisers and retarders, which are commonly employed in structured light systems. The developed multifunctional complete Mueller matrix imaging polarimeter is a cost-affordable instrument, ready to be applied to a variety of samples, ranging from optical devices to biosamples.

Resumen

Esta tesis está centrada en el estudio de las propiedades de los moduladores ópticos de cristal líquido (CL), el diseño de nuevas configuraciones de modulación y de nuevos métodos de caracterización de sus propiedaes, y su uso en dos importantes técnicas ópticas: la interferometría y la polarimetría. El trabajo realizado implica moduladores de cristal líquido con diferentes configuraciones, como la configuración de CL nemático con giro, la configuración de CL ferroeléctrico, o la configuración de CL nemático de alineamiento paralelo, ésta última tanto en forma una única celda o en forma de un modulador pixelado o modulador espacial de luz (SLM).

En este trabajo, estos dispositivos de CL se han empleado en el desarrollo e implementación de dos sistemas ópticos: 1) un interferómetro de desplazamiento de fase y de camino común y 2) un polarímetro de imágenes de matriz de Mueller. Estos sistemas proporcionan información cuantitativa de la fase y del estado de polarización respectivamente, un tipo de información que no puede obtenerse simplemente analizando las imágenes de intensidad en una cámara.

La tesis se presenta como un compendio de cinco publicaciones. La primera parte de la tesis está dedicada al estudio de dos moduladores de CL: una celda de CL nemático con giro, y una celda de CL ferroeléctrioa. Como la mayoría de los moduladores de CL, sus propiedades de modulación se basan en la modificación del estado de polarización de la luz que lo atraviesa. Por lo tanto, su análisis requiere una comprensión integral de la polarización de la luz. Para ello se han aplicado tanto el formalismo matricial de Jones como el formalismo matricial de Mueller-Stokes, este último proporcionando el análisis de las propiedades de despolarización. Ambos formalismos (matriz de Mueller y matriz de Jones) se han comparado para los diferentes regímenes de modulación de un modulador de CL nemático con giro. En el caso del modulador de CL ferroeléctrico, se ha propuesto una configuración no estándar en la que la rotación en el plano del director molecular del CL es de 90^{o}. Si bien esta celda no es adecuada para fines de control de intensidad, proporciona un dispositivo de modulación binario de fase π para todos los estados de polarización, preservando idealmente la polarización de salida en ambos estados de modulación. Un grupo colaborador de la Military University of Technology, Varsovia (Polonia) ha fabricado una celda de CL de este tipo y se han verificado las propiedades ópticas esperadas.

La segunda parte de la tesis está dedicada a la aplicación de un dispositivo SLM de CL nemático de alineamiento paralelo para la realización de una configuración óptica interferométrica de camino común, donde el propio dispositivo actúa como elemento para la generación de un haz de luz estructurada, además de facilitar la implementación de la técnica interferométrica de desplazamiento de fase. Se han diseñado elementos ópticos difractivos de fase y se han combinado con una lente difractiva codificada a su vez en el SLM para enfocar el campo difractado en su plano focal imagen. Esta configuración estándar de la holografía por transformada de Fourier se transforma en un interferómetro de trayectoria común mediante una simple rotación de un polarizador. Ello permite la evaluación de la distribución de fase del haz difractado sin ningún tipo de elemento adicional. Con este sistema se ha demostrado la aplicación de la técnica de interferometría de desplazamiento de fase para diferentes elementos difractivos, incluyendo hologramas generados por ordenador para la generación de luz estructurada, o redes de difracción con diseños de fase continua.

Por último, el polarímetro de matriz de Mueller empleado en la parte inicial de la tesis se mejoró mediante la incoporación de retardadores programables de CL, garantizando así una mejor precisión al evitar partes móviles, y una cámara de polarización con filtros polarizadores incorporados, que permite la captura de cuatro imágenes de polarización lineal en una sola

toma. Se ha aplicado un método de autocalibración del polarímetro que utiliza la cámara de polarización como referencia, eliminando así la necesidad de componentes de calibración adicionales. La precisión y utilidad del polarímetro de imagen se ha comprobado mediante diferentes elementos estructurados tales como polarizadores y retardadores. Este polarímetro multifuncional de imagen de matriz de Mueller es un instrumento de un coste relativamente asequible, listo para ser aplicado a una amplia variedad de muestras, que van desde dispositivos ópticos hasta muestras biológicas.

Table of Contents

1. Introduction

Light technologies have been recognized as key enablers for societal trends including digitalization, intrnet of things (IoT), big data, artificial intelligence or autonomous transportation. As an essential key enabling technology, **optics and photonics** are one of the "building blocks of the current digital revolution" [Phot 2019]. This is also the case of biomedical research, where optical instruments and photonic technologies are playing a crucial role in the development of new biomedical techniques in different areas that range from diagnostic imaging devices, non-invasive procedures and surgical automatic devices, to biosensors, biomarkers, etc [Gigl 2018].

Among the different properties of light, **polarisation** has been recognised to provide extremely useful information, and a number of techniques harnessing biological and clinical research are based on the **vectorial properties of light** [He 2021]. In the last years, there has been great technological advances related to the generation and measurement of polarised light, that provide researchers in this area with new tools and devices. In parallel, there has been great advances in the field of **structured light**. This denomination was introduced to describe light beams with a spatial control of their amplitude, phase or state of polarization [Rubi 2017]. In particular, light beams with non-uniform polarization pattern in the beam tranversal section, known as **vector beams**, are leading to important advances in areas such as microscopy, materials processing, metrology or optical communications [Rosa 2018] [Piqu 2020] [Hern 2017].

There is an increasing interest of using polarimetry in **biomedical and botanical applications** [Rodr 2021] [Ivan 2021] [Paul 2015] [Vize 2017] [Zhou 2024] [Van E 2021]. This is a technique that provides information about the polarization changes that occur in a sample, changes that are not visible under standard imaging, but which can serve as channels of information to build images with better contrast. Nowadays, these polarimetric imaging techniques use primarily **optoelectronic liquid-crystal modulators**, devices capable of changing the polarization state in a controlled way. Therefore, automatic computer-controlled procedures can be designed to capture all the different required images under different polarization configurations.

In addition, liquid-crystals are the core of one of the most important electronic imaging technologies, namely: liquid-crystal displays (LCDs). In the form of microdisplays they are used also as **spatial light modulators** (SLM), pixelated optical modulation devices with very high spatial resolution and large number of pixels. SLMs are essential devices for adaptive optics and for active optics, where they are used to display dynamic diffractive and polarisation optical elements.

In parallel, the production of spatially-patterned ultra-flat polarisation elements, fabricated with metamaterials [Wen 2021] or with birefringent materials, typically liquid-crystals [De Si 2016], is providing a complete generation of optical elements and tools useful for developing imaging systems [Curc 2020] and for advanced polarimetry [Ange 2019]. As an example, polarisation cameras with attached pixilated polariser microgrid arrays allow snapshot imaging of different polarisation components. The characterisation and evaluation of the optical

properties of such components and new instruments is also very relevant to use them effectively. **Optical interferometric and polarimetric techniques** are specially well-suited for developing accurate inspection techniques.

1.1 Goals and objectives

This report is presented to achieve the PhD degree at the Doctoral Program of Bioengineering of *Universidad Miguel Hernandez de Elche* (UMH). The work has been developed mostly at the TecnOPTO Labs of the UMH Institute of Bioengineering, and partially during a one month stay at the Military University of Technology (WAT), Warsaw (Poland).

The study has been centered in advancing aspects related to the use of liquid-crystal technology in the generation and control of structured light beams, in optical interferometry and in optical polarimetric imaging. In particular the work was centered in three main goals: 1) the development of new optical modulation devices and new characterisation techniques based on liquid-crystal materials, and 2) the use of liquid-crystal spatial light modulators to generate and characterise structured light beams, and 3) the realisation of an imaging polarimeter using modern liquid-crystal modulators and a polarisation camera.

Having these general goals in mind, the specific objetives of the work are:

- To extend the well established microscopic physical models used to evaluate the optical modulation properties of common twisted nematic liquid-crystal modulators, which are typically developed within the Jones matrix formalism, to the corresponding Mueller matrix approach.

- To propose new liquid-crystal modulator configurations that can be useful for improving aspects related to their use in phase or in polarization control with improved characteristics compared to the standard configurations in commercial devices.

- To develop a complete imaging polarimetric system based on liquid-crystal modulators, such that all the required images under different polarisation conditions of the incident beam and of the detection system, are all performed without any moving elements.

- To apply the developed polarimetric system in analyzing other polarisation components, including other liquid-crystal modulators, geometric-phase elements and patterned polarisers. These elements constitute the building blocks of advanced optical imaging systems based on structured light, and they can serve as precise tests checking the accuracy of the polarimeter. In addition, their precise characterisation serves for their optimal use in structured light systems.

- To improve the performance of the developed polarimetric system by including a polarisation camera, capable of measuring the different polarisation components in a single-shot. Also, to apply optimisation methods useful to compoensate for possible errors in the generation and in the detection of polarised light in the polarimeter, using the polarisation camera as a self-reference.

- To develop a common-path polarisation interferometer based on a liquid-crystal spatial light modulator (SLM) and to apply the well-known phase-shifting interferometry (PSI) techniques to evaluate the reconstruction of complex-valued holograms displayed onto the SLM. The ultimate scope here is being able to retrieve experimentally the intensity and the phase of shaped beams.

- To apply the developed technique to measure the quadratic phase generated in the output plane of the interferometer, and then compansate it to achieve a precise determination of the phase of diffraction orders generated with phase-only diffraction gratings with tailored properties. This will enable the experimental characterization of polarisation diffraction gratings, useful for developing snapshot polarimeters.

1.2 Thesis organization

Having all these points in mind, this report is organised as follows: after this brief introductory chapter, Chapter 2 deals with the materials and methods applied during the thesis. The different main aspects related to the control of polarised light, the liquid-crystal technology and the polarimetric and interferometric measurements are briefly reviewed. Chapter 3 presents a discussion of the main results, presented together with the collection of the five articles that constitute the thesis. Finally, Chapter 4 contains the conclusions of the work. The report is completed with the list of references and with an appendix that contains the five articles.

2. Material and methods

This chapter describes the relevant materials and methods applied to obtain the results discussed in this thesis. The chapter briefly reviews the concept of polarisation of light, its mathematical description in the Jones formalism and in the Mueller-Stokes formalism, the liquid-crystal technology, and the basis of the optical polarimetry and the phase shifting interferometry techniques.

2.1 Polarised light and the polarisation ellipse

Light is a transverse electromagnetic wave with electric and magnetic fields oscillating perpendicular to each other on a plane transverse to the direction of propagation [Lauf 1996]. The trajectory of the electric field in this transversal plane defines the state of polarisation of light. For light propagating along the z axis, an arbitrary polarisation state can be considered as a superposition of two orthogonal electric fields E_x and E_y as:

$$E_x = A_x e^{i\delta_x} e^{i(\omega t - kz)}$$
$$E_y = A_y e^{i\delta_y} e^{i(\omega t - kz)} \quad (1)$$

where A_x and A_y are the magnitudes of the electric field in the x and y directions, δ_x and δ_y are their respective phase shifts, ω is the angular frequency and k is the magnitude of the wave vector. The superposition takes the vectorial form:

$$\vec{E} = \left(A_x e^{i\delta_x}\hat{\imath} + A_y e^{i\delta_y}\hat{\jmath}\right) e^{i(\omega t - kz)} \quad (2)$$

where $\hat{\imath}$ and $\hat{\jmath}$ are the unitary vectors in the x and y direction.

If the electric field oscillations are confined to one plane, light is said to be linearly polarised. These situations occur when either one amplitude is zero ($A_x = 0$ or $A_y = 0$) or when the phase difference is $\delta \equiv \delta_y - \delta_x = 0$ or $\delta = \pi$. However, for cases $\delta = \pm\pi/2$ and equal magnitude $A_x = A_y$, the electric field sweeps a circle thus yielding the circularly polarised states. When the tip of the electric field vector sweeps the circle clockwise, right circular polarisation is obtained while for counterclockwise sweeping, light is left circularly polarised. In this thesis we will use the denomination H and V for linear states with horizontal and vertical orientations, D and A for linear states oriented at $+45^{\circ}$ (diagonal) and -45° (antidiagonal), and R and L for right and left circular states. We refer to them as the six cardinal states of polarisation. Figure 1 illustrates these polarisation states.

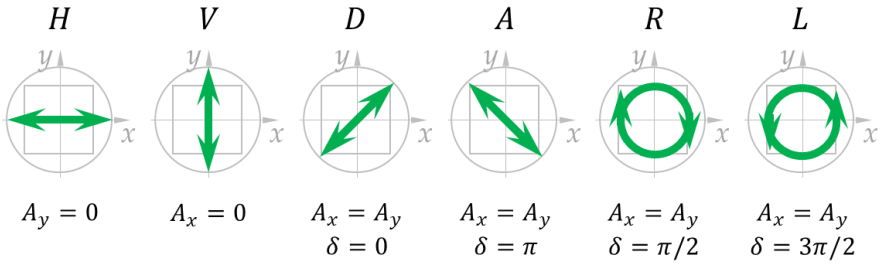

Figure 2.1: Illustration of the six cardinal polarisation states. (a) Linear horizontal, (b) Linear vertical, (c) Linear diagonal, (d) Linear antidiagonal, (e) Right circular, (f) Left circular.

Linear and circular polarisation states are only special cases of the more general elliptical polarisation states. As the light propagates, the tip of the electric field vector describes an ellipse in the transversal plane. The shape of the ellipse depends on the relative relation among the amplitudes A_x and A_y, and on the phase difference δ between the two orthogonal components [Coll 2005].

The ellipse equation in the transversal plane takes the form.

$$\left[\frac{E_x}{A_x}\right]^2 + \left[\frac{E_y}{A_y}\right]^2 - \frac{2E_xE_y}{A_xA_y}\cos(\delta) = \sin^2(\delta) \tag{3}$$

The polarisation ellipse is often described in polar coordinates, defined by the ellipticity (ε) and azimuth (orientation) (α) angles, as indicated in Fig. 2.2. The azimuth α is the angle between the major axis of the ellipse and the positive direction of the x - axis and defines the orientation of the ellipse in its plane. It is given by the following relation [Coll 2005]:

$$\tan(2\alpha) = \frac{2A_xA_y}{A_x^2 - A_y^2}\cos(\delta), \qquad -\frac{\pi}{2} \le \alpha \le \frac{\pi}{2} \tag{4}$$

The ellipticity is the ratio between the lengths of the semi-minor axis of the ellipse (b in Fig. 2.2) and its semi-major axis (a in Fig. 2.2) and it can be related to the amplitudes, phase difference and azimuth as:

$$\tan(\varepsilon) = \frac{b}{a} = \pm\sqrt{\frac{A_x^2\sin^2(\alpha) + A_y^2\cos^2(\alpha) - A_xA_y\cos(\delta)\sin\left(\frac{\alpha}{2}\right)}{A_x^2\cos^2(\alpha) + A_y^2\sin^2(\alpha) + A_xA_y\cos(\delta)\sin\left(\frac{\alpha}{2}\right)}} \tag{5}$$

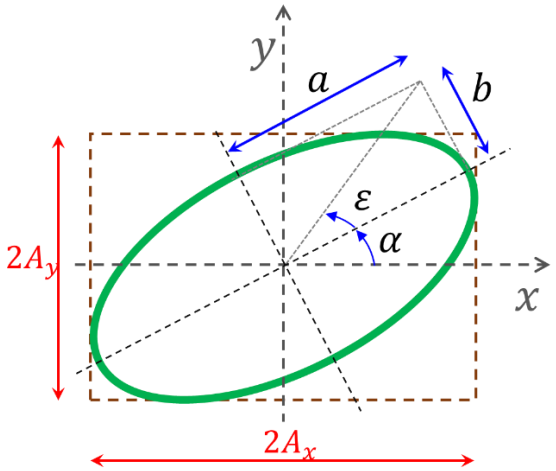

Figure 2.2: Representation of the polarisation ellipse with the corresponding ellipticity (ε) and azimuth (α) angles. a and b are the semi-major and semi-minor axes of the ellipse.

2.2 Jones matrix formalism for polarised light

This section decribes polarised light and different optical polarising elements using the Jones matrix formulation. The Jones calculus, which was developed in 1941 by Robert Clark Jones [Jone 1941], is a widely employed formalism that offers an understanding of fully polarised and fully coherent light. In this formalism, polarised light is described by a two-dimensional vector (Jones vector), and the optical elements changing the polarisation in a linear way are represented by 2×2 matrices (Jones matrices).

2.2.1 Jones vectors

An arbitrary polarisation state described in Eq.(1) can be expressed as:

$$\begin{bmatrix} E_x \\ E_y \end{bmatrix} = \begin{bmatrix} A_x e^{i\delta_x} \\ A_y e^{i\delta_y} \end{bmatrix} e^{i(\omega t - kz)} = A\,\mathbf{J}\, e^{i(\omega t - kz + \Delta)} \tag{6}$$

where $A = \sqrt{{A_x}^2 + {A_y}^2}$, $\Delta = \frac{1}{2}(\delta_x + \delta_y)$ is the average phase and $\mathbf{J}$ is the normalised Jones vector given by,

$$\mathbf{J} = \frac{1}{A}\begin{bmatrix} A_x\, e^{-i\frac{\delta}{2}} \\ A_y\, e^{+i\frac{\delta}{2}} \end{bmatrix} \tag{7}$$

The Jones vector is a complex-valued two dimensional vector that defines the polarisation state and can also be expressed in terms of the azimuth and ellipticity angles as:

$$\mathbf{J} = \begin{bmatrix} \cos\alpha \cos\varepsilon - i \sin\alpha \sin\varepsilon \\ \sin\alpha \cos\varepsilon + i \cos\alpha \sin\varepsilon \end{bmatrix} \tag{8}$$

The intensity is considered as the square of the magnitude of the electric field, so is $I = \langle E_x^* E_x \rangle + \langle E_y^* E_y \rangle = A^2$, where the symbol $\langle \cdot \rangle$ represents the time expectation value of the electric field

components products, implied in the intensity measurements. Thus, the normalised Jones vector in Eqs. (7) and (8) has intensity $I = 1$.

For linearly polarised states, the ellipticity angle is $\varepsilon = 0^{\circ}$ and therefore $\mathbf{J} = [\cos\alpha \quad \sin\alpha]^T$ where T indicates the transposed matrix. For circularly polarised states, the azimuth angle is $\alpha = \pm 90^{\circ}$ and the ellipticity is $\varepsilon = \pm 45^{\circ}$ thus $\mathbf{J} = \frac{1}{\sqrt{2}}[1 \quad \pm i]^T$, where the $\pm$ sign refers to the R and L states, respectively.

It must be noted that a global common phase that multiplies both components of the Jones vector does not change the state of polarisation. Therefore, in general in Jones calculus a global phase can be neglected if only the state of polarization is of interest.

Table 2.1 below shows the normalised Jones vectors of the six cardinal polarisation states described in Fig. 2.1.

Polarisation state	H	V	D	A	R	L
Normalised Jones vector ($\mathbf{J}$)	$\begin{bmatrix}1\\0\end{bmatrix}$	$\begin{bmatrix}0\\1\end{bmatrix}$	$\frac{1}{\sqrt{2}}\begin{bmatrix}1\\1\end{bmatrix}$	$\frac{1}{\sqrt{2}}\begin{bmatrix}1\\-1\end{bmatrix}$	$\frac{1}{\sqrt{2}}\begin{bmatrix}1\\i\end{bmatrix}$	$\frac{1}{\sqrt{2}}\begin{bmatrix}1\\-i\end{bmatrix}$

Table 2.1. The normalised Jones vector representation of the six cardinal normalised polarisation states.

2.2.2 Jones matrices

Assuming the usual situation where the components of the Jones vector $\mathbf{J}_2$ describing the polarisation emerging from a polarising element are linearly related to the components of the incident beam $\mathbf{J}_1$ (Fig. 2.3), 2x2 matrices can be used to describe these non-depolarising optical devices [Fowl 1968]. These are the Jones matrices $\mathbf{M}$ that relate input and output Jones vectors as:

$$\mathbf{J}_2 = \mathbf{M} \cdot \mathbf{J}_1 = \begin{bmatrix} M_{xx} & M_{xy} \\ M_{yx} & M_{yy} \end{bmatrix} \cdot \mathbf{J}_1 \tag{9}$$

where the matrix elements M_{ij} are in general complex values.

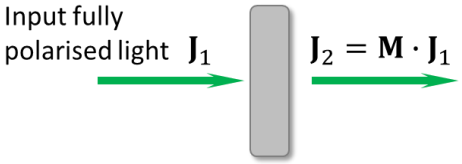

Figure 2.3: Jones matrix representation of light propagating through a polarising optical element.

For cases where light propagates through more than one optical element (Fig. 2.4), the Jones matrix $\mathbf{M}_\mathrm{T}$ of a cascade of elements is the matrix product of the individual elements since the output Jones vector from one preceding element is the input vector for the next element.

$$\mathbf{J}_{out} = \mathbf{M}_n \ldots \mathbf{M}_3 \cdot \mathbf{M}_2 \cdot \mathbf{M}_1 \cdot \mathbf{J}_1 = \mathbf{M}_\mathrm{T} \cdot \mathbf{J}_1 \tag{10}$$

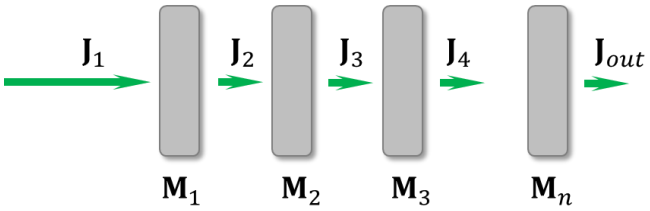

Figure 2.4: Jones matrix representation of light propagating through a cascade of polarising optical elements.

Some of the commonly applied optical polarising elements include linear polarisers, linear retarders, and polarisation rotators.

A **polariser** is an optical filter that lets light waves of a specific polarisation pass through while blocking the orthogonal polarisation. The most common type is the linear polariser which transmits the light that is linearly polarised along the polariser's transmission axis and blocks the orthogonal linear component. Assuming that the polariser transmission axis is oriented horizontal or vertical, this element can be described with the following Jones matrix:

$$\mathbf{P} = \begin{bmatrix} P_x & 0 \\ 0 & P_y \end{bmatrix} \tag{11}$$

where the real values $0 \leq P_x \leq 1$ and $0 \leq P_y \leq 1$ are the transmission factors of the x and y-components of electric field. In the ideal case, for horizontal and vertical polarisers $P_x = 1$ and $P_y = 0$ and $P_x = 0$ and $P_y = 1$ respectively, and the corresponding Jones matrices take respectively the form:

$$\mathbf{P}(0^{\circ}) = \begin{bmatrix} 1 & 0 \\ 0 & 0 \end{bmatrix} \tag{12a}$$

$$\mathbf{P}(90^{\circ}) = \begin{bmatrix} 0 & 0 \\ 0 & 1 \end{bmatrix} \tag{12b}$$

Another classical polarisation optical element is the **linear retarder** or **waveplate** which alters the polarisation state of a light wave travelling through it without changing the intensity. It does this by increasing the relative phase by $+\beta$ along the fast axis and decreasing the relative phase by $-\beta$ along the slow axis. Therefore, the linear retarder introduces a phase shift (or retardance) 2β between the electric field components aligned with the fast and slow axes, thus changing the output polarisation. If the fast and slow axes are considered aligned along the x and y axes, the Jones matrix of an ideal retarder with 2β phase shift takes the form:

$$\mathbf{W}(2\beta) = \begin{bmatrix} e^{i\beta} & 0 \\ 0 & e^{-i\beta} \end{bmatrix} \tag{13}$$

The fast and slow axes of the retarder are known as the neutral axes since an input beam linearly polarised along one of them maintains its polarisation after traversing the retarder. Again, a global phase does not affect the emerging state of polarisation.

Some of the commonly used linear retarders include the **quarter-wave plate** (QWP) and **half-wave plate** (HWP) having a retardance of $2\beta = \pi/2$ and $2\beta = \pi$ respectively. Their respective Jones matrices take the form:

$$\mathbf{W}_Q \equiv \mathbf{W}(2\beta = \pi/2) = \begin{bmatrix} 1 & 0 \\ 0 & -i \end{bmatrix} \tag{14a}$$

$$\mathbf{W}_H \equiv \mathbf{W}(2\beta = \pi) = \begin{bmatrix} 1 & 0 \\ 0 & -1 \end{bmatrix} \tag{14b}$$

when the neutral axes are aligned with the x and y axes (note that in the case of the QWP a global phase term $e^{i\pi/4}$ is ignored compared to Eq. (13), since it does not change the output polarisation, and in the case of the HWP a phase term $e^{i\pi/2}$ has been neglected as well). QWPs are often applied together with a linear polariser to build a circular polariser. HWPs are commonly used to invert the helicity of an input circularly polarised beam or to change the orientation of linearly polarised light.

Finally, a **polarisation rotator**, also known as circular retarder, rotates the azimuth of the polarisation ellipse while maintaining its ellipticity. Considering θ as the angle through which the polarisation ellipse is rotated, the Jones matrix of the rotator takes the form:

$$\mathbf{R}(\theta) = \begin{bmatrix} \cos\theta & -\sin\theta \\ \sin\theta & \cos\theta \end{bmatrix} \tag{15}$$

The rotator matrix allows the description of in-plane rotations of the other optical elements. If $\mathbf{M}$ is the Jones matrix of a polariser or of a retarder with axes along the $x - y$ directions (described by Eq. (11) and Eq. (13) respectively), the Jones matrix $\mathbf{M}(\theta)$ of the same optical element rotated an angle θ is obtained as:

$$\mathbf{M}(\theta) = \mathbf{R}(\theta) \cdot \mathbf{M} \cdot \mathbf{R}(-\theta) \tag{16}$$

Explicitly, the Jones matrices of the linear polariser and the optical retarder rotated at an angle θ with respect to the x-axis are given respectively by:

$$\mathbf{P}(\theta) = \begin{bmatrix} \cos^2(\theta) & \sin(\theta)\cos(\theta) \\ \sin(\theta)\cos(\theta) & \sin^2(\theta) \end{bmatrix} \tag{17}$$

$$\mathbf{W}(2\beta,\theta)=\begin{bmatrix}\cos(\beta)-i\sin(\beta)\cos(2\theta) & -i\sin(\beta)\sin(2\theta)\\ -i\sin(\beta)\sin(2\theta) & \cos(\beta)+i\sin(\beta)\cos(2\theta)\end{bmatrix} \tag{18}$$

For instance, the Jones matrices of the diagonal and antidiagonal polarisers are obtained from Eq. (17) with $\theta=\pm 45^{o}$ and the result is:

$$\mathbf{P}(\pm 45^{o})=\frac{1}{2}\begin{bmatrix}1 & \pm 1\\ \pm 1 & 1\end{bmatrix} \tag{19}$$

and the Jones matrix for a rotated HWP is:

$$\mathbf{W}_H(\theta)=\begin{bmatrix}\cos(2\theta) & \sin(2\theta)\\ \sin(2\theta) & -\cos(2\theta)\end{bmatrix} \tag{20}$$

Next, two simple examples of Jones calculus useful in the works in this thesis are described.

Example1: Polarisation rotator by combination of two HWPs

The combination of two HWPs forms a polarisation rotator. If we consider the first HWP oriented at 0^{o} and the second HWP rotated by θ (Fig. 2.5), the resulting Jones matrix is:

$$\mathbf{W}_H(\theta)\cdot\mathbf{W}_H=[\mathbf{R}(\theta)\cdot\mathbf{W}_H\cdot\mathbf{R}(-\theta)]\cdot\mathbf{W}_H=\begin{bmatrix}\cos(2\theta) & -\sin(2\theta)\\ \sin(2\theta) & \cos(2\theta)\end{bmatrix}=\mathbf{R}(2\theta) \tag{21}$$

This Jones matrix is equivalent to a polarisation rotator described in Eq. (15) with rotation angle 2θ.

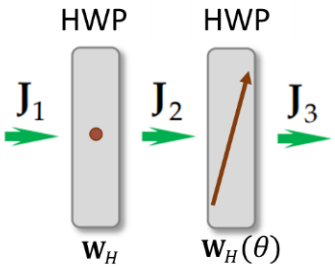

Figure 2.5: Realisation of an optical rotator using a combination of two half wave plates.

Example 2: Circular polariser by combination of a QWP and a linear polariser

The combination of two $x-y$ aligned QWPs and a linear polariser in between, oriented at $\pm 45^{o}$, produces a circular polariser [Coll 2005]. Figure 2.6 shows this assembly. The first QWP transforms a circular polarisation state onto a linear state at $\pm 45^{o}$ ($+45^{o}$ for input R and $-45^{o}$for input L) that is fully absorbed or fully transmitted by the linear polariser. A second QWP, crossed to the first one

transforms the light again onto the input circular polarisation state. Therefore, this assembly can operate both as a circular polariser and as a circular analyser.

The Jones matrix for the circular polarisers is thus given by:

$$\mathbf{P}_{R/L} = \mathbf{W}_Q(90^0) \cdot \mathbf{P}(45^o) \cdot \mathbf{W}_Q = \frac{1}{2}\begin{bmatrix} 1 & \mp i \\ \pm i & 1 \end{bmatrix} \tag{22}$$

where the upper sign refers to a R polariser and the bottom sign to a L polariser. In practical circular analysers, the last QWP is not necessary if only the final intensity is of interest.

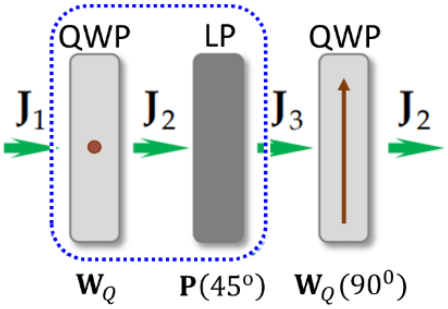

Figure 2.6: Realisation of a circular polariser.

Table 2.2 summarises the Jones matrices of some basic polarisation elements.

Polarising element	Horizontal linear polariser	Vertical linear polariser	Diagonal linear polarisers	Circular polarisers	Centered HWP	Centered QWP
	$\mathbf{P}(0^o)$	$\mathbf{P}(90^o)$	$\mathbf{P}(\pm 45^o)$	$\mathbf{P}_{R/L}$	$\mathbf{W}_H$	$\mathbf{W}_Q$
Jones matrix	$\begin{bmatrix} 1 & 0 \\ 0 & 0 \end{bmatrix}$	$\begin{bmatrix} 0 & 0 \\ 0 & 1 \end{bmatrix}$	$\frac{1}{2}\begin{bmatrix} 1 & \pm 1 \\ \pm 1 & 1 \end{bmatrix}$	$\frac{1}{2}\begin{bmatrix} 1 & \mp i \\ \pm i & 1 \end{bmatrix}$	$\begin{bmatrix} 1 & 0 \\ 0 & -1 \end{bmatrix}$	$\begin{bmatrix} 1 & 0 \\ 0 & -i \end{bmatrix}$

Table 2.2. Summary of some basic Jones matrices.

2.3 Stokes parameters and the Mueller matrix formalism

2.3.1 Stokes parameters and degree of polarisation

Polarisation of light can also be described by the **Stokes parameters**, which were introduced by George Gabriel Stokes in 1852 [Gold 2017]. These parameters offer a mathematically convenient way to describe fully polarised light, but also partially and unpolarised light (these latter not directly covered by the Jones calculus). The Stokes parameters are a set of four values that describe the polarisation state of light simply by intensity measurements. They are often arranged as a column matrix which is referred to as the Stokes vector:

$$\mathbf{S} = \begin{bmatrix} S_0 \\ S_1 \\ S_2 \\ S_3 \end{bmatrix} = \begin{bmatrix} I_x + I_y \\ I_x - I_y \\ I_D - I_A \\ I_R - I_L \end{bmatrix} = \begin{bmatrix} \langle E_x^* E_x \rangle + \langle E_y^* E_y \rangle \\ \langle E_x^* E_x \rangle - \langle E_y^* E_y \rangle \\ \langle E_x^* E_y \rangle - \langle E_y^* E_x \rangle \\ i\langle E_y^* E_x \rangle - i\langle E_x^* E_y \rangle \end{bmatrix} \tag{23}$$

Therefore, the S_0 parameter accounts for the total intensity of the optical beam. Parameter S_1 describes the preponderance of the linear H polarisation over the linear V polarisation. Similarly, parameter S_2 describes the preponderance of the linear D polarisation over the linear A polarisation. Finally, S_3 gives the preponderance of the circular R polarisation over the circular L polarisation.

The Stokes vector spans the space of unpolarised, partially polarised, and fully polarised light. The **degree of polarisation** (p) of an optical beam accounts for the fraction of the total beam intensity that is fully polarised and is defined as:

$$p = \frac{\sqrt{S_1^2 + S_2^2 + S_2^2}}{S_0} \qquad 0 \leq p \leq 1 \tag{24}$$

where $p = 1$ indicates fully polarised light, $p = 0$ indicates completely unpolarised light and $0 < p < 1$ represents partially polarised light.

Often, we work with the normalised Stokes vector $\mathbf{s} = \mathbf{S}/S_0 = [1 \quad s_1 \quad s_2 \quad s_3]^T$. The normalised Stokes parameters are obviously related to the ellipticity and azimuth parameters (ε, α) of the polarisation ellipse. The vector $\mathbf{s}$ can be expressed in terms of the azimuth and ellipticity as [Gold 2017]:

$$\mathbf{s}(p) = \begin{bmatrix} 1 \\ s_1 \\ s_2 \\ s_3 \end{bmatrix} = \begin{bmatrix} 1 \\ p\cos(2\varepsilon)\cos(2\alpha) \\ p\cos(2\varepsilon)\sin(2\alpha) \\ p\sin(2\varepsilon) \end{bmatrix} \tag{25}$$

For totally unpolarised light, $p = 0$, so $\mathbf{s}(p) = [1 \quad 0 \quad 0 \quad 0]^T$. Therefore, a general normalised Stokes vector in Eq. (25) can be written in the following general way:

$$\mathbf{s} = (1-p)\begin{bmatrix} 1 \\ 0 \\ 0 \\ 0 \end{bmatrix} + p\begin{bmatrix} 1 \\ \cos(2\varepsilon)\cos(2\alpha) \\ \cos(2\varepsilon)\sin(2\alpha) \\ \sin(2\varepsilon) \end{bmatrix} \tag{26}$$

where the first term in the summation represents the unpolarised component of the beam and the second term is the fully polarised component. Thus, the non-polarised intensity of the Stokes vector $\mathbf{S}$ in Eq. (23) is $S_0(1-p)$ and the fully polarised intensity is $S_0 p$, with S_0 being the total intensity of the optical beam.

The normalised Stokes vectors of the most common polarisation states are given in Table 2.3.

Polarisation state	*H*	*V*	*D*	*A*	*R*	*L*	*Unpolarised*
Normalised Stokes vector ($\mathbf{s}$)	$\begin{bmatrix} 1 \\ 1 \\ 0 \\ 0 \end{bmatrix}$	$\begin{bmatrix} 1 \\ -1 \\ 0 \\ 0 \end{bmatrix}$	$\begin{bmatrix} 1 \\ 0 \\ 1 \\ 0 \end{bmatrix}$	$\begin{bmatrix} 1 \\ 0 \\ -1 \\ 0 \end{bmatrix}$	$\begin{bmatrix} 1 \\ 0 \\ 0 \\ 1 \end{bmatrix}$	$\begin{bmatrix} 1 \\ 0 \\ 0 \\ -1 \end{bmatrix}$	$\begin{bmatrix} 1 \\ 0 \\ 0 \\ 0 \end{bmatrix}$

Table 2.3. Normalised Stokes vectors of the six cardinal polarisation states and for unpolarised light.

2.3.2 Mueller matrices

Within the Stokes formulation, polarising optical elements are described by **Mueller matrices**. These are 4×4 matrices whose elements are always real values (as opposed to the complex-valued Jones matrices), and they are represented as:

$$\widetilde{\mathbf{M}} = \begin{bmatrix} m_{00} & m_{01} & m_{02} & m_{03} \\ m_{10} & m_{11} & m_{12} & m_{13} \\ m_{20} & m_{21} & m_{22} & m_{23} \\ m_{30} & m_{31} & m_{32} & m_{33} \end{bmatrix} \tag{27}$$

Figure 2.7 illustrates the action of a polarising element, now described by its Mueller matrix $\widetilde{\mathbf{M}}$, which transforms an input polarisation state defined by a Stokes vector $\mathbf{S_1}$ into the output polarisation state defined by the Stokes vector $\mathbf{S_2}$.

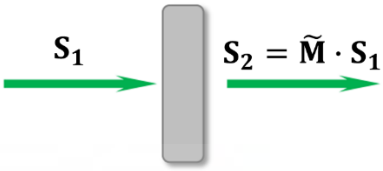

Figure 2.7: Mueller matrix representation of light propagating through a polarising optical element.

The optical elements discussed before with Jones matrices (polarisers, linear retarders, and optical rotators) can also be described by 4×4 Mueller matrices. But in addition, since Stokes parameters allow describing light with arbitrary degree of polarisation, depolarising optical devices are as well covered by Mueller calculus.

The Mueller matrix describing an element which is described by Jones matrix $\mathbf{M}$ can be calculated as [Gold 2017]:

$$\widetilde{\mathbf{M}} = \mathbf{a} \cdot [\mathbf{M} \otimes \mathbf{M}] \cdot \mathbf{a}^{-1} \tag{28}$$

where $\otimes$ denotes the tensor (Kronecker) product, and $\mathbf{a}$ is the 4×4 matrix given by:

$$\mathbf{a} = \begin{bmatrix} 1 & 0 & 0 & 1 \\ 1 & 0 & 0 & -1 \\ 0 & 1 & 1 & 0 \\ 0 & i & -i & 0 \end{bmatrix} \tag{29}$$

Alternatively, the elements m_{ij} of the Mueller matrix can be derived from the Jones matrix by:

$$m_{ij} = \frac{1}{2} \operatorname{Trace}\left[\mathbf{M} \cdot \boldsymbol{\sigma}_i \cdot \mathbf{M}^{\dagger} \cdot \boldsymbol{\sigma}_j\right] \tag{30}$$

where † denotes the Hermitian conjugate matrix and σ are Pauli matrices given by:

$$\boldsymbol{\sigma}_0 = \begin{bmatrix} 1 & 0 \\ 0 & i \end{bmatrix}, \boldsymbol{\sigma}_1 = \begin{bmatrix} 1 & 0 \\ 0 & -i \end{bmatrix}, \boldsymbol{\sigma}_2 = \begin{bmatrix} 0 & 1 \\ 1 & 0 \end{bmatrix}, \boldsymbol{\sigma}_3 = \begin{bmatrix} 0 & -i \\ i & 0 \end{bmatrix} \tag{31}$$

The Mueller matrix $\widetilde{\mathbf{P}}$ of a linear polariser equivalent to the Jones matrix in Eq. (11) takes the form:

$$\widetilde{\mathbf{P}} = \frac{1}{2}\begin{bmatrix} {P_x}^2 + {P_y}^2 & {P_x}^2 - {P_y}^2 & 0 & 0 \\ {P_x}^2 - {P_y}^2 & {P_x}^2 + {P_y}^2 & 0 & 0 \\ 0 & 0 & 2P_xP_y & 0 \\ 0 & 0 & 0 & 2P_xP_y \end{bmatrix} \tag{32}$$

where again P_x and P_y are real values representing the transmission for x and y linear polarisation respectively.

The perfect horizontal polariser ($P_x = 1, P_y = 0$) and the perfect vertical polariser ($P_x = 0, P_y = 1$) are then described by the following Mueller matrices:

$$\widetilde{\mathbf{P}}(0^o) = \frac{1}{2}\begin{bmatrix} 1 & 1 & 0 & 0 \\ 1 & 1 & 0 & 0 \\ 0 & 0 & 0 & 0 \\ 0 & 0 & 0 & 0 \end{bmatrix} \tag{33a}$$

$$\widetilde{\mathbf{P}}(90^o) = \frac{1}{2}\begin{bmatrix} 1 & -1 & 0 & 0 \\ -1 & 1 & 0 & 0 \\ 0 & 0 & 0 & 0 \\ 0 & 0 & 0 & 0 \end{bmatrix} \tag{33b}$$

Similarly, the Mueller matrix of a linear retarder with retardance 2β and neutral axes oriented along the $x - y$ directions, described with Jones matrix in Eq. (13) is:

$$\widetilde{\mathbf{W}}(2\beta) = \begin{bmatrix} 1 & 0 & 0 & 0 \\ 0 & 1 & 0 & 0 \\ 0 & 0 & \cos(2\beta) & -\sin(2\beta) \\ 0 & 0 & \sin(2\beta) & \cos(2\beta) \end{bmatrix} \tag{34}$$

The QWP and HWP with axes aligned with $x - y$ have respectively Mueller matrices:

$$\widetilde{\mathbf{W}}_Q = \begin{bmatrix} 1 & 0 & 0 & 0 \\ 0 & 1 & 0 & 0 \\ 0 & 0 & 0 & -1 \\ 0 & 0 & 1 & 0 \end{bmatrix} \tag{35}$$

$$\widetilde{\mathbf{W}}_H = \begin{bmatrix} 1 & 0 & 0 & 0 \\ 0 & 1 & 0 & 0 \\ 0 & 0 & -1 & 0 \\ 0 & 0 & 0 & -1 \end{bmatrix} \tag{36}$$

Finally, the Mueller matrix of a polarisation rotator takes the form:

$$\widetilde{\mathbf{R}}(\theta) = \begin{bmatrix} 1 & 0 & 0 & 0 \\ 0 & \cos(2\theta) & -\sin(2\theta) & 0 \\ 0 & \sin(2\theta) & \cos(2\theta) & 0 \\ 0 & 0 & 0 & 1 \end{bmatrix} \tag{37}$$

Like the Jones calculus, the rotation Mueller matrix applied to a polariser or to a retarder Mueller matrix, performs the in-plane rotation of the corresponding aligned element, and the transformation rule is given by:

$$\widetilde{\mathbf{M}}(\theta) = \widetilde{\mathbf{R}}(\theta) \cdot \widetilde{\mathbf{M}}(0) \cdot \widetilde{\mathbf{R}}(-\theta) \tag{38}$$

For a rotated linear polariser, it results in:

$$\widetilde{\mathbf{P}}(\theta) = \frac{1}{2}\begin{bmatrix} 1 & \cos(2\theta) & \sin(2\theta) & 0 \\ \cos(2\theta) & \cos^2(2\theta) & \sin(2\theta)\cos(2\theta) & 0 \\ \sin(2\theta) & \sin(2\theta)\cos(2\theta) & \sin^2(2\theta) & 0 \\ 0 & 0 & 0 & 0 \end{bmatrix} \tag{39}$$

and for a rotated linear retarder takes the form:

$$\widetilde{\mathbf{W}}(2\beta,\theta) = \begin{bmatrix} 1 & 0 & 0 & 0 \\ 0 & c^2(2\theta) + c(2\beta)\, s^2(2\theta) & (1 - c(2\beta))\, s(2\theta)\, c(2\theta) & -s(2\beta)\, s(2\theta) \\ 0 & (1 - c(2\beta))\, s(2\theta)\, c(2\theta) & s^2(2\theta) + c(2\beta)\, c^2(2\theta) & s(2\beta)\, c(2\theta) \\ 0 & s(2\beta)\, s(2\theta) & s(2\beta)\, c(2\theta) & c(2\beta) \end{bmatrix} \tag{40}$$

where c and s denote the cosine and sine functions.

As mentioned, in addition to polarisers, retarders and polarisation rotators, which can be described with Jones matrices, Mueller matrices can also describe depolarising elements. This is relevant especially for scattering samples, like biological tissues, where depolarisation is a major effect [Cana 2024]. The Mueller matrix of a **depolariser** with its principal depolarising axes aligned along the S_1, S_2 and S_3 axes is given by:

$$\widetilde{\mathbf{M}}_{\Delta} = \begin{bmatrix} 1 & 0 & 0 & 0 \\ 0 & a_1 & 0 & 0 \\ 0 & 0 & a_2 & 0 \\ 0 & 0 & 0 & a_3 \end{bmatrix} \tag{41}$$

where a_j are known as the principal depolarisation factors, and $\Delta_j = 1 - a_j$ are the depolarisances along the S_1, S_2 and S_3 axes. An ideal complete depolariser $\widetilde{\mathbf{M}}_{\Delta}$, which fully depolarises any input light is described by a Mueller matrix where all elements are zero except $m_{00} = 1$.

Table 2.4 below shows the Mueller matrices of the same elements described with the Jones matrices in Table 2.2, and for the total depolariser.

Polarising Element	Horizontal linear polariser	Vertical linear polariser	Diagonal linear polarisers	Circular polarisers
Mueller matrix	$\widetilde{\mathbf{P}}(0^o)$	$\widetilde{\mathbf{P}}(90^o)$	$\widetilde{\mathbf{P}}(\pm 45^o)$	$\widetilde{\mathbf{P}}_{\mathrm{R/L}}$
	$\begin{bmatrix} 1 & 1 & 0 & 0 \\ 1 & 1 & 0 & 0 \\ 0 & 0 & 0 & 0 \\ 0 & 0 & 0 & 0 \end{bmatrix}$	$\begin{bmatrix} 1 & -1 & 0 & 0 \\ -1 & 1 & 0 & 0 \\ 0 & 0 & 0 & 0 \\ 0 & 0 & 0 & 0 \end{bmatrix}$	$\begin{bmatrix} 1 & 0 & \pm 1 & 0 \\ 0 & 0 & 0 & 0 \\ \pm 1 & 0 & 1 & 0 \\ 0 & 0 & 0 & 0 \end{bmatrix}$	$\begin{bmatrix} 1 & 0 & 0 & \pm 1 \\ 0 & 0 & 0 & 0 \\ 0 & 0 & 0 & 0 \\ \pm 1 & 0 & 0 & 1 \end{bmatrix}$

Polarising Element	Centered HWP	Centered QWP	Total depolariser
Mueller matrix	$\widetilde{\mathbf{W}}_H$	$\widetilde{\mathbf{W}}_Q$	$\widetilde{\mathbf{M}}_\Delta$
	$\begin{bmatrix} 1 & 0 & 0 & 0 \\ 0 & 1 & 0 & 0 \\ 0 & 0 & -1 & 0 \\ 0 & 0 & 0 & -1 \end{bmatrix}$	$\begin{bmatrix} 1 & 0 & 0 & 0 \\ 0 & 1 & 0 & 0 \\ 0 & 0 & 0 & -1 \\ 0 & 0 & 1 & 0 \end{bmatrix}$	$\begin{bmatrix} 1 & 0 & 0 & 0 \\ 0 & 0 & 0 & 0 \\ 0 & 0 & 0 & 0 \\ 0 & 0 & 0 & 0 \end{bmatrix}$

Table 2.4. The Mueller matrices of the same common polarising optical elements.

2.4 The Poincaré sphere

The Stokes parameters can be graphically represented using the Poincaré sphere. This is a very convenient 3D representation to describe polarised light, as well as the action of retarders and polarisers on an input polarisation state [Gold 2017]. Recalling the equations that relate cartesian coordinates to spherical coordinates, the normalised Stokes parameters s_1, s_2 and s_3 of the fully polarized component in Eq. (25) are the three cartesian coordinates of a point on the surface of the sphere of radius p and located at latitude 2α and altitude 2ε.

This is shown in Fig. 2.8. Linearly polarized states have ellipticity angle $\varepsilon = 0^0$, and therefore they lie on the equator of the Poincaré sphere. Circular R and L states (where $\varepsilon = \pm 45^0$) lie on the north and south poles respectively. The north and south hemispheres correspond to right and left helicities respectively, and the states along a parallel have the same ellipticity while states along a meridian share the same azimuth. Polarisation states that are orthogonal lie in antipodal points on the sphere. The degree of polarisation p is the radius of the point represented in the sphere. Therefore, partially polarised light lies inside the sphere and the centre of the sphere corresponds to totally unpolarised light.

As light interacts with different polarisation optical elements, the resulting transformation of the polarisation state can be represented on the Poincaré sphere. For instance, the action of a retarder is visualised as rotation of the Poincaré sphere. A retarder is defined by its two eigenstates and its retardance. The eigenstates correspond to polarisation states that are not modified after transmission through the retarder, and they define the fast (F) and slow (S) states that are phase-shifted in the retarder. In the typical case of a linear retarder, the two eigenstates lie in opposite points in the equator. They define the axis of rotation on the Poincaré sphere, with a rotation angle equal to the retardance 2β, as shown in Fig. 2.9(a). This way, the action of the retarder is visualised directly for all states of polarisation in a single figure.

On the other hand, the action of a polariser is visualised as a projection onto the state P that is fully transmitted, typically a linear state parallel to the transmission axis of a linear polariser. All states on the Poincaré sphere with the same spherical angle γ with this point P transmit a relative intensity $T(\gamma) = \cos^2(\gamma)$, a relation which is known as the generalised Malus law. This is shown in Fig. 2.9(b).

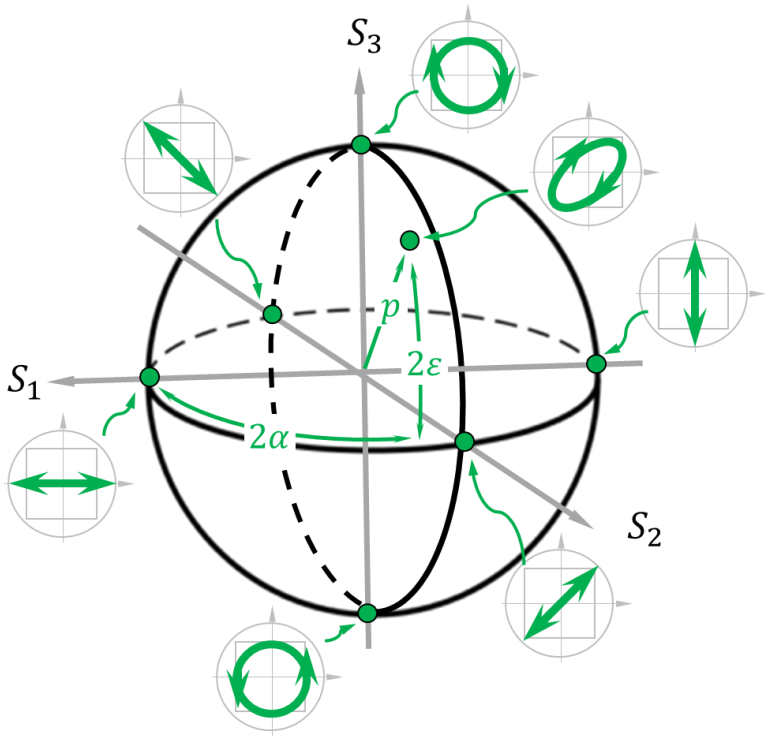

Figure 2.8: Graphical representation of polarisation states on the Poincaré sphere.

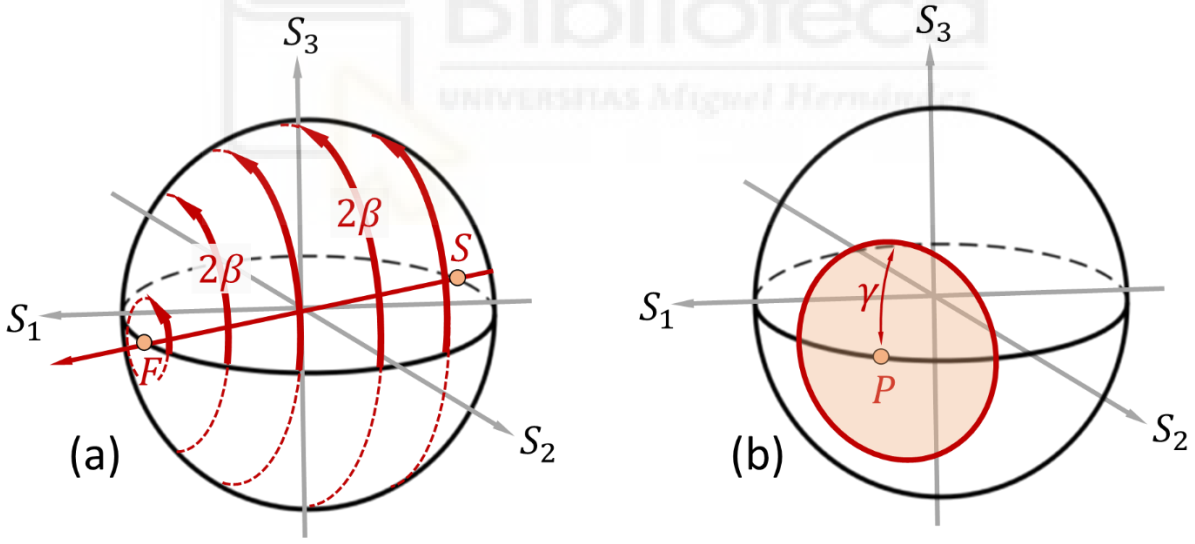

Figure 2.9: Poincaré sphere transformation as light propagates through polarisation optical devices (a) Retarder (b) Linear polariser.

2.5 Liquid-Crystal Modulators

The thesis comprises of several liquid crystal-based devices useful for controlling the polarisation of light. Liquid crystals (LCs) are categorised according to their respective phases, commonly referred to as mesophases [Scha 2006]. On a molecular scale, these mesophases are distinguished according to their type of ordering, i.e. positional order and orientational order [Mito 2014]. Positional order regards to whether molecules are arranged in any manner of ordered lattice and orientational order

to whether molecules are mostly pointing in the same direction [DeGe 1993] [DiLi 2001]. This alignment along a preferential direction is called the **LC director** axis. The common mesophases include nematic phases, smectic phases, and chiral phases.

The nematic is the simplest LC phase, whose molecules lack a positional order although perform self-alignment with their long axes roughly parallel, as shown in figure 2.10(a). Nematic LCs have fluidity similar to that of ordinary isotropic liquids. Therefore, they can easily be aligned by an external magnetic or electric field. In addition, they exhibit uniaxial optical properties [Scha 2006].

On the other hand, in smectic phases the molecules form well-defined layers that can slide over one another. Thus, smectics LCs are considered positionally ordered along one direction. They can further be categorized into two phases, the smectic A phase, whose molecules orient along the layer normal, while in the smectic C phase the molecules tilt away from it as shown in the Fig. 2.10(b) below.

Finally, the chiral phases exhibit chirality (handedness) and a twisting of the molecules perpendicular to the director [Gray 1973] as shown in Fig. 2.10(c). The significant twist angle between adjacent molecules is due to their asymmetric packing.

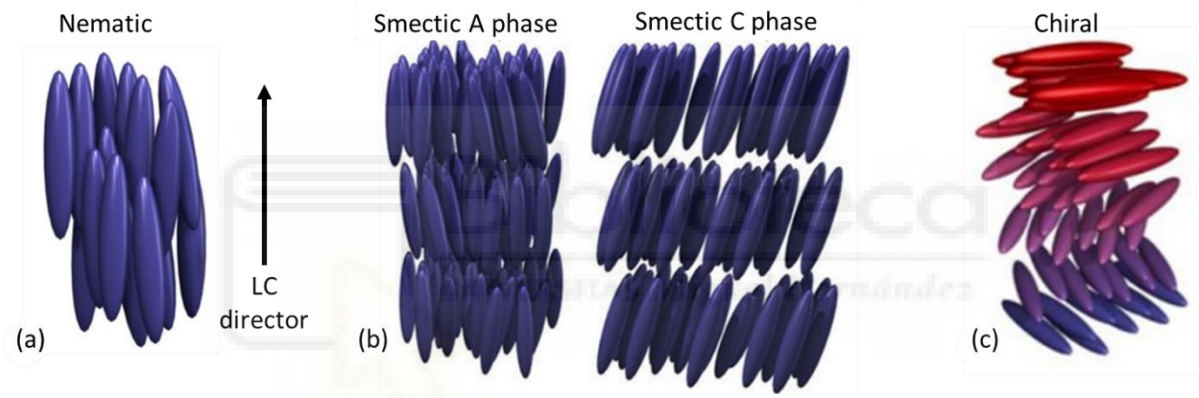

Figure 2.10: Liquid crystal phases (a) Nematic phase (b) Smectic phase (c) Chiral phase (figure adapted from Wikipedia Link)

LC modulators are optical devices that use LC materials to modify and control the intensity, phase, or polarisation of light waves. The orientation of LC molecules in the modulator can be modified by an external electric field to produce the optical modulation. Their most popular application is for displaying images in pixilated displays (LCDs). However, their ability to modulate the phase and the state of polarisation makes these devices extremely useful in interferometric, polarimetric and diffractive optical systems.

Figure 2.11 shows the typical structure of a LC modulator cell. The active LC material is sandwiched between alignment layers, precision glass substrates and protective cover glasses. Spacers are included to assure a precise thickness of the LC layer. Typically, they include also anti-reflection coatings and sometimes also polarisers.

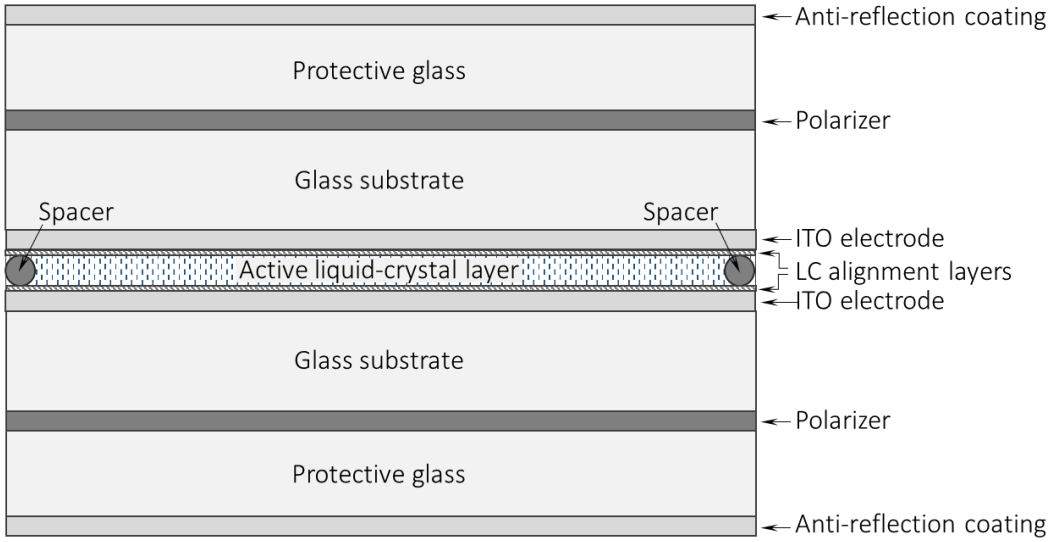

Figure 2.11: Structural representation of a standard LC cell.

The alignment layers define the orientation of the LC molecules and serve to design different configurations of the LC modulators. Historically, alignment of the LC layer was realised by rubbing electrodes on polymer covered glass substrates. These techniques were widely applied in mass production of LCDs. However, mechanical contact during rubbing can result in impurities and damaged products. Rubbing also creates a static charge that might damaged sensitive and increasingly miniature electronics in displays [Seki 2014]. More recently photoalignment involves orienting LCs to a desired alignment by exposure to short wavelength polarized light. It is basically a contactless process which allows LC alignment even in mechanically inaccessible areas. Another advantage is the possible alignment of small domains which results in extremely high-quality precision with the aid of optical imaging techniques. The technique facilitates the production of thin-film optical patterned retarder devices known as geometric-phase diffractive waveplates [Ji 2017].

The modulation characteristics of the LC cell are facilitated by the transparent and conductive electrodes. Usually, indium tin oxide (ITO) films are used for creating an electric field on the LC layers. Most LC molecules tend to align in a direction parallel to the electric field generated by these two transparent electrodes. However, due to the advancement in technical demands of different applications, with a need for flexible LCDs and multilayer structures [Hako 2017], some alternative candidates have been applied, like graphene, which exhibits high optical transparency, chemical inertness, and excellent conductivity [Zuru 2014].

The structure of the modulator cell (Fig. 2.11) is similar in most modulators. But different modulators configurations have been developed depending on the alignment of the LC layers. Applying the nematic, smectic, and chiral LC phases results in different modulators of varying optical properties.

2.5.1 Electrically-controlled birefringence (ECB) modulators

Firstly, the implementation of nematic phase material in parallel aligned configuration results in linear retarders with tunable retardance. These are known as electrically-controlled birefringence (ECB) modulators. These are two main types: the parallel-aligned (PAL) modulator and the vertically-aligned (VAN) modulator. The figure 2.12(a) below shows the principle of operation of the most common PAL modulator. When no voltage is applied the LC director is parallel to the substrate and maximum

birefringence is observed. When $V > 0$, the electric field provokes a tilt of the molecular LC director that causes a reduction of the effective birefrigence.

In the VAN configuration shown in Fig. 2.12(b), the LC molecules are arranged perpendicular to the glass substrates (homeotropic alignment) and the LC material must respond to the electric field by orienting the director in the perpendicular direction. The use of vertical aligned nematic (VAN) modulators is not as popular for phase-only modulators as compared to PAL modulators. However, it is used for displaying applications due to the high on-axis contrast ratio, wide viewing angle, good cost-performance, and simultaneous usability for reflective and transmissive mode.

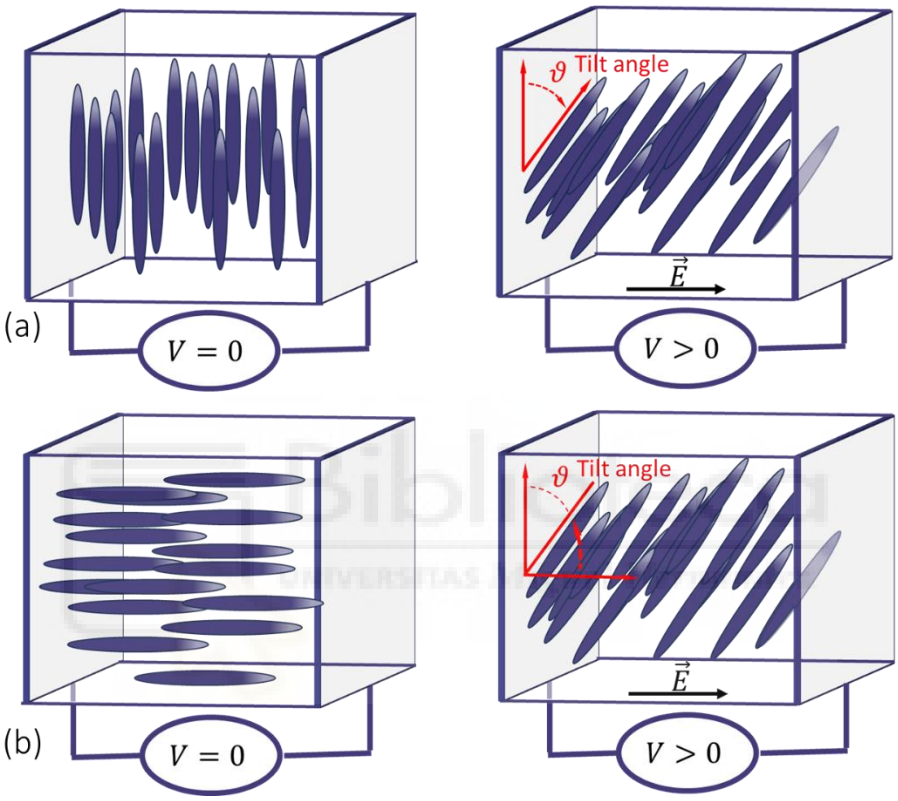

Figure 2.12: Operation of electrically-controlled birefringence (ECB) modulators (a) Parallel aligned nematic (PAL) liquid crystal modulator (b) vertically aligned nematic (VAN) liquid crystal modulator.

Essentially, the PAN and VAN modulators are equivalent in the sense that they are both linear retarders. That is why they are together referred to as ECB modulators or liquid-crystal retarders (LCRs). The Jones matrix describing the polarisation properties of these LC modulators is:

$$\mathbf{M}_{LCR} = \begin{bmatrix} e^{i\varphi_o} & 0 \\ 0 & e^{i\varphi_e(V)} \end{bmatrix} \equiv \begin{bmatrix} 1 & 0 \\ 0 & e^{i2\beta(V)} \end{bmatrix} \tag{42}$$

where the LC axis is considered oriented vertically. The ordinary phase φ_o is therefore aligned in the x-axis and does not change with the applied voltage V. The extraordinary phase $\varphi_e(V)$ changes with the applied voltage, so does the effective retardance $2\beta(V) = \varphi_e(V) - \varphi_o$. The tilt angle is controlled by the applied voltage $\vartheta = \vartheta(V)$, so

$$2\beta(\vartheta) = \frac{2\pi}{\lambda}\Delta n_{eff}(\vartheta) \cdot t \tag{43}$$

with t being the thickness of the LC layer, λ the wavelength of the light and Δn_{eff} the effective birefringence of the cell given by $\Delta n_{eff} = n_{eff}(\vartheta) - n_{\mathrm{o}}$, where the effective extraordinary index of refraction depends on the tilt angle as:

$$\frac{1}{n_{eff}^2(\vartheta)} = \frac{\cos^2(\vartheta)}{n_e^2} + \frac{\sin^2(\vartheta)}{n_{\mathrm{o}}^2} \tag{44}$$

If a linearly polarized beam of light is impinged onto the ECB-LC modulator, parallel to the LC director, the phase of the beam is modulated without change of the polarisation state, i.e., phase only modulation occurs [Marti 2014]. Using Jones calculus, this is shown as:

$$\mathbf{M}_{LCR} \cdot \begin{bmatrix} 0 \\ 1 \end{bmatrix} = e^{i2\beta(V)} \begin{bmatrix} 0 \\ 1 \end{bmatrix} \tag{45}$$

However, if the polarisation of the impinged light is at 45^0 with respect to the orientation of the LC director, polarisation modulation occurs. This is described in Jones formulation as:

$$\mathbf{M}_{LCR} \cdot \frac{1}{\sqrt{2}}\begin{bmatrix} 1 \\ 1 \end{bmatrix} = \frac{1}{\sqrt{2}}\begin{bmatrix} 1 \\ e^{i2\beta(V)} \end{bmatrix} \tag{46}$$

showing that the emerging polarisation state always has azimuth $\alpha = \pm 45^0$, but changes ellipticity as the retardance 2β changes with voltage. Following the discussion on Fig. 2.9(a), the voltage-controlled variations in β results in a trajectory in the Poincaré sphere along the meridian in the $S_2 - S_3$ plane. For $2\beta = \pi/2$ or $2\beta = 3\pi/2$, circular states are obtained. For $2\beta = \pi$, the linear state with $\alpha = 135^0$ azimuth is obtained.

Lastly, intensity modulation can be attained by placing the modulator between polarisers oriented at 45^0. In this case, the Jones matrix sequence is given by:

$$\frac{1}{2}\begin{bmatrix} 1 & 1 \\ 1 & 1 \end{bmatrix} \cdot \mathbf{M}_{LCR} \cdot \frac{1}{\sqrt{2}}\begin{bmatrix} 1 \\ 1 \end{bmatrix} = \cos[\beta(V)]\frac{1}{\sqrt{2}}\begin{bmatrix} 1 \\ 1 \end{bmatrix} \tag{47}$$

The corresponding normalised transmittance of the output beam is $I = \cos^2(\beta)$, which shows a transition from null to full transmission with β as it changes from $\pi/2$ to zero.

This intensity modulation is usually employed to characterise ECB-LC modulators [Wu 1984]. In this situation, the normalised intensity transmission given by Eq. (47) can be used to calculate the retardance with monochromatic light by changing the applied voltage. Alternatively, illuminating the

retarder with a broad spectrum and analysing with a spectrometer [Varg 2013] [Mess 2018], the spectral retardance function $\beta(\lambda, V)$ can be measured.

2.5.2 Twisted-nematic modulators

Twisted nematic (TN) LC technology is the oldest and primal technology breakthrough that made LCDs practical in display technology (intensity modulation). The nature of the TN-LC modulator incorporates a twist due to the perpendicular alignment of the LC molecules on each side of the LC cell (Fig. 2.13(a)). The twist angle is typically of 90^0, although super-twisted modulators have been also produced. When a voltage is applied to the electrodes, the electric field reorients the LC molecular director which tends to be aligned with the field, thus tilting and destroying the twist structure. Only the LC layers coated to the surfaces of the cell are not capable to tilt (Fig. 2.13(b)).

Without voltage input linearly polarised light follows the twist angle, and this happens approximately in wide range of wavelength, thus allowing a polarisation rotation, as shown in Fig. 2.13(a). When voltage is applied and the twist structure disappears, the polarisation rotation is cancelled.

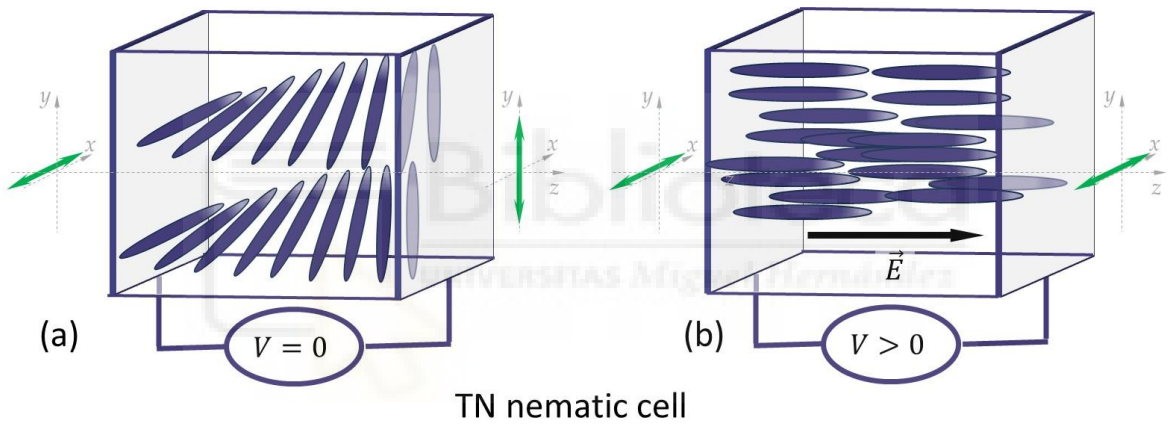

Figure 2.13: Operation of a twisted nematic (TN) liquid crystal modulator.

The Jones matrix for such twisted anisotropic structure was derived by Yariv and Yeh [Yari 1984] who described it by considering the cell divided in N layers, each with width $\Delta Z = t/N$, a retardance $\Delta\beta = (\beta/t)\Delta Z$, and a rotation with respect to the previous layer $\Delta\alpha = (\alpha/t)\Delta Z$. Here β is the global retardance given by Eq. (43) and α is the total twist from the input to the output surface of the LC modulator. This allows an analytical calculation that leads to a Jones matrix that depends only on α and β parameters and takes the form [Marq 2000] [Fern 2000]:

$$\mathbf{M}_{TNLC} = e^{-i\beta}\,\mathbf{R}(\alpha)\begin{bmatrix} X - iY & Z \\ -Z & X + iY \end{bmatrix} \tag{48}$$

where,

$$X = \cos\gamma \tag{49a}$$

$$Y = \frac{\beta}{\gamma}\sin\gamma \tag{49b}$$

$$Z = \frac{\alpha}{\gamma}\sin\gamma \tag{49c}$$

$$\gamma = \sqrt{\alpha^2 + \beta^2} \tag{49d}$$

Later, Lu and Saleh [Lu 1990] introduced a voltage dependant retardance parameter $\beta(V)$ like in Eq. (43) to describe the optical modulation properties of the TN-LC modulator, a work that was taken as the reference to evaluate and optimise TN-LC modulators and led to other more refined models which consider the edge LC layers that cannot tilt [Marq 2000].

2.5.3 Ferroelectric liquid crystal modulators

Implementation of the smectic phase materials in modulators is commonly referred to as ferroelectric LC modulators (FLC). The commonest arrangement is in surface stabilized geometry [Clar 1984] [Lage 2004]. This configuration involves an in-plane switching of the FLC director between two stable orientations upon application of a bipolar voltage. Figure 2.14 shows the operation of a standard FLC modulator where the retardance is adjusted to a HWR retarder for the operating wavelength and the switching angle is of 45^0. In this situation, input linearly polarised light oriented parallel to the LC director in one of the stable positions remains with the same output polarisation, while for the second LC stable state rotates to the perpendicular orientation. In fact, for any input linear state, the two outputs are two orthogonal linear states [Martí 2006].

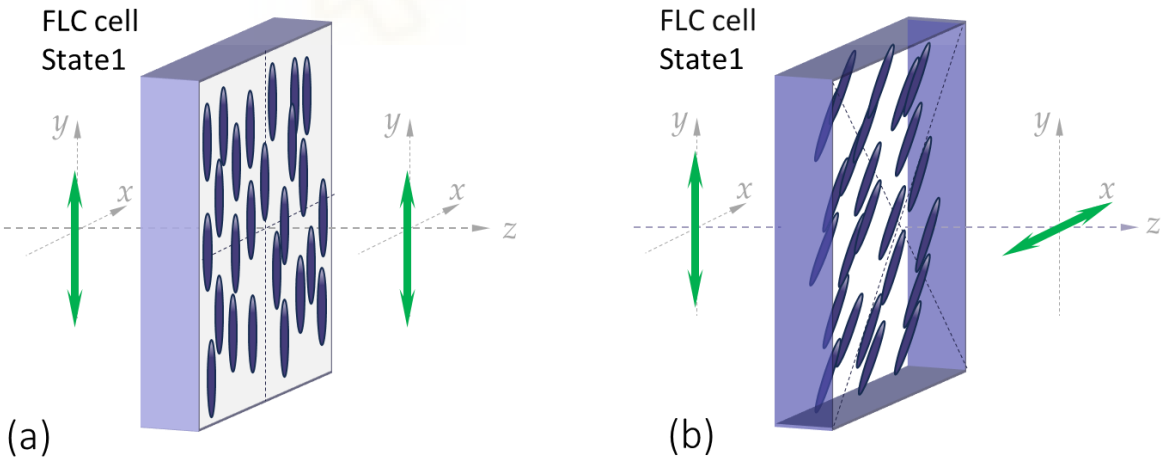

Figure 2.14: Operation of a ferroelectric liquid crystal (FLC) modulator.

Intensity and phase modulation is achieved with this configuration simply by the placing a linear polariser (analyser) after the FLC modulator. When the analyser is oriented parallel or perpendicular to one of the polarisation states emerging from the modulator as shown below in Fig. 2.15(a), the intensity modulation is realised, with ideally null transmission for one state and ideally maximum transmission for the second state. On the other hand, orienting the analyser at 45^0 with respect to the

polarisations of the emerging beam, the binary π phase-only modulation is achieved, as indicated in Fig. 2.15(b). The two electric fields of the light emerging from the FLC modulator project with opposite directions onto the polariser transmission axis, thus leading to the relative π phase shift.

The great advantage of FLC modulators is that they can be operated at frequencies much higher than nematic LC modulators. However, they are limited to be binary modulators as opposed to nematic modulators that produce continuous modulation.

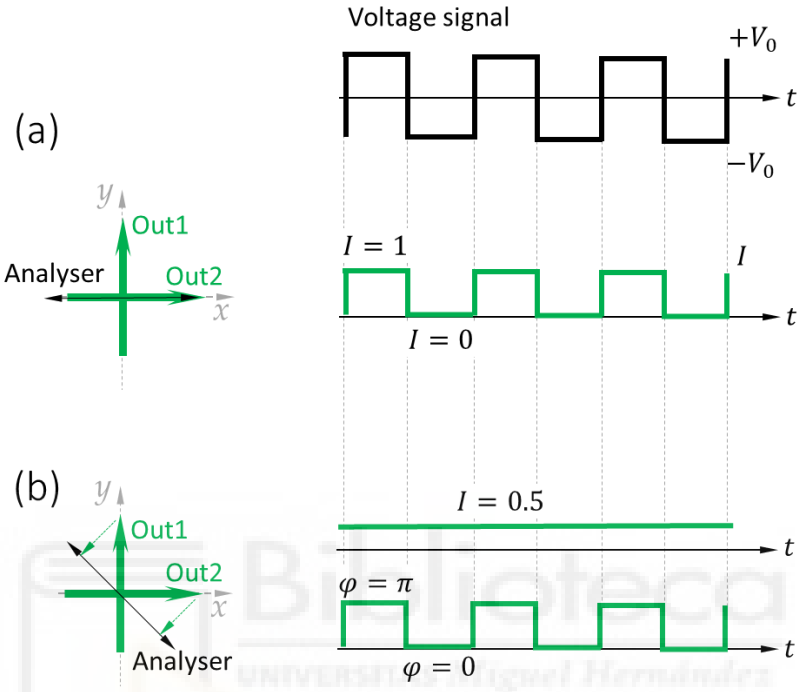

Figure 2.15: Scheme for FLC modulation (a) Binary intensity modulation configuration (b) Binary π phase modulation configuration.

2.6 Optical polarimetry

Polarimetry is a sensitive non-destructive measuring technique that uses the changes in the polarisation state to measure properties of different materials [Tinb 1996]. Application of optical polarimetry cuts across different fields of science, for instance, in remote sensing such as planetary science, astronomy, and weather radar [Dubo 2019], in biological, biomedical and clinical imaging [He 2021] as well as in materials science and gemology [Mart 1989].

A polarimeter comprises of three major parts: the polarisation state generator (PSG), the sample under study and a polarisation state analyser (PSA), as shown in figure 2.16. The PSG is an optical system that generates the different states of polarisation that are used to illuminate the sample. The PSA is another optical system that incorporates a detector and polarisation filters to measure different polarisation components.

The different polarimetric systems are categorised according to the polarisation acquisition techniques [Powe 2013]. Depending on the application at hand, polarimetric information can be acquired in image form using a detector camera (imaging polarimeter) or with single point measurements applying devices like photodiodes or powermeters (point polarimeter). However, imaging polarimeters are of much more interest since they provide a 2D map of polarisation changes.

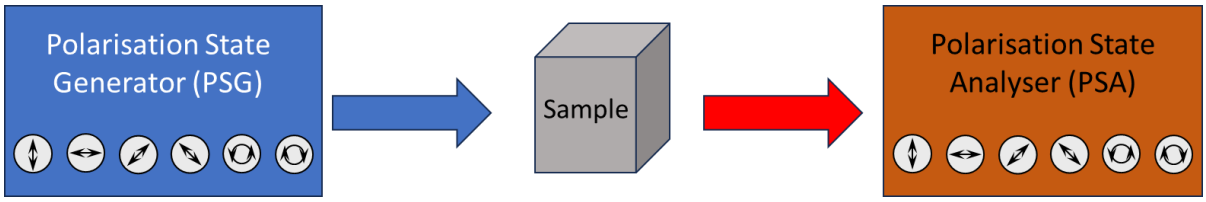

Figure 2.16: Structural representation of a basic polarimetric system.

Some of the commonly applied schemes include division-of-time (DoT) polarimeter, which involves placement of in-time varying optical filters in front of the imaging capturing device, division-of amplitude (DoA) polarimeter, which requires splitting of the image into multiple paths with different optics as well as image planes, and division-of-focal plane (DoFP) polarimeter, where the image is split by a repeated pattern of pixel-pitch matched polarisation filters that are directly placed onto the pixel of the camera detector, known as polarisation cameras [More 2016]. These techniques can record either complete or partial Stokes parameters across the image plane. Many different polarimetric set-ups have been implemented to measure the full 4×1 Stokes vector $\mathbf{S}$ (Stokes polarimeter) or the 4×4 Mueller matrix $\widetilde{\mathbf{M}}$ (Mueller polarimeter) [Azza 2016].

2.6.1 Mueller matrix polarimetry formulation

A typical Mueller matrix polarimetric system as the one shown in Figure 2.19 involves the generation with the PSG of different input states of polarisation. A minimum number of 4 states is required, but traditionally the generation and analysis of the 6 cardinal states of polarisation (H, V, A, D, R and L) has been used [Chip 1995]. Similarly, the PSA incorporates polariser analysers that transmit the same states of polarisation.

The use of liquid-crystal retarders (LCR) in polarimetric systems has widely been adopted as they eliminate any mechanical movements in the system [Lópe 2020]. Other advantages include wider spectral range of operation, low power consumption and increased operational speed of the system.

When the six standard cardinal states are used as the input PSA and output PSA states, the Mueller matrix elements can be retrieved with the equations indicated in Table 2.5 [Gold 2017]. These equations assume ideal PSG and PSA, with the first index of the intensities I_{ij} representing the analysed state (PSA) and the second index indicating the input or generated state (PSG).

m_{00} $\frac{1}{2}\begin{pmatrix} I_{HH}+I_{VH} \\ +I_{HV}+I_{VV} \end{pmatrix}$	m_{01} $\frac{1}{2}\begin{pmatrix} I_{HH}+I_{VH} \\ -I_{HV}-I_{VV} \end{pmatrix}$	m_{02} $\frac{1}{2}\begin{pmatrix} I_{HD}+I_{DV} \\ -I_{HA}-I_{VA} \end{pmatrix}$	m_{03} $\frac{1}{2}\begin{pmatrix} I_{HR}+I_{VR} \\ -I_{HL}-I_{VL} \end{pmatrix}$
m_{10} $\frac{1}{2}\begin{pmatrix} I_{HH}-I_{VH} \\ +I_{HV}-I_{VV} \end{pmatrix}$	m_{11} $\frac{1}{2}\begin{pmatrix} I_{HH}-I_{VH} \\ -I_{HV}+I_{VV} \end{pmatrix}$	m_{12} $\frac{1}{2}\begin{pmatrix} I_{HD}-I_{VD} \\ -I_{HA}+I_{VA} \end{pmatrix}$	m_{13} $\frac{1}{2}\begin{pmatrix} I_{HR}-I_{VR} \\ -I_{HL}+I_{VL} \end{pmatrix}$
m_{20} $\frac{1}{2}\begin{pmatrix} I_{DH}-I_{AH} \\ +I_{DV}-I_{AV} \end{pmatrix}$	m_{21} $\frac{1}{2}\begin{pmatrix} I_{DH}-I_{AH} \\ -I_{AV}+I_{AV} \end{pmatrix}$	m_{22} $\frac{1}{2}\begin{pmatrix} I_{DD}-I_{YD} \\ -I_{DA}+I_{AA} \end{pmatrix}$	m_{23} $\frac{1}{2}\begin{pmatrix} I_{DR}-I_{AR} \\ -I_{DL}+I_{AL} \end{pmatrix}$
m_{30} $\frac{1}{2}\begin{pmatrix} I_{RH}-I_{LH} \\ -I_{LV}+I_{RV} \end{pmatrix}$	m_{31} $\frac{1}{2}\begin{pmatrix} I_{RH}-I_{LH} \\ -I_{RV}+I_{LV} \end{pmatrix}$	m_{32} $\frac{1}{2}\begin{pmatrix} I_{RD}-I_{LD} \\ -I_{RA}-I_{LA} \end{pmatrix}$	m_{33} $\frac{1}{2}\begin{pmatrix} I_{RR}-I_{LR} \\ -I_{RL}-I_{LL} \end{pmatrix}$

Table 2.5. Mueller matrix elements obtained from intensity information of a sample assuming PSA and PSA generating ideal cardinal H, V, A, D, R and L states.

However, the generation and detection of polarisation states typically include errors, thus affecting the retrieved result of the Mueller matrix elements. The sequential polarimeter calibration and optimization (SPCO) method [Garc 2013] is a procedure to compensate for possible errors in the PSG and PSA that consists of 3 relevant steps before introducing the sample into the system [Pein 2010] [Cofr 2017]. These steps include: (1) the separate calibration of the PSG to obtain the PSG-matrix $\mathbf{S}$, (2) the calibration of the PSA together with the PSG to obtain the intensity matrix $\mathbf{I}$ of the polarimeter without any sample, and lastly, (3) mathematical calculations of the PSA-matrix $\mathbf{A}$ from the experimental $\mathbf{S}$ and $\mathbf{I}$ matrices.

The $\mathbf{S}$ matrix is obtained by measuring the Stokes parameters of each PSG input state. They are written as columns given by S_{ig} where index $i = 0, 1, 2, 3$, represents the Stokes parameters and index $g = 0, 1, 2 \ldots . N - 1$ indicates the N states generated by the PSG. Thus, $\mathbf{S}$ is a $4 \times N$ matrix illustrated as:

$$\mathbf{S} = \begin{pmatrix} S_{00} & S_{01} & S_{02} & \ldots S_{0N-1} \\ S_{10} & S_{11} & S_{12} & \ldots S_{1N-1} \\ S_{20} & S_{21} & S_{22} & \ldots S_{2N-1} \\ S_{30} & S_{31} & S_{32} & \ldots S_{3N-1} \end{pmatrix} \tag{50}$$

A minimum number of $N = 4$ is required to achieve complete Stokes polarimetry. The Stokes parameters are measured with a calibrated polarimeter that is taken as a reference.

Then, the PSA section in introduced to the system, thus attaining a complete Mueller polarimeter. The PSA is defined by its analysers. For each input state generated by the PSG and for each configuration of the PSA, an intensity measurement I_{ag} is obtained as:

$$I_{ag} = (A_{a0} \quad A_{a1} \quad A_{a2} \quad A_{a3}) \begin{pmatrix} S_{0g} \\ S_{1g} \\ S_{2g} \\ S_{3g} \end{pmatrix} \tag{51}$$

where $(S_{0g} \quad S_{1g} \quad S_{2g} \quad S_{3g})^T$ denotes the Stokes parameters of the input state in the PSG (already measured in the $\mathbf{S}$ matrix) and $(A_{a0} \quad A_{a1} \quad A_{a2} \quad A_{a3})$ defines the state to which it is projected, i.e., the analyser. Here g is the index defining the PSG configuration and a is the index defining the PSA configuration.

The intensity matrix takes the form:

$$\mathbf{I} = \begin{pmatrix} I_{00} & I_{01} & I_{02} & \cdots I_{0\,N-1} \\ I_{10} & I_{11} & I_{12} & \cdots I_{1\,N-1} \\ I_{20} & I_{21} & I_{22} & \cdots I_{2\,N-1} \\ \vdots & \vdots & \vdots & \vdots \\ I_{N-1\,0} & I_{N-1\,1} & I_{N-1\,2} & \cdots I_{N-1\,N-1} \end{pmatrix} = \tag{52}$$

$$= \begin{pmatrix} A_{00} & A_{01} & A_{02} & A_{03} \\ A_{10} & A_{11} & A_{12} & A_{13} \\ A_{20} & A_{21} & A_{22} & A_{23} \\ \vdots & \vdots & \vdots & \vdots \\ A_{N-1\,0} & A_{N-1\,1} & A_{N-1\,2} & A_{N-1\,3} \end{pmatrix} \cdot \begin{pmatrix} S_{00} & S_{01} & S_{02} & \dots S_{0N-1} \\ S_{10} & S_{11} & S_{12} & \dots S_{1N-1} \\ S_{20} & S_{21} & S_{22} & \dots S_{2N-1} \\ S_{30} & S_{31} & S_{32} & \dots S_{3N-1} \end{pmatrix}$$

which can be written in compact form as:

$$\mathbf{I} = \mathbf{A} \cdot \mathbf{S} \tag{53}$$

where $\mathbf{S}$ is the $4 \times N$ matrix defined in Eq. (50), $\mathbf{A}$ is a $N \times 4$ matrix defining the PSA, and $\mathbf{I}$ is a $N \times N$ matrix (we assume that the same polarisation states are used in the PSG and PSA).

From equation (53), the $\mathbf{A}$ matrix can be calculated as:

$$\mathbf{A} = \mathbf{I} \cdot \mathbf{S}^{-1} \tag{54}$$

At this point the Mueller polarimeter is calibrated and the sample to analyse can be introduced into the system. Then, the sample Mueller matrix $\widetilde{\mathbf{M}}_S$ can be obtained from the $\mathbf{S}$ and $\mathbf{A}$ matrices as:

$$\widetilde{\mathbf{M}}_S = \mathbf{A}^{-1} \cdot \mathbf{I}_S \cdot \mathbf{S}^{-1} \tag{55}$$

where $\mathbf{I}_S$ is the new intensity matrix measured when the sample is introduced in the polarimeter. Matrices $\mathbf{A}$ and $\mathbf{S}$ are only square for $N = 4$. For higher values of N, $\mathbf{A}^{-1}$ and $\mathbf{S}^{-1}$ must be calculated as the pseudo inverses of $\mathbf{A}$ and $\mathbf{S}$ respectively, given by:

$$\mathbf{A}^{-1} = [\mathbf{A}^T \cdot \mathbf{A}]^{-1} \cdot \mathbf{A}^T \tag{56a}$$

$$\mathbf{S}^{-1} = \mathbf{S}^T \cdot [\mathbf{S} \cdot \mathbf{S}^T]^{-1} \tag{56b}$$

where the formula in Eq. 56(a) is valid for multiplying a matrix on the left, and the formula in Eq. 56(b) is valid for multiplying a matrix on the right.

2.6.2 Polarizance and diattenuation

The Mueller matrix (Eq. (27)) provides the complete information of the polarisation properties of the sample. It can be written in a compact way as:

$$\widetilde{\mathbf{M}} = m_{00} \begin{bmatrix} 1 & \vec{D}^T \\ \vec{P} & \mathbf{m} \end{bmatrix} \tag{57}$$

where $\vec{P}$ and $\vec{D}$ are the polarizance vector and diattenuation vector respectively, and $\mathbf{m}$ is the 3×3 normalised submatrix. m_{00} is the intensity transmitted by the sample when illuminated with totally unpolarised light. In this situation

$$\widetilde{\mathbf{M}} \cdot \begin{bmatrix} 1 \\ 0 \\ 0 \\ 0 \end{bmatrix} = \begin{bmatrix} m_{00} \\ m_{10} \\ m_{20} \\ m_{30} \end{bmatrix} \tag{58}$$

so the output S_0 parameter is m_{00}. The other three Stokes parameters of the output in Eq. (58) define the polarizance vector:

$$\vec{P} = \frac{1}{m_{00}} \begin{bmatrix} m_{10} \\ m_{20} \\ m_{30} \end{bmatrix}, \qquad P \equiv \left|\vec{P}\right| = \frac{1}{m_{00}} \sqrt{m_{10}^2 + m_{20}^2 + m_{30}^2} \tag{59}$$

Thus, its magnitude corresponds to the degree of polarisation of the output when the sample is illuminated with unpolarised light. It represents the ability of the sample to polarise unpolarised light.

On the other hand, the diattenuation vector is defined as:

$$\vec{D} = \frac{1}{m_{00}} \begin{bmatrix} m_{01} \\ m_{02} \\ m_{03} \end{bmatrix}, \qquad D \equiv \left|\vec{D}\right| = \frac{1}{m_{00}} \sqrt{m_{01}^2 + m_{02}^2 + m_{03}^2} \tag{60}$$

Its magnitude defines the changes in the intensity transmitted by the sample for different incident polarisation states as:

$$\left|\vec{D}\right| = \frac{T_{\max} - T_{\min}}{T_{\max} + T_{\min}} \tag{61}$$

where $T_{\max}$ and $T_{\min}$ are the intensities transmitted by the sample for the input states with maximum and with minimum transmission.

While for a polariser D and P are equivalent, the following example illustrates their differences: let us consider a combination of a horizontal linear polariser and a perfect depolariser. If the polariser is placed first, the total Mueller matrix of the combination is:

$$\widetilde{\mathbf{M}}_{\Delta} \cdot \widetilde{\mathbf{P}}(0^{\mathrm{o}}) = \begin{bmatrix} 1 & 0 & 0 & 0 \\ 0 & 0 & 0 & 0 \\ 0 & 0 & 0 & 0 \\ 0 & 0 & 0 & 0 \end{bmatrix} \cdot \begin{bmatrix} 1 & 1 & 0 & 0 \\ 1 & 1 & 0 & 0 \\ 0 & 0 & 0 & 0 \\ 0 & 0 & 0 & 0 \end{bmatrix} = \begin{bmatrix} 1 & 1 & 0 & 0 \\ 0 & 0 & 0 & 0 \\ 0 & 0 & 0 & 0 \\ 0 & 0 & 0 & 0 \end{bmatrix} \tag{62}$$

In this case the polarizance is null since the output is always unpolarised (the depolariser is placed as the last element). However, the diattenuation is $\vec{D} = [1 \quad 0 \quad 0]^T$ and $|\vec{D}| = 1$, since the input H state is fully transmitted, while the input V state is totally blocked.

On the contrary, if the depolariser is placed first, the Mueller matrix of the combined elements is now:

$$\widetilde{\mathbf{P}}(0^o) \cdot \widetilde{\mathbf{M}}_\Delta = \begin{bmatrix} 1 & 1 & 0 & 0 \\ 1 & 1 & 0 & 0 \\ 0 & 0 & 0 & 0 \\ 0 & 0 & 0 & 0 \end{bmatrix} \cdot \begin{bmatrix} 1 & 0 & 0 & 0 \\ 0 & 0 & 0 & 0 \\ 0 & 0 & 0 & 0 \\ 0 & 0 & 0 & 0 \end{bmatrix} = \begin{bmatrix} 1 & 0 & 0 & 0 \\ 1 & 0 & 0 & 0 \\ 0 & 0 & 0 & 0 \\ 0 & 0 & 0 & 0 \end{bmatrix} \tag{63}$$

Now the polarizance is $\vec{P} = [1 \quad 0 \quad 0]^T$ and $|\vec{P}| = 1$, indicating that input polarised light gets totally polarised. But diattenuation is null since any input state is transmitted with the same intensity. The reason is that the depolariser, located as the first element, provides always unpolarised light onto the polariser, thus always giving the same transmission for all inputs. Therefore, $|\vec{D}| = 0$.

2.6.3 The Mueller matrix polar decomposition

Different parameters of interest can be extracted from the information in the Mueller matrix and different decompositions have been proposed [Orte 2011] [Gil 2022]. The complete measurement of the Mueller matrix allows examining of different polarimetric parameters that characterise the sample and include typically the retardance, the depolarisation and the diattenuation [Lope 2020].

The classical Lu-Chipman polar decomposition [Lu 1996] describes a Mueller matrix $\widetilde{\mathrm{M}}$ as the product of three matrices:

$$\widetilde{\mathbf{M}} = \widetilde{\mathbf{M}}_\Delta \cdot \widetilde{\mathbf{M}}_R \cdot \widetilde{\mathbf{M}}_D \tag{64}$$

where $\widetilde{\mathrm{M}}_\Delta$ is a pure depolariser, $\widetilde{\mathrm{M}}_R$ is a pure retarder and $\widetilde{\mathrm{M}}_D$ is a pure diattenuator. Equation (64) can explicitly be expressed as:

$$\widetilde{\mathbf{M}} = m_{00} \begin{bmatrix} 1 & \vec{0}^T \\ \vec{P} & \mathbf{m}_\Delta \end{bmatrix} \cdot \begin{bmatrix} 1 & \vec{0}^T \\ \vec{0} & \mathbf{m}_R \end{bmatrix} \cdot \begin{bmatrix} 1 & \vec{D}^T \\ \vec{D} & \mathbf{m}_D \end{bmatrix} \tag{65}$$

Here $\vec{D}$ is the diattenuation vector, $\vec{P}$ is the polarizance vector as defined in Eqs. (59)-(60), $\mathbf{m}_\Delta$, $\mathbf{m}_R$ and $\mathbf{m}_D$ are the 3×3 submatrices of $\widetilde{\mathbf{M}}_\Delta$, $\widetilde{\mathbf{M}}_R$, $\widetilde{\mathbf{M}}_D$, and $\vec{0}^T = [0\ 0\ 0]$.

The decomposition procedure primarily begins with the extraction of the diattenuation matrix $\widetilde{\mathbf{M}}_D$. The 3×3 submatrix $\mathbf{m}_D$ is calculated as:

$$\mathbf{m}_D = \sqrt{1 - D^2}\, \boldsymbol{I_d} + \left(1 - \sqrt{1 - D^2}\right) \vec{D}\, \vec{D}^T \tag{66}$$

where $D = |\vec{D}|$ and $\boldsymbol{I_d}$ is the 3×3 identity matrix. The nature of $\widetilde{\mathbf{M}}_D$ determines the next steps of extraction of retardance and depolarisation matrix.

Case 1: When the diattenuation matrix is singular, as it is the case for polarisers, the decomposition of Mueller matrix $\widetilde{\mathbf{M}}$ takes the following form:

$$\widetilde{\mathbf{M}} = m_{00}\begin{bmatrix} 1 & \vec{D} \\ \vec{P} & \vec{P}\cdot\vec{D}^T \end{bmatrix} = \begin{bmatrix} 1 & \vec{0}^T \\ \vec{0} & P\boldsymbol{I_d} \end{bmatrix}\cdot\widetilde{\mathbf{M}}_R\cdot m_{00}\begin{bmatrix} 1 & \vec{D}^T \\ \vec{D} & \vec{D}\vec{D}^T \end{bmatrix} \tag{67}$$

The retardance vector is calculated as:

$$\vec{R} = \frac{\vec{P}\times\vec{D}}{\left|\vec{P}\times\vec{D}\right|}\arccos\left(\frac{\vec{P}}{\left|\vec{P}\right|}\cdot\vec{D}\right) \tag{68}$$

The depolarisation parameter on the other hand takes the form $\Delta = 1 - \left|\vec{P}\right|$ and the orientation of the polariser transmission axis is obtained as:

$$\theta_T = \frac{1}{2}\arctan\left(\frac{m_{02}}{m_{01}}\right) \tag{69}$$

Case 2: In the general case when the diattenuation matrix is non-singular $\widetilde{\mathbf{M}}_D^{-1}$ can be calculated as:

$$\widetilde{\mathbf{M}}_D^{-1} = \frac{1}{a^2}\begin{bmatrix} 1 & \vec{D}^T \\ -\vec{D} & \boldsymbol{I_d} \end{bmatrix} + \frac{1}{a^2(a+1)}\begin{bmatrix} 0 & \vec{0}^T \\ \vec{0} & \vec{D}\vec{D}^T \end{bmatrix} \tag{70}$$

where $a = \sqrt{1-D^2}$. $\widetilde{\mathbf{M}}_R$ and $\widetilde{\mathbf{M}}_\Delta$ are then retrieved from the matrix $\widetilde{\mathbf{M}}' = \widetilde{\mathbf{M}}\cdot\widetilde{\mathbf{M}}_D^{-1} = \widetilde{\mathbf{M}}_R\cdot\widetilde{\mathbf{M}}_\Delta$ expressed as:

$$\widetilde{\mathbf{M}}' = \begin{bmatrix} 1 & \vec{0}^T \\ \vec{P}_\Delta & \mathbf{m}_\Delta \end{bmatrix}\cdot\begin{bmatrix} 1 & \vec{0}^T \\ \vec{0} & \mathbf{m}_R \end{bmatrix} = \begin{bmatrix} 1 & \vec{0}^T \\ \vec{P}_\Delta & \mathbf{m}_\Delta\mathbf{m}_R \end{bmatrix} \tag{71}$$

where $\mathbf{m}_\Delta$ and $\mathbf{m}_R$ are 3×3 sub-matrices of $\widetilde{\mathbf{M}}_\Delta$and $\widetilde{\mathbf{M}}_R$.

$\vec{P}_\Delta$ is the polarizance vector associated to the depolariser, which is given by:

$$\vec{P}_\Delta = \frac{\vec{P}-\mathbf{m}\cdot\vec{D}}{1-D^2} \tag{72}$$

Considering $\mathbf{m}' = \mathbf{m}_\Delta\cdot\mathbf{m}_R$ and $\lambda_1,\lambda_2,\lambda_3$ the eigen values of $\mathbf{m}'\cdot(\mathbf{m}')^T$, then $\mathbf{m}_\Delta$ is defined as:

$$\mathbf{m}_\Delta = \pm\left[\mathbf{m}'(\mathbf{m}')^T + \left(\sqrt{\lambda_1\lambda_2} + \sqrt{\lambda_2\lambda_3} + \sqrt{\lambda_1\lambda_3}\right)\boldsymbol{I_d}\right]^{-1}\left[\left(\sqrt{\lambda_1} + \sqrt{\lambda_2} + \sqrt{\lambda_3}\right)\mathbf{m}'(\mathbf{m}')^T + \sqrt{\lambda_1\lambda_2\lambda_3}\,\boldsymbol{I_d}\right] \quad (73)$$

The sign in Eq. (73) is positive if $\det(\mathbf{m}') > 0$ and negative if $\det(\mathbf{m}') < 0$. Having $\vec{P}_\Delta$ and $\mathbf{m}_\Delta$ completes the elements required to obtain the depolarisation matrix $\widetilde{\mathbf{M}}_\Delta$. The depolarisation parameter Δ is then calculated as:

$$\Delta = 1 - \frac{1}{3}\left[\mathrm{trace}\left(\widetilde{\mathbf{M}}_\Delta\right) - 1\right], \qquad 0 \le \Delta \le 1 \quad (74)$$

Finally, the retarder matrix $\widetilde{\mathbf{M}}_R$ is obtained from $\widetilde{\mathbf{M}}_R = \widetilde{\mathbf{M}}_\Delta^{-1}\widetilde{\mathbf{M}}'$ and the corresponding retardance parameter is calculated as:

$$R = \begin{cases} \arccos\left[\frac{1}{2}\mathrm{trace}\left(\widetilde{\mathrm{M}}_R\right) - 1\right] & \text{if } 0 \le R \le \pi \\ 2\pi - \arccos\left[\frac{1}{2}\mathrm{trace}\left(\widetilde{\mathrm{M}}_R\right) - 1\right] & \text{if } \pi \le R \le 2\pi \end{cases} \quad (75)$$

The retardance vector $\vec{R}$ can be obtained from the Mueller elements of the matrix $\widetilde{\mathbf{M}}_R$ as [Gold 2017]:

$$\vec{R} = \begin{bmatrix} R_1 \\ R_2 \\ R_3 \end{bmatrix} = \frac{R}{2\sin R}\begin{bmatrix} \widetilde{\mathrm{M}}_{R23} - \widetilde{\mathrm{M}}_{R32} \\ \widetilde{\mathrm{M}}_{R31} - \widetilde{\mathrm{M}}_{R13} \\ \widetilde{\mathrm{M}}_{R12} - \widetilde{\mathrm{M}}_{R21} \end{bmatrix} \quad (76)$$

This vector defines the fast (F) and slow (S) axes around which the Poincare sphere rotates. In case of a linear retarder, the orientation of the optical axis θ_S is calculated as:

$$\theta_S = \frac{1}{2}\arctan\left(\frac{R_2}{R_1}\right) \quad (77)$$

2.7 Phase-shifting interferometry

Interferometry is the technique implemented to retrieve information from the interference of superimposed waves. This section reviews the phase-information retrieval technique commonly referred to as the phase shifting interferometry (PSI). This is a well-established technique that relies on digitalisation of interferograms acquired adding controlled phase shifts in one of the interfering beams [DeGr 2011]. The principle of operation of the PSI technique requires a number N of phase-shift steps [Crea 1988] [Kinn 1988]. The classical method for producing the phase modulation between the two beams was by means of a piezoelectric transducer (PZT). Another method uses a variation of

frequency of the laser [Lai 1991]. However, the emergence of the LC technology made LCRs common devices for implementing the PSI technique.

In addition, the polarisation sensitivity of LC modulators makes them useful to build polarisation common-path interferometers. Common-path interferometry refers to the interferometric arrangements where the reference and test beams are not separated; instead, they follow the same path, with the great advantage that they are insensitive to vibrations, thus suitable for applications in non-controlled environments. Polarisation common path interferometers usually employ birefringent beam splitters like Wollaston and Rochon prisms [Fran 1971]. Also, through holography, LC displays can enable the simultaneous building of the interferometer, either by displaying a diffraction grating [Marti 2016] or using the light reflected on the device coating [Marc 2020].

2.7.1 PSI algorithms

Many different PSI algorithms have been proposed, depending on the number of phase steps and the phase values. Here we review the most common cases, summarized in Table 2.5. The intensity of an interference pattern of two beams takes the form [Kinn 1988]:

$$I(x,y) = I_0(x,y)\{1 + V(x,y)\cos[\alpha(x,y) + \varphi]\} \tag{78}$$

where $I_0(x,y)$ is the intensity, $V(x,y)$ is the visibility of the interference fringes, $\alpha(x,y)$ is the phase pattern to be measured, φ is an arbitrary reference constant phase value, and (x,y) denote the coordinates of the camera in the interferometric setup, where the fringe pattern is detected.

The PSI algorithms use N-interferograms $I_n(x,y)$ captured by varying the constant phase term $\varphi = \varphi_n$. Equation (78) can be expanded as:

$$\begin{aligned} I_n(x,y) = I_0(x,y) + I_0(x,y)V(x,y)\cos[\alpha(x,y)]\cos(\varphi_n) - \\ - I_0(x,y)V(x,y)\sin[\alpha(x,y)]\sin(\varphi_n) \end{aligned} \tag{79}$$

Now multiplying each interference pattern $I_n(x,y)$ by $\cos\varphi_n$ or by $\sin\varphi_n$, summing with respect to $n = 0, 1, 2, \ldots N-1$, and applying the orthogonality of trigonometry functions, the following relations are obtained:

$$C(x,y) = \sum_{n=0}^{N-1} I_n(x,y)\cos\varphi_n = \frac{N}{2} I_0(x,y)V(x,y)\cos[\alpha(x,y)] \tag{80a}$$

$$S(x,y) = \sum_{n=0}^{N-1} I_n(x,y)\sin\varphi_n = \frac{N}{2} I_0(x,y)V(x,y)\sin[\alpha(x,y)] \tag{80b}$$

$$\sum_{n=0}^{N-1} I_n(x,y) = N I_0(x,y) \tag{80c}$$

From relations 80(a) and 80(b), the phase pattern $\alpha(x,y)$ can be retrieved as:

$$\tan[\,\alpha(x,y)] = \frac{C(x,y)}{S(x,y)} \tag{81}$$

which does not depend on the average intensity $I_0(x,y)$, neither on the visibility $V(x,y)$.

In most cases, the phase-shifts are selected equi-spaced in the 2π phase range, i.e., if N steps are selected, the phase values are:

$$\varphi_n = n\frac{2\pi}{N} \qquad n = 0,1,2,\ldots.N-1 \tag{82}$$

and therefore $\alpha(x,y)$ can be calculated from Eq. (81) as:

$$\tan[\alpha(x,y)] = -\frac{\sum_{n=0}^{N-1} I_n(x,y)\sin(\varphi_n)}{\sum_{n=0}^{N-1} I_n(x,y)\cos(\varphi_n)} \tag{83}$$

The typical case considers $N = 4$, with phase shifts of $\pi/2$. In this case, Eq. (83) leads to

$$\tan[\alpha(x,y)] = \frac{I_2 - I_0}{I_3 - I_1} \tag{84}$$

where for simplicity we omit the (x,y) dependence of the intensities I_n.

If a greater number N of phase-shifts are applied, the accuracy of the phase retrieval can be improved. For instance, for $N = 8$ equi-spaced phase-shifts, Eq. (83) leads to

$$\tan[\alpha(x,y)] = \frac{2(I_0 - I_4) + \sqrt{2}(I_1 - I_3 - I_5 + I_7)}{2(I_2 - I_6) + \sqrt{2}(I_1 + I_3 - I_5 - I_7)} \tag{85}$$

On the contrary, for $N = 3$ steps, with equi-spaced phase-shifts of $2\pi/3$, Eq. (83) leads to

$$\tan[\alpha(x,y)] = \frac{\sqrt{3}\,(I_1 - I_0)}{2I_2 - I_1 - I_0} \tag{86}$$

For $N = 3$ however, it has been demonstrated that a better approach is to use three steps separated by phase-shift of $\pi/2$. In this case, Eq. (83) does not hold, and the general procedure [Crea 1988] leads to the asymmetric solution:

$$\tan[\alpha(x,y)] = \frac{I_2 - I_1}{I_0 - I_1} \tag{87}$$

In some cases, the standard case with $N = 4$ (Eq. (84)) suffers from phase mismatch in the device producing the phase-shift. In this case, adding a fifth phase step with $\varphi_4 = 2\pi$ has proven useful, a technique called the Schwider-Hariharan algorithm [Goodw 2006]. In principle, I_4 should be equal to I_0, but if there are differences, the phase is retrieved as:

$$\tan[\alpha(x,y)] = \frac{2(I_3 - I_1)}{2I_2 - I_0 - I_4} \tag{88}$$

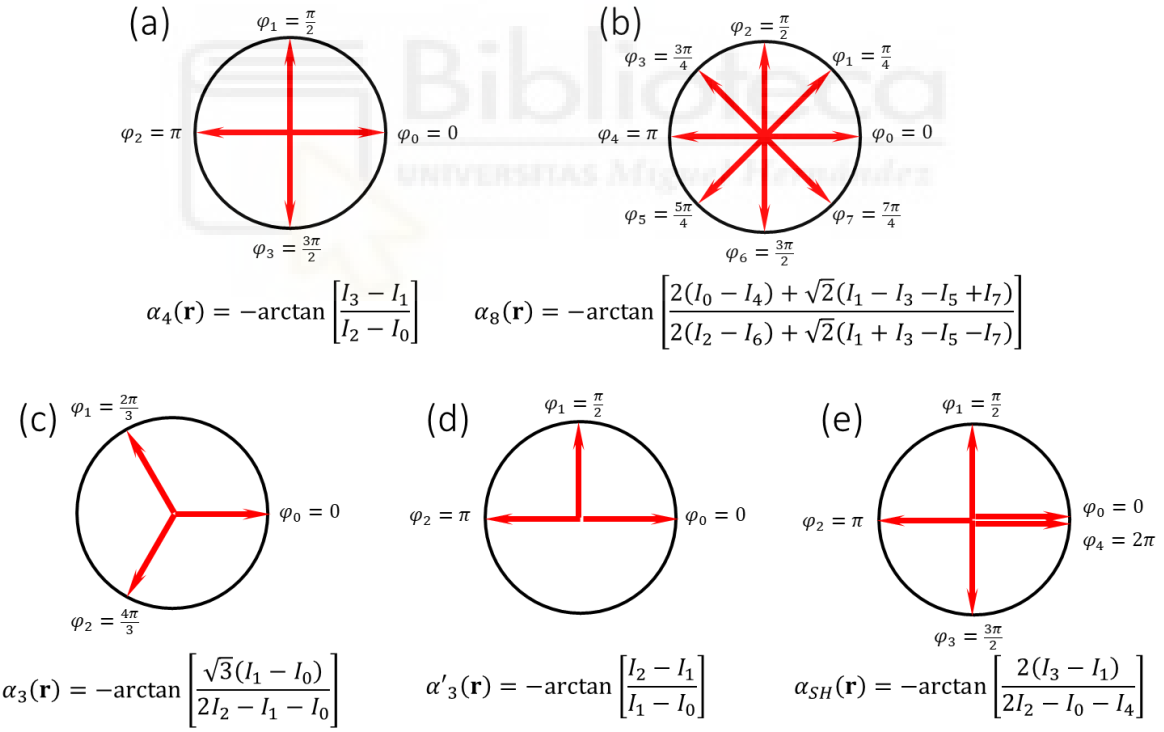

Table 2.5. Summary of examples of some classical PSI algorithms: (a-c) Algorithms with equally spaced phase shifts with (a) $N = 4$, (b) $N = 8$ and (c) $N = 3$ steps. (d) Algorithm with $N = 3$ and non-equally spaced phase shifts. € Schwider-Hariharan algorithm.

2.8 Spatial light modulators and digital holography

Digital holography is a technique that typically uses phase-only holograms displayed on a pixilated micro-display (known as spatial light modulator (SLM)) to generate a light beam with shaped properties, a field that is known as **structured light** [Rubi 2017]. It has in general facilitated new advances in classical and quantum optics, including communication, microscopy, imaging, or metrology. The computer-generated holograms are displayed onto the SLM as gray-tone images displayed from a computer [Rosa 2017].

2.8.1 Spatial light modulators (SLM)

SLMs are devices that modulate the intensity, phase, or polarization of light in a spatially varying manner. Thanks to their high resolution and number of pixels, these devices have been widely used to provide laser beam shaping, aberration control, optical computing, etc through the display of diffractive optical elements (DOE).

There are reflective and transmissive SLMs [Harr 2005]. However, most of the SLM devices are reflective since they can be produced with higher resolution. Reflective SLMs are categorised into two main technologies: Liquid-crystal SLMs and digital micromirror devices (DMDs). LC-SLMS are limited in terms of refresh rate and threshold intensity limit as compared to DMDs. However, they pose a significant advantage especially to directly produce phase and polarisation modulation [Marc 2019], a task that cannot be performed by DMDs as they are limited to binary amplitude modulation.

In this thesis, we have used a PAL liquid crystal on silicon (LCOS) SLM. The LC layer is embedded between a transparent electrode as shown in Fig. (2.11) and a pixelated electrode layer. This allows a pixel level adjusting of the effective birefringence by applying a voltage controlled via the gray level image addressed from a computer. Just like single pixel LC modulators, LC-SLMs can be produced as ECB, TN or FLC modulators. Parallel-aligned (PAL) LC-SLMs are very popular since they are phase-only SLMs for linearly polarised light parallel to the LC director.

This pixilated LC retarder operates as a phase-only modulator or a retarder modulator on the principle discussed in subsection 2.5.1. An important task before implementing digital holography in the SLM is its calibration. This is performed by applying a technique discussed before, where the LC retarder is placed between crossed polarisers and the intensity transmission is measured. The actual calibration of the LCOS-SLM device used in this thesis is provided in the discussion chapter.

Other than the LC material used, the effectiveness of the SLM also depends on the pixel pitch and interpixel gaps which generates a 2D grid and diffraction orders. Some secondary effects that might degrade the response of the SLM are the flicker (which is exhibited as a phase fluctuation), the crosstalk between pixels (referred to as fringing effect), and backplane deformation that introduce aberrations [Marc 2019]. Due to all these effects, the diffraction efficiency of SLMs is not 100%. These ineffectiveness of the operation of the SLMs are practically visualised as a light component that is not affected by the displayed computer-generated hologram which is normally 5% to 20% depending on the fabrication quality of the modulator [Rosa 2017]. This light component normally propagates on axis together with the modulated component and if not separated, the two interfere. In this thesis, this phenomenon is utilised to an advantage of realising a common path interferometer. However, the separation of the two components can be achieved simply by adding a blazed diffraction grating to the displayed hologram, this moving the modulated component an angle away from the axis.

2.8.2 Phase-only diffraction gratings

The simplest digital hologram to display in the SLM can be considered to be a diffraction grating. In the thesis, the standard approximations in Fourier optics are considered, i.e. the diffractive element is evaluated in a Fourier transform (FT) related plane, within the paraxial approximation, obtained either by analysing the far field diffraction (Fraunhofer diffraction) or by using a converging lens to obtain the FT in its back focal plane. The diffractive element has features larger than the wavelength, so the scalar approximation can be considered [Goodm 2005]. Under such conditions, the transmission profile of a diffraction grating can be decomposed into an infinite sum of plane waves by means of a Fourier series as:

$$t(x) = e^{i\alpha(x)} = \sum_{-\infty}^{+\infty} t_n e^{in2\pi x/p} \tag{89}$$

where a one-dimensional phase-only grating $e^{i\alpha(x)}$ is considered. Here p is the period of the grating.

Every exponential in Eq. (89) is a plane wave generating a diffraction order given by the integer number n. The Fourier coefficient t_n is expressed as:

$$t_n = \frac{1}{p}\int_0^p t(x)e^{-in2\pi x/p}\,dx \tag{90}$$

and gives the amplitude of the corresponding diffraction order. The intensity of each diffraction order is the square of its magnitude $I_n = |t_n|^2$.

The linear phase grating also known as the **blazed grating**, generates a single first diffraction order. Its phase profile is $\alpha_{Blazed}(x) = [2\pi x/p]_{\mathrm{Mod}\ 2\pi}$, so its transmission function takes the form:

$$t_{Blazed}(x) = e^{i2\pi x/p} \tag{91}$$

When displayed on the SLM, blazed gratings have the possibility of achieving almost 100% of the light diffracted in the displaced first order provided the period is large enough so it is not severely affected by quantization.

Another interesting phase-only grating is the **optimal triplicator** grating derived by Gori and colleagues [Gori 1998]. The phase profile is also continuous thus again requiring large periods to avoid quantization. It has the ability of achieving the maximum diffraction efficiency when generating three equi-energetic orders (0 and ± 1) with a scalar phase function. The phase function of the optimal triplicator is:

$$\alpha_{Trip}(x) = \arctan\left[a\cos\left(\frac{2\pi x}{p}\right)\right] \tag{92}$$

where $a = 2.65718\ldots$. The respective transmission function can be approximated as:

$$t_{Trip}(x) = e^{i\alpha_{Trip}(x)} \cong c_0\left(1 + ie^{i2\pi x/p} + ie^{-i2\pi x/p}\right) \tag{93}$$

with $c_0 \cong \sqrt{0.31}$, and where we neglected the other weak higher order terms. Note the i factors in the two exponential terms in Eq. (93) which indicate a $\pi/2$ phase-shift of the ± 1 diffraction orders with respect to the zero order [Marc 2019].

The diffractive lens can be considered as a diffraction grating where the period changes with the square of the radial coordinate. Its transmission function is another phase-only function that takes the form:

$$t_{lens}(x,y) = e^{-i\frac{\pi}{\lambda f}(x^2+y^2)} = e^{-i\frac{\pi r^2}{\lambda f}} \tag{94}$$

where $r = \sqrt{x^2 + y^2}$ is the radial coordinate at the plane of the lens, λ is the wavelength and f is the lens focal length. This is a 2D phase function that can be implemented in a phase-only SLM provided the focal length f is large enough to avoid problems of resolution.

2.8.3 Gaussian modes

In this thesis we have used digital holograms that generate Gaussian modes. The Hermite-Gaussian modes (HG_{nm}) and the Laguerre-Gaussian modes $\left(LG_P^l\right)$ are the set of solutions to the paraxial wave equation in cartesian coordinates and in cylindrical coordinates respectively [Rosa 2017]. Their complex-amplitude is given by:

$$G(x,y,z) = A(x,y)\, e^{-i\alpha(x,y,z)}\, e^{-\frac{r^2}{w^2(z)}}\, e^{i\frac{kr^2}{2R(z)}} \tag{95}$$

where, $w(z)$ is the beam width and $R(z)$ is the beam radius of curvature, given by:

$$w(z) = w_0\left[1 + \left(\frac{z}{z_R}\right)^2\right] \tag{96}$$

$$R(z) = z\left[1 + \left(\frac{z_R}{z}\right)^2\right] \tag{97}$$

Here w_0 is the beam waist and z_R is Rayleigh range of the beam.

The magnitude function $A(x,y)$ for the HG modes is given by:

$$A_{HG}(x,y,z) = \frac{A_{mn}}{w(z)}\, H_m\left(\frac{\sqrt{2}\,x}{w(z)}\right) H_n\left(\frac{\sqrt{2}\,y}{w(z)}\right) \tag{98}$$

while for the LG modes is given by:

$$A_{LG}(x,y) = \frac{A_p^{|\ell|}}{w(z)}\left(\frac{\sqrt{2}\,r}{w(z)}\right)^{|\ell|} L_p^{|\ell|}\left(\frac{\sqrt{2}\,r^2}{w^2(z)}\right) \tag{99}$$

In Eq. (98), $A_{mn} = \sqrt{2^{1-m-n}/\pi\, m!\, n!}$ and H_m is the $m-th$ Hermite polynomial, while in Eq. (99), $A_p^{|\ell|} = \sqrt{2/(\pi\, p! + (|\ell| + p)!)}$ and $L_p^{|\ell|}$ is the generalised Laguerre polynomial.

The corresponding phases $e^{-i\alpha}$ in Eq. (95) take the form:

$$e^{-i\alpha_{HG}} = e^{-i(n+m+1)\xi(z)} \tag{100}$$

$$e^{-i\alpha_{LG}} = e^{-i(2p+|\ell|+1)\xi(z)}\, e^{il\vartheta} \tag{101}$$

where, n, m are positive integers, ℓ the topological charge, p the radial index, ϑ the azimuthal angle. $\xi(z)$ is known as the Gouy phase which is an additional phase shift that the wavefront acquires around the focal region, which takes the form:

$$\xi(z) = \arctan\left(\frac{z}{z_R}\right) \tag{102}$$

Figure 2.17 shows the magnitude and phase of some of these Gaussian beams.

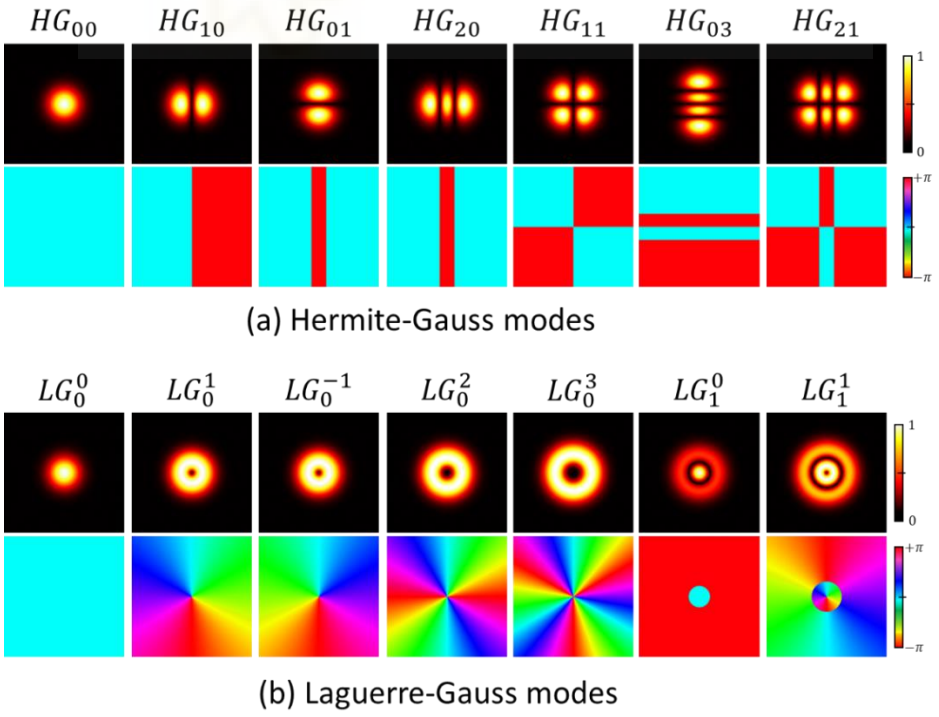

Figure 2.17: Some examples of structured Gaussian beam on a spatial light modulator.

2.8.4 Encoding complex functions on phase-only SLMs

Phase-only SLMs such as the LCOS device employed in this thesis cannot be used to directly encode complex-valued holograms (as required for instance to encode the Gaussian modes discussed in the previous subsection). This is why several techniques have been proposed to design phase-only functions that are capable to reproduce complex functions [Marti 2018]. This is usually achieved by diffracting light out of the main beam, so this can be filtered to behave as if there has been magnitude modulation.

In this thesis we have applied one popular technique [Arri 2003] [Mend 2014] where the main modulated beam is on axis. In the technique, given a target complex function $F(x,y) = M(x,y)e^{i\alpha(x,y)}$ (M and α denote here the magnitude and phase of the complex function), then a new phase-only function $e^{i\alpha_H(x,y)}$ is calculated as:

$$\alpha_H(x,y) = \alpha(x,y) + (-1)^{m+n}\arccos[M(x,y)] \tag{103}$$

where m,n are now the integer numbers denoting the pixel coordinates at the SLM and $M(x,y)$ is assumed normalised with values in the range $[0,1]$.

The term $(-1)^{m+n}$ in Eq. (103) is equivalent to a π-phase binary checkboard 2D diffraction grating that is modulated by the arccosine term. A binary-phase diffraction grating has no light on the zero diffraction order when the phase difference between the two levels is π. Therefore, when displaying the phase-only hologram $\alpha_H(x,y)$, regions where $M(x,y)$ is small will diffract light away from the centre while the light remains on axis in the regions where $M(x,y)$ is large. Consequently, filtering these higher orders, leaves only the beam on the axis that well reproduces the complex function $F(x,y)$.

3. Discussions

This chapter discusses the main results and achievements obtained in the thesis. It also summarizes the experimental and theoretical procedures taken to accomplish the objectives of the thesis, which have led to these results. It elaborates the practical realisation and characterisation of two liquid-crystal optical modulators showing different optical characteristics that are discussed in the previous chapter i.e., a twisted nematic LC modulator and a ferroelectric LC modulator. These kind of devices (both in single and in pixelated nature) are implemented in the two core optical systems discussed in this thesis, namely: a Mueller matrix imaging polarimeter and a common-path-phase shifting interferometer.

The studies have yielded the following five articles published in peer-reviewed international journals:

(a). **E. Nabadda**, G. López-Morales, D. Marco, M. M. Sánchez-López, and I. Moreno. "Mueller matrix polarimetric analysis applied to characterize the physical parameters of a twisted-nematic liquid-crystal modulator." *Optics and Laser Technology* 156(3), 108567 (2022). DOI JCR Index 5.0 (JCR 2022, Optics, Q1)

(b). **E. Nabadda**, N. Bennis, M.Czerwinski, A.Walewska, L. R. Jaroszewicz, M. M. Sánchez-López, and I. Moreno. "Ferroelectric liquid-crystal modulator with large switching rotation angle for polarization-independent binary phase modulation." *Optics and Lasers in Engineering* 159(2), 107204 (2022). DOI JCR Index 4.2 (JCR 2022, Optics, Q1)

(c). **E. Nabadda**, P. García-Martínez, M. M. Sánchez-López, and I. Moreno. "Phase-shifting common-path polarization self-interferometry for evaluating the reconstruction of holograms displayed on a phase-only display." *Frontiers in Physics* 10, 920111 (2022). DOI JCR Index 3.1 (JCR 2022, Physics-Multidisciplinary, Q2)

(d). **E. Nabadda**, M. M. Sánchez-López, P. García-Martínez, and I. Moreno. "Retrieving the phase of diffraction orders generated with tailored gratings." *Optics Letters* 48(2), 267-270 (2023). DOI JCR Index 3.6 (JCR 2022, Optics, Q2) **[selected in Editor's pick]**

(e). **E. Nabadda**, M. M. Sánchez-López, A. Vargas, A. Lizana, J. Campos, and I. Moreno. "Mueller matrix imaging polarimeter with polarization camera self-calibration applied to structured light components." *Journal of the European Optical Society - Rapid Publications* 20(1), 5 (2024). DOI JCR Index 1.5 (JCR 2022, Optics, Q4)

In addition, I presented these works in the following conferences:

- Work (a) was presented as a poster at the *XXIII Conference on Liquid Crystals 2021* held in Karpacz, Poland, and again virtually presented as a poster at the *XIII Reunión Nacional de Óptica 2021*.
- Work (b) was presented as a poster at the *2022 Siegman International School on Lasers* held in Chęciny, Poland.

- Work (c) was orally presented at the *XXXVIII Reunión Bienal de la Real Sociedad Española de Física, 2022* held in Murcia, Spain, and virtually presented as a poster at the *2022 Workshop on Structured light and its Applications*, Jena, Germany, where it won the first prize for the best poster presentation.
- Work (e) was presented as a poster at the *XIII Reunión Nacional de Optoelectrónica (OPTOEL 2023)* held in Sevilla, Spain, and presented as an oral presentation at the *European Optical Society Annual Meeting (EOSAM 2023)* held in Dijon, France.

Next, the five articles are introduced in the context of the thesis and summarised. The first two articles deal with the optical properties and characterisation of two types of LC modulators: a twisted nematic and a ferroelectric modulator respectively. The third and fourth articles demonstrate a new technique to operate a pixelated LC spatial light modulator as a common-path polarisation interferometer, and its application to analyse complex structured light beams generated by digital holograms as well as tailored diffraction gratings. Finally, the fifth article presents a multifunctional complete Mueller matrix imaging polarimeter. The polarimeter incorporates single-pixel LC modulators and a polarisation camera, which allows capturing polarimetric images without any moving elements at a reduced number of PSG-PSA configurations, as well as the utilisation of the polarisation camera for the self-calibration of the polarimeter.

3.1 Mueller matrix polarimetric analysis applied to characterize the physical parameters of a twisted-nematic liquid-crystal modulator

This first work of the thesis was carried out in the academic year 2021-2022. Here, a laser Mueller matrix polarimeter was calibrated, and then implemented for the complete characterisation of a single pixel twisted-nematic liquid crystal (TNLC) modulator. The polarimeter employed LC retarders in the polarisation state generator (PSG) which where calibrated using a commercial point polarimeter, while the polarisation state analyser (PSA) incorporated a quarter waveplate and a linear polariser. With this polarimeter, we characterised a commercially available TNLC modulator from Jenoptik with properties like those discussed in subsection 2.5.2. We reviewed the physical models that describe the cell and, by means of polarimetric measurements, we provided an analysis of the different modulation regimes.

The motivation and novelty of this work is based on two aspects. While TNLC modulators have been used for many years and their optical modulation properties have been studied extensively, these studies have mostly considered the Jones matrix formulation for their description [Yari 1984] [Durá 2006] [Yama 2005]. Physical simplified models had been developed to account for the complex (amplitude and phase) modulation achieved with these modulators and helped to find optimised configurations to operate them as phase-only modulators, useful for diffractive optics [Lu 1996]. Only when modern LC-SLMs having digital electronic control were affected by flickering effects, the Mueller matrix formulation was adopted to study the related effective depolarisation effects, mostly at the phenomenological level [Martí 2014]. In this first work of the thesis, we provided a description of the microscopic physical models reported in the literature [Yama 2005] [Márq 2000] [Coy 1996], but within the Mueller matrix formalism. Therefore, we first review the analytical Jones matrices describing the microscopic physical models and then derive the corresponding Mueller matrices in the different modulation regimes.

Secondly, we emphasize that, the proper application of these physical models requires a prior precise determination of the twist angle (α) and the LC orientation (ψ). This orientation cannot be measured directly as in the standard case of a linear retarder that is discussed in subsection 2.2.6. Rather, researchers have adopted techniques that require several measurements and the simultaneous fitting of the experimental curves to numerical data involving the microscopic physical

model parameters, namely ψ, α and the maximum retardance β_{max}. Such techniques have proven to be successful, despite being cumbersome since they require multiple wavelengths or spectroscopic procedures [Moren 2008] [Gius 1998]. In this work, we show that a Mueller matrix polarimetric analysis allows characterising the physical parameters of the TNLC cell to describe the different modulation regimes exhibited by the modulator. This polarimetric procedure simplifies previous techniques and resolves the ambiguities in determining the physical parameters. For instance, the twist angle α can easily be determined when the TNLC acts as a pure polarization rotator (situation that can be easily determined by observing the LC modulator between crossed circular polarisers). It is also shown that the polarization eigenstates give a direct measurement of the LC orientation ψ, thus enabling an independent single wavelength measurement of these two parameters.

In addition to the twist angle and LC orientation parameters, analysis of different Mueller matrix elements offers extra important information. For instance, variations in elements m_{12} and m_{13} of the Mueller matrix provide the sense of rotation of the LC director inside the cell and also identifies the orientation of the extraordinary and ordinary axes.

Finally, a simplified procedure for a fast characterisation of the modulator is provided considering the modulator as a pure retarder. This could be applied since the depolarisation and diattenuation values obtained from the general procedure were very small and negligible. Polarimetric measurements involving illumination of the TNLC modulator with three different states of polarisation, this simplified technique offers all the necessary parameters for the characterisation of the modulator. For verification purposes, a test was successfully performed to confirm the ability of the technique to predict the optical modulation in other polarization configurations that were not employed in the calibration.

The effectiveness in this characterisation procedure of the TNLC modulator is of great interest since it can be extended to characterise other optical elements without requiring prior knowledge of their physical parameters. The simplified procedure on the other hand, serves as a time saving characterisation technique for researchers employing TNLC devices.

3.2 Ferroelectric liquid-crystal modulator with large switching rotation angle for polarization-independent binary phase modulation

This second work focuses on another LC technology: a ferroelectric liquid crystal (FLC) modulator. Contrary to the standard structure of the FLC cell discussed in subsection 2.5.3 intended to provide light intensity modulation, the one fabricated and characterised in this work has a non-standard large switching rotation angle (close to 90^0) that allows polarisation-independent π phase modulation. This work is a result of a collaboration with the Military University of Technology (WAT), Warsaw, Poland. The design of the FLC cell was done at the TECNOPTO-UMH laboratories using numerical simulations. Later, the fabrication of the modulator was carried out at WAT. The characterisation of the modulator optical properties was performed at both facilities using different characterisation procedures, as described below.

The novelty of our design lies in the FLC modulator's ability to perform a binary π phase modulation for any input states of polarisation with maximum light conversion efficiency in the spectral region where the LC layer is close to a half-wave retarder. The ability to attain a π phase modulation using this modulator is not the core element of this work as this can be obtained by many other existing LC modulators. The relevance lies in the fact that this operation occurs for all input states of polarisation whilst preserving the maximum light efficiency. This eliminates the need for a specific input

polarisation and for an output analyser to filter the modulated beam. Such scenarios are discussed in subsection 2.5.3.

The LC mixture (W-212) used in this work was conceived and developed at the Institute of Chemistry (WAT), meeting the FLC requirements: a broad temperature range of the ferroelectric phase, a relatively low melting point and an optimized ferroelectric electro-optical response. Microscopy techniques were employed to assemble and validate the structure of the cell. The physico-chemical properties of the W-212 mixture were measured during my one month stay at WAT, using the readily available equipment. Namely, a temperature and environmental-controlled stage compatible with a polarisation optical microscope. The characterisation demonstrated the temperature dependence of the helical pitch of the mixture, the sense of the helical twist and the tilt angle as a function of temperature.

At TECNOPTO-UMH laboratories, the optical modulation parameters (LC director stable positions, rotation angle and spectral retardance) were optically characterised by reverse engineering experiments. Firstly, the two stable states of the modulator were obtained upon application of a bipolar voltage (i.e. a square signal of $20\mathrm{V_{pp}}$) as well as the corresponding switching rotation angle and the sense of rotation. The rotation angle was found to be slightly lower (85^0) than the targeted 90^0. Obtaining these parameters enabled the proper alignment of the polarisation elements required to characterise the modulator and in the rest of the optimisation experiments.

A spectral analysis of the FLC modulator was performed by illuminating the modulator with a broadband light source while being sandwiched between two crossed linear polarisers with the input polariser oriented at 45^0 with respect to one of the LC director stable positions (this technique is discussed in subsection 2.5.1). The spectral measurements indicated a π phase modulation at 575 nm instead of 633 nm, which was our wavelength of interest. The retardance value at 633nm obtained from the spectral measurements was 164^0. Nevertheless, this retardance value is close enough to 180^0, so the FLC device was operated using a He-Ne laser source of 633nm.

FLC modulators are popular for their fast response as compared to other nematic LC modulators. Therefore, it was essential to investigate the time response (or frequency limit) of the FLC modulator. For the $20\mathrm{V_{pp}}$ signal, we found that 50Hz is the frequency limit that ensures a full switch of the LC director, and therefore, a good operation. Also, the effect of the voltage peak to peak amplitude $\mathrm{V_{pp}}$ applied to the modulator was experimentally analysed. It was observed that the $\mathrm{V_{pp}}$ value played a significant role on the frequency limit of the modulator. It was found that increasing the $\mathrm{V_{pp}}$ amplitude compensates the degradation of the optical signal and allows higher frequency limits.

Since the aim of this FLC design was to achieve π phase modulation independent of the input polarisation state, this aspect was verified. Interferometric measurements were carried out at WAT using a very versatile specially adapted Young's interferometer that detects the optical interference pattern by a bicell photodetector. Upon illumination of the modulator with different input states of polarisation, the results showed good visibility and the contrast inversion of the interference patterns, thus demonstrating the targeted π phase-shift independent of the input state.

This work thus demonstrated the successful design and fabrication of a FLC modulator with large switching rotation angle whose properties are attractive for diffractive optics, as it poses the possibility of manufacturing FLCs that would be binary phase modulators with the highest diffraction efficiency and polarisation independent. Therefore, they would operate with unpolarized light, a situation that is not possible with the common nematic LC-SLMs or with standard FLC-SLMs of smaller rotation angles.

4.3 Phase-shifting common-path polarization self-interferometry for evaluating the reconstruction of holograms displayed on a phase-only display

After the first works on single-pixel LC modulators, I started working with a pixelated liquid-crystal spatial light modulator (LC-SLM). We developed a novel technique to retrieve the phase spatial pattern of structured light beams generated with this LC-SLM. These were scalar Hermite-Gauss (HG) and Laguerre-Gauss beams (LG), as well as superpositions of different LG modes forming sophisticated intensity and phase patterns. Here, the classical phase-shifting interferometry (PSI) technique was employed [Crea 1988] to retrieve the phase distribution of complex light generated with holograms displayed onto a parallel-aligned liquid-crystal on silicon (LCOS)-SLM.

The novelty of this work relies on characterising both the intensity and phase spatial distribution of sophisticated patterns of light using a single experimental set-up. Here the phase-only modulation response of the SLM is not only used for displaying the holograms that generate these complex beams, but also for evaluating the phase distribution of the propagated field. This is usually measured with additional optical elements like a wave-front sensor or by interferometric techniques. In our case however, we take advantage of the SLM employed in the system to create a polarisation common-path interferometer. The SLM's nature of only modulating the polarisation component parallel to the LC director while allowing the orthogonal polarisation component to propagate unmodulated on the same axis, allows the building of a common-path interferometer simply by rotating a polariser placed before the SLM. Secondly, nematic LC-SLMs can perform continuous phase modulation, which allows performing the phase-shifting procedure with arbitrary phase bias values as discussed in section 2.7. The details of the PSI technique employed are explained in subsection 2.7.1 and the method to encode the complex functions onto the phase-only modulating device is described in subsection 2.8.4.

This way, the system makes the most of the modulation properties of the commercial parallel-aligned LCOS display employed (Hamamastu, model X10468-01, 800×600 pixels). The characterisation of its phase modulation can be achieved simply by placing the SLM in between input and output polarisers oriented at 45^0 with respect to the LC director as discussed in subsection 2.5.1. Figure 3.1(a) shows the normalised transmitted intensity curves versus gray level for parallel and crossed configuration of the polarisers. When the gray-scale image is encoded from black (0) to white (255) through 256 gray levels, then the light reflected on the SLM undergoes a relative phase change from 0 to more than 2π. Dots in Fig. 3.1 represent the experimental measurements while the continuous line represents the best fit. Figure 3.1(b) shows that this SLM provides a phase modulation that exceeds 2π for the operating wavelength of 633nm. Currently, most typical commercial SLMs offer a phase shift of at least 2π for most wavelengths.

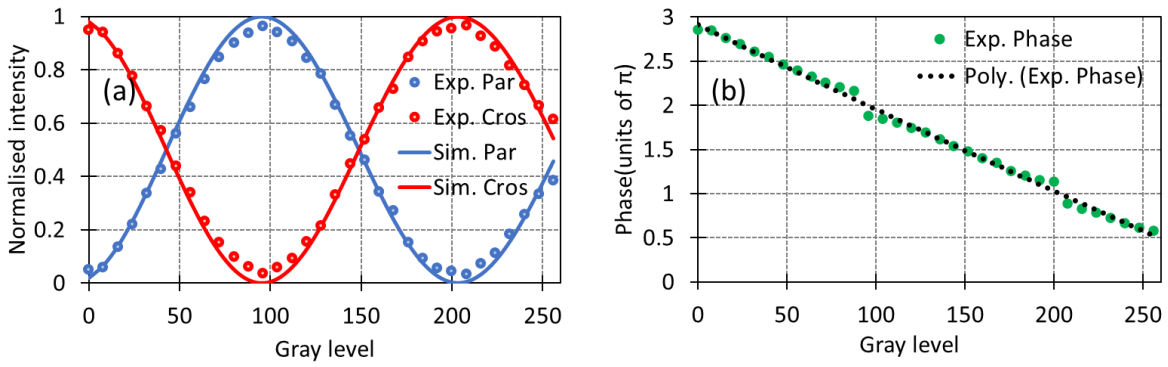

Figure 3.1: SLM calibration. (a) Normalised transmitted intensity versus gray level curves with the SLM between crossed (red) and parallel (blue) polarisers with the input polarisation oriented at 45^o. (b) Phase modulation.

Finally, let us emphasise that the intensity and phase distribution of the beam was obtained by the same experimental set-up with high accuracy for even rapidly varying phase patterns (for instance the superposition of four LG beams $\mathrm{LG}_{01} + \mathrm{LG}_{05} + \mathrm{LG}_{0,30} + \mathrm{LG}_{0,-30}$ shown in Fig. 4 in the paper) by merely changing the polarisation of light impinged onto the SLM. The number of steps required in the phase-shifting process was investigated, showing successful retrieval of the phase distribution of the tailored beams with steps as low as three (which is the minimum required steps in the PSI technique).

3.4 Retrieving the phase of diffraction orders generated with tailored gratings

This work was an extension of the previous one. The same common-path self-interferometric set up and PSI algorithm was employed to retrieve the intensity and phase distribution of different phase-only diffraction grating designs. The motivation of this work relies on the necessity of characterising polarisation diffraction gratings (PDG), where the relative phase between diffraction orders controls the state of polarisation at each order. These PDGs featuring diffraction orders with different polarisation are very useful for developing snapshot polarimeters. The technique proposed in the previous work involves encoding in the SLM the phase of the hologram generating the complex beam plus the phase of the diffractive lens that focuses the generated beam on the reconstruction plane (Fourier plane). Since the hologram and the lens are codified in the same plane (the SLM plane), this implies that a quadratic phase term is present in the Fourier transform plane. This additional quadratic phase did not pose a significant effect in the previous work, as most beams were evaluated at the centre of the transversal plane. However, in this work where we encode diffraction gratings, the area on the detector plane is much larger, and consequently this quadratic phase cannot be ignored. We evaluated this quadratic phase and compensated for it in all the diffraction grating designs.

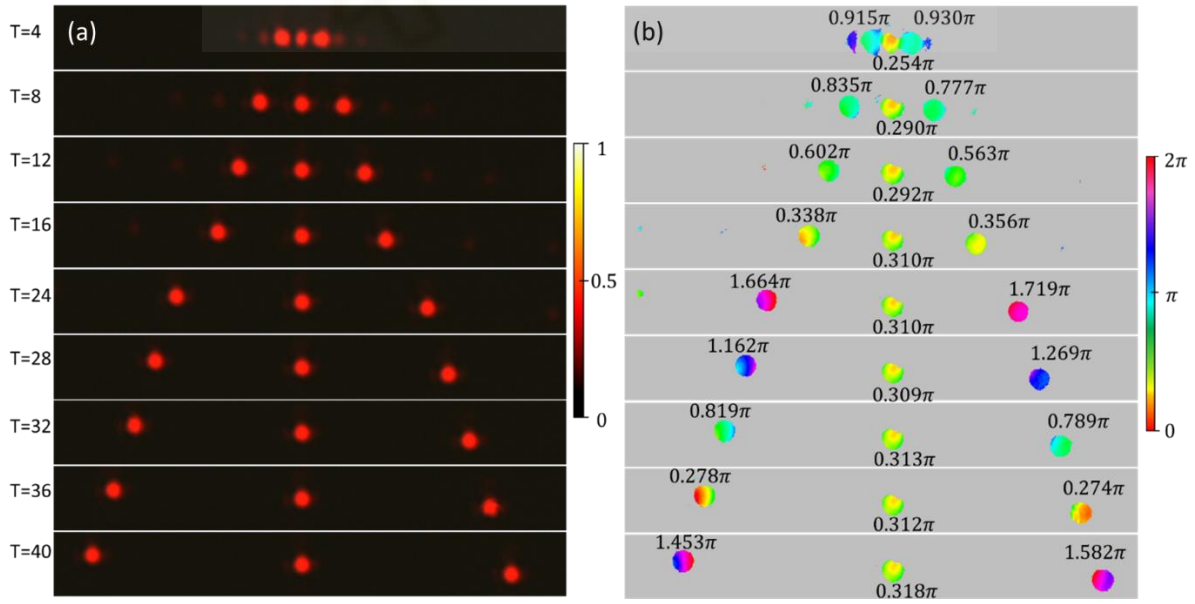

Figure 3.2: Triplicator gratings at varying periods. (a) Intensity captures of the gratings (b) Phase of the gratings (in units of π). Parameter T is the spatial frequency where $n = 1024/T$ is the grating's period, both expressed in pixels.

The characterisation of such quadratic phase was achieved using the well-known optimal triplicator grating profile [Gori 1998], whose expression is provided in subsection 2.8.2. The triplicator phase profile generates three diffraction orders (zero and ± 1) with equal intensity. The characterisation procedure involves displaying a sequence of triplicator gratings with varying periods. Figure 3.2 shows the intensity and phase distributions obtained at the detection plane for triplicators with different periods.

As demonstrated in [Marc 2019], there must be a 0.5π phase difference between the zero and ± 1 orders, which is not the case in the results of Fig. 3.2. They clearly show an added phase that arises from the quadratic phase. The quadratic phase profile at the detector plane can be deduced from the triplcator phase values by subtracting the expected 0.5π phase shift between the zero and the ±1 orders.

It is important to note that the effect of this quadratic phase is greater as the radial coordinate increases. This can be noticed in Fig. (3.2b) (before compensation). For large periods, the phases of the diffraction orders were close to the expected values. On the contrary there are greater variations for smaller periods. This implies that for experiments where the hologram is focused on the centre of the detector or for high period diffraction gratings, this procedure of quadratic phase compensation can be ignored. Figure 3.3 shows the quadratic phase at the detector plane, and the phases of the triplicator diffraction orders after compensation.

Finally, the technique was successfully applied in the phase retrieval of different triplicator diffraction gratings. Namely, triplicators with varying periods, with lateral displacements and a combination of a horizontal and a vertical triplicator. Furthermore, three custom designed gratings with continuous phase profiles and with tailored intensity and phase of the diffraction orders were experimentally evaluated. These gratings can possibly be employed to fabricate PDGs useful for a single shot polarimeter. The experimental results showed very good agreement with respect to the numerical designs.

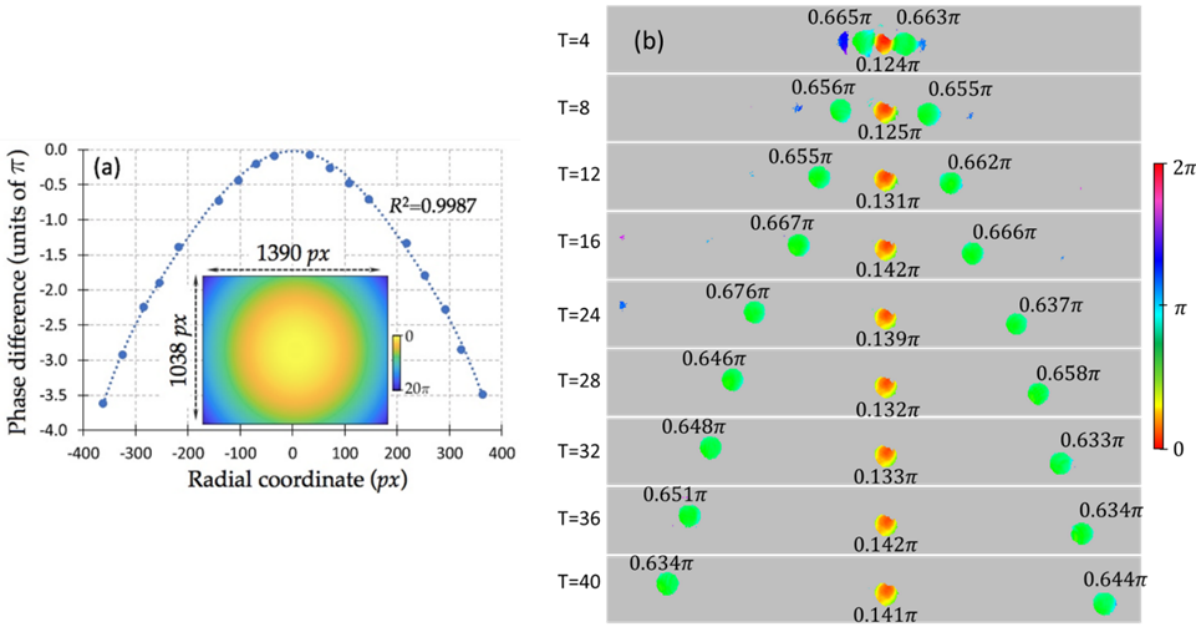

Figure 3.3: Compensation of the quadratic phase resulting from the additional lens function encoded on the hologram (a) Retrieved phase profile of the lens (b) Triplicator gratings with the quadratic phase compensated.

3.5 Mueller matrix imaging polarimeter with polarization camera self-calibration applied to structured light components

Finally, this fifth work developed during the last period of my thesis is a continuation of the work on Mueller matrix polarimetry performed in the beginning of the thesis which was discussed in section 3.1. Based on the experience acquired on LC devices, the objective of this final thesis project was to develop a multifunctional complete Mueller matrix imaging polarimeter. Hence, the work accomplishes several advances in the optical components and in the operating algorithms employed in the polarimeter to improve its performance. These advances include:

i. Fully replacing all moving components in the PSG and PSA of the polarimeter with tunable LC retarders (two LCRs in the PSG and one LCR in the PSA). The system is now made completely programmable and does not require physical placement or rotation of any device during the polarimetric measurements. This minimised any human errors and also offers stability of the system.
ii. To widen the spectral range of the polarimeter, a multiwavelength LED source and respective spectral filters were used to provide red, green and blue channels, centred respectively at 660nm, 565nm and 470nm. Also, employing a multiwavelength LED source avoids the speckle noise of laser sources and the interference patterns in the captured images, caused by multiple reflections between the optical components of the polarimeter.
iii. Another structural adjustment is the installation of the PSA on a rotating breadboard which allows operating the polarimeter in both transmission and reflection configuration. Since many samples of interest (including biological samples) scatter light, they are better analysed in the reflection configuration. Hence, this imaging polarimeter is not limited by the physical nature of the sample.
iv. Other than the structural adjustments in the polarimetric system, an optimising algorithm is applied where the polarisation camera is employed as the reference in the polarimeter calibration. This sequential polarisation camera self-calibration method compensates errors in the measurements arising from inconsistencies in the polarimeter components (both in the PSG and PSA). This is very convenient because the polarimeter can be fully optimised in situ and at pixel level, without requiring an external commercial polarimeter. We take into account the extinction ratio of the grid polarizers in the camera and calculate the error induced on the Mueller matrix elements by the limited extinction ratio. This is of interest for users of this kind of cameras in imaging systems, which are becoming very popular.

With all the advances made, our polarimeter still remains cost efficient. Summing up the cost of the Kiralux polarization camera (about 3000 euros) and the rest of components in our polarimeter, the total cost is much lower (below 8000 euros) than that of commercial Mueller matrix polarimeters, such as the Hinds Mueller polarimeters (about 100,000 euros), which are inaccessible to many laboratory scientists. Furthermore, birefringent imaging systems, with similar applications to Mueller matrix polarimeters but which offer limited information, are also much more expensive (about 30,000 euros) as compared to our polarimeter.

Figure 3.4 shows the experimental set-up of the Mueller matrix imaging polarimeter with the above discussed advances. The set-up elaborates the sequential polarimeter calibration and optimization method discussed in subsection 2.6.1. Figure 3.4(a) represents the PSG which includes two LCRs and Fig. 3.4(b) shows a picture of the complete polarimeter, where the PSA includes now the last LCR.

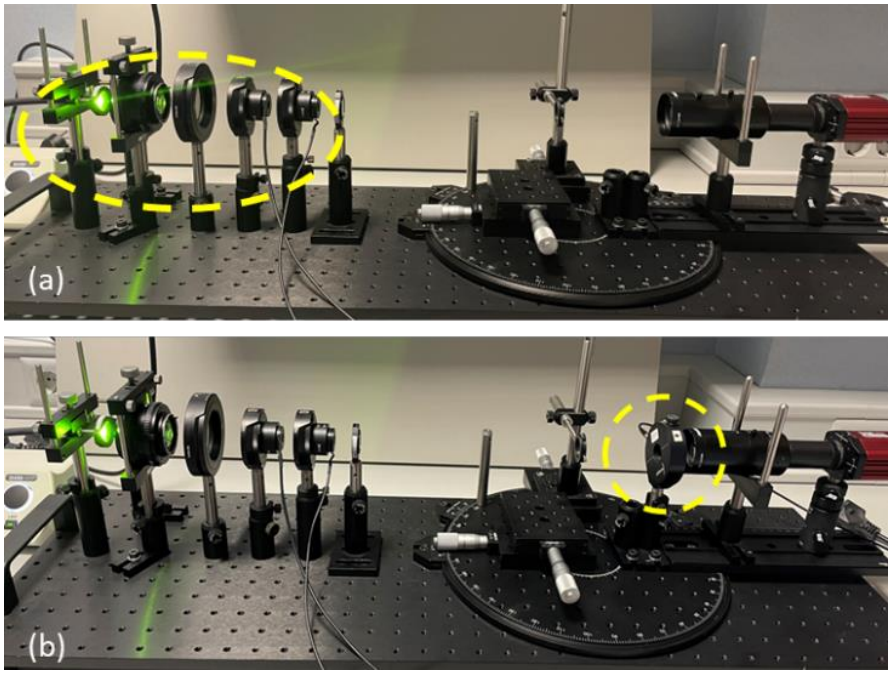

Figure 3.4: Mueller matrix imaging polarimeter set-up. (a) System for calibrating the PSG (b) Complete polarimetric system where the last LCR is incorporated to the PSA.

For verification purposes, we tested the polarimeter by characterising several known devices used in structured light at a multiwavelength basis (depending on the wavelength-of-interest of each device). The devices selected were two pure retarders, a pure diattenuator, and a pure depolarizer, thus modifying the input polarisation by three distinct physical mechanisms.

Two patterned linear retarders commonly used in structured light were characterised namely: a birefringent NBS 1963A resolution test and a q-plate device, both under the red channel illumination. The devices showed the expected result for a retarder, where the Mueller matrix (MM) elements $m_{0j} = m_{j0} \approx 0$, for $j = 0, 1, 2, 3$ indicating null polarizance and null diattenuation. Other relevant parameters like the retardance and azimuth were also retrieved, indicating uniformity in the retardance for both devices and differing azimuth values between the inscribed marks and the background of the resolution test, and azimuthal distribution of the neutral axis of the q-plate, as expected.

The pure diattenuator selected was a radial polariser. This patterned device consists of twelve segments where the transmission axis is aligned radially, thus being shifted 30º between adjacent segments. In this case the last row and column of the Mueller matrix become null, $m_{3j} = m_{j3} \approx 0$, for $j = 0, 1, 2, 3$. Also, the other MM elements clearly show the segmentation of the polariser and further quantitative analysis proves that it is purely a linear deattenuating device. Lastly, the calculated polariser transmission angle confirmed the expected radial rotation.

To emulate depolarisation, a standard single-pixelated FLC modulator was used while modulating at a frequency higher than the camera's capturing rate. In this case we used the green channel where the FLC layer behaves closely to the half-wave retardance condition. All the elements of the retrieved Mueller matrix were close to zero, except $m_{00} = 1$ and $m_{33} = -1$ as anticipated for a linear depolarising sample. All these results confirmed the usefulness and accuracy of the developed imaging polarimeter.

However, to further test the accuracy of the polarimeter, we compared the results with those obtained with a commercial birefringence imaging system (BIS) from the company Thorlabs, model LCC7201 as shown in Fig. 3.5. This is an instrument designed to measure stress- and strain-induced birefringence in flat samples for a variety of applications ranging from materials science and biological research. Contrary to the developed imaging polarimeter, this BIS instrument is limited only to linear retarder samples providing as parameters only the retardance and axis azimuth details of the sample under investigation. It uses a LED source of 633nm wavelength and provides images with quantitative information of the linear retardance, limited to the range $[0, \pi)$ and the orientation (azimuth) of the fast axis.

Figure 3.5: Picture of the birefringence imaging system (BIS LCC7201).

Firstly, we applied the polarimeter imaging system to a birefringent NBS 1963A resolution test (Thorlabs R2L2S1B). This is a patterned linear retarder with uniform retardance but where the resolution test is encoded with different azimuth than the background. The experimental Mueller matrix shown in Fig. 3.6(a), which shows the numbers "1.4" in the resolution test measured under red light (660 nm). The normalized Mueller matrix shows null values in the m_{0j} and m_{j0} elements, $j = 1,2,3$, as expected for a pure retarder sample. Figure 3.6(b) provides additional polarimetric parameters: diattenuation (D), depolarization (Δ) and retardance (R). The results agree with those expected: the diattenuation and depolarisation are negligible, and the retardance appears uniform, only with linear component. Lastly, we calculate the retarder eigenstate azimuth (α) and ellipticity (ε). As expected for a linear retarder, $\varepsilon \approx 0$ at all points, but the orientation shows a difference $\Delta\alpha \simeq 33^{\circ}$ between the background and the numbers.

Since this is a pure linear retarder sample, the results can be compared with those of the commercial BIS instrument. Since the light source in the BIS emits at 633 nm wavelength, it can only be compared with our system with the central wavelength 660 nm. The comparison is shown in Fig. 3.6(b), bottom line. The results show very similar values for the retardance (with average value $R = 0.71\pi$ with our Mueller matrix polarimeter and $R = 0.76\pi$ according to the BIS instrument), and for the azimuth values (the inscribed numbers and the background show average azimuth angles $\alpha \simeq 52^{\circ}$ and $\alpha \simeq 89^{\circ}$ with the polarimeter, and $\alpha \simeq 55^{\circ}$ and $\alpha \simeq 87^{\circ}$ with the BIS instrument). These results thus confirm and validate the imaging polarimeter.

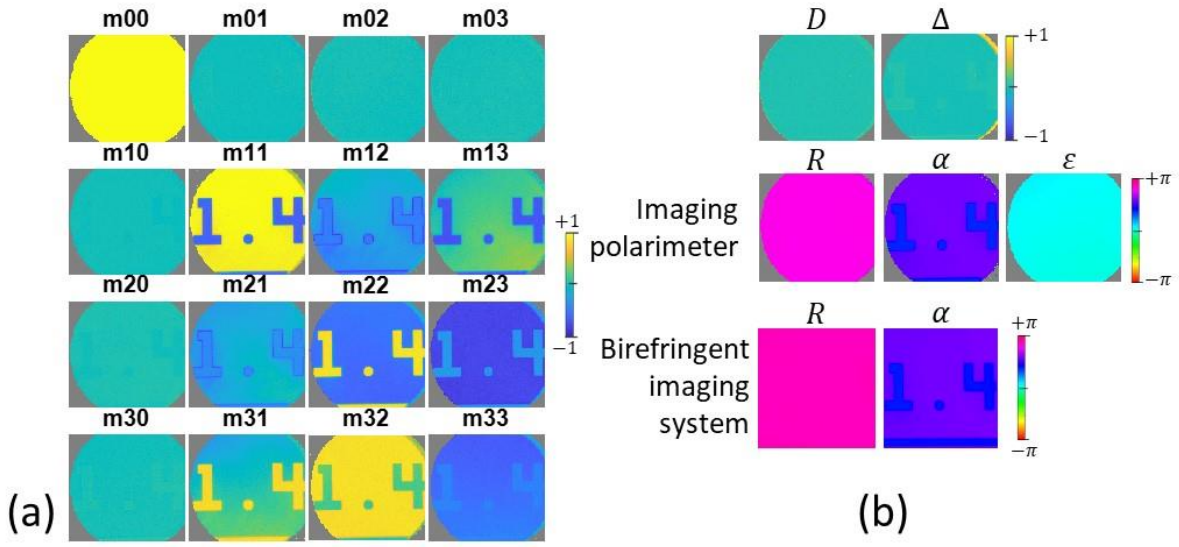

Figure 3.6: Polarimetric analysis of the birefringent NBS 1963A resolution test. (a) Mueller matrix (b) Diattenuation (D), depolarization (Δ), retardance (R) parameters, and orientation (α) and ellipticity (ε) of retarder eigenstates; the bottom row shows the equivalent results for the retardance, and axis orientation obtained with the commercial BIS instrument.

Given the great interest of using optical polarimetry in bioimaging, the imaging polarimeter, a preliminary example of application was conducted on two microscopic samples prepared in slides by Bresser GmhH (No.5986003) are analysed: the longitudinal section of a basswood stem sample and a loose connective tissue. We first use a Nikon polarization microscope (Eclipse LV100POL) to aid in the selection of these samples of interest. Figure 3.7 shows microscope images of these samples obtained with white light illumination, and without analyser (Fig. 3.7(a,b)) and between crossed polarisers (Fig. 3.7(c,d)). The coloured transmission observed between crossed polarisers is an indication that a significant level of birefringence or depolarisation is present in these samples.

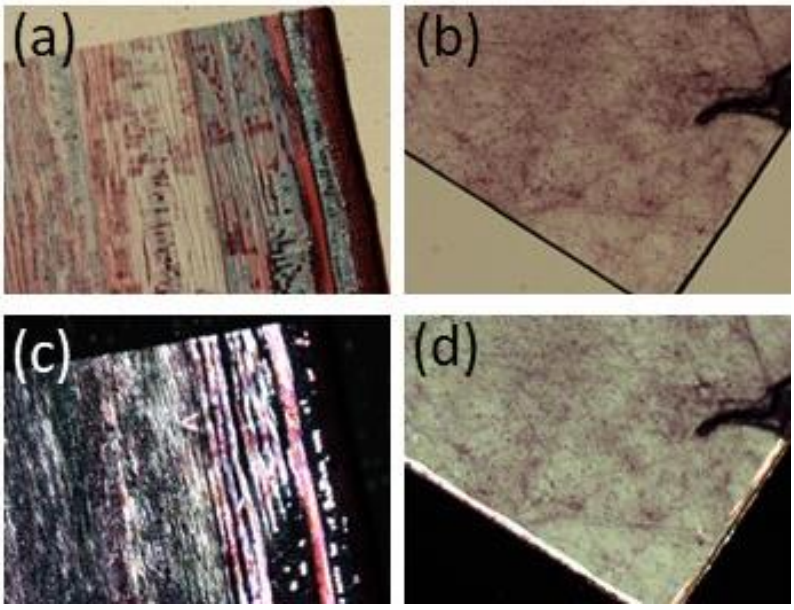

Figure 3.7: Microscope images of basswood stem (a,c) and loose connective tissue (b,d), obtained without analyser polariser (a,b) and with crossed polarisers (c,d).

Next, we inspected these samples with the imaging polarimeter. Figure 3.8 shows the results for the basswood sample. Again, we show the measured Mueller matrix (Fig. 3.8(a)) and some polarimetric parameters (Fig 3.8(b)). The basswood stem comprises of three major sections, the pith (central part), xylem or wood (middle part) and bark (outer part) [Wied 2021]. Notably, the bark exhibits a relatively higher degree of depolarisation and diattenuation. The structural content of the bark comprises of suberin, a waxy sub-stance that cuts down water loss from the stem (suberin is impregnated in layers of dead cork cells). This brings the scattering effect that is replicated as depolarization and diattenuation. The presence birefringence can be attributed to the layers of parenchyma cells and xylem vessels that facilitate photosynthesis and storage of food (the regions contain chloroplast, water, and minerals) which are birefringent in nature [Chaf 1974].

Figures 3.8(c,d) shows the results for the loose connective tissue. This tissue generally works to hold organs, anatomic structures, and tissues in place [Poll 2017]. The extracellular matrix of loose connective tissue is composed of amorphous ground substance, extracellular fluid, collagen, and elastic fibers which are all highly birefringent. The analysis in Fig. 3.8(d) indicates that this tissue has a significant retardance. We measure an average retardance value $R = 0.65\pi$ with an average azimuth $\alpha \simeq 83^{o}$.

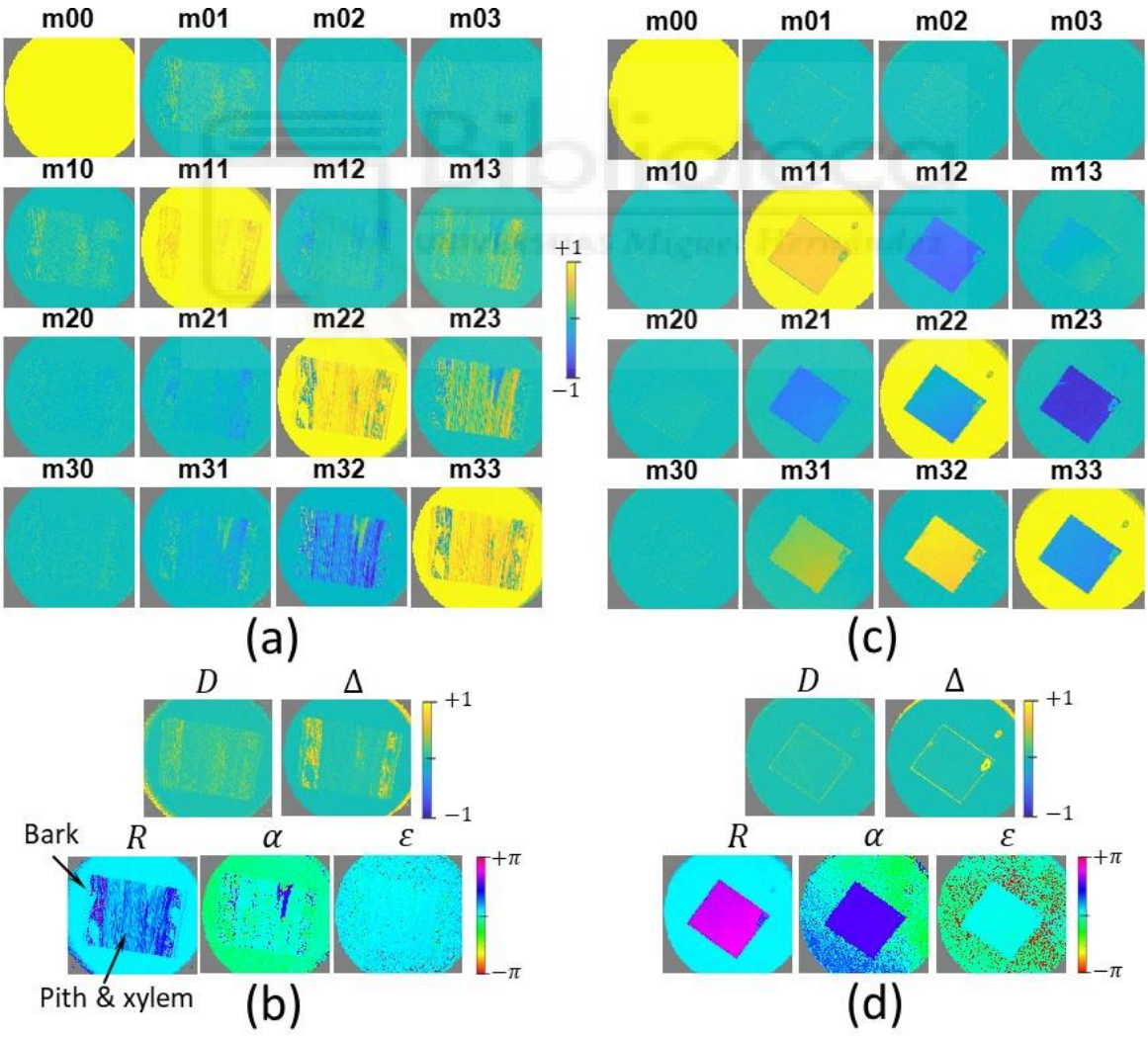

Figure 3.8: (a,b) Results for a basswood stem sample: Mueller matrix (a) and polarimetric parameters (b). (c,d) Results for a loose connective tissue: Mueller matrix (a) and polarimetric parameters (b).

4. Conclusions

In summary, this thesis embeds new research and findings applicable in the fields of structured light, optical interferometry, and optical polarimetry, sharing all a common aspect of using LC optical modulators.

In the first part of the thesis I have reviewed the most common LC optical modulators, namely, the twisted nematic LC modulator, the parallel-aligned LC nematic modulator, and the ferroelectric LC modulator. Then, as a first contribution of this thesis, a polarimetric analysis of the TN-LC cell has been developed. The study first considers the physical models that describe the twisted optical anisotropic structure of these modulators. These models were developed in the past using the Jones matrix formalism. As explained in Chapter 2 when introducing the Jones formalism, this is valid only for totally polarised light. However, LC modulators can exhibit depolarisation effects, which cannot be accounted with the Jones formalism, thus requiring the use of the Mueller-Stokes formalism. Nevertheless, most of the studies dealing with LC modulators within this formalism make a phenomenological treatment. The study developed in this thesis derives the Mueller matrices describing the twisted nematic modulator in its different modulation regimes by applying the general relations between Jones and Mueller matrices. This allowed the extension of the TN-LC physical microscopic models to the Mueller matrix formalism.

Based on this study, the analysis of the Mueller matrix elements of the TN-LC modulator has been shown to offer a single-wavelength characterisation of its internal physical parameters, namely the birefringence, the twist angle, and the orientation of the LC director axis, as well as resolving of the ambiguities typically incurred in the identification of the TN-LC's parameters, thus simplifying previous approaches.

The thesis also covers the ferroelectric liquid crystal (FLC) modulator. A FLC cell has been designed and fabricated featuring the special characteristic that the switching rotation angle is selected as close as possible to $90°$ and the retardance is adjusted to be of $180°$ (HWP regime). This FLC modulator provides a binary π phase-shift between the two polarisation states emerging from the modulator corresponding to the two stable positions of the FLC director axis, independent of the input state of polarisation. Therefore, it poses the possibility of building binary phase modulators with the highest diffraction efficiency, useful for all states of polarisation, including unpolarised light, a situation that is not possible with the common nematic LC modulators or with standard FLC modulators.

Thanks to our collaboration with the team of Dr. Bennis at the Military University of Technology, Warsaw (Poland), such a FLC modulator was fabricated. The device physical parameters were characterised: the orientation of the LC director in its two stable positions, the sense of rotation upon applying a square voltage signal, and its spectral retardance. The transient times between stable positions of the FLC modulator were also analysed in terms of the frequency and magnitude of the applied voltage. Finally, the binary π phase modulation properties of the modulator were experimentally probed for various input polarization states.

The second part of the thesis is devoted to the application of parallel-aligned (PAL) LC modulators in two important optical techniques, namely optical interferometry, and optical polarimetry, here focused on their use in the field of structured light, i.e. the generation of light beams with spatial patterns in the intensity, phase, and state of polarisation.

One relevant system developed for the thesis is a common-path phase-shifting interferometer (PSI) based on a PAL LCOS-SLM device. The pixelated SLM is used to display phase-only digital holograms in the common arrangement where the input beam is linearly polarised parallel to the LC director axis. The hologram uses a technique to encode complex (magnitude and phase) functions onto phase-only modulators, and it is combined with the phase of a diffractive lens, to focus the light beam without requiring an external lens.

But the polarisation properties of the PAL nematic configuration are exploited to transform this standard system into a common-path interferometer arrangement simply by a rotation of a polariser. The polarisation component crossed to the LC director axis remains unaffected by the hologram displayed on the SLM and serves as the reference beam. Therefore, the LCOS SLM is demonstrated to be useful to simultaneously display the hologram and to apply the phase-shifting required to retrieve the phase distribution from the interferograms.

The common-path interferometer offers great stability of the system, and the SLM provides precise and arbitrary phase-shifting values. This interferometric arrangement has been shown to provide a measurement of the phase of the focused light beam generated by the hologram, eliminating the requirement of any additional external system. The technique has been shown successful by retrieving the intensity and phase information of different structured beams, including exotic combinations of Gaussian beams. The possibility of adding arbitrary phase-shifts has been tested for comparing the performance of different PSI algorithms.

The joint display of the digital hologram with the diffractive lens in the LCOS-SLM provides an additional quadratic phase term in the Fourier transform detection plane. This phase is added to the expected phase distribution generated by the hologram. To improve the detection, a calibration method of this quadratic phase has been devised, based on displaying a phase triplicator diffraction grating. The triplicator grating design has he property to generate three diffraction orders (zero and first orders), where the two lateral orders have a $\pi/2$ phase shift with respect to the zero order. By displaying such triplicator diffraction gratings with different periods, and performing PSI on the generated diffraction orders, a precise determination of the phase at the generated diffraction orders has been demonstrated, which follows the expected quadratic profile. Then, once it has been characterised, this quadratic phase term can be subtracted from the phase measurements, providing the correct results even in a large area of the Fourier transform domain. The experimental results obtained with other specially tailored phase diffraction gratings demonstrated the usefulness of the proposed technique.

Finally, a complete Mueller matrix imaging polarimeter has been built, based on the use of PAL nematic LC retarders (LCR). Based on a first polarimeter system used to characterise the Mueller matrix of the TN LC modulator used in the first part of the thesis, some significant advancements were incorporated. First, any mechanically movable elements were eliminated thanks to the use of the LC modulators incorporated both on the polarisation state generator (PSG) and in the polarisation state analyser (PSA). The PSA system is mounted onto a rotatable breadboard, so the polarimeter can be operated both in a reflection configuration or in a in transmission configuration. A multi-wavelength LED source was incorporated to allow performing polarimetry in different spectral bands and avoid the speckle noise derived from the laser source used in the first polarimeter. The PSA detector consists in

a pixelated polarization camera which enables the simultaneous capture of the four cardinal linear states with a single shot.

A procedure has been described where the polarisation camera is further used as the reference in a proposed self-calibration technique that applies the compensation time sequential method that accounts for possible errors in the generation and detection of polarisation states. The procedure was applied at pixel level, and it has been illustrated step by step. Different samples used in structured light applications with well-known polarization properties were evaluated, including patterned retarders with constant retardance but different orientation of the optical axis, a patterned linear polariser, and a linear depolarizer based on a fast-switching FLC modulator. The results for these optical elements with well-known polarisation properties confirm the accuracy of the Mueller matrix imaging polarimeter developed in this thesis.

In conclusion, this thesis renders relevant information on LC technology, and its application in two optical techniques: polarimetry and interferometry, with great importance due to their many applications in many different areas. The thesis can be used as a guide in practical applications of LC devices since it offers different characterisation and optimising techniques.

4. Conclusiones

En resumen, esta tesis incorpora nuevas investigaciones aplicables en los campos de la luz estructurada, la interferometría óptica, y la polarimetría óptica, compartiendo todas ellas el aspecto común del uso de moduladores ópticos de cristal líquido.

En la primera parte de la tesis se revisaron los moduladores ópticos de cristal líquido más comunes, a saber, el modulador de cristal líquido nemático con giro (modulador TN-LC), el modulador de cristal líquido nemático de alineamiento paralelo (modulador PAL-LC) y el modulador de cristal líquido ferroeléctrico (modulador FLC). La primera contribución de esta tesis consistió en un análisis polarimétrico de la celda TN-LC. El estudio considera los modelos físicos que describen la estructura óptica anisotrópica con giro de estos moduladores. Estos modelos se desarrollaron en el pasado utilizando el formalismo de la matriz de Jones. Sin embargo, los moduladores de cristal líquido pueden exhibir efectos de despolarización, que no pueden tenerse en cuenta con el formalismo de Jones, lo que requiere el uso del formalismo de Mueller-Stokes. Sin embargo, la mayoría de los estudios que tratan sobre los moduladores TN-LC dentro de este formalismo hacen un tratamiento fenomenológico. El estudio desarrollado en esta tesis deriva las matrices de Mueller que describen el modulador TN-LC en sus diferentes regímenes de modulación mediante la aplicación de las relaciones generales entre las matrices de Jones y de Mueller. Esto ha permitido la extensión de los modelos físicos microscópicos que se usan para describir los moduladores TN-LC al formalismo de matriz de Mueller.

Basado en este estudio, el análisis de los elementos de la matriz de Mueller del modulador TN-LC ha demostrado ofrecer una caracterización con una sola longitud de onda de sus parámetros físicos internos, a saber, la birrefringencia, el ángulo de giro y la orientación del eje director del cristal líquido, así como la resolución de las ambigüedades típicamente incurridas en la identificación de los parámetros del TN-LC, simplificando así enfoques previos.

La tesis cubre también el modulador de cristal líquido ferroeléctrico (FLC). Se diseñó y fabricó una celda FLC con la característica especial de que el ángulo de rotación al conmutar la señal de voltaje aplicada se selecciona lo más cercano posible de 90° y con un retardo ajustado a 180° (régimen de retardador de media onda). Este diseño de modulador FLC proporciona un cambio binario de fase π entre los dos estados de polarización emergentes del modulador correspondientes a las dos posiciones estables del eje director, independientemente del estado de polarización de entrada. Por lo tanto, plantea la posibilidad de construir moduladores de fase binaria con la máxima eficiencia de difracción, útiles para todos los estados de polarización, incluida la luz no polarizada, una situación que no es posible con los moduladores de cristal nemático comunes o con los moduladores FLC estándar.

Gracias a la colaboración con el equipo del Dr. Bennis en la Military University of Technology, Varsovia (Polonia), se fabricó un modulador FLC con estas características. Los parámetros físicos del dispositivo fueron caracterizados: la orientación del director LC en sus dos posiciones estables, el sentido de rotación al aplicar una señal de voltaje cuadrada y su función de retardo espectral. Los tiempos transitorios entre las posiciones estables del modulador FLC también se analizaron en

términos de la frecuencia y la magnitud del voltaje aplicado. Finalmente, las propiedades de modulación binaria de fase π del modulador se comprobaron experimentalmente para varios estados de polarización de entrada.

La segunda parte de la tesis está dedicada a la aplicación de moduladores PAL-LC en dos técnicas ópticas importantes, a saber, interferometría óptica y polarimetría óptica, aquí enfocadas en su uso en el campo de la luz estructurada, es decir, la generación de haces de luz con patrones espaciales en la intensidad, fase y estado de polarización.

Un sistema relevante desarrollado para la tesis es un interferómetro de desplazamiento de fase y de camino común basado en un dispositivo modulador espacial de luz (SLM) de tipo PAL LCOS (cristal líquido sobre silicio). El dispositivo SLM se utiliza para generar hologramas digitales de fase en la disposición común donde el haz de entrada está linealmente polarizado paralelo al eje director del cristal líquido. El holograma se diseña con una codificación de funciones complejas (magnitud y fase) en una función sólo de fase, y se combina con la fase de una lente difractiva para enfocar el haz de luz sin requerir una lente externa.

Pero las propiedades de polarización de la configuración de modulador nemático PAL se explotan para transformar este sistema estándar en un sistema interferómetro de camino común simplemente mediante una rotación de un polarizador. La componente de polarización cruzada respecto al eje director del cristal líquido no se ve afectada por el holograma mostrado en el SLM y sirve como el haz de referencia del interferómetro. Por lo tanto, sistema basado en el SLM tipo PAL LCOS es útil para generar el holograma que produce el haz de luz diseñado y simultáneamente aplicar la técnica de desplazamiento de fase requerido para medir la distribución de fase.

El interferómetro de camino común aporta una gran estabilidad al sistema, y el SLM proporciona valores de desplazamiento de fase precisos y arbitrarios. Se ha demostrado que este interferómetro proporciona una medición de la fase del haz de luz focalizado generado por el holograma, eliminando la necesidad de cualquier sistema externo adicional. La técnica permite recuperar la información de la intensidad y de la fase de diferentes haces estructurados, incluidas combinaciones exóticas de haces gaussianos. Se ha comprobado la posibilidad de agregar desplazamientos de fase arbitrarios para comparar el rendimiento de diferentes algoritmos de desplazamiento de fase.

La visualización conjunta del holograma digital con la lente difractiva en el dispositivo LCOS SLM proporciona un término de fase cuadrática adicional en el plano de detección de la transformada de Fourier. Esta fase se suma a la distribución de fase esperada generada por el holograma. Para mejorar la detección, se ha ideado un método de calibración de esta fase cuadrática, basado en generar en el modulador una red de difracción de fase triplicadora. El diseño de la red triplicadora tiene la propiedad de generar tres órdenes de difracción (órdenes cero y ± 1), donde los dos órdenes laterales tienen un desfase de $\pi/2$ con respecto a la orden central. Al generar en el SLM redes triplicadoras con diferentes períodos, y aplicar la técnica de desplazamiento de fase, se puede realizar una determinación precisa de la fase en los órdenes de difracción generados, que sigue el perfil cuadrático esperado. Una vez caracterizado, este término de fase cuadrática puede restarse de las mediciones de fase, proporcionando los resultados correctos incluso en un área amplia en el plano de la transformada de Fourier. Los resultados experimentales obtenidos con otras redes de difracción de fase especialmente diseñadas demostraron la utilidad de la técnica propuesta.

Finalmente, se ha construido un polarímetro completo de imagen de matriz de Mueller, basado en el uso de retardadores PAL-LC nemático, también conocidos como retardadores de cristal líquido (LCR). Basándose en un primer sistema de polarímetro utilizado para caracterizar la matriz de Mueller del

modulador LC-TN utilizado en la primera parte de la tesis, se incorporaron algunos avances significativos. En primer lugar, se eliminaron todos los elementos mecánicamente móviles gracias al uso de los moduladores PAL-LC incorporados tanto en el generador de estados de polarización (PSG) como en el analizador de estados de polarización (PSA). El sistema PSA está montado en un soporte rotatorio, por lo que el polarímetro puede funcionar tanto en una configuración de reflexión como en una configuración de transmisión. Se incorporó una fuente LED de múltiples longitudes de onda para permitir la realización de polarimetría en diferentes bandas espectrales y evitar el ruido de speckle derivado de la fuente láser utilizada en el primer polarímetro. El detector PSA consiste en una cámara de polarización pixelada que permite la captura simultánea de los cuatro estados lineales cardinales con una única captura.

Se ha descrito un procedimiento en el que la cámara de polarización se utiliza además como referencia en una técnica de auto-calibración de polarímetro, que aplica el método secuencial de compensación que tiene en cuenta posibles errores en la generación y detección de los estados de polarización. El procedimiento se aplicó a píxel a píxel, y se ha ilustrado paso a paso. Se evaluaron diferentes muestras utilizadas en aplicaciones de luz estructurada con propiedades de polarización bien conocidas, incluyendo retardadores estructurados con retardo constante pero diferente orientación del eje óptico, un polarizador lineal estructurado, y un despolarizador lineal basado en un modulador de tipo FLC de rápida conmutación. Los resultados para estos elementos ópticos con propiedades de polarización bien conocidas confirman la precisión del polarímetro de imagen de matriz de Mueller desarrollado en esta tesis.

En conclusión, esta tesis proporciona información relevante sobre la tecnología de los moduladores de cristal líquido, y su aplicación en dos técnicas ópticas, polarimetría e interferometría, de gran importancia debido a sus múltiples aplicaciones en muchas áreas diferentes. La tesis puede ser utilizada como una guía en aplicaciones prácticas de los dispositivos de cristal líquido ya que ofrece diferentes técnicas de caracterización y de optimización.

References

[Ange 2019]: J. P. Angelo, T. A. Germer, and M. Litorja, "Structured illumination Mueller matrix imaging", *Biomed. Opt. Express* 10(6), 2861-2868 (2019). DOI

[Arri 2003]: V. Arrizón, "Optimum on-axis computer-generated hologram encoded into low-resolution phase-modulation devices", *Opt Lett*. 28(24), 2521–2523 (2003). DOI

[Azza 2016]: R. M. A. Azzam, "Stokes-vector and Mueller-matrix polarimetry", *J. Opt. Soc. Am. A* 33(7), 1396-1408 (2016). DOI

[Cana 2024]: M. Canabal-Carbia, I. Estévez, E. Nabadda, E. Garcia-Caurel, J. J. Gil, R. Ossikovski, A. Márquez, I. Moreno, J. Campos, and A. Lizana, "Connecting the microscopic depolarizing origin of samples with macroscopic measures of the indices of polarimetric purity", *Opt. Lasers Eng*. 172, 107830 (2024). DOI

[Chaf 1974]: S. C. Chafe, "Cell wall structure in the xylem parenchyma of Cryptomeria", *Protoplasma* 81, 63–76 (1974). DOI

[Chip 1995]: R. A. Chipman, "Polarimetry", Ch. 15 in Handbook of Optics, 2nd Ed, McGraw-Hill, New York (1995). DOI

[Clar 1984]: N. A. Clark and S.T. Lagerwall, "Submicrosecond bistable electro-optic switching in liquid crystals", *Appl. Phys. Lett*. 36, 899–901 (1980). DOI

[Cofr 2017]: A. Cofré, A. Vargas, F. A. Torres-Ruiz, J. Campos, A. Lizana, M. M Sánchez-López, and I. Moreno, "Quantitative performance of a polarization diffraction grating polarimeter encoded onto two liquid crystal-on-silicon displays", *Opt. Laser Technol*. 96, 219-226 (2017). DOI

[Coll 2005]: E. Collett, "The Polarization Ellipse", Ch. 5 in Field Guide to Polarization. SPIE Press, Bellingham, WA (2005). DOI

[Coy 1996]: J. A. Coy, M. Zaldarriaga, D. F. Grosz, and O. E. Martínez. "Characterization of a liquid crystal television as a programmable spatial light modulator", *Opt. Eng*. 35(1), 15–19 (1996). DOI

[Crea 1988]: K. Creath, "Phase-measurement interferometry techniques", *Prog. Opt.* 26, 349–93, (1988). DOI

[Curc 2020]: V. Curcio, L. A. Alemán-Castañeda, T. G. Brown, S. Brasselet, and M. A. Alonso, "Birefringent Fourier filtering for single molecule coordinate and height super-resolution imaging with dithering and orientation", *Nature Commun*. 11(1), 1-13 (2020). DOI

[DeGe 1993]: P. G. de Gennes and J. Prost. "Liquid crystals", Ch. 1 in The Physics of Liquid Crystals, 2nd Ed., Oxford University Press (1993). DOI

[DeGr 2011]: P. de Groot, "Optical measurement of surface topography", Ch. 8 in Phase Shifting Interferometry, Springer, Berlin, Heidelberg (2011). DOI

[DeSi 2016]: L. De Sio, D. E. Roberts, Z. Liao, S. Nersisyan, O. Uskova, L. Wickboldt, N. Tabiryan, D. M. Steeves, and B. R. Kimball, "Digital polarization holography advancing geometrical phase optics", *Opt. Express* 24(16), 18297-18306 (2016). DOI

[DiLi 2001]: G. A DiLisi, "Phases of liquid crystals", Ch. 4 in An Introduction to Liquid Crystals, Morgan & Claypool Publishers (2019). DOI

[Dubo 2019]: O. Dubovik, Z. Li, M. I. Mishchenko, D. Tanré, Y. Karol, B. Bojkov, B. Cairns, D. J. Diner, W. R. Espinosa, P. Goloub, X. Gu, O. Hasekamp, J. Hong, W. Hou, K. D. Knobelspiesse, J. Landgraf, L. Li, P. Litvinov, Y. Liu, A. Lopatin, T. Marbach, H. Maring, V. Martins, Y. Meijer, G. Milinevsky, S. Mukai, F. Parol, Y. Qiao, L. Remer, J. Rietjens, I. Sano, P. Stammes, S. Stamnes, X. Sun, P. Tabary , L. D. Travis, F. Waquet, F. Xu, C. Yan, and D. Yin, "Polarimetric remote sensing of atmospheric aerosols, Instruments, methodologies, results, and perspectives", *J. Quantitat. Spectrosc. Rad. Transf.* 224(1), 474-511 (2019). DOI

[Durá 2006]: V. Durán, J. Lancis, E. Tajahuerce, and Z. Jaroszewicz, "Equivalent retarder-rotator approach to on-state twisted nematic liquid crystal displays", *J. Appl. Phys.* 99, 113101 (2006). DOI

[Fern 2000]: C. R. Fernández-Pousa, I. Moreno, N. Bennis, and C. Gomez-Reino, "Generalized formulation and symmetry properties of anisotropic devices application to liquid crystal displays", *J. Opt. Soc. Am A* 17(11) 2074–2080. (2000). DOI

[Fowl 1968]: G. R. Fowles, "The vectorial nature of light", Ch. 2 in Introduction to Modern Optics, Dover Publications, New York (1968). DOI

[Fran 1971]: M. Francon and S. Mallick, Polarization Interferometers, Wiley (1971). DOI

[Garc 2013]: E. Garcia-Caurel, R. Ossikovski, M. Foldyna, A. Pierangelo, B. Drévillon, and A. De Martino, "Advanced Mueller ellipsometry instrumentation and data analysis", Ch. 2 in Ellipsometry at the Nanoscale, Springer Verlag, Berlin (2013). DOI

[Gigl 2018]: B. Gigler, A. Casorati, A. Verbeek, "Financing the digital transformation – Unlocking the value of photonics and microelectronics", European Investment Bank. Publications Office (2018). DOI

[Gil 2022]: J. J. Gil and R. Ossikovski, Polarized Light and the Mueller Matrix Approach, CRC Press, New York (2022). DOI

[Gius 1998]: R. Giust and J. P. Goedgebuer, "Determination of the twist angle and the retardation properties of twisted nematic liquid crystal television by spectral measurements", *Opt. Eng.* 37(2), 629–634 (1998). DOI

[Gold 2017]: D. H. Goldstein, Polarized Light, 3rd Ed., CRC Press, Boca Raton (2017). DOI

[Goodm 2005]: J. W. Goodman, Introduction to Fourier Optics, 3rd Ed., Roberts & Co. Publishers, Englewood (2005). DOI

[Goodw 2006]: E. P Goodwin and J. C Wyant, Field Guide to Interferometric Optical Testing, SPIE Press (2006). DOI

[Gori 1998]: F. Gori, M. Santarsiero, S. Vicalvi, R. Borghi, G. Cincotti, E. Di Fabrizio, and M. Gentili. "Analytical derivation of the optimum triplicator", *Opt Commun*. 157(1), 13-16, (1998). DOI

[Gray 1973]: G. W. Gray, K. J. Harrison, and J. A. Nash, "New family of nematic liquid crystals for displays", *Electron. Lett.* 6(9), 130–131 (1973). DOI

[Hako 2017]: N. H. Hakobyan, H. L Margaryan, V. K. Abrahamyan, V. M. Aroutiounian, A. S D. Gharghani, A. B. Kostanyan, T. D. Wilkinson, and N. Tabirian, "Electro-optical characteristics of a liquid crystal cell with graphene electrodes", *J. Nanotechnol.* 8(1), 2802–2806 (2017). DOI

[Harr 2005]: J. Harriman, S. Serati, and J. Stockley, "Comparison of transmissive and reflective spatial light modulators for optical manipulation applications", SPIE Conference Series 5930(1), 605-614 (2005). DOI

[He 2021]: C. He, H. He, J. Chang, B. Chen, H. Ma, and M. J. Booth, "Polarisation optics for biomedical and clinical applications: a review", *Light Sci. Appl.* 10, 194 (2021). DOI

[Hern 2017]: C. Hernández-García, A. Turpin, J. San Román, A. Picón, R. Drevinskas, A. Cerkauskaite, P. G. Kazansky, C. G. Durfee, and I. J. Sola, "Extreme ultraviolet vector beams driven by infrared lasers", *Optica* 4(5), 520-526 (2017). DOI

[Ivan 2021]: D. Ivanov, V. Dremin, E. Borisova, A. Bykov, T. Novikova, and I. Meglinski, "Polarization and depolarization metrics as optical markers in support to histopathology of ex vivo colon tissue", *Biomed. Opt. Express* 12(7), 4560-4572 (2021). DOI

[Ji 2017]: W. Ji, B. Wei, P. Chen, W. Hu, and Y. Lu, "Optical field control via liquid crystal photoalignment", *Mol. Cryst. Liq. Cryst.* 644(1), 3–11 (2017). DOI

[Jone 1941]: R. C. Jones, "A new calculus for the treatment of optical systems I. Description and discussion of the calculus", *J. Opt. Soc. Am.* 31(7), 488-493 (1941). DOI

[Kinn 1988]: K. Kinnstaetter, A. W. Lohmann, J. Schwider, and N. Streibl, "Accuracy of phase shifting interferometry", *Appl. Opt*. 27(24), 5082-5089 (1988). DOI

[Lage 2004]: S. T. Lagerwall, "Ferroelectric and antiferroelectric liquid crystals", *Ferroelectrics* 301(1), 15–45 (2004). DOI

[Lai 1991]: G. Lai and T. Yatagai, "Generalized phase-shifting interferometry", *J. Opt. Soc. Am. A* 8(5), 822-827 (1991). DOI

[Lauf 1996]: G. Laufer. "Propagation and applications of polarized light", Ch. 5 in Introduction to Optics and Lasers in Engineering, Cambridge University Press (1996). DOI

[Lópe 2020]: G. López-Morales, M. M. Sánchez-López, A. Lizana, I. Moreno, and J. Campos, "Mueller matrix polarimetric imaging analysis of optical components for the generation of cylindrical vector beams", *Crystals* 10(12), 1155 (2020). DOI

[Lu 1990]: K. Lu and E. A. B. Saleh, "Theory and design of the liquid crystal TV as an optical spatial phase modulator", *Opt. Eng.* 29(3), 240–246 (1990). DOI

[Lu 1996]: S. Lu and R. A. Chipman, “Interpretation of Mueller matrices based on polar decomposition”, *J. Opt. Soc. Am. A* 13(5), 1106-1113 (1996). DOI

[Marc 2019]: D. Marco, M. M. Sánchez-López, A. Cofré, A. Vargas, and I. Moreno. “Optimal triplicator design applied to a geometric phase vortex grating”, *Opt. Express* 27(10), 14472-14486 (2019). DOI

[Marc 2020]: D. Marco, A. Vargas, M. M. Sánchez-López, and I. Moreno, “Measuring the spatial deformation of a liquid-crystal on silicon display with a self-interference effect”, *Opt. Lett.* 45(16), 4480-4483 (2020). DOI

[Mart 1989]: F. Martin, H. Mkrigoux, and P. Zecchini, “Reflectance infrared spectroscopy in gemology”, *Gems & Gemology* 25(4), 226-231 (1989). DOI

[Martí 2006]: A. Martínez, N. Beaudoin, I Moreno, M. M. Sanchez-López, and P. Velasquez. “Optimization of the contrast ratio of a ferroelectric liquid crystal optical modulator”, *J. Opt. A: Pure Appl. Opt.* 8(1), 1013–1018 (2006). DOI

[Martí 2014]: J. L. Martínez, I. Moreno, M. M. Sánchez-López, A. Vargas, and P. García-Martínez. “Analysis of multiple internal reflections in a parallel aligned liquid crystal on silicon SLM”, *Opt. Express* 22(21), 25866-25879 (2014). DOI

[Marti 2016]: J. L. Martínez, E. J. Fernández, P. M. Prieto, and P. Artal, “Interferometric method for phase calibration in liquid crystal spatial light modulator using a self-generated diffraction grating”, *Opt. Express* 24(13), 14159–14171 (2016). DOI

[Marti 2018]: J. L. Martínez-Fuentes and I. Moreno, “Random technique to encode complex valued holograms with on-axis reconstruction onto phase-only displays”, *Opt. Express* 26(5), 5875-5893 (2018). DOI

[Marq 2000]: A. Márquez, J. Campos, M. J. Yzuel, I. Moreno, J. A. Davis, C. Iemmi, A. Moreno, and A. Robert, “Characterization of edge effects in twisted nematic liquid crystal displays”, *Opt. Eng.* 39(12), 3301–3307 (2000). DOI

[Mend 2014]: O. Mendoza-Yero, G. Mínguez-Vega, and J. Lancis, “Encoding complex fields by using a phase-only optical element”, *Opt. Lett.* 39(7), 1740–1743 (2014). DOI

[Mess 2018]: A. Messaadi, M. M. Sánchez-López, A. Vargas, P. García-Martínez, and I. Moreno, “Achromatic linear retarder with tunable retardance”, *Opt. Lett.* 43(14), 3277-3280 (2018). DOI

[Mito 2014]: M. Mitov, “Liquid-crystal science from 1888 to 1922: Building a revolution”, *ChemPhysChem* 15(7), 1245-1250 (2014). DOI

[More 2016]: O. Morel, R. Seulin, and D. Fofi, “Handy method to calibrate division-of-amplitude polarimeters for the first three Stokes parameters”, *Opt. Express* 24(12), 13634-13646 (2016). DOI

[Moren 2008]: I. Moreno, A. M. Cutillas, M. M. Sánchez-López, P. Velasquez, and F. Mateos. “Full prediction of the broadband optical modulation performance of a twisted nematic liquid crystal cell”, *Opt. Commun.* 281(22), 5520–5526 (2008). DOI

[Orte 2011]: N. Ortega-Quijano and J. L. Arce-Diego, “Mueller matrix differential decomposition”, *Opt. Lett*. 36(10), 1942-1944 (2011). DOI

[Paul 2015]: D. W. Paul, P. Ghassemi, J. C. Ramella-Roman, N. J. Prindeze, L. T. Moffatt, A. Alkhalil, and J. W. Shupp, "Noninvasive imaging technologies for cutaneous wound assessment: A review", *Wound Rep. Reg.* 23(2), 149-162 (2015). DOI

[Pein 2010]: A. Peinado, A. Lizana, J. Vidal, C. Iemmi, and J. Campos, "Optimization and performance criteria of a Stokes polarimeter based on two variable retarders", *Opt. Express* 18(8), 9815-9830 (2010). DOI

[Phot 2019]: Photonics21, "Photonics technologies empower every sector and our society", Ch. 3 in Europe's Age of Light! - How Photonics will Power Growth and Innovation, Photonics21 Multiannual Strategic Roadmap 2021-2027 (2019). DOI

[Piqu 2020]: G. Piquero, R. Martínez-Herrero, J. C. G. de Sande, and M. Santarsiero, "Synthesis and characterization of non-uniformly totally polarized light beams: tutorial", *J. Opt. Soc. Am. A* 37(4), 591-605 (2020). DOI

[Poll 2014]: T. D. Pollard, W. C. Earnshaw, J. Lippincott-Schwartz, G. T. Johnson, "Connective tissues", Ch. 33 Cell Biology, Elsevier, 3rd Ed. (2017). DOI

[Powe 2013]: S. B. Powell and V. Gruev, "Calibration methods for division-of-focal-plane polarimeters", *Opt. Express* 21(18), 21039-21055 (2013). DOI

[Rodr 2021]: O. Rodríguez-Núñez, P. Schucht, E. Hewer, T. Novikova, and A. Pierangelo. "Polarimetric visualization of healthy brain fiber tracts under adverse conditions: ex vivo studies", *Biomed. Opt. Express* 12(10), 6674-6685 (2021). DOI

[Rosa 2017]: C. Rosales-Guzmán and A. Forbes, "How to shape light with spatial light modulators", SPIE Press, Bellingham, Washington (2017). DOI

[Rosa 2018]: C. Rosales-Guzmán, B. Ndagano, and A. Forbes, "A review of complex vector light fields and their applications", *J. Opt.* 20, 123001 (2018). DOI

[Rubi 2017]: H. Rubinsztein-Dunlop, A. Forbes, M. V. Berry, M. R. Dennis, D. L. Andrews, M. Mansuripur, C. Denz, C. Alpmann, P. Banzer, T. Bauer, E. Karimi, L. Marrucci, M. Padgett, M. Ritsch-Marte, N. M Litchinitser, N. P Bigelow, C. Rosales-Guzmán, A. Belmonte, J. P. Torres, T. W. Neely, M. Baker, R. Gordon, A. B. Stilgoe, J. Romero, A. G. White, R. Fickler, A. E. Willner, G. Xie, B. McMorran, and A. M Weiner, "Roadmap on structured light", *J. Opt.* 19(1), 013001 (2017). DOI

[Scha 2006]: T. Scharf, "Polarized Light", Ch. 1 in Polarized Light in Liquid Crystals and Polymers, Wiley (2006). DOI

[Seki 2014]: T. Seki, "New strategies and implications for the photoalignment of liquid crystalline polymers", *Polym. J.* 46(1), 751–768 (2014). DOI

[Tinb 1996]: J. Tinbergen, "Polarization algebra and graphical methods", Ch. 4 in Astronomical Polarimetry, Ch. 4, Cambridge University Press (1996). DOI

[VanE 2021]: A. Van Eeckhout, E. Garcia-Caurel, T. Garnatje, J. C. Escalera, M. Durfort, J. Vidal, J. J. Gil, J. Campos, and A. Lizana, "Polarimetric imaging microscopy for advanced inspection of vegetal tissues", *Sci. Reports* 11, 3913 (2021). DOI

[Varg 2013]: A. Vargas, R. Donoso, M. Ramírez, J. Carrión, M. M. Sánchez-López, and I. Moreno. "Liquid-crystal retarder spectral retardance characterization based on a Cauchy

dispersion relation and a voltage transfer function", *Opt. Rev*. 20(1), 378–384 (2013). DOI

[Vize 2017]: J. Vizet, J. Rehbinder, S. Deby, S. Roussel, A. Nazac, R. Soufan, C. Genestie, C. Haie-Meder, H. Fernandez, F. Moreau, and A. Pierangelo, "In vivo imaging of uterine cervix with a Mueller polarimetric colposcope", *Sci. Reports* 7(1), 2471 (2017). DOI

[Wen 2021]: D. Wen and K. B. Croizier, "Metasurfaces 2.0: Laser-integrated and with vector field control", *APL Photonics* 6(1), 1-12 (2021). DOI

[Wu 1984]: S. T Wu, U. Efron, and L. D Hessz, "Birefringence measurements of liquid crystals", *Appl. Opt*. 23(21), 3911-3915 (1984). DOI

[Yama 2005]: M. Yamauchi, "Jones-matrix models for twisted-nematic liquid-crystal devices", *Appl. Opt.* 44 (21), 4484–4493 (2005). DOI

[Yari 1984]: A. Yariv and P. Yeh, "Light propagation in twisted anisotropic media", Ch. 5.3 in Optical Waves in Crystals, John Wiley & Sons, New York (1984). DOI

[Wied 2021]: A. Wiedenhoeft, "Structure and function of wood", Ch. 3 in Wood Handbook, General Technical Report, Madison, Wisconsin (2021). DOI

[Zhou 2024]: X. Zhou, L. Ma, H.K. Mubarak, D. Palsgrove, B. D. Sumer, A. Y. Chen, and B. Fei. "Polarized hyperspectral microscopic imaging system for enhancing the visualization of collagen fibers and head and neck squamous cell carcinoma", *J. Biomed. Opt.* 29(1), 1-16 (2024). DOI

[Zuru 2014]: A. Zurutuza and C. Marinelli, "Challenges and opportunities in graphene commercialization", *Nature Nanotech*. 9, 730–734 (2014). DOI

4. Publications

Optics & Laser Technology 156 (2022) 108567

Contents lists available at ScienceDirect

Optics and Laser Technology

journal homepage: www.elsevier.com/locate/optlastec

Mueller matrix polarimetric analysis applied to characterize the physical parameters of a twisted-nematic liquid–crystal modulator

Esther Nabadda [a], Guadalupe López-Morales [a,b], David Marco [a], María del Mar Sánchez-López [a,c], Ignacio Moreno [a,d,*]

[a] Instituto de Bioingeniería, Universidad Miguel Hernández de Elche, 03202 Elche, Spain
[b] Instituto de Investigación e Innovación en Energías Renovables, Universidad de las Ciencias y las Artes de Chiapas, Mexico
[c] Departamento de Física Aplicada, Universidad Miguel Hernández de Elche, 03202 Elche, Spain
[d] Departamento de Ciencia de Materiales, Óptica y Tecnología Electrónica, Universidad Miguel Hernández de Elche, 03202 Elche, Spain

ARTICLE INFO

Keywords:
Twisted Nematic Liquid-Crystal Modulators
Polarimetry
Mueller Matrix
Linear and Circular Retardance

ABSTRACT

This work presents a complete polarimetric study of a twisted-nematic (TN) liquid–crystal (LC) cell. We review the physical models that describe the cell and analyze the different modulation regimes. We extend the usual Jones matrix approach, where these microscopic physical models were developed, to the corresponding Mueller matrix approach. This polarimetric analysis is then used to obtain the effective linear and circular retardance components of the cell and to characterize its physical parameters like the twist angle, the orientation of the LC director axis and the maximum retardance. The technique simplifies previous approaches with the advantage of employing a single wavelength. Noteworthy, it also resolves the ambiguities in the determination of the physical parameters. Experimental evidence of the effectiveness in predicting the optical modulation is shown for a single-pixel TN-LC cell. Finally, a simplified procedure is presented under the assumption that the TN-LC cell is a pure retarder component, which is useful to perform a rapid calibration of the device.

1. Introduction

Twisted-nematic liquid crystals (TN-LC) constitute a well-established and widely employed display technology. They are also useful to build optical phase modulators, either as single cell devices or in the form of pixelated spatial light modulators (SLMs) [1]. They are linear retarders with special structures where the LC director axis (which is typically the extraordinary axis) rotates through an angle from the input to the output surface, commonly known as the twist angle. The retardance can be tuned via an applied voltage that causes the LC director axis to tilt. Recently, TN-LC components have also received considerable interest for manufacturing broadband retarders with improved properties using multi-twist stacks [2]. The twisted retarder structure is very interesting as a polarization transforming device because it can be regarded as a combination of effective linear retardance and effective optical rotation (circular retardance).

Different methods were developed in the past to describe the polarization properties of twisted anisotropic media [3], including the early works of R. C. Jones [4]. Because of the interest of using TN-LC modulators as phase-only spatial light modulators (SLM), Lu and Saleh [5] extended these Jones matrices by introducing the optical modulation assuming a voltage-dependent effective extraordinary refractive index $n_{ef}(V)$, thus leading to a variable retardance $\beta(V)$. After this seminal work, different approaches aimed at predicting the optical modulation with higher accuracy were proposed. Such refined models considered the LC edge layers coated to the device surfaces, where the LC director is unable to tilt freely as it does in the center of the LC cell, therefore adding a second retardance parameter $\delta(V)$ [6–8].

The analytical Jones matrices used in these previous works are expressed in a reference framework where the LC director at the input surface of the modulator is aligned with the x-axis. Therefore, the proper application of these models requires a prior precise determination of the twist angle (α) and the LC orientation (ψ_D). This orientation cannot be measured directly as in the standard case of a linear retarder, where the neutral axes can be found simply by looking for maximum light extinction between crossed polarizers. Instead, techniques using different wavelengths or spectroscopic procedures have been applied, where the spectral dependence of the maximum retardance ($\beta_{max}(\lambda)$)

* Corresponding author.
E-mail address: i.moreno@umh.es (I. Moreno).

https://doi.org/10.1016/j.optlastec.2022.108567
Received 12 August 2021; Received in revised form 29 July 2022; Accepted 1 August 2022
Available online 12 August 2022

provides sufficient information to solve possible ambiguities [9,10]. Other approaches are based on a single wavelength characterization and measurements with different polarization configurations [11,12]. All these techniques typically retrieve the LC parameters by simultaneously fitting a set of experimental curves to numerical values of ψ_D, α and β_{max}. Because ψ_D and α are fixed parameters, and $\beta_{max}(\lambda)$ can be interpolated using standard dispersion relations, the spectral modulation can be derived out of measurements made at sample wavelengths [13]. Additional experiments are required to univocally determine the sense of rotation of the LC director (sign of α) and to distinguish between the extraordinary and ordinary LC axes [14]. These techniques were proved successful in the characterization of TN-LC cells. However, their application requires performing several measurements and the simultaneous fitting of the microscopic physical parameters ψ_D, α and β_{max} to numerical data. To avoid such cumbersome calibration procedures, other approaches avoid any assumption on the LC microscopic physical model and directly measure the Jones matrix [15,16], or an equivalent retarder-rotator system [17].

Another standard mathematical description of polarization is the Mueller-Stokes (MS) approach [18]. Within this formalism, polarization states are described by the four Stokes parameters and polarization devices are described by 4x4 Mueller matrices. Some works used the MS formalism to describe TN-LCDs [19–22] since it provides a more complete polarimetric description, including parameters like depolarization, diattenuation and polarizance. The MS approach became especially relevant when liquid–crystal on silicon (LCOS) technology [23] emerged. In these devices the phase fluctuations originated by flicker can result in an effective depolarization [24] that cannot be measured in the Jones matrix approach. Hence, Mueller-matrix polarimetry has become a standard technique for characterizing polarization components and devices, including TN-LC modulators. However, the works that apply the MS approach do not generally consider a physical model for the TN-LC cell; they are based instead on empirical polarization measurements. This implies that the TN modulator must be fully calibrated for each wavelength of interest. In addition, the MS approach does not account for phase modulation, and therefore a combined approach is required to fully predict the complex optical modulation [25].

In the last decade, LCOS devices with vertically-aligned (VAN) or zero-twist electrically controlled birefringence (ECB) configurations became the dominant technology for phase-only SLMs [23]. Even though TN-LC SLMs proved to be very effective as phase-only SLMs with properly adjusted polarization configurations [26–29], they have generally been abandoned for this purpose, mainly due to the complex and time-consuming techniques required to achieve these phase-only configurations. They could not compete with the ease of configuring VAN/ECB LC devices, which only require finding the direction of the principal axes and aligning the input linear polarization parallel to the modulating axis. Regardless, TN-LC SLMs remain more affordable as compared to the costly VAN/ECB LCOS devices.

In this work we consider a physical model of the TN-LC cell and perform a complete Mueller matrix polarimetric analysis to fully characterize its physical parameters and its optical modulation. We first review the analytical Jones matrices describing the physical model of the TN-LC modulator and derive the corresponding Mueller matrices in the different modulation regimes. We show that a MS polarimetric analysis allows to characterize the physical parameters of the TN-LC cell. For instance, α can easily be determined when the TN-LC acts as a pure polarization rotator, while the polarization eigenstates give a direct measurement of ψ_D, thus enabling an independent single wavelength measurement of these two parameters. The Mueller matrix further provides an unambiguous distinction between the fast and slow axes, and the sense of rotation of the LC director. Then, we identify the elements of the Mueller matrix that yield a full characterization of the TN-LC optical modulation retardances $\beta(V)$ and $\delta(V)$ related, respectively, to the central and edge LC layers in the cell [5,7]. These procedures provide a complete description of the modulation properties. Finally, based on the assumption that the TN-LC is a pure retarder component, a simplified method is presented at the end of the paper. This simplified characterization requires fewer measurements than the full Mueller matrix characterization, thus enabling a rapid configuration of the modulator in the laboratory.

The paper is organized as follows. After this introduction, Section 2 reviews the Jones matrix and the Mueller matrix describing the TN-LC cell, and the description of its polarization eigenstates and retardance vector. Then, Section 3 shows the experimental Mueller matrix characterization, including the location of the pure polarization rotator regime, and how this can be used to completely determine the device physical parameters and its optical modulation. Section 4 develops the simplified procedure, valid under the assumption of a pure retarder device, which is shown to yield equivalent results. Finally, Section 5 gives the conclusions.

2. Review of the TN-LC cell and its modulation regimes

In this section we review the polarization transformations induced by a TN-LC cell. At this point we consider the model by Lu and Saleh [5].

2.1. Jones matrix for the TN-LC cell

According to this model, the Jones matrix of a TN-LC cell where the LC director axis of the first layer is assumed to be aligned along the x-axis of the coordinate system, reads

$$\mathbf{M}_{\mathbf{TNLC}} = e^{-i\beta}\mathbf{R}(-\alpha)\cdot\mathbf{M}(X,Y,Z), \tag{1}$$

where $\mathbf{R}(-\alpha)$ is the 2×2 rotation matrix (we follow the notations by Saleh and Teich in [30]):

$$\mathbf{R}(\alpha) = \begin{bmatrix} \cos\alpha & \sin\alpha \\ -\sin\alpha & \cos\alpha \end{bmatrix}, \tag{2}$$

and $\mathbf{M}(X,Y,Z)$ is given by [13]:

$$\mathbf{M}(X,Y,Z) = \begin{bmatrix} X-iY & Z \\ -Z & X+iY \end{bmatrix}, \tag{3}$$

with the restriction $X^2+Y^2+Z^2=1$. After symmetry considerations, the matrix decomposition in Eqs. (1)–(3) was demonstrated to be the general expression for any TN-LC cell, independent of the specific distribution of the twist and tilt angle along the cell [31]. Therefore, we will henceforth use the X,Y,Z functions.

In the standard model by Lu and Saleh [5], X,Y,Z depend on the twist angle α and on the LC retardance $2\beta = (2\pi/\lambda)\Delta n\cdot t$ (here λ denotes the wavelength, $\Delta n = n_e - n_o$ is the birefringence of the LC material, and t is the thickness of the LC layer) as.

$$X = \cos\gamma,\ Y = \frac{\beta}{\gamma}\sin\gamma,\ Z = \frac{\alpha}{\gamma}\sin\gamma, \tag{4}$$

where $\gamma = \sqrt{\alpha^2+\beta^2}$. This model provides a very accurate description of the TN-LC cell in the absence of applied voltage.

Upon applying a voltage to the modulator, the LC tilts an angle $\theta(V)$ in the central region of the LC cell. The standard Lu and Saleh model [5] considers the optical modulation driven by the voltage-dependent retardance parameter $\beta(V)$ which now depends on the tilt angle as

$$\beta(V) = \frac{\pi}{\lambda}\left[n_{ef}(\theta(V)) - n_o\right]\cdot t, \tag{5}$$

where the effective extraordinary index n_{ef} is related to the LC tilt angle θ by.

$$\frac{1}{n_{ef}^2(\theta)} = \frac{\sin^2(\theta)}{n_o^2} + \frac{\cos^2(\theta)}{n_e^2}. \tag{6}$$

By changing the value of parameter β in Eq. (5) three interesting regimes can be found:

(a) The *adiabatic regime* [3], also named *Maugin limit* [32], which is achieved when $\beta \gg \alpha$, and therefore $\gamma \simeq \beta$, so the matrix in Eq. (1) can be approximated as:

$$\mathbf{M_{TNLC}}(\beta \gg \alpha) = e^{-i\beta}\mathbf{R}(-\alpha)\cdot\begin{bmatrix} e^{-i\beta} & 0 \\ 0 & e^{+i\beta} \end{bmatrix}, \tag{7a}$$

i.e., the TN-LC cell behaves as a combination of a polarization rotator and linear retarder.

(b) When $\gamma = m\pi$ (m being an integer number) the device becomes a pure polarization rotator since the Jones matrix $\mathbf{M}$ in Eq. (3) becomes the identity matrix, i.e.:

$$\mathbf{M_{TNLC}}(\gamma = m\pi) = e^{-i\beta}\mathbf{R}(-\alpha)(-1)^m. \tag{7b}$$

This situation is known as the *Gooch-Tarry relation* [32] or as a *local adiabatic point* [33].

(c) (Finally, in the limit of low birefringence $\beta \to 0$ we find that $\gamma \to \alpha$ and the matrix $\mathbf{M}$ in Eq. (3) becomes a rotation matrix $\mathbf{R}(+\alpha)$ that cancels $\mathbf{R}(-\alpha)$ in Eq. (1), so the global TN-LC Jones matrix becomes the identity matrix $\mathbf{M_{TNLC}}(\beta \to 0) = \mathbf{I}$.

In TN-LC modulators the twist angle is typically $\alpha = \pm\pi/2$ and the birefringence parameter varies between the limit $\beta = 0$ and at least the first adiabatic point, $\gamma = \pi$. In such case the Jones matrix changes from being the identity matrix, thus not changing the input polarization, to become a pure rotator matrix $\mathbf{R}(-\alpha)$, thus rotating the input polarization by the twist angle.

Finally, let us emphasize that this form of the Jones matrix in Eq. (1) is valid provided the LC director at the input surface of the modulator is aligned along the x-coordinate axis of the reference framework. In case the LC director forms an angle ψ_D with the x-axis, the Jones matrix must be calculated using the standard rotation transformation given by [30]:

$$\mathbf{M_{TNLC}}(\psi_D) = \mathbf{R}(-\psi_D)\cdot\mathbf{M_{TNLC}}\cdot\mathbf{R}(+\psi_D). \tag{8}$$

2.2. Mueller matrix for the TN-LC cell

The previous section provides an analytical description of the TN-LC cell within the Jones matrix formalism. However, the MS formalism allows to obtain additional polarimetric information. The Mueller matrix $\widetilde{\mathbf{M}}$ of a pure retarder can be calculated from the corresponding Jones matrix $\mathbf{M}$ as [18]:

$$\widetilde{\mathbf{M}} = \mathbf{A}\cdot(\mathbf{M}\otimes\mathbf{M})\cdot\mathbf{A}^{-1}, \tag{9}$$

where $\otimes$ denotes the tensor (Kronecker) product and where

$$\mathbf{A} = \begin{bmatrix} 1 & 0 & 0 & 1 \\ 1 & 0 & 0 & -1 \\ 0 & 1 & 1 & 0 \\ 0 & i & -i & 0 \end{bmatrix}. \tag{10}$$

Alternatively, the elements m_{ij} of the Mueller matrix ($i,j = 0,1,2,3$) can be obtained as [18]:

$$m_{ij} = \frac{1}{2}\mathrm{Tr}\left(\mathbf{M}\cdot\sigma_i\cdot\mathbf{M}^{+}\cdot\sigma_j\right), \tag{11}$$

where $\mathrm{Tr}(\bullet)$ denotes the trace of the matrix, $+$ the Hermitian conjugate and σ are the set of four 2×2 matrices comprising the identity matrix and the Pauli matrices, i.e.

$$\sigma_0 = \begin{pmatrix} 1 & 0 \\ 0 & 1 \end{pmatrix}, \sigma_1 = \begin{pmatrix} 1 & 0 \\ 0 & -1 \end{pmatrix}, \sigma_2 = \begin{pmatrix} 0 & 1 \\ 1 & 0 \end{pmatrix}, \sigma_3 = \begin{pmatrix} 0 & -i \\ i & 0 \end{pmatrix} \tag{12}$$

For the case of a pure retarder element (i.e., an element without diattenuation, polarizance or depolarization) the Mueller matrix takes the form:

$$\widetilde{\mathbf{M}}_R = \begin{bmatrix} 1 & \overrightarrow{0} \\ \overrightarrow{0}^T & \widetilde{\mathbf{m}}_R \end{bmatrix}, \tag{13}$$

where $\overrightarrow{0} = (0,0,0)$ and $\widetilde{\mathbf{m}}_R$ is a 3×3 real unitary matrix. In this section we consider ideal TN-LC cells that are pure retarder elements described by the Jones matrix in Eqs. (1)–(3). Therefore, the corresponding Mueller matrix can be described only by submatrix $\widetilde{\mathbf{m}}_R$.

Considering Eqs. (1), (9)–(12), the Mueller submatrix $\widetilde{\mathbf{m}}_{\mathrm{TNLC}}$ describing the TN-LC cell results in an equivalent product $\widetilde{\mathbf{m}}_{\mathrm{TNLC}} = \widetilde{\mathbf{R}}(-\alpha)\bullet\widetilde{\mathbf{m}}$, where the rotation matrix $\widetilde{\mathbf{R}}(\alpha)$ and the matrix $\widetilde{\mathbf{m}}$ now in the Mueller formalism read:

$$\widetilde{\mathbf{m}}_{\mathrm{TNLC}} = \widetilde{\mathbf{R}}(-\alpha)\cdot\widetilde{\mathbf{m}} =$$

$$= \begin{bmatrix} \cos(2\alpha) & \sin(2\alpha) & 0 \\ -\sin(2\alpha) & \cos(2\alpha) & 0 \\ 0 & 0 & 1 \end{bmatrix}\cdot\begin{bmatrix} 1-2Z^2 & 2XZ & -2YZ \\ -2XZ & 2X^2-1 & -2XY \\ -2YZ & 2XY & 1-2Y^2 \end{bmatrix}. \tag{14}$$

The adiabatic regime achieved when $\beta \gg \alpha$ (or equivalently $\gamma \simeq \beta$) (Eq. (7a)) results in:

$$\widetilde{\mathbf{m}}_{\mathrm{TNLC}}(\beta \gg \alpha) = \widetilde{\mathbf{R}}(-\alpha)\cdot\begin{bmatrix} 1 & 0 & 0 \\ 0 & \cos(2\beta) & -\sin(2\beta) \\ 0 & \sin(2\beta) & \cos(2\beta) \end{bmatrix}. \tag{15}$$

Similarly, the pure rotator regime achieved when $\gamma = \pi$ (Eq. (7b)) leads to the Mueller matrix $\widetilde{\mathbf{m}}_{\mathrm{TNLC}}(\gamma = \pi) = \widetilde{\mathbf{R}}(-\alpha)$, and the limit $\beta \to 0$ results in an identity Mueller matrix.

The matrix product $\widetilde{\mathbf{m}}_{\mathrm{TNLC}} = \widetilde{\mathbf{R}}(-\alpha)\cdot\widetilde{\mathbf{m}}$ n Eq. (14) results in.

$$\widetilde{\mathbf{m}}_{\mathrm{TNLC}} = \begin{bmatrix} 2XZs + (1-2Z^2)c & 2XZc + (2X^2-1)s & 2XYs - 2YZc \\ (1-2Z^2)s - 2XZc & (2X^2-1)c + 2XZs & -2XYc - 2YZs \\ -2YZ & 2XY & 1-2Y^2 \end{bmatrix} \tag{16}$$

where $s = \sin(2\alpha)$ and $c = \cos(2\alpha)$. For the standard twist angle $\alpha = \pm\pi/2$ it results in:

$$\widetilde{\mathbf{m}}_{\mathrm{TNLC}} = \begin{bmatrix} 2Z^2-1 & -2XZ & 2YZ \\ 2XZ & 1-2X^2 & 2XY \\ -2YZ & 2XY & 1-2Y^2 \end{bmatrix}. \tag{17}$$

Finally, like in the Jones formalism, the Mueller matrix in Eq. (14)-(17) is valid provided the LC director at the input surface of the modulator is aligned with the x-axis of the reference framework. In case it is rotated by an angle ψ_D the corresponding Mueller matrix is calculated as $\widetilde{\mathbf{m}}_{\mathrm{TNLC}}(\psi_D) = \widetilde{\mathbf{R}}(-\psi_D)\cdot\widetilde{\mathbf{m}}_{\mathrm{TNLC}}\cdot\widetilde{\mathbf{R}}(+\psi_D)$.

Table 1 summarizes the Jones and the Mueller matrices for the different regimes of the TN-LC cell, as well as the general case for the standard twist angle $\alpha = \pm\pi/2$.

Fig. 1(a) illustrates the variation of the X, Y, Z functions in the Lu and Saleh model [5] (Eqs. (4) and (5)) represented versus the retardance parameter β for a TN-LC cell with $\alpha = +\pi/2$. The horizontal axis is displayed in inverse sense to better compare with the experimental results presented in the next section. Note that for $\beta = \sqrt{3}\pi/2 = 0.866\pi$ the first pure rotator (local adiabatic) point is reached. This is marked with a vertical line in the graph, noting that $Y = Z = 0$ and $X = -1$ at this point. Fig. 1(b) shows the corresponding elements m_{ij} ($i,j = 1,2,3$) of the Mueller submatrix as a function of β, again for a TN-LC cell with $\alpha = +\pi/2$. These curves also illustrate the transition from the identity matrix ($\beta = 0$) to the pure rotation matrix achieved when $\beta = 0.866\pi$, where $m_{11} = m_{22} = -1$ and $m_{33} = +1$ and all the rest of elements vanish. Let us highlight the large variation of the element m_{22}, which changes from $+1$ to -1 and back to $+1$. For a TN-LC cell with $\alpha = \pi/2$ the Lu

Table 1
Jones and Mueller matrices for different regimes of the TNLC cell.

Regime	Jones matrix $\mathbf{M}_{\mathrm{TNLC}}$	Mueller submatrix $\widetilde{\mathbf{m}}_{\mathrm{TNLC}}$
General case	$e^{-i\beta}\mathbf{R}(-\alpha)\cdot\begin{bmatrix} X-iY & Z \\ -Z & X+iY \end{bmatrix}$	$\widetilde{\mathbf{R}}(-\alpha)\cdot\begin{bmatrix} 1-2Z^2 & 2XZ & -2YZ \\ -2XZ & 2X^2-1 & -2XY \\ -2YZ & 2XY & 1-2Y^2 \end{bmatrix}$
Adiabatic limit ($\beta \gg \alpha$)	$e^{-i\beta}\mathbf{R}(-\alpha)\cdot\begin{bmatrix} \exp(-i\beta) & 0 \\ 0 & \exp(i\beta) \end{bmatrix}$	$\widetilde{\mathbf{R}}(-\alpha)\cdot\begin{bmatrix} 1 & 0 & 0 \\ 0 & \cos(2\beta) & -\sin(2\beta) \\ 0 & \sin(2\beta) & \cos(2\beta) \end{bmatrix}$
First pure rotator point ($\gamma = \pi$)	$-e^{-i\beta}\begin{bmatrix} \cos(\alpha) & -\sin(\alpha) \\ \sin(\alpha) & \cos(\alpha) \end{bmatrix}$	$\begin{bmatrix} \cos(2\alpha) & -\sin(2\alpha) & 0 \\ \sin(2\alpha) & \cos(2\alpha) & 0 \\ 0 & 0 & 1 \end{bmatrix}$
General case with standard twist $\alpha = \pi/2$	$e^{-i\beta}\begin{bmatrix} Z & -X-iY \\ X-iY & Z \end{bmatrix}$	$\begin{bmatrix} 2Z^2-1 & -2XZ & 2YZ \\ 2XZ & 1-2X^2 & 2XY \\ -2YZ & 2XY & 1-2Y^2 \end{bmatrix}$

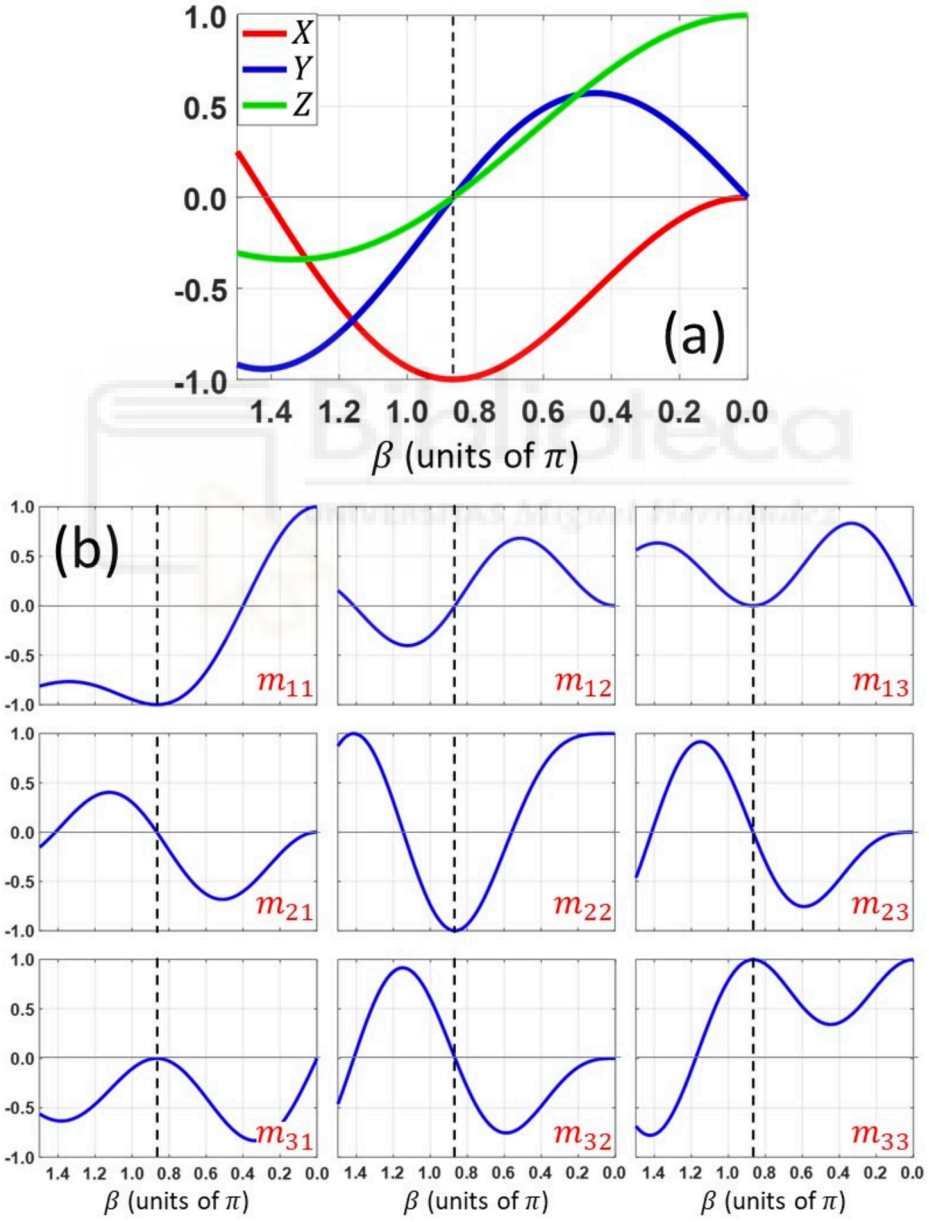

Fig. 1. (a) Evolution of the X, Y, Z functions with respect to β for a TN-LC cell with $\alpha = +\pi/2$ in the Lu and Saleh model [5]. (b) m_{ij} elements of the corresponding Mueller submatrix. The pure rotator (local adiabatic point) is found at $\beta = 0.866\pi$ (marked with a vertical line).

and Saleh model [5] leads to the relation $m_{22} = 1 - 2X^2 = -\cos(2\gamma)$. The large variation of m_{22} makes it ideal for an accurate measurement of γ_{max}, and consequently of $\beta_{max} = \sqrt{\gamma_{max}^2 - \alpha^2}$.

The normalized transmission of the TN-LC cell between linear polarizers (T_L) can be calculated using either the Jones matrix or the Mueller matrix. If the input and output polarizers have orientations ξ_1 and ξ_2 relative to the LC director at the input surface ($x-$ axis), the normalized transmission is given by the relation.

$$T_L(\xi_1,\xi_2) = \left(X\cos(\xi_1 - \xi_2 + \alpha) + Z\sin(\xi_1 - \xi_2 + \alpha)\right)^2 + \left(Y\cos(\xi_1 + \xi_2 - \alpha)\right)^2 \quad (18)$$

while when the TN-LC cell is inserted between circular polarizers, it is given by.

$$T_{C\perp} = Y^2 \text{ and } T_{C\parallel} = X^2 + Z^2 \quad (19)$$

where $T_{C\perp}$ and $T_{C\parallel}$ denote respectively the transmission for crossed and parallel circular polarizers. Note that the relations in Eq. (19) are independent of the TN-LC cell orientation, i.e., independent of ψ_D, thus being useful to find the adiabatic point even without knowing the correct orientation.

2.3. Retardance vector and polarization eigenstates

Retarders can be characterized by the retardance vector $\vec{\mathbf{R}}$ [34–36], whose magnitude R is given by the total retardance, which is obtained from the Mueller matrix as.

$$\cos(R) = \frac{1}{2}\mathrm{Tr}[\widetilde{\mathbf{M}}_R] - 1 = \frac{1}{2}\mathrm{Tr}[\widetilde{\mathbf{m}}_R] - \frac{1}{2}, \quad (20)$$

and whose components can be calculated as.

$$\vec{\mathbf{R}} = R\widehat{\mathrm{R}} = \begin{bmatrix} R_H \\ R_{45} \\ R_C \end{bmatrix} = R\frac{1}{2\sin(R)}\begin{bmatrix} m_{R23} - m_{R32} \\ m_{R31} - m_{R13} \\ m_{R12} - m_{R21} \end{bmatrix}, \quad (21)$$

where $R_L = \sqrt{R_H^2 + R_{45}^2}$ is the total linear retardance and R_C the circular retardance. Alternatively, an equivalent approach can be applied within the Jones formalism for instance by applying the parametrization by Arteaga and Canillas [37].

The application of Eqs. (20)–(21) to the Mueller matrix in Eq. (16) allows obtaining analytical expressions for the retardance vector in terms of the X, Y, Z functions describing the TN-LC cell. The total retardance is given by.

$$\cos(R) = \left(X^2 - Z^2\right)\cos(2\alpha) + 2XZ\sin(2\alpha) - Y^2, \quad (22)$$

which can be reduced to

$$\cos\left(\frac{R}{2}\right) = X\cos(\alpha) + Z\sin(\alpha), \quad (23)$$

and the retardance vector is

$$\vec{\mathbf{R}} = \frac{R}{\sin R}\begin{bmatrix} -XY(1+\cos(2\alpha)) - YZ\sin(2\alpha) \\ -YZ(1-\cos(2\alpha)) - XY\sin(2\alpha) \\ 2XZ\cos(2\alpha) - 2\left(X^2 - Z^2\right)\sin(2\alpha) \end{bmatrix}. \quad (24)$$

For the standard twist angle $\alpha = \pi/2$, then $\cos(R/2) = Z$ and the retardance vector reduces to

$$\vec{\mathbf{R}} = R\frac{1}{\sqrt{X^2 + Y^2}}\begin{bmatrix} 0 \\ -Y \\ -X \end{bmatrix}, \quad (25)$$

so the linear and circular retardances are given by $R_H = 0$, $R_{45}/R = -Y/\left(\sqrt{X^2 + Y^2}\right)$ and $R_C/R = -X/\left(\sqrt{X^2 + Y^2}\right)$. Let us emphasize that these retardances are effective parameters. The liquid–crystal layer is a linear retarder, but its twisted structure generates the effective circular retardance. Fig. 2(a) illustrates the evolution of R,R_L and R_C as a function of β for the standard case of a twist $\alpha = \pi/2$. The special value $\beta = 0.866\pi$ corresponding to the first local adiabatic point is again marked to highlight that at this value, the cell behaves as a pure polarization rotator, and therefore it only exhibits circular retardance.

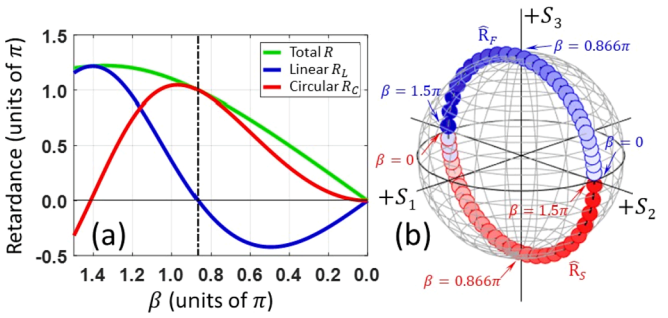

Fig. 2. (a) Total, linear and circular retardances of a TN-LC cell with $\alpha = +\pi/2$ with respect to β. The pure rotator (local adiabatic point) is found at $\beta = 0.866\pi$. (b) Evolution in the Poincaré sphere of the polarization eigenstates $\widehat{\mathrm{R}}_F$ (blue dots) and $\widehat{\mathrm{R}}_S$ (red dots) of $\mathbf{M}_{\mathbf{TNLC}}$. (For interpretation of the references to colour in this figure legend, the reader is referred to the web version of this article.)

The normalized vector $\widehat{\mathrm{R}}_F = \vec{\mathbf{R}}/R$ provides the Stokes parameters $\widehat{\mathrm{R}}_F = (S_1, S_2, S_3)^T$ of the fast polarization eigenstate of the equivalent elliptical retarder, while the orthogonal state $\widehat{\mathrm{R}}_S = -\widehat{\mathrm{R}}_F$ is the slow polarization eigenstate. The eigenstates $\widehat{\mathrm{R}}_F$ and $\widehat{\mathrm{R}}_S$ are polarization states that are transmitted though the TN-LC cell without changing its polarization, simply gaining a phase. This concept was employed for the configuration of the TN-LC modulators as phase-only SLMs devices [26]. The orientation (ψ) and ellipticity (ε) angles of the eigenvectors are given by their Stokes parameters as $\tan(2\psi) = S_2/S_1$ and $\tan(2\varepsilon) = S_3/\sqrt{S_1^2 + S_2^2}$ [18]. Therefore, from Eq. (25), the fast eigenstate of the TN-LC cell has an azimuth angle given by.

$$\tan(2\psi) = \frac{Z(1-\cos(2\alpha)) + X\sin(2\alpha)}{X(1+\cos(2\alpha)) + Z\sin(2\alpha)}. \quad (26)$$

Using simple trigonometric relations, this equation can be simplified to $\tan(2\psi) = \tan(\alpha)$, which shows that the orientation of the polarization eigenstate is constant, equal to $\psi = \alpha/2$. For the standard twist $\alpha = \pi/2$, $\widehat{\mathrm{R}}_F$ is oriented at $\psi = \pi/4$ while its ellipticity changes as $2\varepsilon = \arctan(X/Y)$. In this derivation we used the Mueller matrix (Eq. (14)-(16)) for a TN cell with the LC director at the input surface parallel to the x-axis. Therefore, the eigenstate azimuth constant value $\psi = \alpha/2$ is relative to the x-axis. This angle is useful to locate the orientation of the LC director in the laboratory frame reference once α is known, i.e., it allows determining the angle ψ_D.

Fig. 2(b) illustrates the evolution of the fast and slow eigenstates as a function of β, again for the standard case of twist angle $\alpha = +\pi/2$ and for a variation in the range $\beta \in [0, 1.5\pi]$. As expected from the previous discussion, these states are aligned along the meridian in the plane $S_2 - S_3$ of the Poincaré sphere while the ellipticity changes with β. At the local adiabatic point, where the TN-LC cell becomes a pure polarization rotator, the eigenstates become circularly polarized.

3. Experimental Mueller matrix polarimetric characterization

In this section we experimentally verify the former predictions by using a standard Mueller matrix polarimeter, with a polarization state generator (PSG) composed of a linear polarizer and a quarter-wave plate (QWP), and a polarization state analyzer (PSA) composed by a second

QWP and a second polarizer. We use the standard polarization states (linear states horizontal, vertical and at $\pm 45^{\circ}$, and circular R and L states), both in the PSG and in the PSA. A He-Ne laser (Melles Griot, 25-LHP-151–230) of 632.8 nm wavelength is used. In the experiments we consider the x-axis aligned along the horizontal direction in the laboratory, and we measure positive angles as counterclockwise rotated from the analyzer point of view.

We tested a 2 cm diameter circular single cell TN-LC modulator

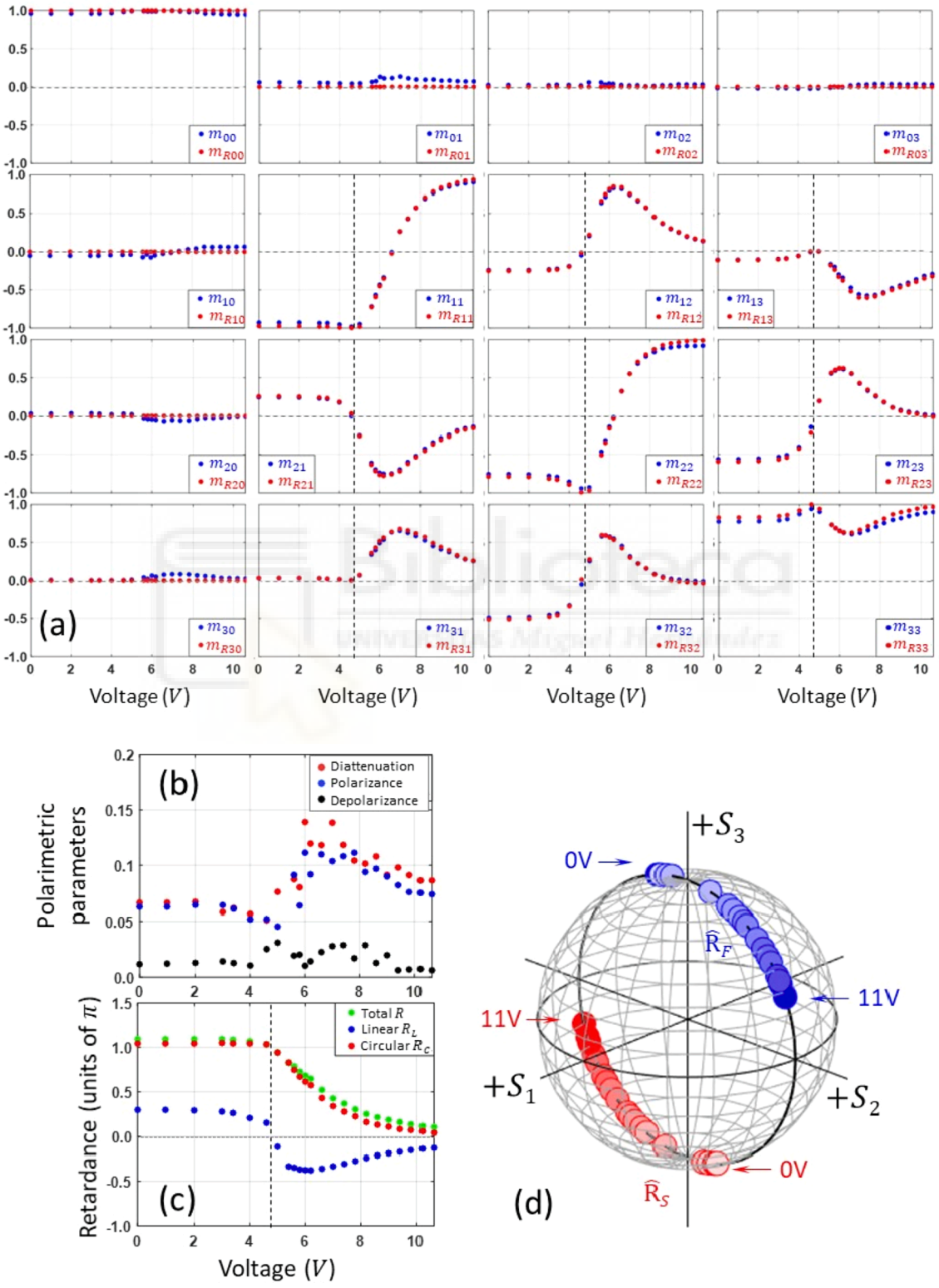

Fig. 3. (a) Experimental measurement of the Mueller matrix elements for the TN-LC modulator as a function of the applied voltage (blue dots) and the corresponding retarder matrix derived from the Lu -Chipman decomposition (red dots). (b) Diattenuation, polarizance and depolarizance. (c) Total, linear and circular retardances. (d) Polarization eigenstates of the retarder represented in the Poincaré sphere. (For interpretation of the references to colour in this figure legend, the reader is referred to the web version of this article.)

(Jenoptic, model ALM) that is driven by a wavefunction generator, which addresses a 2 kHz square DC balanced electrical signal of peak-to-peak voltage (Vpp) ranging from zero to 11 V. The Mueller matrix is calibrated for each Vpp value. Fig. 3(a) shows the 16 elements of the measured matrix and their evolution with Vpp (blue dots). All curves were normalized to the maximum value of m_{00} measured for the complete voltage range. The results are close to those expected for a pure retarder element, i.e., with $m_{00} = 1$, $m_{i0} = 0$ and $m_{0j} = 0$ $(i,j = 1,2,3)$. However, non-negligible variations are observed in the elements of the first row and first column. Therefore, we applied the Lu-Chipman polar decomposition [35], which expresses the measured Mueller matrix as $\widetilde{\mathbf{M}} = \widetilde{\mathbf{M}}_\Delta \cdot \widetilde{\mathbf{M}}_R \cdot \widetilde{\mathbf{M}}_D$ where $\widetilde{\mathbf{M}}_D$,$\widetilde{\mathbf{M}}_R$ and $\widetilde{\mathbf{M}}_\Delta$ are the diattenuator, retarder and depolarizer matrix components. The polarizance and diattenuation values in Fig. 3(b) are comprised below 0.15 in the complete range, and the depolarizance remains below 0.05.

Fig. 3(a) also shows (red dots) the retarder matrix $\widetilde{\mathbf{M}}_R$ obtained within the Lu-Chipman polar decomposition. These curves are very close to those of $\widetilde{\mathbf{M}}$. The curves show no variation for Vpp between zero and 3 V, since the threshold voltage to induce LC molecular tilt is not reached yet. In the other extreme, for voltages above 10 Vpp the matrix approaches the identity matrix (limit $\beta \to 0$). In between, large variations are observed in the elements of the 3×3 submatrix $\widetilde{\mathbf{m}}_R$, which follow a behavior like the simulation in Fig. 2(a) for values of β in the range $[1.1\pi, 0]$.

At Vpp = 4.6 V, the effective linear retardance goes to zero, and all the retardance becomes circular. At this voltage, the TN-LC cells is in the first adiabatic point and behaves as a pure polarization rotator. Therefore, the rotation angle for input linearly polarized light at this point directly provides a direct measurement of the twist angle. In our device we measured a rotation of $90° \pm 1°$, where the uncertainty comes from the minimum scale we can measure in the rotating mount of the polarizer. In fact, since the rotation is related to the circular retardance as $\alpha = R_C/2$, the value $R_C = \pi$ measured at Vpp = 4.6 V confirms the twist angle $\alpha = \pi/2$.

A second useful result is shown in Fig. 3(d). The retardance vector is calculated using Eqs. (20) and (21) and its components provide the effective linear and circular retardances, as shown in Fig. 3(c). The normalized vectors $\widehat{\mathrm{R}}_F$ and $\widehat{\mathrm{R}}_S$ related to the fast and slow eigenstates are shown in Fig. 3(d) represented on the Poincaré sphere. Note that the eigenstates are oriented along the $S_2 - S_3$ plane, as expected from the discussion of Fig. 2. This confirms that the TN-LC cell was correctly aligned with respect to the laboratory x-axis ($\psi_D = 0$). If the TN-LC cell had not been correctly oriented ($\psi_D \neq 0$) these eigenstates would appear aligned along another meridian of the Poincaré sphere, oriented at an azimuth $\psi = \pi/4 + \psi_D$.

Since the TN-LC cell is oriented with the LC director parallel to the x-axis of the laboratory framework ($\psi_D = 0$), the measured Mueller matrix elements in Fig. 3(a) follow a qualitative behavior like Eq. (17). In this situation the Mueller matrix measurement also resolves two remaining ambiguities. The sign of α indicates the rotation sense of the LC director inside the cell, while the change in ψ_D to $\psi_D + \pi/2$ exchanges the orientation of the extraordinary and ordinary axes. Since the extraordinary axis depends on the applied voltage, this ambiguity was traditionally resolved by means of additional experiments that depend on the phase modulation [13,14]. However, these ambiguities can be easily resolved from the data in Fig. 3, for instance, by noting the variations on the m_{12} and m_{13} Mueller matrix elements. Fig. 4 shows a simulation of the four situations that may occur. Changing the sign of α inverts also the sign of both m_{12} and m_{13} elements. On the contrary, changing $\psi_D \to \psi_D + \pi/2$ inverts the sign of the element m_{13}, while leaving m_{12} unaltered. Therefore, according to the experimental result in Fig. 3 (a) one can conclude the positive sense of the twist angle in our device and the value $\psi_D = 0$, thus indicating that the $x-$ axis of the laboratory coincides with the LC director at the input face of the LC cell.

Finally, it is also interesting to obtain the retardances modulation parameters related to the microscopic description of the TN-LC cell. Here we use the Lu & Saleh model [5] that considers the retardance parameter $\beta(V)$, corrected by the edge LC layers [7] by means of a second retardance parameter $\delta(V)$. For this refined model, the X, Y functions in Eq. (4) must be modified to.

$$X = \cos(\gamma)\cos(2\delta) - \frac{\beta}{\gamma}\sin(\gamma)\sin(2\delta), \tag{27a}$$

$$Y = \cos(\gamma)\sin(2\delta) + \frac{\beta}{\gamma}\sin(\gamma)\cos(2\delta), \tag{27b}$$

while Z is insensitive to the edge layers. The diagonal elements of the Mueller matrix for the twist angle $\alpha = \pm\pi/2$ [Eq. (17)] provide a direct measurement of the X, Y, Z functions as:

$$X = \sqrt{\frac{1}{2}(1 - m_{22})},\ Y = \sqrt{\frac{1}{2}(1 - m_{33})},\quad Z = \sqrt{\frac{1}{2}(1 + m_{11})} \tag{28}$$

In case the twist angle was different, a similar calculation could be obtained from Eq. (16) once the matrix product $\widetilde{\mathbf{m}} = \widetilde{\mathbf{R}}(+\alpha)\cdot\widetilde{\mathbf{m}}_{\mathrm{TNLC}}$ is calculated.

Fig. 5(a) shows the functions $X(V)$, $Y(V)$ and $Z(V)$ calculated from

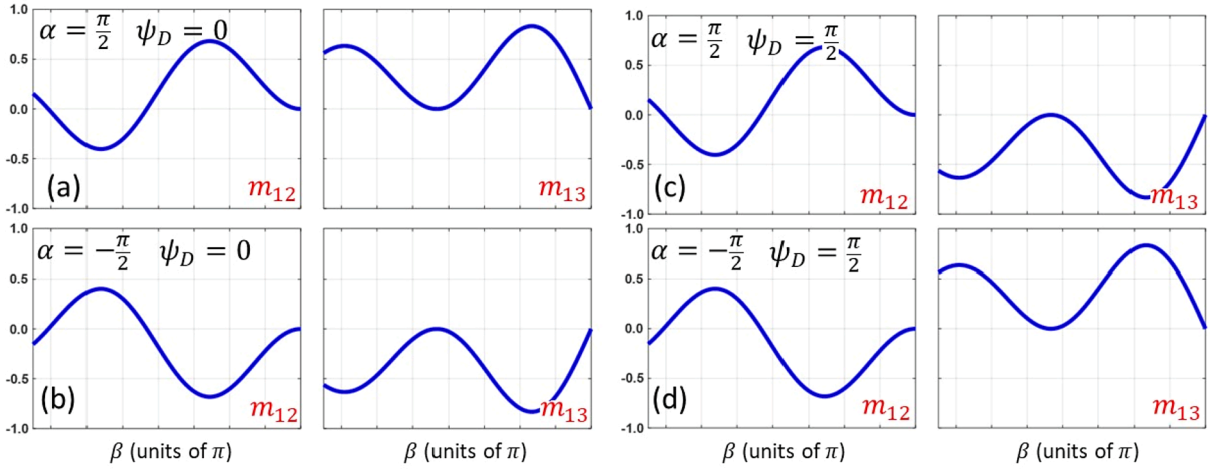

Fig. 4. Evolution of the m_{12} and m_{13} elements of the Mueller matrix with respect to β for a TN-LC cell in the Lu and Saleh model [5] for (a) $\alpha = +\pi/2$, $\psi_D = 0$, (b) $\alpha = -\pi/2$, $\psi_D = 0$, (c) $\alpha = +\pi/2$, $\psi_D = \pi/2$ and (d) $\alpha = -\pi/2$, $\psi_D = \pi/2$.

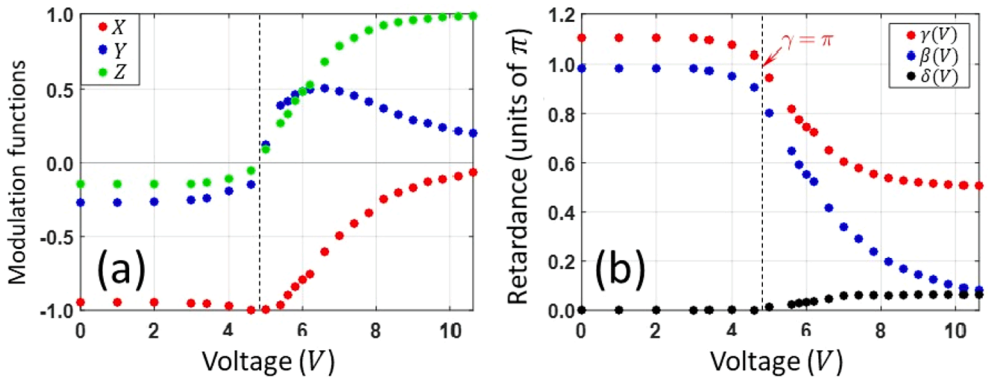

Fig. 5. (a) Experimental values of the modulation functions $X(V)$, $Y(V)$ and $Z(V)$ derived from the diagonal terms of the Mueller matrix in Fig. 3(a). (b) Experimental values of the retardance parameters $\gamma(V)$, $\beta(V)$ and $\delta(V)$ of the microscopic model by Lu & Saleh [5] corrected with the edge layers [7].

the retarder matrix that is obtained by performing the polar decomposition to the experimental Mueller matrix. For low voltages, the Lu and Saleh model is very accurate and $\delta = 0$. The experimental values of X, Y, Z for $V = 0$ allow obtaining the maximum value of the Lu and Saleh parameters through Eq. (4), giving the result $\gamma_{max} = 1.10\pi$, and $\beta_{max} = \sqrt{\gamma_{max}^2 - \alpha^2} = 0.98\pi$ (where we took $\alpha = \pi/2$).

For other voltages we first consider $Z = (\alpha \sin\gamma)/\gamma$ to obtain the evolution with the applied voltage of $\gamma(V)$ and $\beta(V) = \sqrt{(\gamma(V))^2 - \alpha^2}$. Note that the Z function is insensitive to the edge layers. Hence, the curves $X(V)$, $Y(V)$ are employed to determine the edge layer retardance parameter $\delta(V)$ from Eq. (27a), (27b). Fig. 5(b) illustrates the result, which shows the expected behavior. The adiabatic point where $\gamma(V) = \pi$ has been marked.

4. Simplified procedure

The previous polarimetric characterization reveals that the Mueller matrix is very useful to provide the full characterization of the TN-LC cell parameters. The ability to decouple the measurement of the twist angle (α), the cell orientation (ψ_D) and the maximum retardance (β_{max}) is particularly interesting since such independent measurement avoids possible ambiguities. Therefore, calibration with multiple wavelengths is not necessary. The experimental Mueller matrix in Fig. 3 also enables predicting the transmission at any other polarization configuration. However, the experimental determination of the Mueller matrix does require several measurements (in this case 6×6 measurements for each voltage).

Therefore, we propose a simplified approach, based on the assumption that the TN-LC cell is a pure retarder component (devoid of depolarization, diattenuation or polarizance), which proves to be accurate enough. This simplified approach consists in the following steps:

Step 1: First, TN-LC cell must be placed between crossed circular polarizers; in this situation the normalized transmission is given by $T_1 = T_{C\perp} = Y^2$ (Eq. (19)). This equation holds independently of any rotation of the device, thus being valid when the cell is not aligned with the reference framework ($\psi_D \neq 0$). When reaching the local adiabatic point, the cell acts as a pure polarization rotator, and the output polarization remains circularly polarized orthogonal to the circular analyzer. Hence, null transmission is obtained which can be easily observed, even with the naked eye. Then, with the cell tuned at the adiabatic point, it is illuminated with linearly polarized light, and the rotation of the polarization plane provides the twist angle α. Again, this measurement can be done with the naked eye, since a linear polarizer can be used to seek for null transmission before and behind the LC cell. The sign of α can be easily determined by detuning the LC cell from the adiabatic point and detecting the sense of the polarization rotation.

Step 2: Once the twist angle is retrieved, the orientation of the LC director at the input surface (ψ_D) can be found by searching for the orientation of the polarization eigenstates, as previously explained in Fig. 3. However, this requires measuring the Mueller matrix. An alternative approach consists in placing the cell between parallel linear polarizers and change the relative angle [10]. In this situation, if the parallel polarizers are not aligned with the LC director then $\xi_1 = \xi_2 = \psi_D$ and Eq. (18) becomes.

$$T_L(\xi_1 = \xi_2) = (X\cos\alpha + Z\sin\alpha)^2 + (Y\cos(2\psi_D - \alpha))^2 \tag{29}$$

Upon applying a constant voltage and taking measurements by rotating the LC cell the curve $T_L(\psi_D)$ is a sinusoidal function with the maxima located at $\psi_D = \alpha/2$ and $\psi_D = \alpha/2 + \pi/2$. The remaining ambiguity on which of these two values corresponds to the LC director can be resolved by setting a linear analyzer at 0° and illuminating the LC with input linearly polarized light at 45° and with right circularly polarized light. For a pure retarder element, these configurations provide a transmission given by $T = (1 + m_{12})/2$ and $T = (1 + m_{13})/2$ respectively, so the same kind of reasoning as in Fig. 4 can be applied.

Step 3: Finally, placing the cell between linear polarizers but now with angles $\xi_1 = 0$ (parallel to the input LC director orientation) and $\xi_2 = \alpha + \pi/2$ (crossed to the output LC director orientation), Eq. (19) becomes $T_2 = Z^2$. Then, by setting the linear polarizers at $\xi_1 = \pi/4$ and $\xi_2 = \alpha + \pi/4$, Eq. (19) reduces to the relation $T_3 = X^2$.

Fig. 6 shows the results of this simplified procedure. The blue curve in Fig. 6(a) corresponds to the transmission $T_1 = Y^2$ between crossed circular polarizers. It easily identifies the local adiabatic point at the expected value of 4.6 Vpp where a null transmission is obtained. This curve is invariant to the orientation of the LC cell. The twist angle $\alpha = \pi/2$ is measured simply by measuring the rotation induced on linearly polarized light at this voltage. Then, Fig. 6(b) shows the experiment where the LC cell is placed between parallel linear polarizers, so the cell orientation can be found. Here, instead of rotating the TN-LC cell, the two polarizers were simultaneously rotated from zero to 180°. The oscillatory curve expected from Eq. (29) is obtained, with the maxima located at the orientations $\xi = 45°$ and $\xi = 135°$ as expected for a cell with $\alpha = \pi/2$. Once the ambiguities have been resolved, the two remaining curves in Fig. 6(a), corresponding to the transmission $T_2 = Z^2$ and $T_3 = X^2$, can be measured. If required, these data in Fig. 6(a), can be used to retrieve the microscopic retardance parameters $\beta(V)$ and $\delta(V)$, following the procedure described in the previous section.

Finally, we test and confirm the ability of the technique to predict other polarization configurations not employed in the calibration. For this purpose, we calculate the transmission for an arbitrary configuration. Fig. 6(c) and 6(d) compare the prediction and the experimental measurement, for two different configurations. The predictions are drawn as continuous curves, while the green dots indicate the corresponding measurements. In the predictions we use two approaches: one based on the measured Mueller matrix presented in Fig. 3. The second

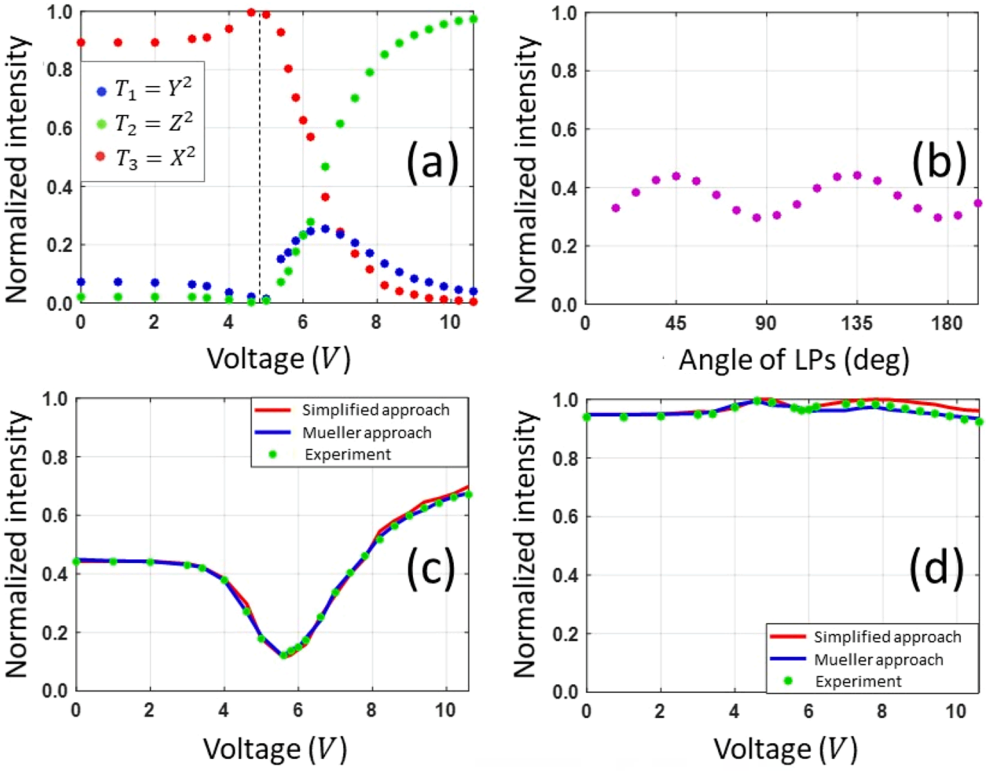

Fig. 6. (a) Normalized transmission of the TN-LC cell placed between crossed circular polarizers $T_2 = Y^2$ and between linear polarizers with transmissions $T_2 = Z^2$ and $T_3 = X^2$. (b) Normalized transmission between parallel linear polarizers as a function of the polarizers' angle. Predictions of the Mueller matrix approach and of the simplified approach and experimental measurement on the transmitted intensity of (c) the configuration with linear polarizers at ($\xi_1 = 30°, \xi_2 = 60°$) and (d) the average rotated eigenvector configuration.

one is based on the calibration of the $X(V)$, $Y(V)$, and $Z(V)$ functions within the simplified approach. First, Fig. 6(c) shows a configuration with linear polarizers oriented at $\xi_1 = 30°$ and $\xi_2 = 60°$. There is an almost perfect coincidence between the experiment and the predictions using the Mueller matrix approach and the simplified approach.

Fig. 6(d) shows the configuration of the average rotated polarization eigenstates. This configuration corresponds to the eigenstates of the **M** matrix in Eq. (3) and it was highly employed for operating TN-LC SLMs as phase-only modulators [27,28]. In this configuration, the TN-LC cell is placed between two QWPs, aligned with the fast axis parallel to the LC director on each side of the cell, and the input and output polarizers form angles $+\zeta$and $-\zeta$ with respect to these directions. In our device we used input and output QWP oriented with angles 0 and $\pi/2$ respectively, and the highest uniform transmission was obtained when setting the polarizers at $\xi_1 = +\zeta = 35°$ and $\xi_2 = \pi/2 - \zeta = 55°$. The agreement is excellent, confirming the accuracy in the characterization process. Note that the prediction of the Mueller matrix is more accurate, as expected. Nevertheless, the simplified procedure also provides very good results.

5. Conclusions

In summary, we have provided a complete polarimetric review of the TN-LC cell. We considered the Jones matrix microscopic models and extended them to the Mueller-Stokes formalism. Based in this review we outline a procedure to fully characterize the modulator and its physical parameters based on the Mueller matrix polarimetric measurement. The calculation of the retardance vector and the polarization eigenstates reveals the orientation of the LC director ψ_D. The identification of the local adiabatic point, where the device operates as a pure polarization rotator, allows finding the twist angle α. Therefore, a characterization of the physical parameters α, ψ_D is achieved with a single wavelength and without requiring a simultaneous fit of a set of different curves unlike other approaches [9,10]. Furthermore, the proposed Mueller matrix technique easily resolves the ambiguity in the sign of α and in the identification of the fast axis.

Once the TN-LC is aligned with the LC director parallel to the reference framework, the diagonal elements of the Mueller matrix provide the evolution of the $X(V)$, $Y(V)$ and $Z(V)$ functions. These functions can be directly related to the microscopic retardance parameters, the $\beta(V)$ retardance function in the Lu and Saleh standard model [5] and the correction $\delta(V)$ edge layer retardance parameter [7]. Again, these two parameters are measured decoupled, since $\beta(V)$ is determined from the $Z(V)$ function, while $\delta(V)$ is determined from the $X(V), Y(V)$ functions. The whole process can be applied with a single wavelength.

Although complete Mueller matrix polarimetry requires many measurements (here we did 6×6 measurements), valuable information can be obtained from simplified experiments. In addition, the use of polarimetric cameras helps reducing the number of measurements, as in the imaging Mueller matrix polarimeter we recently developed [38] where 12 measurements suffice. Finally, a simplified version of the technique is proposed assuming that the cell is a pure retarder component. This simplified technique can help to rapidly calibrate and configure TN-LC modulators for a desired optical modulation response.

CRediT authorship contribution statement

Esther Nabadda: Investigation, Visualization, Writing – original draft. **Guadalupe López-Morales:** Investigation, Visualization, Methodology, Validation. **David Marco:** Methodology, Validation. **María del Mar Sánchez-López:** Methodology, Validation, Supervision, Writing – review & editing. **Ignacio Moreno:** Conceptualization, Validation, Supervision, Writing – review & editing.

Declaration of Competing Interest

The authors declare that they have no known competing financial interests or personal relationships that could have appeared to influence the work reported in this paper.

Data availability

No data was used for the research described in the article.

Acknowledgements

We acknowledge funding from Ministerio de Ciencia, Innovación y Universidades from Spain (RTI2018-097107-B-C33). Esther Nabadda acknowledges a grant from Generalitat Valenciana, Santiago Grisolia Program (ref. GRISOLIAP/2020/004).

References

[1] N. Konforti, E. Marom, S.-T. Wu, Phase-only modulation with twisted nematic liquid-crystal spatial light modulators, Opt. Lett. 13 (3) (1988) 251–253.
[2] R.K. Komanduri, K.F. Lawler, M.J. Escuti, Multi-twist retarders: broadband retardation control using self-aligning reactive liquid crystal layers, Opt. Express 21 (1) (2013) 404–420.
[3] A. Yariv, P. Yeh, "Light propagation in twisted anisotropic media", Section 5.4 in Optical Waves in Crystals, John Wiley & Sons, New York, 1984.
[4] R.C. Jones, A new calculus for the treatment of optical systems: VII. Properties of the N-matrices, J. Opt. Soc. Am. 38 (8) (1948) 671–685.
[5] K. Lu, B.E.A. Saleh, Theory and design of the liquid crystal TV as an optical spatial phase modulator, Opt. Eng. 29 (3) (1990) 240–246.
[6] J.A. Coy, M. Zaldarriaga, D.F. Grosz, O.E. Martinez, Characterization of a liquid crystal television as a programmable spatial light modulator, Opt. Eng. 35 (1) (1996) 15–19.
[7] A. Marquez, J. Campos, M.J. Yzuel, I. Moreno, J.A. Davis, C. Iemmi, A. Moreno, A. Robert, Characterization of edge effects in twisted nematic liquid crystal displays, Opt. Eng. 39 (12) (2000) 3301–3307.
[8] M. Yamauchi, Jones-matrix models for twisted-nematic liquid-crystal devices, Appl. Opt. 44 (21) (2005) 4484–4493.
[9] R. Giust, J.-P. Goedgebuer, Determination of the twist angle and the retardation properties of twisted nematic liquid crystal television by spectral measurements, Opt. Eng. 37 (2) (1998) 629–634.
[10] J.A. Davis, D.B. Allison, K.G. D'Nelly, M.L. Wilson, I. Moreno, Ambiguities in measuring the physical parameters for twisted-nematic liquid-crystal spatial light modulators, Opt. Eng. 38 (4) (1999) 705–709.
[11] H. Kim, Y.H. Lee, Unique measurement of the parameters of a twisted-nematic liquid-crystal display, Appl. Opt. 44 (9) (2005) 1642–1649.
[12] V. Durán, J. Lancis, E. Tajahuerce, Z. Jaroszewicz, Cell parameter determination of a twisted-nematic liquid crystal display by single-wavelength polarimetry, J. Appl. Phys. 97 (4) (2005) 043101.
[13] I. Moreno, A.M. Cutillas, M.M. Sánchez-López, P. Velásquez, F. Mateos, Full prediction of the broadband optical modulation performance of a twisted nematic liquid crystal cell, Opt. Commun. 281 (22) (2008) 5520–5526.
[14] J.A. Davis, P. Tsai, K.G. D'Nelly, I. Moreno, Simple technique for determining the extraordinary axis direction for twisted nematic liquid crystal spatial light modulator, Opt. Eng. 38 (5) (1999) 929–932.
[15] I. Moreno, P. Velásquez, C.R. Fernández-Pousa, M.M. Sánchez-López, F. Mateos, Jones matrix method for predicting and optimizing the optical modulation properties of a liquid-crystal display, J. Appl. Phys. 94 (6) (2003) 3697–3702.
[16] A.J. Macfaden, T.D. Wilkinson, Characterization, design, and optimization of a two-pass twisted nematic liquid crystal spatial light modulator system for arbitrary complex modulation, J. Opt. Soc. Am. A 34 (2) (2017) 161–170.
[17] V. Durán, J. Lancis, E. Tajahuerce, Equivalent retarder-rotator approach to on-state twisted nematic liquid crystal displays, J. Appl. Phys. 99 (2006), 113101.
[18] D. Goldstein, Polarized Light, 3rd edition, CRC Press, 2010.
[19] J.E. Wolfe, R.A. Chipman, Polarimetric characterization of liquid-crystal-on-silicon panels, Appl. Opt. 45 (8) (2006) 1688–1703.
[20] A. Márquez, I. Moreno, C. Iemmi, A. Lizana, J. Campos, M.J. Yzuel, Mueller-Stokes characterization and optimization of a liquid crystal on silicon display showing depolarization, Opt. Express 16 (3) (2008) 1669–1685.
[21] R.S. Verma, M.K. Swami, S.S. Manhas, P.K. Gupta, Mueller matrix-based optimization of reflective type twisted nematic liquid crystal SLM at oblique incidences, Opt. Commun. 283 (12) (2010) 2580–2587.
[22] K. Dev, A. Asundi, Mueller–Stokes polarimetric characterization of transmissive liquid crystal spatial light modulator, Opt. Lasers Eng. 50 (4) (2012) 599–607.
[23] Z. Zhang, Z. You, D. Chu, Fundamentals of phase-only liquid crystal on silicon (LCOS) devices, Light: Sci. Appl. 3 (10) (2014) e213.
[24] F.J. Martínez, A. Márquez, S. Gallego, J. Francés, I. Pascual, A. Beléndez, Retardance and flicker modeling and characterization of electro-optic linear retarders by averaged Stokes polarimetry, Opt. Lett. 39 (4) (2014) 1011–1014.
[25] I. Moreno, A. Lizana, J. Campos, A. Marquez, C. Iemmi, M.J. Yzuel, Combined Mueller and Jones matrix method for evaluation of the complex modulation in liquid-crystal-on-silicon display, Opt. Lett. 33 (6) (2008) 627–629.
[26] J.L. Pezzaniti, R.A. Chipman, Phase-only modulation of a twisted nematic liquid-crystal TV by use of the eigenpolarization states, Opt. Lett. 18 (18) (1993) 1567–1569.
[27] J.A. Davis, I. Moreno, P. Tsai, Polarization eigenstates for twisted-nematic liquid crystal displays, Appl. Opt. 37 (5) (1998) 937–945.
[28] I. Moreno, J.A. Davis, K.G. D'Nelly, D.B. Allison, Transmission and phase measurements for polarization eigenvectors in twisted-nematic liquid-crystal spatial light modulators, Opt. Eng. 37 (11) (1998) 3048–3052.
[29] J. Nicolás, J. Campos, M.J. Yzuel, Phase and amplitude modulation of elliptic polarization states by non-absorbing anisotropic elements: application to liquid-crystal devices, J. Opt. Soc. Am. A 19 (5) (2002) 1013–1020.
[30] B.E.A. Saleh, M.C. Teich, Fundamentals of Photonics, 2nd Edition,, John Wiley and Sons Inc., 2007.
[31] C.R. Fernández-Pousa, I. Moreno, N. Bennis, C. Gómez-Reino, Generalized formulation and symmetry properties of anisotropic devices. Application to liquid crystal displays, J. Opt. Soc. Am A 17 (11) (2000) 2074–2080.
[32] Z. Zhuang, Y.J. Kim, J.S. Patel, Achromatic linear polarization rotator using twisted nematic liquid crystals, Appl. Phys. Lett. 76 (26) (2000) 3995–3997.
[33] I. Moreno, N. Bennis, J.A. Davis, C. Ferreira, Twist angle determination in liquid crystal displays by location of local adiabatic points, Opt. Commun. 158 (1–6) (1998) 231–238.
[34] R.A. Chipman, Mueller matrices, Ch. 14 in *Handbook of Optics*, Vol. 1, third ed., in: M. Bass, V.N. Mahajan (Eds.) McGraw-Hill, New York (2010).
[35] S.Y. Lu, R.A. Chipman, Interpretation of Mueller matrices based on polar decomposition, J. Opt. Soc. Am. A 13 (5) (1996) 1106–1113.
[36] S. Manhas, M.K. Swanmi, P. Buddhiwant, N. Ghosh, P.K. Gupka, K. Singh, Mueller matrix approach for determination of optical rotation in chiral turbid media in backscattering geometry, Opt. Express 14 (1) (2006) 190–202.
[37] O. Arteaga, A. Canillas, Pseudopolar decomposition of the Jones and Mueller-Jones exponential polarization matrices, J. Opt. Soc. Am A 26 (4) (2009) 783–793.
[38] G. López-Morales, M.M. Sánchez-López, A. Lizana, I. Moreno, J. Campos, Mueller matrix polarimetric imaging analysis of optical components for the generation of cylindrical vector beams, Crystals 10 (12) (2020) 1155.

Optics and Lasers in Engineering 159 (2022) 107204

Contents lists available at ScienceDirect

Optics and Lasers in Engineering

journal homepage: www.elsevier.com/locate/optlaseng

Ferroelectric liquid-crystal modulator with large switching rotation angle for polarization-independent binary phase modulation

Esther Nabadda[a], Noureddine Bennis[b], Michał Czerwinski[b], Aleksandra Walewska[b], Leszek R. Jaroszewicz[b], María del Mar Sánchez-López[a,c,*], Ignacio Moreno[a,d]

[a] Instituto de Bioingeniería. Universidad Miguel Hernández de Elche, Elche E-03202, Spain
[b] Faculty of New Technologies and Chemistry. Military University of Technology, Warsaw 00-908, Poland
[c] Departamento de Física Aplicada. Universidad Miguel Hernández de Elche, Elche E-03202, Spain
[d] Departamento de Ciencia de Materiales, Óptica y Tecnología Electrónica, Universidad Miguel Hernández de Elche, Elche E-03202, Spain

ARTICLE INFO

Keywords:
Ferroelectric liquid-crystal
Polarization
Phase modulation

ABSTRACT

In this work a ferroelectric liquid crystal (FLC) modulator with a non-standard large switching rotation angle, close to 90°, is fabricated and characterized. The modulator acts as a switchable wave-plate with an in-plane rotation of the principal axis under the action of a bipolar voltage. In the ideal situation of half-wave retardance, the device is shown to behave as a binary π phase modulator independently of the input state of polarization. We provide physico-chemical properties of the liquid crystalline mixture used to fabricate the FLC modulator with such large switching angle. The characterization method of the device optical properties is presented, which allows the localization of the two LC stable states, the unambiguous determination of the rotation angle, and the evaluation of the spectral retardance function. We demonstrate the polarization-independent π phase shift using an adapted Young's type interferometer for real-time measurements, where we further analyze the operational frequency limits of the device. This FLC operational mode can be exploited to produce binary-phase polarization-independent diffractive optical elements.

1. Introduction

Ferroelectric liquid crystals (FLC), also known as chiral smectic or smectic *C phase (Sm*C), have a long history and they have been used to fabricate many different types of optical modulators [1]. In comparison with the more common nematic LC modulators, they present bistable faster response and low consumption. In their typical configuration as surface stabilized ferroelectric liquid-crystals (SSFLC) they operate as a switchable linear retarder (waveplate) with two stable in-plane orientations of the LC director. These properties make them very interesting elements for fast optical switches [2–4]. They have been employed as achromatic phase shifters [5], optical depolarizers [6] and for designing polarimetric instruments [7,8]. Recent advances include using them to fabricate fast refocusing lenses [9] or LiDAR systems [10]. A recent review of the state of the art of FLC modulators can be found in [11].

A major application of FLCs is on the production of liquid-crystal displays (LCD), where their fast response is especially useful to reduce motion blur and to achieve field sequential color (FSC) displays. Ferroelectric LCDs (FLCDs) are typically designed with a retardance of $\phi = 180^{\circ}$, i.e., as a half-wave plate (HWP), and with in-plane switching rotation angle of $\theta = 45^{\circ}$. In this situation, if the FLC modulator is illuminated with linearly polarized light, it provides output light with two orthogonal linear states of polarization (SOP). These can be converted into a maximum contrast binary light intensity modulation by setting an analyser at the output, crossed to one of the two emerging states [12,13].

In this work, instead of regarding the display application, we are more interested in FLCDs as phase-only spatial light modulators (SLM) for diffractive and/or adaptive optics. FLC-SLMs have been used for a long time to display binary phase diffraction gratings [14] and binary-phase computer generated holograms [15]. Although not as popular as nematic LC-SLMs, FLC SLMs are also commercially available [16] and they have been applied in systems where a fast modulation response is required, as for instance laser speckle reduction [17], microscopy with structured illumination [18,19] or optogenetic stimulation [20]. These FLC-SLM commercial devices, though, are fabricated with $\theta \approx 45^{\circ}$ (or less) switching rotation angle of the FLC director. Although a binary π phase modulation operational scheme can be obtained with these modulators by properly orienting an output analyzer to filter the modulated beam [21], this is at the expense of losing light efficiency.

Here we analyze the properties of a FLC modulator with $\theta \approx 90^{\circ}$ switching angle. We illustrate how this device provides, when the LC layer is a half-wave retarder, a binary π phase modulation for any input

* Corresponding author at: Instituto de Bioingeniería, Universidad Miguel Hernández de Elche, Elche E-03202, Spain.
E-mail address: mar.sanchez@umh.es (M.d.M. Sánchez-López).

https://doi.org/10.1016/j.optlaseng.2022.107204
Received 20 March 2022; Received in revised form 24 June 2022; Accepted 26 July 2022

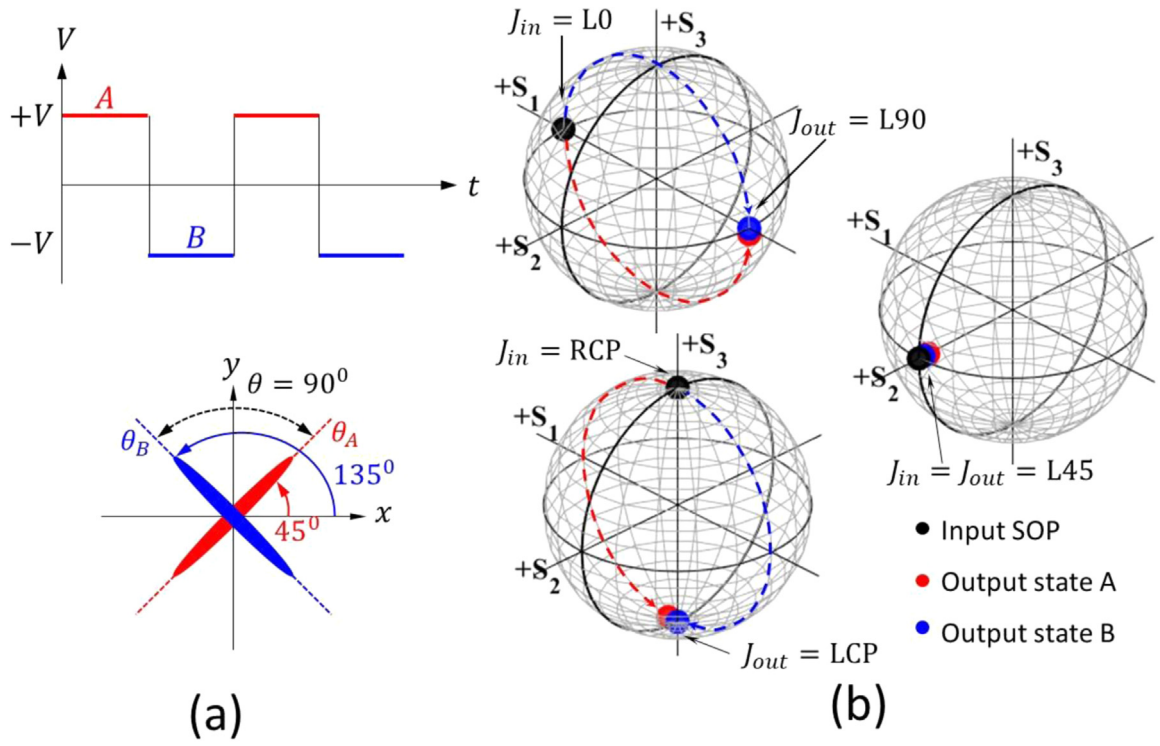

Fig. 1. Ideal FLC modulator for binary π phase modulation with maximum efficiency: (a) Switching of the FLC director between stable states A and B. (b) Evolution on the PS showing the output polarization for various input SOP.

SOP and with maximum light conversion efficiency. Since the binary π phase modulation regime occurs for any SOP, it could be operated even with unpolarized light. Consequently, light efficiency can be further improved since there is no need to use polarizers. Although this configuration was proposed many years ago [22–25], and LC materials with high tilt angle (like the CS2005 or the CDRR8 mixture) were investigated [26], the SLM industry has not considered it. With this work we would like to stimulate the recovery of this old idea. In addition, the in-plane rotation of the FLC modulators can be regarded to imprint a geometric phase to the input beam, also known as the Pancharatnam-Berry phase, thus being useful to design a new generation of geometric-phase-based diffractive optical elements [27]. Therefore, FLC modulators can be viewed as binary geometric phase elements as well.

After this introduction, the paper is organized as follows: in the next section we present the theory of the ideal FLC device and provide the physical insight of the SOP transformations described within the Poincaré sphere formalism. In Section 3, the physico-chemical properties of the LC mixture used to fabricate the FLC cell modulator are described. In Section 4 we provide a procedure for the complete optical characterization of the device light modulation properties. The time response is presented in Section 5. Section 6 further illustrates the binary π phase modulation for any input SOP by means of an adapted experimental Young's type interferometer arrangement [28]. Finally, the conclusions of the work are given in the last section.

2. Operation of a FLC modulator with 90° rotation and 180° retardance

In this section we analyze the operation of the FLC modulator considering the ideal situation where the retardance is $\phi = 180°$ i.e., it is a half wave plate (HWP), with the LC director switching between two stable positions A and B (θ_A and θ_B), where the switching rotation angle is $\theta = \theta_B - \theta_A = 90°$. Note that the rotation angle is $\theta = 2\vartheta_T$, twice the so-called tilt angle ϑ_T.

Considering the Jones matrix formalism for polarized light, and assuming that the FLC layer acts as a HWP, the FLC modulator at position A is described by

$$\mathbf{M}_A = \begin{bmatrix} \cos 2\theta_A & \sin 2\theta_A \\ \sin 2\theta_A & -\cos 2\theta_A \end{bmatrix}, \tag{1}$$

while for FLC position B the Jones matrix is

$$\mathbf{M}_B = \begin{bmatrix} \cos 2\theta_B & \sin 2\theta_B \\ \sin 2\theta_B & -\cos 2\theta_B \end{bmatrix} = -\begin{bmatrix} \cos 2\theta_A & \sin 2\theta_A \\ \sin 2\theta_A & -\cos 2\theta_A \end{bmatrix} = -\mathbf{M}_A, \tag{2}$$

where the relation $\theta_B = \theta_A + 90°$ was used. Therefore, since $\mathbf{M}_B = -\mathbf{M}_A$, for any input polarization, the two output SOPs are identical except for a minus sign which implies a π phase shift between them.

Fig. 1 illustrates this situation. In Fig. 1(a) two FLC director orientations $\theta_A = 45°$ and $\theta_B = 135°$ are drawn, thus leading to $\theta = 90°$, corresponding to the two values of a bipolar addressed electrical signal. The two output SOPs suffer a transformation with respect to the input SOP (except for the eigenstates, i.e., the linear polarised states parallel or crossed to the FLC director). However, since the FLC modulator is a HWP, the two emerging SOPs are the same for the two positions A and B. These transformations can be visualized on the Poincaré sphere (PS) [29]. The PS is a geometrical representation of all SOPs, where the latitude coordinate is directly related to the light ellipticity and the longitude coordinate is directly related to the polarization azimuth. The two circularly SOPs are the poles of the PS, while the linear SOPs lie in the equator. The interest of the PS in describing retarder elements (as the FLC modulator) is that the action of the device on any input SOP is a rotation of the PS around the axis defined by the two eigenstates, with an angle equal to the retardance. In this case of a HWP FLC modulator, the PS rotates an angle equal to $\phi = 180°$. Fig. 1(b) illustrates these transformations. Given the orientations of the FLC director in Fig. 1(a), both A and B positions share the same eigenstates; namely, the linear states oriented at 45° and 135°. Therefore, the PS rotation is in both cases around the S_2 axis. However, the rotation of the FLC director interchanges the fast and slow axes of the retarder and, consequently, the PS rotates in

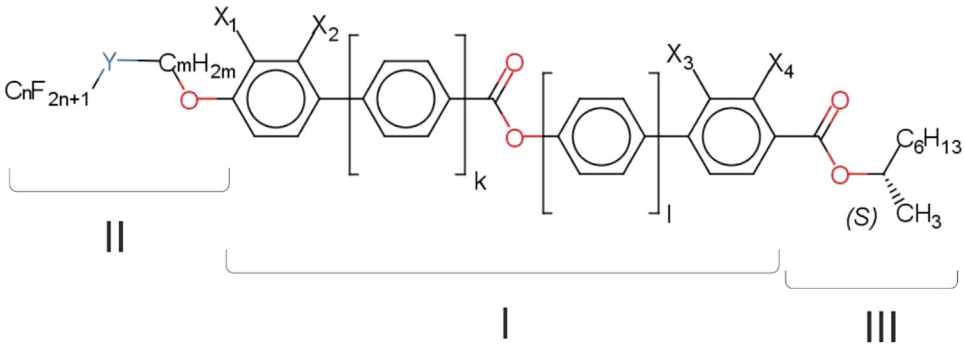

Fig. 2. Chemical structure of the components of the W-212 mixture used in this work.

the opposite direction. This is shown in Fig. 1(b) for various input SOPs (black dots): a linear horizontal SOP (located on the $+S_1$ axis), a linear SOP oriented at 45° (located on the $+S_2$ axis) and a right circular SOP (RCP) (located on the $+S_3$ axis, at the north pole). Although the final SOP is the same for both A and B positions, the trajectory on the PS has opposite direction, which provides an opposite geometric phase between the two emerging SOPs. Even in the case of an input linear SOP oriented at 45°, which does not suffer any polarization transformation, there is a π phase difference originated from the switch between the fast and slow axes of the FLC retarder.

3. Structure and properties of the FLC mixture and fabrication of the cell

The FLC cell was produced at the Military University of Technology (Warsaw). Here the details on the preparation of the LC mixture and on the device fabrication are provided.

3.1. Preparation of a multicomponent FLC mixture

The LC mixture used in this work was proposed and developed at the Institute of Chemistry (Military University of Technology). This mixture is intended to achieve all the properties required in FLC applications, such as broad temperature range of the ferroelectric phase, relatively low melting point and optimized ferroelectric electro-optical response. The mixture was prepared according to a procedure based on mixing selected chiral compounds with ferroelectric and antiferroelectric properties, with the scope of finding a composition which presents a frustrated ferroelectric phase as in [30]. The components of the obtained W-212 mixture are made up of a rigid ring structure formed by biphenyl benzoate or phenyl biphenylate structure (I), nonchiral partially fluorinated alkoxy terminal chain in one side of molecules (II) and chiral 1-methylheptyloxy chain (III), which is connected to the rigid core using carboxylate bridge in the other side (Fig. 2). This structure is like those shown in [31], where homologue mixtures to W-212 with very short helical pitch were reported. To ensure uniform alignment in the electro-optical cell with thickness higher than 2mm, a small amount of racemic chiral dopant was added to increase the helical pitch in the final W-212 mixture. This mixture has been synthesized according to the procedure found in the original publication [32].

3.2. Physico-chemical properties of the W-212 mixture

We show next results of the phase transition temperatures, the director tilt angle and spontaneous polarization measurements for the W-212 mixture. Increasing the temperature, a variety of thermodynamically stable intermediary states between crystal (Cr) and isotropic (Iso) state are observed. These intermediate mesophases are stable thermotropic liquid crystalline states termed enantiotropic [33]. Using differential scanning calorimetry (DSC) and polarizing microscopy techniques, the following phase transitions were observed upon heating at 2 °C/min:

$$\mathrm{Cr} \underset{10°\mathrm{C}}{\rightarrow} \mathrm{SmC}^* \underset{99.8-101.5°\mathrm{C}}{\rightarrow} \mathrm{SmA}^* \underset{117.5-126.0°\mathrm{C}}{\rightarrow} \mathrm{ISO}$$

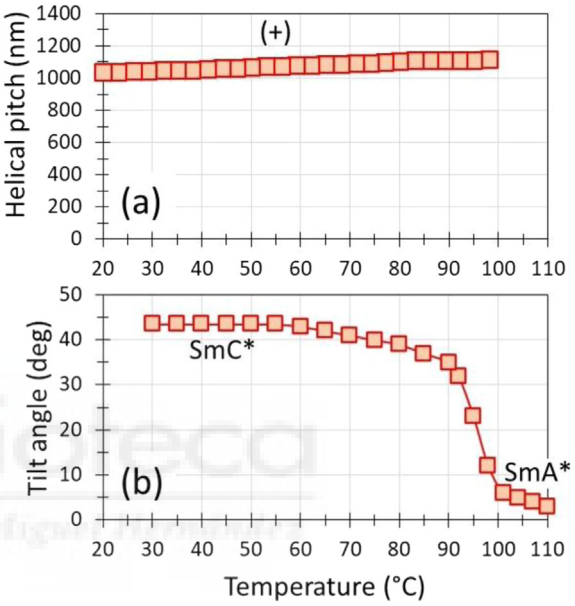

Fig. 3. (a) Temperature dependence of the helical pitch for the W-212 mixture. The sense of the helical twist is indicated by "+" for the right-handed helix. (b) Tilt angle as a function of temperature.

Bulk states in W-212 exhibit helical structures induced by the twisting power due to chirality. The helical pitch P was determined in the temperature range that covers the tilted chiral smectic phase SmC* by measuring the transmittance spectra with a spectrophotometer of 360–3000 nm spectral range. P is calculated with the relation $P = \lambda_C/n$, where λ_C is the central wavelength of the reflection band and n is the average refractive index. The W-212 mixture was placed on a glass plate coated with a surfactant, thus promoting the homeotropic orientation of the molecular director while the other surface of the specimen was left free. More experimental details of the helical pitch and helical twist sense measurements were reported in previous works [34–36]. Here we present the temperature dependence of the pitch for the W-212 mixture, which slowly increases with temperature in the SmC* phase, reaching a maximum value about 1150 nm at 100 °C (Fig. 3(a)), just below the transition temperature from SmC* to SmA*.

To measure the tilt angle ϑ_T (half the switching rotation angle of the LC director), the LC was introduced in cells aligning the molecular director parallel to the substrate surface. In this case, the cell consists of two ITO-coated glass that are patterned to give a 7×7 mm^2 electrode area. The glass surface was processed with a Nylon 6 as aligning material and unidirectionally rubbed prior to cell assembly, in order to produce

a homogenous alignment. Then, the two-substrate glasses were joined together with an epoxy glue containing 2.5 mm spacers. The FLC material was placed at one of the cell's edges. The cell was then heated until the material was in the isotropic phase, to allow the material flow inside the cell by capillary forces. Furthermore, the cell was cooled down at controlled rate (0.1 ˚C/min) while applying an AC electric field to form the aligned ferroelectric liquid crystal at room temperature.

The helical structure is suppressed by the surface effect resulting in a molecular tilting plane parallel to the surface, thus obtaining the surface-stabilized ferroelectric liquid crystal (SSFLC) configuration. The cell was placed in a temperature and environmental control stage (Linkam THMS 600) compatible with a polarization optical microscope (Biolar PI-PZO). When the cell is under DC electric field the material aligns in a single direction. The tilt angle $\vartheta_T = \theta/2$ is typically measured by placing the FLC cell between the crossed polarizers of the microscope and orienting it such that extinction is obtained. In this orientation the optical axis of the material is parallel to one of the polarizers. By reversing the polarity of the applied DC field, the FLC molecules reorient, and the cell appears brighter. The FLC cell is rotated on the microscope stage to bring the dark state of the cell back again. This rotation is thus the switching angle θ and $\vartheta_T = \theta/2$ is the tilt angle. However, in the case of a perfect value $\theta = 90^{\circ}$ the dark state would remain after reversing the field. Nevertheless, we could apply the procedure following the temperature variations and Fig. 3(b) shows the results for the measured tilt angle. They show that the tilt angle rises rapidly into the SmC* phase on cooling from the SmA* phase before saturating at 43˚ in the broad temperature range (below 55 ˚C) of the ferroelectric phase. Following a similar procedure, the retardance was measured, and the birefringence of the material could be estimated to be $\Delta n = 0.11 \pm 0.01$, with no significant variation in the SmC* phase temperature range between 30 ˚C and 80 ˚C.

The magnitude of the tilt angle of the LC molecules in the ferroelectric phase has an influence on the value of the spontaneous polarization. Usually, the higher the tilt angle the higher the spontaneous polarization and the material could reorient faster in an optical modulator. Accordingly, it is important to determine the magnitude de the spontaneous polarization. This can be measured using a triangular waveform voltage, in this case with a frequency of 50 Hz. The current through the circuit was monitored and the polarization was determined by measuring the charge produced upon polarization reversal (Fig. 4(a)). This was measured for different temperatures and the dependence shown in Fig. 4(b) exhibits a behavior similar to the tilt angle, increasing its value as the temperature is reduced, reaching about 115nC/cm^2 at 25 ˚C.

Finally, the bistable nature of the FLC cell is analyzed. The cell is now addressed with a low frequency triangular voltage signal of 20 Vpp and 0.1 Hz. Fig. 4(c) shows the optical transmittance between crossed polarizers as a function of the applied voltage, both for the rise (black curve) and for the fall (brown curve) of the applied signal. As described previously, the material employed in this work is a frustrated ferroelectric phase [31] and the transmittance exhibits a ferroelectric loop with anomalous hysteresis showing a W-shape, as demonstrated in Fig. 4(c).

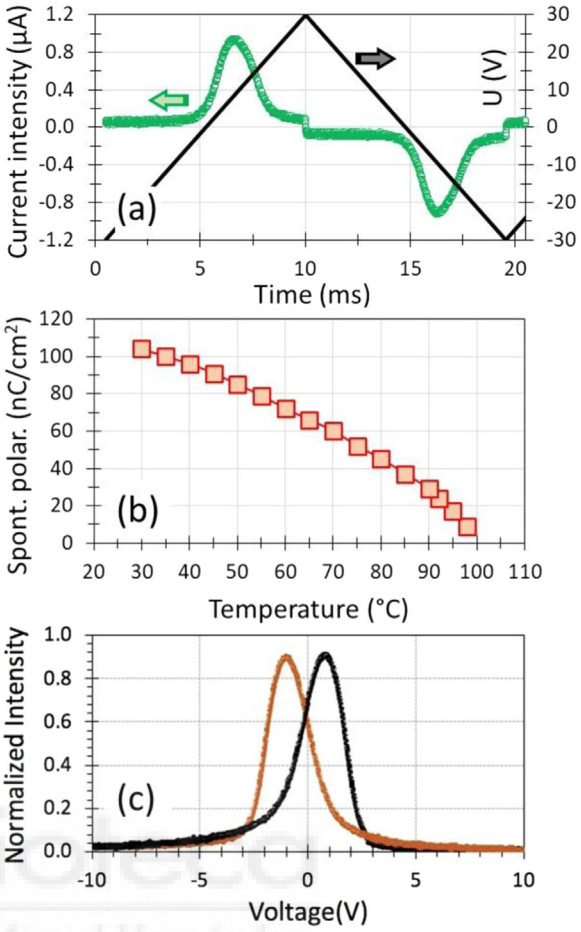

Fig. 4. (a) Polarization switching current response for the W-212 mixture by applying a triangular waveform voltage of 50 Hz. (b) Temperature dependence of the spontaneous polarization for the W-212 mixture. (c) Measured hysteresis loop (black and brown curves correspond respectively to the rise and fall of the low frequency triangular voltage signal).

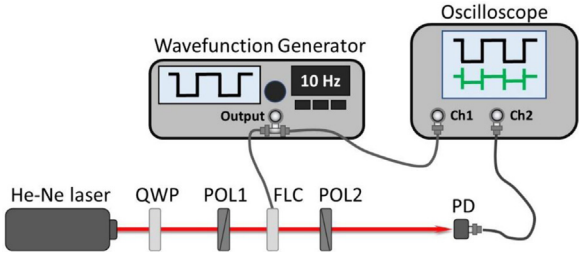

Fig. 5. Scheme of the optical setup. QWP: quarter-wave plate; POL: linear polarizer; PD: photodetector.

4. Characterizing the optical parameters of the FLC modulator

These previous experiments require the use of equipment specially designed for the characterization of LC materials. However, it is a quite common situation, especially when employing LC commercial devices, that the user does not have access to the fabrication details. In these situations, it is necessary to develop reverse engineering techniques aiming at determining the physical parameters that influence the optical modulation properties. In this section we present the set of reverse engineering procedures that we have performed to experimentally verify the physical parameters of the FLC modulator described in the last section. Namely, the orientation of the LC director, the LC layer retardance (ϕ) and the switching angle (θ). These experiments require relatively simple equipment and can be done even without knowledge whatsoever of the fabrication parameters.

4.1. Locating the FLC director and the switching angle

We first searched for the orientation of the FLC director following a similar procedure as in [13,21]. Fig. 5 shows a scheme of the optical setup. The system is illuminated with a He-Ne laser beam of wavelength 632.8 nm. Since the laser is linearly polarized, a quarter-wave plate (QWP) was added to produce circularly polarized light. Then, the polarizer – FLC modulator – analyser system was placed behind. Both polarizers were mounted on rotating mounts. Having generated circularly polarized light ensures that the input polarizer can be rotated to

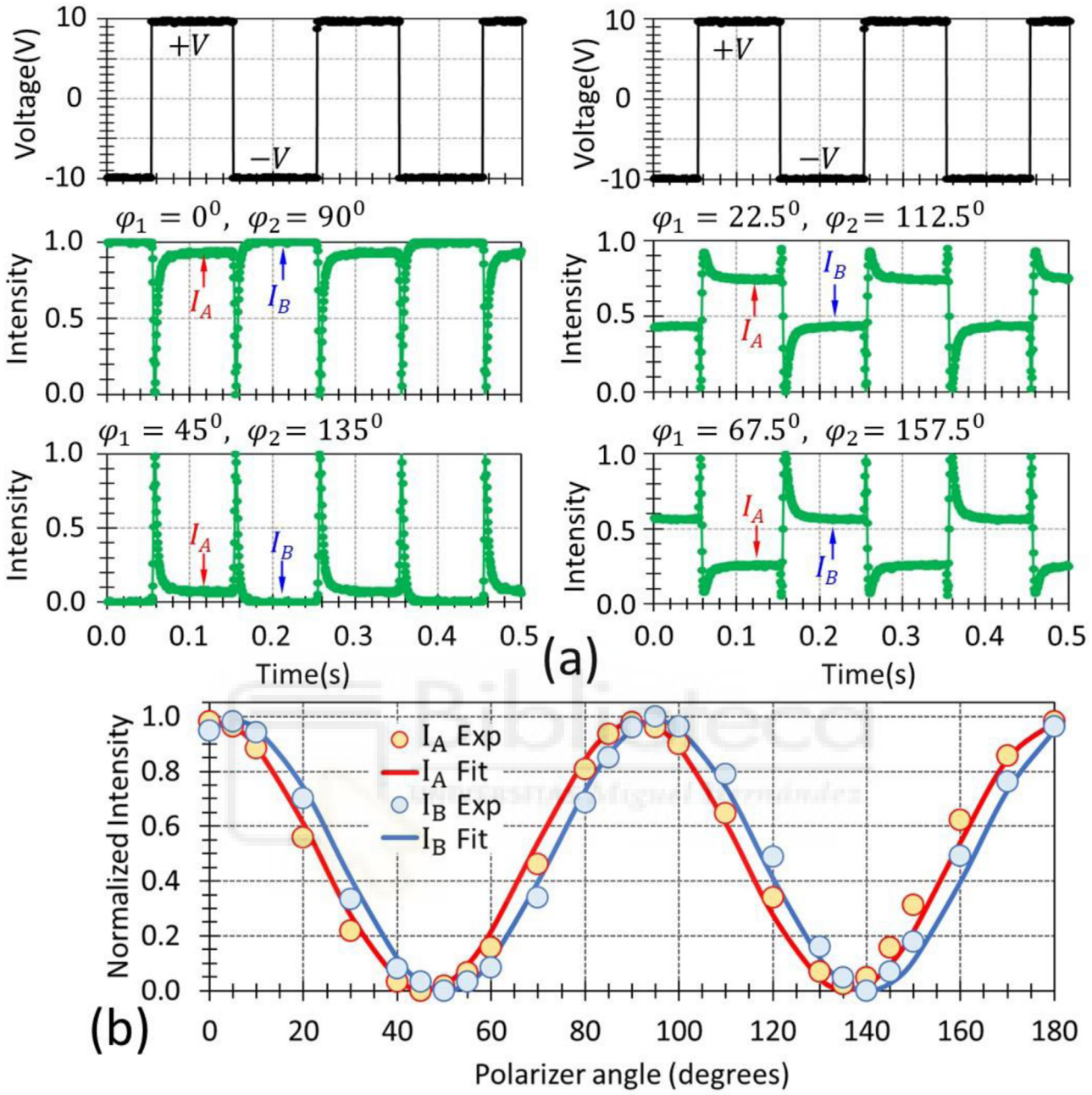

Fig. 6. FLC modulator between crossed polarizers (a) Captured normalized intensity signal for input polarizer angle at $\varphi_1 = 0$, 22.5°, 45° and 67.5°. (b) Normalized intensity transmission for the two FLC stable states (A and B) as a function of the input polarizer angle.

arbitrary angles, while maintaining the input intensity on the FLC modulator. A photodetector (Newport 818-SL) captures the transmitted intensity and displays it on an oscilloscope with temporal resolution. The FLC modulator was addressed with a bipolar voltage of 10 Hz, 20Vpp and null DC value from a wavefunction generator. The oscilloscope displays simultaneously the addressed signal and the signal detected on the photodetector (PD).

For crossed polarizers the normalized transmitted signal (i.e., the ratio between the intensity after POL2 and the intensity incident on the FLC modulator) takes the form [21]:

$$T_{cross} = \sin^2(2\alpha)\sin^2\left(\frac{\phi}{2}\right), \tag{3a}$$

where $\alpha = \varphi_1 - \theta_{A/B}$ denotes the difference between the input polarizer angle (φ_1) and the FLC principal axis, which takes the angles $\theta_{A/B}$ for the two stable positions of the FLC director. For normalization purposes, the same experiment was performed with parallel polarizers, where the normalized transmission is given by

$$T_{par} = 1 - \sin^2(2\alpha)\sin^2\left(\frac{\phi}{2}\right). \tag{3b}$$

According to Eqs. 3(a), when the input polarizer is either parallel ($\alpha = 0°$) or perpendicular ($\alpha = 90°$) to the LC director, the transmission is null for crossed polarizers. Maximum transmittance for crossed polarizers occurs when the relative orientation between the input polarizer and the LC director is set at $\alpha = 45°$. In this latter situation, the transmittance for crossed polarizers is equal to $\sin^2(\phi/2)$ and reaches 100% transmission when the retardance is $\phi = 180°$. Therefore, by fitting the experimental transmittance for crossed polarizers we will retrieve the retardance of the FLC cell.

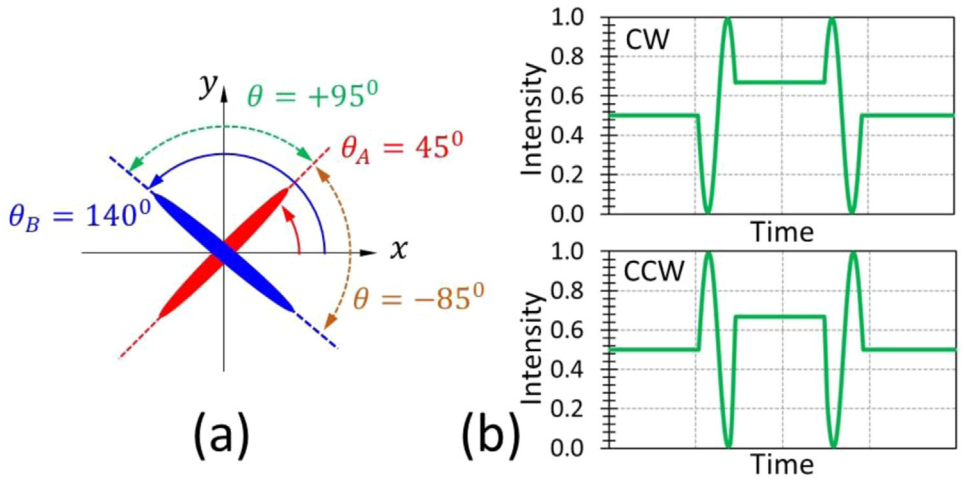

Fig. 7. (a) Rotation of the FLC director in the real situation. (b) Numerical simulation of the normalized transmission for clockwise and counter-clockwise (CCW) rotation of the FLC director with the cell placed between two crossed linear polarizers and input polarizer at 22.5°.

Fig. 6(a) presents the experimental normalized transmitted signal of the FLC cell placed between crossed polarizers, as a function of time. The black curves indicate the bipolar voltage signal addressed to the cell while the green dots refer to the signal measured by the photodetector and captured in the oscilloscope. This signal shows two stable intensity values (I_A and I_B) that correspond to the two applied voltage levels, with short transition peaks in between. These peaks correspond to the transient response where the LC director reorients, and they were studied in detail in the past [37,38] where they were shown to be related to soliton type switching which occurs under fixed boundary conditions. These transient states can be used to provide continuous amplitude or phase modulation with FLC modulators [39]. Here, however, we concentrate on the standard operation as binary modulators.

In the ideal situation described in Section 2 (90° switching angle and 180° retardance), the two stable intensity values should be identical. However, their slight difference indicates that the modulator parameters are close to the ideal conditions, although they are not perfect. Fig. 6(a) shows four captures where the input polarizer was oriented in the laboratory framework at angles $\varphi_1 = 0°$, 22.5°, 45° and 67.5° while the analyzer was kept crossed at angles $\varphi_2 = 90°$, 112.5°, 135° and 157.5° respectively.

Similar measurements were taken for different orientations of the input polarizer (φ_1), while rotating the analyzer to always keep them crossed. At each angle φ_1, we recorded the two stable intensity values (I_A and I_B) occurring for the positive and negative level of the applied voltage. For normalization purposes, the equivalent procedure was taken setting the FLC between parallel polarizers. Fig. 6(b) represents the normalized transmission (in the crossed configuration) as a function of the input polarizer angle, for the two stable FLC positions A and B. The dots represent the experimental data while the continuous curves were obtained from fitting these data to Eq. 3(a). The two curves display the expected oscillating behavior, with maximum transmission close to 100%, thus verifying that the retardance is very close to the ideal value of $\phi = 180°$. Two possible retardance values were obtained from the best fit curves: $\phi = 164°$ or $\phi = 196°$. This ambiguity stems from the $\sin^2(\phi/2)$ term in Eq. (3), but it can be resolved with a spectral technique [40], as will be shown next.

Note that the two curves in Fig. 6(b) are slightly shifted laterally: while the red curve (A) minima lie at $\varphi_{1A} = 45°$ and $\varphi_{1A} = 135°$, the blue curve (B) minima are located at $\varphi_{1B} = 50°$ and $\varphi_{1B} = 140°$. These minima were determined from the best fit curves, with an estimated uncertainty of one degree. As discussed earlier, the transmission is null when the input polarizer is aligned parallel or perpendicular to the FLC director. Therefore, the angles of null transmission gives us the orientations of the neutral axes of the FLC cell in the two stable positions. These stable positions of the fabricated FLC modulator are drawn in Fig. 7(a). In the ideal situation of $\theta = 90°$ rotation angle, the two curves in Fig. 6(b) should overlap. The slight shift is an indication that the ideal value was not achieved in fabrication. From the location of the minima we obtain a rotation angle of either $\theta = 85°$ or $\theta = 95°$, depending on the sense of rotation. Although the previous analysis shown in Fig. 3(b) indicates that the correct value is $\theta = 85°$, next we describe an additional experiment to confirm this hypothesis and determine the sense of rotation of the FLC director.

4.2. Determining the sense of rotation

Considering the positive voltage of the input square signal and the negative voltage as yielding the stable states A and B respectively, the FLC director can rotate either clockwise (CW) or counterclockwise (CCW). The sense of rotation of the FLC director can be derived from the transitions observed in the oscillograms in Fig. 6(a). Fig. 7(b) shows two numerical simulations for the two possible rotation directions, where the input polarizer is set at an angle $\varphi_1 = 22.5°$. We select this configuration since it corresponds to one of the experimental captures in Fig. 6(a) which shows intensity transmission values around $T = 0.5$ for both FLC stable states with transitions in the form of narrow peaks that transit between zero and 100%. Simulations were run considering $\phi = 164°$ retardance and the two possible values of θ with both sense of rotation. In the transitions, the peak goes first to zero and then to 100% transmission, or the opposite, depending on the sense of rotation of the FLC director. Comparing the direction of these transition peaks in the experiments in Fig. 6(a), we conclude that the FLC director rotates clockwise through an angle of $\theta = +85°$.

4.3. Characterization of the spectral retardance

As mentioned in Section 4.1, an ambiguity remains in the retardance, which can take values $\phi = 164°$ or $\phi = 196°$ that equally fit the experimental data. Spectral measurements can be performed to easily resolve this ambiguity [40]. For that purpose, the He-Ne laser in the optical setup of Fig. 5 is replaced by a broadband light source (a quartz tungsten halogen lamp from Oriel, model 66,882). The FLC cell is placed between crossed and parallel linear polarizers, oriented at an angle $\alpha = 45°$ relative to the principal axis of the retarder. The transmitted light is captured by a Stellar-Net spectrometer (STN-BLK-C-SR). Again, a bipolar signal of 20 Vpp is applied to the modulator, now with a very low frequency of only 1 Hz to make possible the capture of the output signal on the spectrometer.

Fig. 9(a) shows the normalized transmission curves in the range from 500 to 800 nm for stable position A (equivalent curves were obtained for position B). These curves show the typical transmission of a zero-order

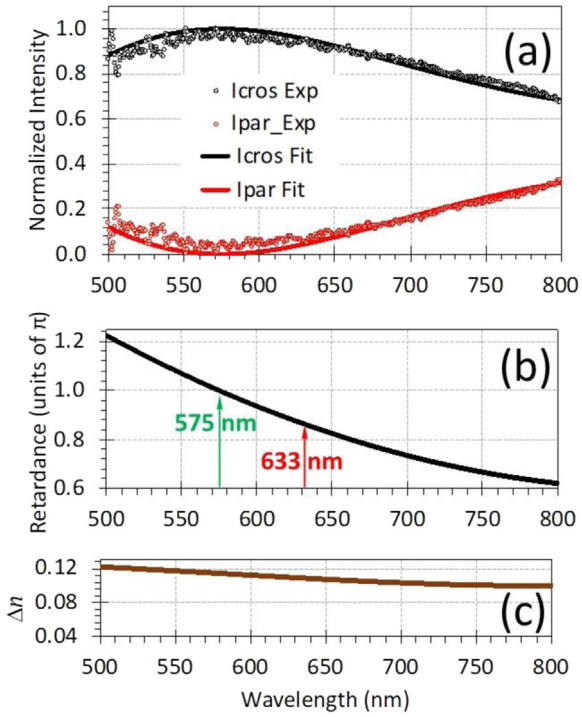

Fig. 8. (a) Normalized spectral intensity transmission of the FLC modulator between crossed and parallel polarizers oriented at 45° with respect to the LC director. (b) Spectral retardance function that best fits the experimental data. (c) Spectral birefringence $\Delta n(\lambda)$.

half-wave plate [40] with a very low transmission for crossed polarizers, below 0.1, in a wide spectral range between 530 nm and 650 nm. From Eqs. 3(a)–3(b), the spectral retardance function can be derived from the transmission data as

$$\phi(\lambda) = 2\arctan\left[\sqrt{\left(\frac{T_{cross}(\lambda)}{T_{par}(\lambda)}\right)}\right]. \quad (4)$$

Since the FLC modulator is composed of a single LC layer, the retardance must follow a relation $\phi(\lambda) = \frac{2\pi}{\lambda}\Delta n \cdot t$, where Δn is the LC birefringence and t is the LC layer thickness. Therefore, $\phi(\lambda)$ typically follows a monotonically decreasing function with the λ. As it was done in [40], we employ a Cauchy equation for the spectral retardance and use it to fit these experimental intensity curves. Fig. 8(a) shows also the best fit obtained for the normalized intensity in crossed and parallel configurations, while the function $\phi(\lambda)$ that best fits the experimental data is plotted in Fig. 8(b). According to this result the retardance obtained for the $\lambda = 633$ nm wavelength is below π, thus verifying the previously obtained value $\phi = 164°$. The ideal HWP retardance would be obtained at 575 nm. Nevertheless, we keep considering operation at 633 nm since it corresponds to the common wavelength of a standard He-Ne laser and the 164° retardance is close enough to the ideal value. Finally, Fig. 8(c) shows the wavelength variation of the birefringence Δn, which is calculated from the previous result as $\Delta n = \lambda\phi(\lambda)/2\pi t$, assuming the LC thickness value of $t = 2.5$ microns. The value $\Delta n = 0.109$ is obtained for $\lambda = 633$ nm, thus confirming previous results.

5. Characterization of the time response

For purposes of its effective performance, it is important to calibrate the frequency limit of the FLC modulator. We then apply a square signal of 20Vpp and increasing frequency up to 200 Hz. Fig. 9 shows the effect

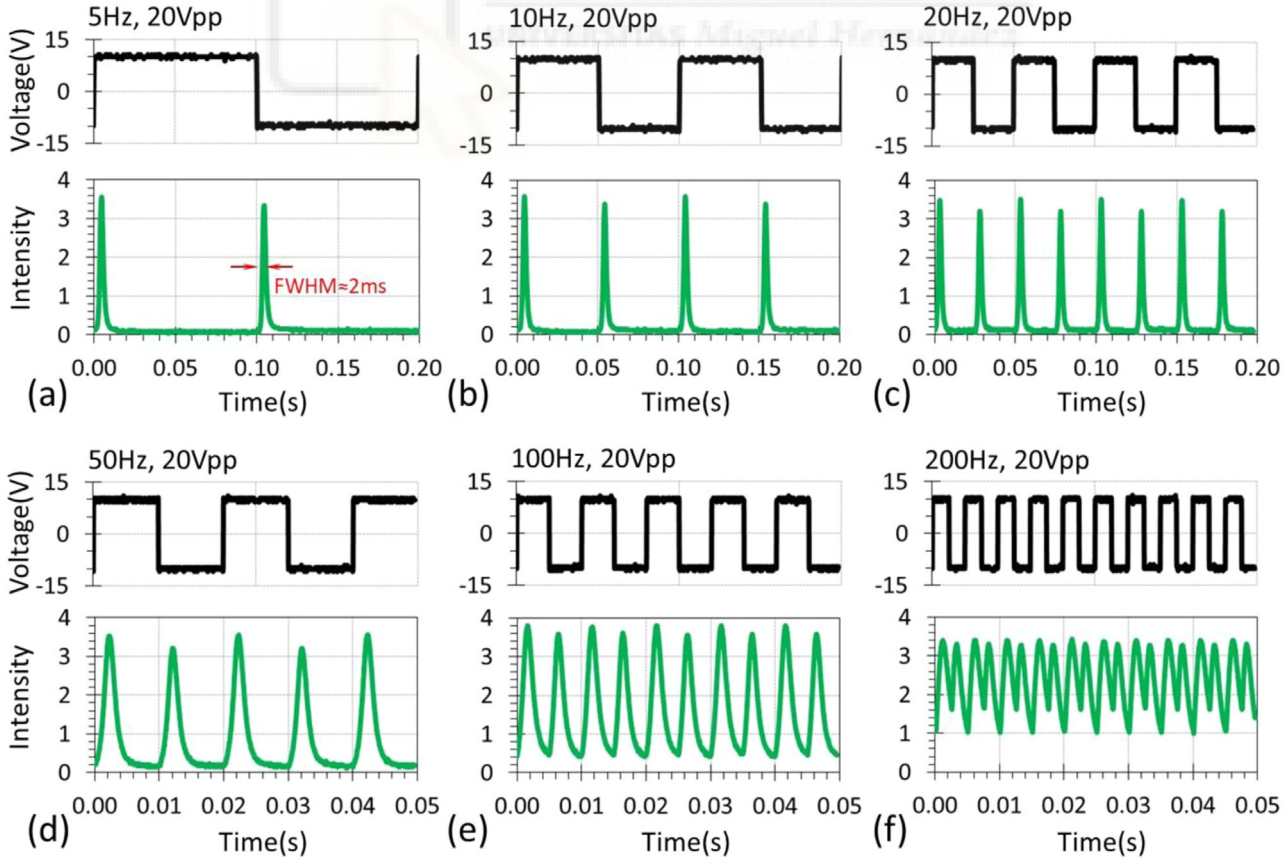

Fig. 9. Measured optical intensity signal (in green) at varying frequencies of the 20 Vpp voltage signal (in black) addressed to the FLC modulator in between crossed polarizers, with the input polarizer parallel to the first stable LC orientation.

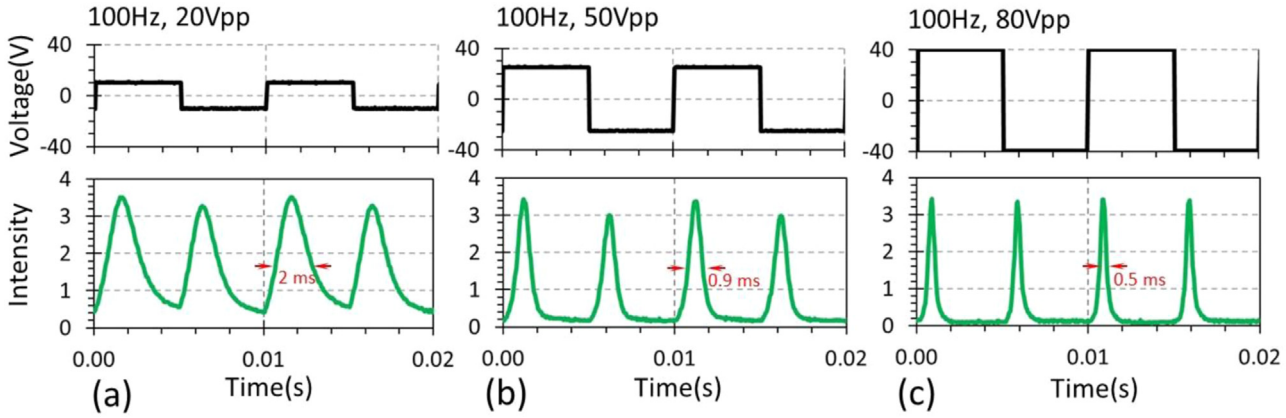

Fig. 10. Comparison of the optical intensity for addressed voltage signals of 100 Hz with (a) 20 Vpp, (b) 50 Vpp and (c) 80 Vpp.

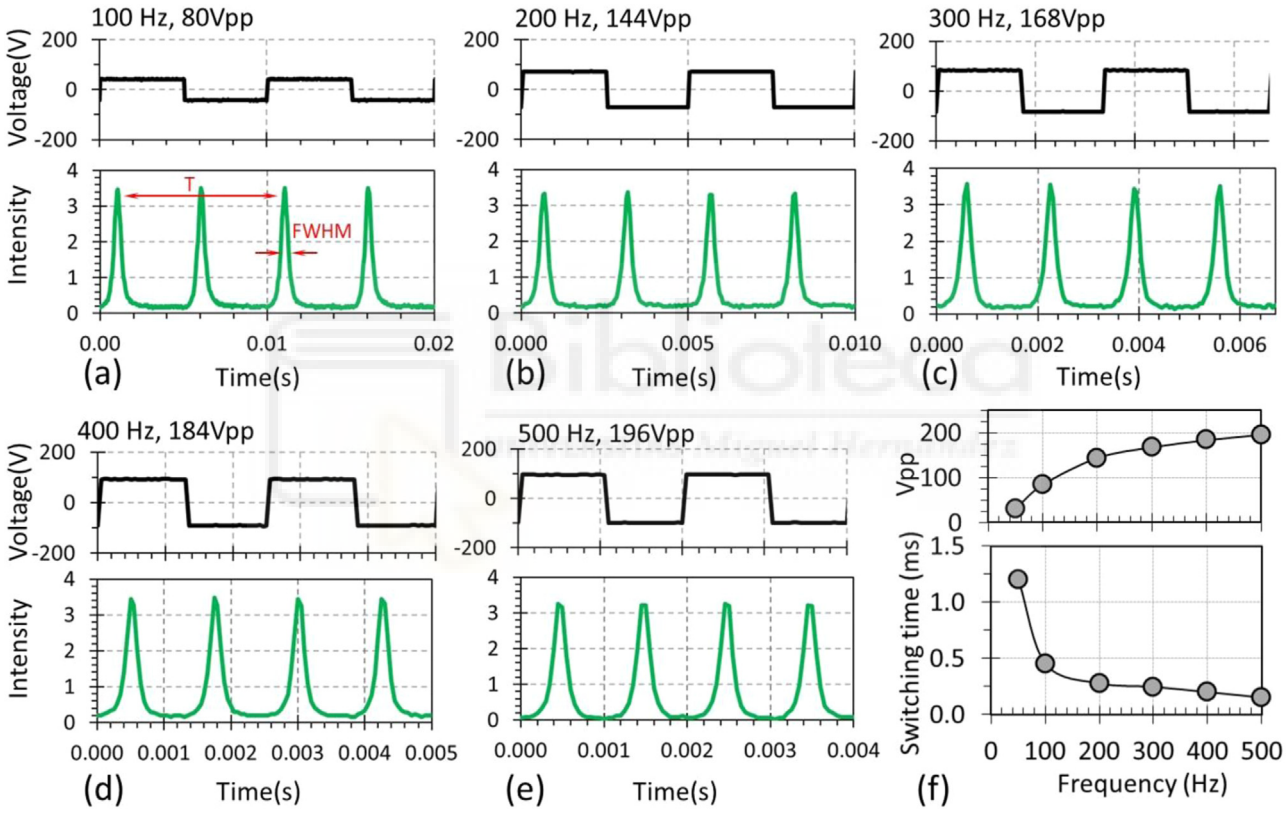

Fig. 11. (a)-(e) Measured optical intensity signal (in green) at varying frequencies. The Vpp value of the voltage signal (in black) is adjusted in each case to provide a ratio $FWHM/T < 1/10$. (e) Required Vpp versus frequency. (f) Measured switching time versus frequency.

on the output optical signal. In these experiments the FLC modulator was placed between crossed polarizers, with the first polarizer parallel to the first stable orientation of the LC director. In this situation the intensity for the two stable states is very low, since the SOP that exits the FLC cell is perpendicular to the analyzer. The change in the LC orientation is visible in the form of transition peaks that approach the maximum 100% normalized transmission. These peaks occur when, on its transition from stable position A to B, the LC director becomes horizontally aligned.

Fig. 9 shows the captured optical intensity signal for frequencies of 5, 10, 20, 50, 100 and 200 Hz. Here the intensity captures are not normalized to better see the effect when increasing the frequency, and the figures show the voltage signal directly measured in the photodetector (green curves). Below 50 Hz the difference between the two stable states is minimal and the transmission at the stable states remains very low. The transition peaks reach the maximum value, with full width at half maximum ($FWHM$) slightly less than 2 ms in all cases. For 100 Hz the optical signal does not reach the lowest value. The optical signal shows a significant degradation for 200 Hz, thus implying that the FLC director does not fully switch through the expected angle of $\phi = 90^{\circ}$ between the two stable states. This simple procedure therefore reveals that we must consider 50 Hz as the proper frequency limit for the effective operation of the FLC cell when addressing a 20 Vpp signal.

However, we can overcome this degradation by increasing the amplitude of the applied voltage signal. The response time or switching time of the FLC cell is expected to lower as the amplitude increases. This is illustrated in Fig. 10 for the frequency of 100 Hz. We show here the data already shown in Fig. 9 (with 20 Vpp) with new captures obtained with 50 Vpp and 80 Vpp. The switching time, measured as the $FWHM$ of the transient peaks, is reduced below the millisecond.

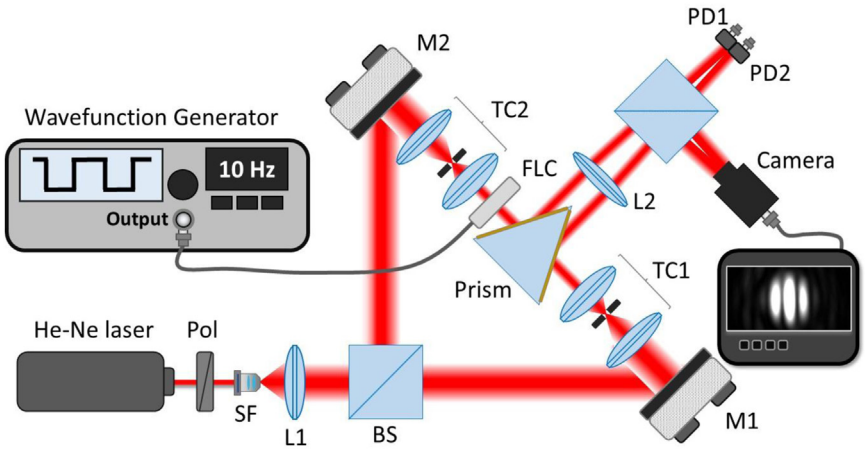

Fig. 12. Scheme of the interferometer setup for measuring the phase modulation. SF: spatial filter; L1: collimating lens; L2 Fourier transform lens; BS: beam-splitter; TC: telescope system; M: mirror; PD: photodetector.

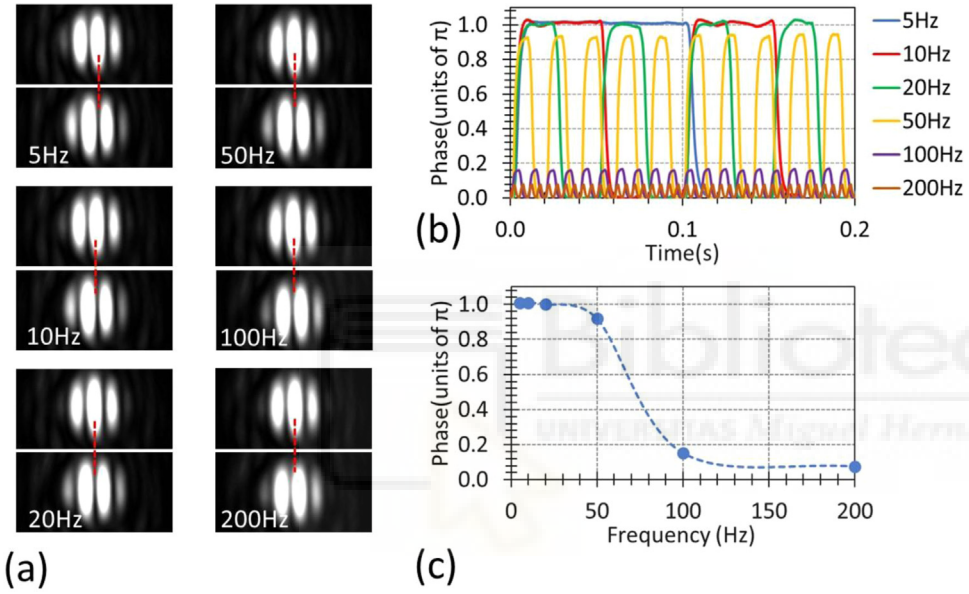

Fig. 13. (a) Interference patterns for the FLC modulator illuminated with horizontal linear polarization for different frequencies of the addressed voltage signal of 20 Vpp and for the two stable states of the FLC. (b) Measured phase modulation at varying frequencies. (c) Maximum phase shift versus frequency.

Therefore, operation at higher frequencies is possible by applying larger voltages. This is demonstrated in Fig. 11, where we present results up to 500 Hz. For each frequency, the voltage amplitude is increased to reach approximately a ratio $FWHM/T < 0.1$ between the switching time and the period (T) of the addressed signal. Figs. 11(a) to 11(e) show transmission peaks with similar relative width with respect to their time interval. Note that the time scale is different in every figure to display only four peaks of each signal. Fig. 11(f) shows the Vpp value that must be applied for each frequency to achieve this situation, and how the switching time progressively diminishes. The result in Fig. 11(e) shows a good optical signal with a switching time close to FWHM=0.2 ms for an addressed voltage of 500 Hz and 196 Vpp. Although these are too high voltage values for practical devices, which require the minimum switching time and must use low voltage FLC mixtures [41], these results illustrate how the device can be operated at different frequencies.

6. Characterization of the phase modulation

The characterization of the FLC modulator optical properties is completed in this section by verifying the expected binary π phase modulation for all polarization states. Despite the fabricated FLC modulator does not fulfill exactly the ideal parameters ($\phi = 180^{\circ}$ and $\theta = 90^{\circ}$), we show next that this phase modulation regime is reproduced quite well.

The phase shift between the two stable states of the FLC modulator was experimentally retrieved with a very versatile specially-adapted Young's interferometer which detects the optical interference pattern by a bicell photo-detector in a back Fourier focal plane [28]. Fig. 12 shows a scheme of this interferometer setup intended to provide time-resolved measurements of the phase modulation. In addition to the ordinary camera-based interferometry, which has limited capturing rate and long processing time for fringe pattern, the bicell detector-based interferometry technique provides enough sampling rate along the time axis. The experimental setup uses a beam-splitter to divide the linearly polarized and spatially filtered beam of a He-Ne laser in a reference and a probe beam. The beam reflected in mirror M1 is the reference beam and that reflected in mirror M2 is the probe beam. The FLC cell was placed in the arm of the probe beam and is reflected on one side of a gold coated right angle prism alongside the reference beam on the opposite side of the prism. The reflected rays from both sides of the prism propagate parallel to each other separated by a distance dependent on the dimensions of the prism. The beams are then combined by a converging lens (L2) to provide the Fourier transform where the interference pattern is observed at the back focal plane, where two photo-detectors are placed. The photodetectors are separated from each other by a distance gap equivalent to that of the two beams being reflected from the prism. For purposes of simultaneously visualizing the interference pattern on a camera we place a beam splitter right after the prism and lens L2.

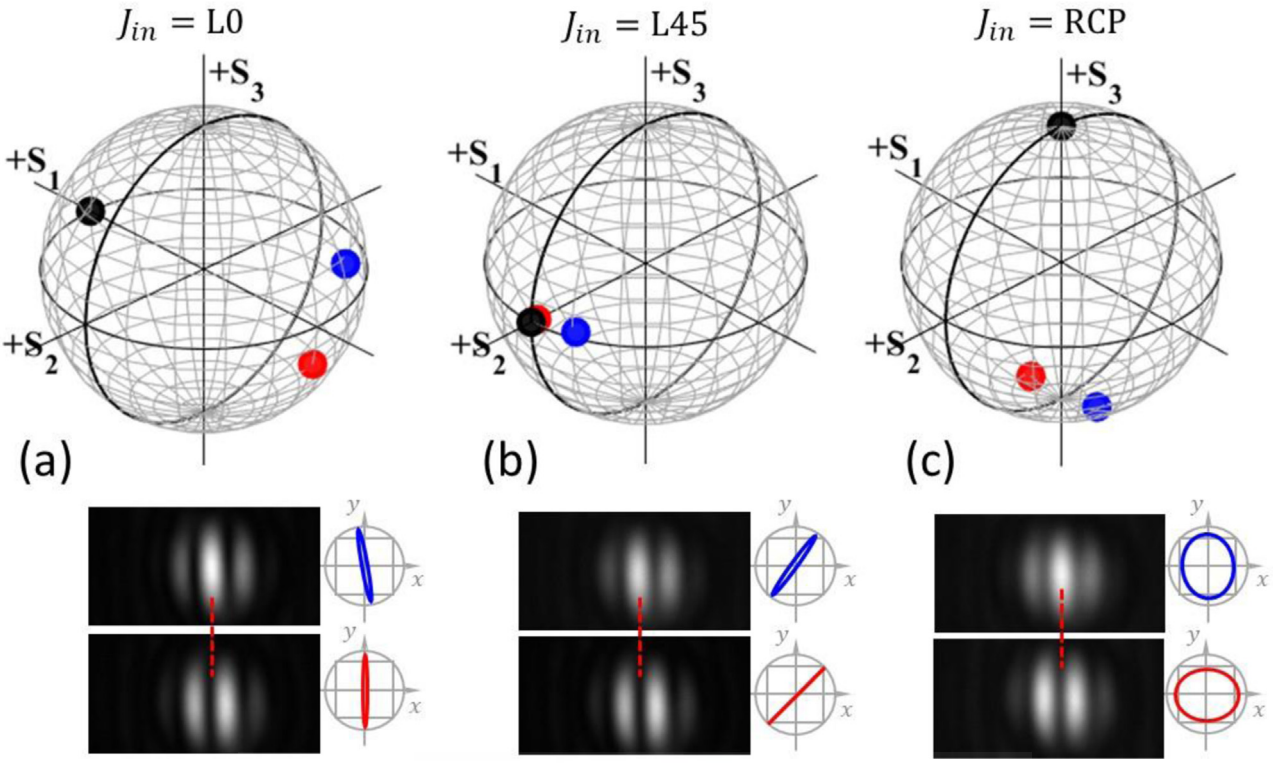

Fig. 14. Transformations of SOP in the PS for the FLC with real parameters $\phi = 164^{\circ}$ and $\theta = 85^{\circ}$ for input SOPs (a) L0, (b) L45 and (c) RCP. Below each case the experimental interference patterns are shown for the two SOP emerging from the FLC modulator.

Table 1
Stokes parameters and ellipticity and azimuth angles expected for the two emerging states of the FLC modulator for three different input SOP.

Input SOP	Output Stokes parameters State A			Output Stokes parameters State B			Ellipticity angle (degrees)		Azimuth Angle (degrees)	
	S_1	S_2	S_3	S_1	S_2	S_3	A	B	A	B
L0	−0.96	0.00	−0.28	−0.90	−0.34	0.28	−8.0	7.9	90.0	−79.8
L45	0.00	1.00	0.00	−0.33	0.94	0.05	0.0	1.4	45.0	54.8
RCP	0.28	0.00	−0.96	−0.27	−0.05	−0.96	−37.0	−37.0	0.0	−85.0

Fig. 13 shows a set of experiments where the FLC cell was illuminated with horizontal linearly polarized light. Again, the modulator was addressed with a bipolar square voltage signal of 20 Vpp and varying frequency (5, 10, 20, 50, 100 and 200 Hz). Fig. 13(a) presents the interference patterns captured on the camera for every frequency of the applied voltage. For each case, two interferograms are presented, corresponding to the two stable states of the FLC modulator. For low frequencies, up to 50 Hz, the interference contrast clearly reverses from each interference pattern (a red discontinuous line was drawn to clearly visualize this effect), thus indicating a π-phase difference between the two FLC states. At higher frequencies, as expected from the previous results in Section 5, the interference pattern does not show contrast inversion.

This is further demonstrated in Fig. 13(b) through quantitative, and time resolved measurements of the phase modulation. For frequencies of 5, 10 and 20 Hz the phase modulation perfectly reproduces a binary function with a π phase shift. At 50 Hz the maximum phase shift does not recover the maximum value, reaching slightly 0.9π As the frequency increases, the binary phase modulation regime is lost and there is a progressive reduction of the maximum phase difference, with values below 0.2π for 100 Hz and below 0.1π for 200 Hz. Fig. 13(c) shows the evolution of the maximum phase shift versus frequency.

Finally, Fig. 14 presents another set of equivalent interferograms for three different input states of polarization: a linear horizontal state, a linear state oriented at 45°, and the RCP state. Here we apply a square voltage signal of 20 Vpp and 5 Hz, so the frequency limit is very far. Fig. 14 shows first the representation on the PS of the input SOP and the two expected emerging SOPs, where the measured FLC physical parameters $\phi = 164$ and $\theta = 85^{\circ}$ were considered in the simulations. The two emerging states have similar SOP and give two very close but different points on the PS. For each input SOP, Table 1 gives the expected SOP in terms of their Stokes parameters as well as their ellipticity and azimuth angles. The polarization ellipses of these states are drawn next to the interferogram patterns.

Since the SOP difference is very small, the interferograms are expected with very good visibility. The second row of Fig. 14 shows, for each input SOP, the two interference patterns captured for each stable position (A and B) of the FLC modulator. The three cases verify the good visibility and the contrast inversion of the interference, thus demonstrating a π phase-shift that is obtained independently of the input state.

7. Conclusions

In summary, we have fabricated a FLC modulator with a large switching rotation angle close to 90° and retardance around 180° (HWP regime) for a wide visible spectral range. Physico-chemical properties of the specific LC mixture used to fabricate the FLC modulator with such large tilt angle were provided. In addition, a reverse engineering procedure was performed for the precise and unambiguous verification of its physical parameters (location of the liquid-crystal director, its sense of rotation upon applying a square voltage signal, and spectral retar-

dance function). An experimental analysis of the frequency limits of the fabricated device has been also included. Finally, the phase modulation properties of the modulator were experimentally probed, and the expected binary π phase-shift was verified for various input polarization states.

Although this principle of operation was proposed years ago [22–25], it has barely been implemented, probably due to the difficult realization of FLC modulators with such large switching rotation angles. The application of this scheme to FLC spatial light modulators could be very interesting, since they would be binary phase modulators with the highest diffraction efficiency and useful for all states of polarization, therefore including unpolarized light, a situation that is not possible with the common nematic LC -SLMs or with standard FLC-SLMs of smaller rotation angles.

Declaration of Competing Interest

The authors declare that they have no known competing financial interests or personal relationships that could have appeared to influence the work reported in this paper.

CRediT authorship contribution statement

Esther Nabadda: Investigation, Visualization, Writing – original draft. **Noureddine Bennis:** Conceptualization, Methodology, Validation, Writing – review & editing. **Michał Czerwinski:** Methodology, Validation. **Aleksandra Walewska:** Investigation, Visualization. **Leszek R. Jaroszewicz:** Supervision. **María del Mar Sánchez-López:** Methodology, Validation, Writing – review & editing. **Ignacio Moreno:** Conceptualization, Validation, Supervision.

Acknowledgements

This work received financial support from Ministerio de Ciencia, Innovación y Universidades, Spain (grant project RTI2018–097107-B-C33), from Wojskowa Akademia Techniczna, Poland (UGB 22–791) and from European Social Fund (NAWA PROM project POWR.03.03.00–00-PN13/18). E.N. acknowledges a grant from Generalitat Valenciana, Santiago Grisolia Program (ref. GRISOLIAP/2020/004).

References

[1] Moddel G. Ferroelectric liquid crystal spatial light modulators. Spatial Light Modulator Technology: Materials, Devices and Applications Chap 6. New York: U Efron Edt Marcel Dekker Inc; 1994.
[2] Gros E, Dupont L. Ferroelectric liquid crystal optical waveguide switches using the double-refraction effect. IEEE Photon. Technol. Lett. 2001;13(2):115–17.
[3] Manolis IG, Wilkinson TD, Redmond MM, Crossland WA. Reconfigurable multilevel phase holograms for optical switches. IEEE Photon. Technol. Lett. 2002;14(15):801–3.
[4] Sirleto L, Coppola G, Breglio G, Abbate G, Righini GC, Otón JM. Electro-optical switch and continuously tunable filter based on a Bragg grating in a planar waveguide with a liquid crystal overlayer. Opt. Eng. 2002;41(47):2890–8.
[5] Hariharan P, Ciddor PE. Improved switchable achromatic phase shifters. Opt. Eng. 1999;38(6):1078–80.
[6] Peinado A, Lizana A, Campos J. Use of ferroelectric liquid crystal panels to control state and degree of polarization in light beams. Opt. Lett. 2014;39(3):659–62.
[7] Jaulin A, Bigué L, Ambs P. High-speed degree-of-polarization imaging with a ferroelectric liquid-crystal modulator. Opt. Eng. 2008;47(3):033201.
[8] Peinado A, Lizana A, Iemmi C, Campos J. Polarization imaging with enhanced spatial resolution. Opt. Commun. 2015;338:95–100.
[9] Mukherjee S, Yuan Z, Sun Z, Li A, Kang C, Kwok H, Srivastava AK. Fast refocusing lens based on ferroelectric liquid crystals. Opt. Express 2021;29(6):8258–67.
[10] Yuan Z, Sun Z, Kwok H, Srivastava AK. Fast LiDAR systems based on ferroelectric liquid crystal dammann grating. Liq. Cryst. 2021;48(10):1402–16.
[11] Guo Q, Yan K, Chigrinov V, Zhao H, Tribelsky M. Ferroelectric liquid crystals: physics and applications. Crystals 2019;9(9):470–90.
[12] Bougrenet de la Tocnaye JL, Dupont L. Complex amplitude modulation by use of a liquid crystal spatial light modulators. Appl. Opt. 1997;36:1730–41.
[13] Martínez A, Beaudoin N, Moreno I, Sanchez-López MM, Velasquez P. Optimization of the contrast ratio of a ferroelectric liquid crystal optical modulator. J. Opt. A: Pure Appl. Opt. 2006;8(1):1013–18.
[14] Gourlay J, Samus S, McOwan P, Vass DG, Underwood I, Worboys M. Real-time binary phase holograms on a reflective ferroelectric liquid-crystal spatial light modulator. Appl. Opt. 1994;33:8251–4.
[15] Le Doucen M, Pellat-Finet P. Polarization properties and diffraction efficiencies of binary anisotropic gratings: general study and experiments on ferroelectric liquid crystals. Opt. Commun. 1998;151:321–30.
[16] Forth Dimension Displays, 2022 https://www.forthdd.com/.
[17] Tong Z, Chen X. A ferroelectric liquid crystal spatial light modulator encoded with orthogonal arrays and its optimized design for laser speckle reduction. Opt. Laser Eng. 2017;90:173–8.
[18] Förster R, Lu-Walther HW, Jost A, Kielhorn M, Wicker K, Heintzmann R. Simple structured illumination microscope setup with high acquisition speed by using a spatial light modulator. Opt. Express 2014;22(17):20663–77.
[19] Schlichenmeyer TC, Wang M, Elfer KN, Brown JQ. Video-rate structured illumination microscopy for high-throughput imaging of large tissue areas. *Biomed. Opt. Express* 2014;5(2):366–77.
[20] Schmieder F, Klapper SD, Koukourakis N, Busskamp V, Czarske J. Optogenetic stimulation of human neural networks using fast ferroelectric spatial light modulator-based holographic illumination. Appl. Sci. 2018;8:1180.
[21] Martínez-García A, Moreno I, Sánchez-López MM, García-Martínez P. Operational modes of a ferroelectric LCoS modulator for displaying binary polarization, amplitude, and phase diffraction gratings. Appl. Opt. 2009;48(15):2903–14.
[22] O'Callaghan MJ, Handschy MA. Diffractive ferroelectric liquid-crystal shutters for unpolarized light. Opt. Lett. 1991;16(10):770–2.
[23] TWarr S, Mears RJ. Polarisation insensitive operation of ferroelectric liquid crystal devices. Electron. Lett. 1995;31:714–16.
[24] Warr ST, Mears RJ. Polarisation insensitive diffractive FLC systems. Ferroelectrics 1996;181(1):53–9.
[25] Brown CV, Kriezis EE. Calculation of the efficiency of polarization-insensitive surface-stabilized ferroelectric liquid-crystal diffraction gratings. Appl. Opt. 2003;42(13):2257–63.
[26] Manolis IG, Redmond MM, Crossland WA, Davey AB, Wilkinson TD. Control of the electro-optic bistability of some ferroelectric liquid crystals useful for binary phase optical modulators. Mol. Cryst. Liq. Cryst. 2000;351:305–14.
[27] Ma Y, Tam AMW, Gan XT, Shi LY, Srivastava AK, Chigrinov V, Kwok HS, Zhao JL. Fast switching ferroelectric liquid crystal Pancharatnam-Berry lens. Opt. Express 2019;27(7):10079–86.
[28] Bennis N, Merta I, Kalbarczyk A, Maciejewski M, Marc P, Spadlo A, Jaroszewicz LR. Real time phase modulation measurements in liquid crystals. Opto Elect. Rev. 2017;25(2):69–73.
[29] Sánchez-López MM, García-Martínez P, Martínez-García A, Moreno I. Poincaré sphere analysis of a ferroelectric liquid crystal optical modulator: application to optimize the contrast ratio. J. Opt. A Pure Appl. Opt. 2009;11:015507.
[30] Matsumoto T, Fukuda A, Johno M, Motoyama Y, Yui T, Seomunc S, Yamashita M. A novel property caused by frustration between ferroelectricity and antiferroelectricity and its application to liquid crystal displays - Frustoelectricity and V-shaped switching. J. Mater. Chem. 1999;9(9):2051–80.
[31] Kurp K, Czerwiński M, Salamon P, Bubnov A, Tykarska M. Design of functional multicomponent liquid crystalline mixtures with nano-scale pitch fulfilling deformed helix ferroelectric mode demands. J. Mole. Liq. 2019;290:111329 1-10.
[32] Drzewiński W, Czupryński K, Dąbrowski R, Neubert M. New antiferroelectric compounds containing partially fluorinated terminal chains. Synthesis and mesomorphic properties. Mol. Cryst. Liq. Cryst. 1999;328:401–10.
[33] Chandrasekhar S. Liquid Crystals. Cambridge University Press; 1977. p. 10. P.
[34] Tykarska M, Czerwiński M, Miszkurka J. Influence of temperature and terminal chain length on helical pitch in homologue series nH6Bi. Liq. Cryst. 2010;37(4):487 49.
[35] Czerwiński M, Tykarska M. Helix parameters in bi- and multicomponent mixtures composed of orthoconic antiferroelectric liquid crystals with three ring molecular core. Liq Cryst 2014;41(6):850–8.
[36] Kuczynski W, Lagerwall T, Matuszczyk M, Skarp K, Stebler B, Wahl J. Fast-switching low-temperature liquid crystal mixtures. Mol. Cryst. Liq. Cryst. 1987;146:173–87.
[37] Abdulhalim I, Moddel G, Clark NA. Director-polarization reorientation via solitary waves in ferroelectric liquid crystals. Appl. Phys. Lett. 1992;60(5):551–3.
[38] Abdulhalim I, Moddel G, Clark NA. Soliton switching in ferroelectric liquid crystals and their transient electro-optic response. J. Appl. Phys. 1994;76(2):820–31.
[39] Abdulhalim I. Continuous phase-only or amplitude light modulation using ferroelectric liquid crystals with fixed boundary orientations. Opt. Commun. 1994;108:219–24.
[40] Messaadi A, Sánchez-López MM, García-Martínez P, Vargas A, Moreno I. Optical system for measuring the spectral retardance function in an extended range. J. Eur. Opt. Soc. Rapid Pub. 2016;12(21):1–9.
[41] Hughes JR, Bannister RW, Graham A, McDonnell DG, Pedlingham HA, Scattergood DC, Smith CJT. A high resolution ferroelectric liquid crystal display. Displays 1994;15(2):117.

frontiers | Frontiers in Physics

BRIEF RESEARCH REPORT
published: 08 July 2022
doi: 10.3389/fphy.2022.920111

Phase-Shifting Common-Path Polarization Self-Interferometry for Evaluating the Reconstruction of Holograms Displayed on a Phase-Only Display

Esther Nabadda[1], *Pascuala García-Martínez*[2]*, *María del Mar Sánchez-López*[1,3] and *Ignacio Moreno*[1,4]

[1]Instituto de Bioingeniería, Universidad Miguel Hernández de Elche, Elche, Spain, [2]Departamento de Óptica y Optometría y Ciencias de la Visión, Universitat de València, Burjassot, Spain, [3]Departamento de Física Aplicada, Universidad Miguel Hernández de Elche, Elche, Spain, [4]Departamento de Ciencia de Materiales, Óptica y Tecnología Electrónica, Universidad Miguel Hernández de Elche, Elche, Spain

OPEN ACCESS

Edited by:
Elizabeth C. Carroll, Delft University of Technology, Netherlands

Reviewed by:
Takanori Nomura, Wakayama University, Japan
Rakesh Kumar Singh, Indian Institute of Technology (BHU), India
Naveen Nishchal, Indian Institute of Technology Patna, India

***Correspondence:**
Pascuala García-Martínez
pascuala.garcia@uv.es

Specialty section:
This article was submitted to Optics and Photonics, a section of the journal Frontiers in Physics

Received: *14 April 2022*
Accepted: *15 June 2022*
Published: *08 July 2022*

Citation:
Nabadda E, García-Martínez P, Sánchez-López MdM and Moreno I (2022) Phase-Shifting Common-Path Polarization Self-Interferometry for Evaluating the Reconstruction of Holograms Displayed on a Phase-Only Display. Front. Phys. 10:920111. doi: 10.3389/fphy.2022.920111

In this work we apply a phase-shifting interferometry (PSI) to evaluate the reconstruction of complex-valued holograms displayed onto a phase-only spatial light modulator (SLM). The interferometer is vibration-free since it uses a common-path polarization arrangement based on the SLM itself, which is used simultaneously to display the hologram and to apply the phase-shifting values. The change from the hologram display configuration to the interferometer configuration involves only a rotation of a polarizer. The continuous phase modulation provided by the SLM allows using PSI with arbitrary phase bias values. Several examples are demonstrated by generating different combinations of modes with an efficient on-axis hologram encoding technique.

Keywords: spatial light modulators, holograms, liquid-crystal on silicon, phase shifting, polarization interferometry

INTRODUCTION

The possibility of encoding arbitrary complex-valued fields in a light beam has led to the generation of the so-called structured light, a research area that has received a great deal of attention [1, 2]. In their most common configuration for this application, SLMs are typically arranged as parallel-aligned liquid-crystal on silicon (LCOS) displays [3]. These are pixelated linear retarders that, under illumination with linearly polarized light parallel to the liquid-crystal (LC) director, produce phase-only modulation. This modulation response does not allow directly displaying complex-valued holograms and several encoding techniques have been developed for this purpose [4–9]. In most cases, the successful generation of the complex beam is verified by regarding the intensity in the far field. In some cases, however, the phase distribution of the propagated field is also of interest, and it is measured typically with a wave-front sensor or through interferometry [8, 10]. These are external systems that must be added to the SLM setup generating the structured light beam to recover the phase distribution, thus adding some complexity to the optical systems.

Phase-shifting interferometry (PSI) is a very efficient and accurate classical technique, where a phase distribution is retrieved from a sequence of phase-shifted interferograms [11]. Although the most common device for phase shifting is a piezoelectric transducer, LC retarders have also been extensively used [12, 13]. LC-SLMs have been also exploited to build several interferometric and

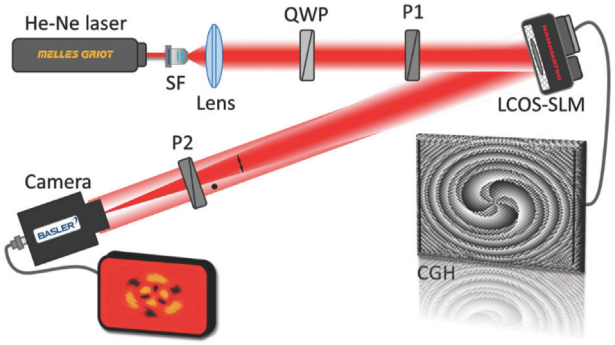

FIGURE 1 | Scheme of the optical system. SF: spatial filter; QWP: quarter-wave plate; P: linear polarizer; CGH: displayed phase-only computer-generated hologram.

holographic systems [14]. On the other hand, the phase modulation properties and/or aberration of LC-SLMs are typically measured by introducing the device in an external interferometer [15]. In the last years some works demonstrated the use of the SLM itself to simultaneously build the interferometer, either by displaying a diffraction grating [16] or using the light reflected on the device coating [17]. These techniques exploit a common-path interferometer, thus becoming very simple, compact and vibration insensitive.

In this work we combine three well-stablished methods in a simple and compact optical system: 1) a technique to encode complex-valued holograms onto a phase-only SLM; 2) a common path interferometer based on polarized light; and 3) the classical PSI technique. The goal is to show how this combination can be exploited to evaluate the quality of the propagated structured light field, not only in intensity but also in its the phase distribution. The hologram is displayed with a checkerboard grating technique that provides on-axis reconstruction [7–9] The same system is employed to retrieve the phase distribution in far field through a PSI algorithm by simply rotating a polarizer. The technique is demonstrated by producing different superpositions of Gaussian modes [18]. The PSI algorithms provides quantitative phase evaluation that complements the traditional intensity pattern evaluation.

METHODS AND TECHNIQUES

Experimental Interferometric Arrangement

Figure 1 shows a scheme of the experimental arrangement. A linearly polarized He-Ne laser (Melles-Griot 05-LHP-991, with a $\lambda = 632.8$ nm wavelength) is spatially filtered and collimated. A quarter-wave plate (QWP) converts it into circularly polarized. This way, a linear polarizer (P1) can be rotated without changing the light intensity. The beam illuminates a LCOS-SLM (Hamamatsu X10,468-01, with 800 × 600 square pixels, 20 μm pixel pitch and 98% fill factor). The SLM director axis is oriented horizontally in the laboratory framework and produces more than 2π phase variation at the operating wavelength [19]. It is addressed with a hologram that includes a converging lens. A camera (Basler scA1390-17fc, 1/2" active area, with 1,390 × 1,038 square pixels of 4.65 μm size) is placed on the back focal plane, where the Fourier transform is focused.

The SLM displays a phase-only function that combines the hologram with a converging lens, $\phi(\mathbf{r}) = \phi_H(\mathbf{r}) + \phi_L(\mathbf{r})$. Here $\mathbf{r} = (x, y)$ denotes the spatial coordinates in the SLM, $\phi_H(\mathbf{r})$ is the hologram phase function and $\phi_L(\mathbf{r}) = -\pi r^2/\lambda f$ is the lens function, where $r = \sqrt{x^2 + y^2}$ is the radial coordinate and f the lens focal length. Since the LCOS-SLM has a horizontal director axis, this phase affects only the horizontal polarization component, which is focused on the camera. In the standard operation in diffractive optics P1 is oriented horizontal so the input beam gets fully modulated by $\phi(\mathbf{r})$. For other orientations there is a vertical polarization component that is simply reflected on the SLM and remains collimated. A second polarizer (P2), oriented at 45°, placed before the camera, cause the interference of the two components.

Complex Hologram Encoding

We encode complex-valued functions on the SLM with a well-established technique that uses a modulated checkerboard diffraction grating [7, 8]. This technique presents the advantage of producing a reconstruction on axis, although it might be severely affected if the SLM presents fringing [9]. Let us consider the complex function $F(\mathbf{r}) = M(\mathbf{r})\exp[i\theta(\mathbf{r})]$, where $M(\mathbf{r})$ and $\theta(\mathbf{r})$ denote its magnitude (modulus) and phase distributions respectively. $M(\mathbf{r})$ is assumed normalized with values in the range [0,1]. Then, a phase-only function is calculated as

$$\phi_H(\mathbf{r}) = \theta(\mathbf{r}) + (-1)^{m+n}\arccos[M(\mathbf{r})]. \quad (1)$$

Here $(m, n) \in [-\frac{N}{2}, .., -1, 0, +1 \ldots, (\frac{N}{2}) - 1]$ are integer indices denoting the pixel coordinates which relate to the spatial coordinates as $(x, y) = (m\Delta, n\Delta)$, Δ being the pixel spacing and the SLM array is assumed to have $N \times N$ pixels. The term $(-1)^{m+n}$ is a checkerboard binary diffraction grating that is modulated by $\arccos[M(\mathbf{r})]$. Therefore, the phase-shift between the two levels of the grating is $\delta = 2\arccos[M(\mathbf{r})]$. When $M(\mathbf{r}) \to 1$ then $\delta \to 0$, while $\delta \to \pi$ when $M(\mathbf{r}) \to 0$. It is well known that a binary phase diffraction grating has the maximum diffraction efficiency when $\delta = \pi$, leading to the cancellation of the zero-diffraction order. On the contrary, when $\delta = 0$ there is no grating, and all the light remains in the zero order. This way, the magnitude of the zero-diffraction order is directly modulated by $M(\mathbf{r})$ [8]. Finally, the original phase $\theta(\mathbf{r})$ is added to the binary phase grating. When displaying the phase-only hologram $\phi_H(\mathbf{r})$, regions where $M(\mathbf{r})$ is small diffract light out of the center, while the beam remains on axis in the regions where $M(\mathbf{r})$ is high. As a result, the complex function $F(\mathbf{r})$ is well-reproduced on axis. The light diffracted out of axis can be easily filtered with an aperture.

Figure 2 illustrates this encoding technique, applied to a Laguerre-Gauss LG_{13} mode. **Figures 2A,B** show the intensity distribution $[M(\mathbf{r})]^2$ and the phase distribution $\theta(\mathbf{r})$ corresponding to this mode. The intensity shows the characteristic double ring pattern while the phase shows two

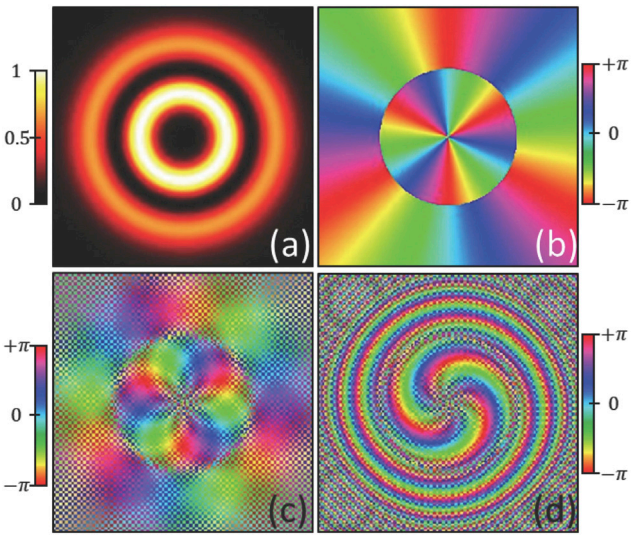

FIGURE 2 | Illustration of the complex encoding technique. LG_{13} mode **(A)** intensity $[M(\mathbf{r})]^2$ and **(B)** phase $\theta(\mathbf{r})$ distributions. **(C)** Phase-only function $\phi_H(\mathbf{r})$ encoding the complex function with the checkerboard grating technique. **(D)** Phase function $\phi(\mathbf{r}) = \phi_H(\mathbf{r}) + \phi_L(\mathbf{r})$ when a lens is added.

spiral phase patterns, with a π phase-jump located at the radius of the dark ring. **Figure 2C** shows the hologram function $\phi_H(\mathbf{r})$ after applying **Eq. 1**. Note that the checkerboard grating appears at the regions with low intensity in **Figure 2A** (in the center, in the dark ring and in the corners), while it disappears in the location of the two bright rings. Finally, **Figure 2D** shows the pattern after a phase lens pattern is added, this being the final phase function $\phi(\mathbf{r}) = \phi_H(\mathbf{r}) + \phi_L(\mathbf{r})$ that is transformed into gray-levels (CGH, in **Figure 1**) to be displayed on the LCOS-SLM.

Common-Path Interferometer

We are interested in experimentally evaluating the hologram reconstruction in the Fourier plane by measuring the intensity and the phase distributions, although the same technique could be applied to Fresnel or fractional Fourier planes. In our approach we use the LCOS-SLM itself to generate the interferometer, thus avoiding any additional components. We follow the scheme presented in [20]. This is based on rotating the input polarizer (P1) so a significant component of the input beam is oriented perpendicular to the LC director of the SLM. This non-modulated polarization component is the reference beam. The second polarizer (P2) produces the interference of the modulated test beam and the reference beam in a common-path configuration, with significant advantages of alignment and stability.

While in ref. [20] the interferometer was demonstrated, here we perform quantitative phase measurements. To this aim we apply the well-known PSI algorithms by adding a known constant phase-shift φ between two beams [11]. The test beam can be considered to have the same functional form $F_G(\mathbf{r}) = M_G(\mathbf{r})\exp\{i[\theta(\mathbf{r}) + \varphi]\}$ in the Fourier plane since we are encoding Gaussian beams. The reference beam remains constant as $F_R(\mathbf{r}) = R_0$ since it is not affected by SLM. Therefore, the intensity captured at the camera is given by $I(\mathbf{r}) = |\cos(\chi)F_G(\mathbf{r}) + \sin(\chi)F_R(\mathbf{r})|^2$ where χ is the angle between polarizer P1 and the LCOS director axis. Thus

$$I(\mathbf{r}) = \cos^2(\chi)[M_G(\mathbf{r})]^2 + \sin^2(\chi)R_0^2 + 2\sin(\chi)\cos(\chi)M_G(\mathbf{r})R_0\cos\left[\frac{\theta(\mathbf{r}) + \varphi}{2}\right]. \quad (2)$$

Given the continuous phase modulation provided by the LCOS-SLM, it is simple to add a constant phase φ to the hologram. This way, the synchronous detection PSI technique [11] can be applied with an arbitrary number N of interferograms $I_n(\mathbf{r})$, each with a relative phase shift φ_n, $n = 0, 1, 2 \ldots N-1$.

If the phase steps are evenly distributed in the range $(0, 2\pi)$, the phase function can be retrieved as [11]:

$$\alpha(\mathbf{r}) = -\arctan\left\{\frac{\sum_{n=0}^{N-1} I_n(\mathbf{r})\sin(\varphi_n)}{\sum_{n=0}^{N-1} I_n(\mathbf{r})\cos(\varphi_n)}\right\}. \quad (3)$$

Well-established classical algorithms are the three-step algorithm, with phase-shifts $\varphi_0 = 0$, $\varphi_1 = \pi/2$ and $\varphi_2 = \pi$, leading to

$$\alpha_3(\mathbf{r}) = -\arctan\left\{\frac{I_2(\mathbf{r}) - I_1(\mathbf{r})}{I_1(\mathbf{r}) - I_0(\mathbf{r})}\right\}, \quad (4)$$

or the standard four-step algorithm, which adds a fourth phase shift $\varphi_3 = 3\pi/2$, leading to the classical relation

$$\alpha_4(\mathbf{r}) = -\arctan\left\{\frac{I_3(\mathbf{r}) - I_1(\mathbf{r})}{I_2(\mathbf{r}) - I_0(\mathbf{r})}\right\}. \quad (5)$$

RESULTS AND DISCUSSION

To illustrate the procedure, **Figure 3** shows a first set of experiments where we encode a Hermite-Gauss and a Laguerre-Gauss beam. **Figures 3A,B** show the HG_{33} characteristic intensity and phase patterns. The phase distribution is plotted only with the color code in the pixels where the intensity distribution is greater than 5% of the maximum intensity. The rest are plotted gray since they are not significant in comparison with the experimental results. **Figure 3C** shows the camera capture which shows the successful realization of the intensity distribution. For this experiment, the input polarizer (P1) was aligned with the LCOS director, so $\chi = 0$ in **Eq. 2** and $I(\mathbf{r}) = [M(\mathbf{r})]^2$.

To retrieve the phase distribution, we rotate P1 such that a significant portion of the input beam is not modulated. The interference pattern is shown in the second and third rows in **Figure 3**. We apply $N = 8$ different phase-shifts with a constant phase step of $\Delta\varphi = \pi/4$. In this case **Eq. 2** leads to the following relation for the measured phase:

$$\alpha_8(\mathbf{r}) = -\arctan\left\{\frac{2(I_0 - I_4) + \sqrt{2}(I_1 - I_3 - I_5 + I_7)}{2(I_2 - I_6) + \sqrt{2}(I_1 + I_3 - I_5 - I_7)}\right\}. \quad (6)$$

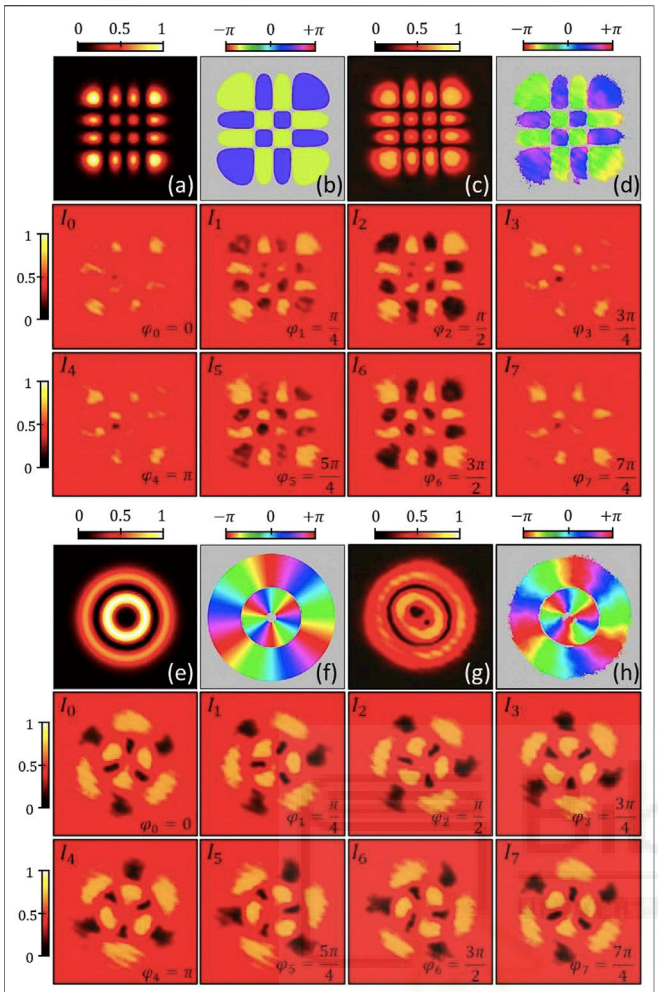

FIGURE 3 | Realization of a HG_{33} **(A–D)** and LG_{13} **(E–H)** beam. Theoretical intensity **(A,E)** and phase **(B,F)** distributions. Experimental intensity **(C,G)** and phase **(D,H)** distributions. The phase distribution of each beam is retrieved from the interferograms shown below each case with eight consecutive phase shifts of step $\Delta\varphi = \pi/4$.

The angle of the polarizer P1 was adjusted to achieve the best contrast before capturing all the sequence of interferograms. Interferograms I_2 and I_6 in **Figure 3**, corresponding to phase shifts $\varphi_2 = \pi/2$ and $\varphi_6 = 3\pi/2$, show the best contrast. On the contrary, the contrast is very low in interferograms I_0 and I_4, as expected from the binary π -phase pattern of this mode. The interferograms in **Figure 3** have been saturated for better visualization, but equivalent non-saturated images were used in the calculations.

We note that, since the hologram and the lens are both displayed on the SLM, the phase in the detector also includes a quadratic phase factor given by $-\phi_L = +\pi r^2/\lambda f$ [21]. The experimental phase shown in **Figure 3D** is the result given by **Eq. 6** where this quadratic phase has been subtracted, showing a very good agreement with the numerical phase. The phase is visualized again with the color code only at pixels where the intensity distribution in **Figure 3C** is significant, leaving the experimental phase image in gray at pixels where the intensity is too low to provide a contrasted interference.

Note that the PSI technique can only retrieve a wrapped phase map, here presented in the range $[-\pi, +\pi]$. The absolute determination of the phase would require the application of phase unwrapping techniques. Nevertheless, the color code used to display the phase (where red is used for values $\pm\pi$) avoids jumps caused by 2π discontinuities. To provide a quantitative comparison of the phase distributions, the experimental function was resized $\alpha_{exp}(\mathbf{r})$ to match the scale of the simulated distribution $\alpha_{sim}(\mathbf{r})$. Then, the phase *RMSE* (Root-Mean Square Error) was used as a metric, defined as:

$$RMSE = \sqrt{\frac{1}{T}\sum_{\mathbf{r}}\left(\alpha_{sim}(\mathbf{r}) - \alpha_{exp}(\mathbf{r})\right)^2}. \quad (7)$$

Here the summation is made only in the region with significant pixels and T is the total number of such pixels. For the HG_{33} beam the calculated phase *RSME* is 0.243π.

Figure 3 shows equivalent results for the LG_{13} beam. The theoretical intensity and phase distributions (**Figures 3E,F**) exhibit its characteristic double ring and spiral pattern. In this case, the experimental interferograms show three bright and three dark lobes inside each of the two intensity rings. The bright and dark lobes are opposite from one ring to the other, as corresponds to the π -phase shift between them, and they progressively rotate as phase-shifts are added in successive interferograms. The experimental distributions shown in **Figures 3G,H** agree very well the theory, with a phase *RMSE* of 0.287π.

We further tested different superpositions of LG beams. The first and second rows in **Figure 4** show their theoretical intensity and phase distributions. The third and fourth rows show the corresponding experiments. As in the previous figures, the phase distributions are plotted with the color code only where the intensity distribution is significant. All cases bear a very good agreement. Note for instance how the simplest case, the LG_{01} mode (**Figure 4A**) exhibits the classical doughnut shape and a spiral phase pattern. This case provides the best phase *RMSE* of only 0.154π.

The collinear superposition of LG beams has been performed by several ways. For instance, in [22] we demonstrated a system with two SLMs, each encoding one mode, which interfere after passing through a polarizer. Here, instead, we numerically calculate the superposition and display it in a single SLM, similar to what was done previously in [18]. In that work, the verification of the experimental phase was performed by simply regarding an interference pattern. Here, we apply the proposed common-path PSI technique to achieve a quantitative evaluation.

Figure 4B,C show respectively the superposition of the fundamental mode LG_{00} with the LG_{03} mode and with the LG_{06} mode. Here the LG_{00} mode provides light on axis despite the axial phase singularity of the LG_{03} or the LG_{06} modes. However, their interference exhibits intensity patterns with

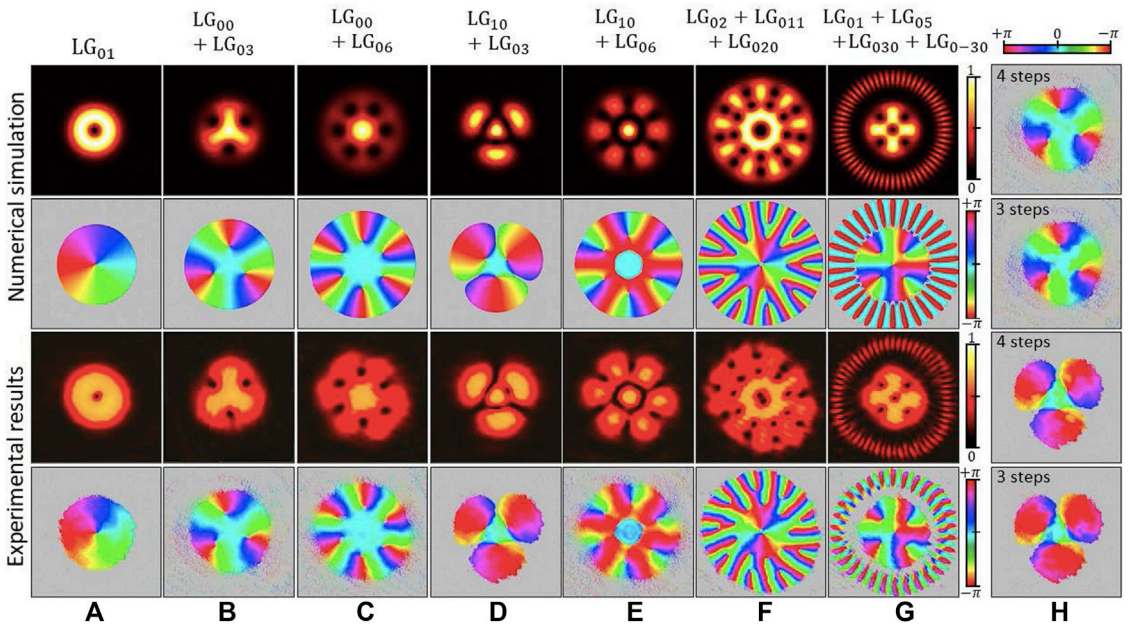

FIGURE 4 | Realization of different superpositions of LG modes: **(A)** LG_{01} **(B)** LG_{0-1} **(C)** $LG_{00} + LG_{06}$, **(D)** $LG_{10} + LG_{03}$, **(E)** $LG_{10} + LG_{06}$, **(F)** $LG_{02} + LG_{0,11} + LG_{0,20}$, **(G)** $LG_{01} + LG_{05} + LG_{0,30} + LG_{0,-30}$. First and second rows show numerical simulations of the intensity and phase distributions. Third and fourth rows show the corresponding experimental results. **(H)** Experimental phase distributions for the superpositions $LG_{00} + LG_{03}$ and $LG_{10} + LG_{03}$ (cases (B) and (D) respectively) when PSI with 4 and 3 steps are considered.

three and six dark spots respectively. The phase pattern presents a constant value in the center and a spiral distribution at the outer part. In between there are points where the phase completely twists around, which coincide with the dark spots in the intensity. The corresponding experimental results displayed in the last two rows corroborate these patterns.

Figure 4D,E present results of the superpositions $LG_{10} + LG_{03}$ and $LG_{10} + LG_{06}$ respectively. Here both intensity patterns show a bright spot in the center, caused by the LG_{10} mode. However, in contrast to the case in **Figure 4C**, the intensity has dark lines separating the central bright spot from the external lobes, with three outer spots in **Figures 4D** and six outer spots in **Figure 4E**. The phase patterns are again constant in the center and spirals in the outer region, but the region in between shows different distributions. The experiments again show a good agreement with the theory. In these results the Gouy phase difference on the propagation was compensated since it can cause a rotation of the patterns [23].

Figure 4F,G more sophisticated patterns obtained by the superposition of three and four different LG modes. **Figure 4F** illustrates the $LG_{02} + LG_{0,11} + LG_{0,20}$ superposition. Here, the three modes present a phase singularity on axis, thus creating a central dark spot. However, the higher the mode azimuthal order, the larger the radius of the ring of maximum intensity. As a result, the intensity pattern shows a central bright ring, while the outer part exhibits bright lobes separated by regions with two dark spots at two radial coordinates. The phase distribution shows a complicated pattern. However, singular points where the phase makes a complete cycle are clearly visible, which coincide with the dark spots in the intensity. Despite the higher increased complexity of this superposition, the experimental distributions show a good agreement with theoretical results.

Finally, **Figure 4G** shows the superposition of four modes, $LG_{01} + LG_{05} + LG_{0,30} + LG_{0,-30}$. All these modes present a singularity on axis and the center shows a dark spot. Near the center, four dark spots are yielded by the interference of the LG_{01} and LG_{05} modes. $LG_{0,30}$ and $LG_{0,-30}$ modes have such a large azimuthal order that their intensity is located far from the center, where they create an azimuthal interference ("petal beam"). Again, the experiments reproduce well the expected patterns. This case shows the fastest spatial variations in the phase distribution, especially in the binary pattern at the outer ring. Therefore, any slight shift of the experiment compared to the simulation yields a higher error compared to other cases, showing the highest *RMSE* phase value of 0.425π.

All the results presented so far were obtained by applying the PSI algorithm with eight phase steps described in **Eq. 6**. We have also tested the results with fewer interferograms. For instance, in **Figure 4H** we present the phase retrieved for two cases, $LG_{00} + LG_{03}$ (**Figure 4B**) and $LG_{10} + LG_{03}$ (**Figure 4D**), but now considering a PSI with four steps (**Eq. 5**) and with three steps (**Eq. 4**). They again agree quite well with numerical simulations. The *RSME* phase values for the $LG_{00} + LG_{03}$ case are 0.346π, 0.377π, and 0.380π for PSI with 8, 4, and 3 steps,

respectively. For the LG_{10} + LG_{03} case, *RSME* values are 0.412π, 0.443π, and 0.447π for 8, 4, and 3 steps, respectively. As expected, the *RSME* increases as less interferograms are used.

CONCLUSION

In summary, we have presented a PSI technique to evaluate the phase distribution of holograms displayed on a phase-only LCOS-SLM. Complex-valued Fourier transform holograms are encoded to generate different kinds of Gaussian beams. Results are given for intensity and phase retrieval of several cases.

The interferometric technique is based on a common-path polarization arrangement in which the LCOS SLM is used to simultaneously display the hologram and to apply the phase-shifting values required to retrieve the phase distribution. A simple rotation of a polarizer changes from a hologram configuration leading to the pure intensity recovery, to a common-path interferometric arrangement useful to measure the phase. Hence, the phase distribution of the beam can be recovered with no need of adding any extra-interferometer or wave-front measurement system.

Results show an excellent agreement with the theory, thus confirming the successful generation of structured light, not only in its intensity but also in its phase distribution, which probes the accuracy and advantage of the technique.

DATA AVAILABILITY STATEMENT

The raw data supporting the conclusions of this article will be made available by the authors, without undue reservation.

AUTHOR CONTRIBUTIONS

EN is a PhD student that did the optical experiments under the supervision of MS-L and IM. PG-M was a visitors professor at the University Miguel Hernandez of Elche that was collaborating in the experiment. PG-M, MS-L, and IM wrote the paper. All authors contributed to the article and approved the submitted version.

FUNDING

This work received financial support from Ministerio de Ciencia, Innovación y Universidades, Spain (grant RTI2018-097107-B-C33). EN acknowledges a grant from Generalitat Valenciana (ref. GRISOLIAP/2020/004).

REFERENCES

1. Rosales-Guzmán C, Ndagano B, Forbes A. A Review of Complex Vector Light fields and Their Applications. *J Opt* (2018) 20:123001. doi:10.1088/2040-8986/aaeb7d
2. Pachava S, Dharmavarapu R, Vijayakumar A, Jayakumar S, Manthalkar A, Dixit A, et al. Generation and Decomposition of Scalar and Vector Modes Carrying Orbital Angular Momentum: A Review. *Opt Eng* (2019) 59(4): 041205. doi:10.1117/1.OE.59.4.041205
3. Zhang Z, You Z, Chu D. Fundamentals of Phase-Only Liquid crystal on Silicon (LCOS) Devices. *Light Sci Appl* (2014) 3:213. doi:10.1038/lsa.2014.94
4. Davis JA, Cottrell DM, Campos J, Yzuel MJ, Moreno I. Encoding Amplitude Information onto Phase-Only Filters. *Appl Opt* (1999) 38(23):5004–13. doi:10.1364/ao.38.005004
5. Ando T, Ohtake Y, Matsumoto N, Inoue T, Fukuchi N. Mode Purities of Laguerre-Gaussian Beams Generated via Complex-Amplitude Modulation Using Phase-Only Spatial Light Modulators. *Opt Lett* (2009) 34(1):34–6. doi:10.1364/ol.34.000034
6. Clark TW, Offer RF, Franke-Arnold S, Arnold AS, Radwell N. Comparison of Beam Generation Techniques Using a Phase Only Spatial Light Modulator. *Opt Express* (2016) 24(6):6249–64. doi:10.1364/oe.24.006249
7. Arrizón V. Optimum on-Axis Computer-Generated Hologram Encoded into Low-Resolution Phase-Modulation Devices. *Opt Lett* (2003) 28(24):2521–3. doi:10.1364/OL.28.002521
8. Mendoza-Yero O, Mínguez-Vega G, Lancis J. Encoding Complex fields by Using a Phase-Only Optical Element. *Opt Lett* (2014) 39(7):1740–3. doi:10.1364/ol.39.001740
9. Davis JA, Wolfe ED, Moreno I, Cottrell DM. Encoding Complex Amplitude Information onto Phase-Only Diffractive Optical Elements Using Binary Phase Nyquist Gratings. *OSA Continuum* (2021) 4(3): 896–910. doi:10.1364/osac.418578
10. Bowman D, Harte TL, Chardonnet V, De Groot C, Denny SJ, Le Goc G, et al. High-Fidelity Phase and Amplitude Control of Phase-Only Computer Generated Holograms Using Conjugate Gradient Minimisation. *Opt Express* (2017) 25:11692–700. doi:10.1364/oe.25.011692
11. Creath K. V Phase-Measurement Interferometry Techniques. *Prog Opt* (1988) 26:349–93. doi:10.1016/s0079-6638(08)70178-1
12. Machuca-Bautista YB, Strojnik M, Flores JL, Serrano-García DI, García-Torales G. Michelson Interferometer for Phase Shifting Interferometry with a Liquid crystal Retarder. *Results Opt* (2021) 5:100197. doi:10.1016/j.rio.2021.100197
13. Ramírez C, Otón E, Iemmi C, Moreno I, Bennis N, Otón JM, et al. Point Diffraction Interferometer with a Liquid-Crystal Monopixel. *Opt Express* (2013) 21(7):8116–25. doi:10.1364/OE.21.008116
14. Haist T, Osten W. Holography Using Pixelated Spatial Light Modulators-Part 2: Applications. *J Micro/Nanolith. MEMS MOEMS* (2015) 14(4):041311. doi:10.1117/1.jmm.14.4.041311
15. He A, Quan C. Wavefront Correction for Spatial Nonuniformity of the Liquid Crystal on Silicon Based Spatial Light Modulator. *Opt Lasers Eng* (2019) 121: 377–88. doi:10.1016/j.optlaseng.2019.05.010
16. Martínez L, Fernández EJ, Prieto PM, Artal P. Interferometric Method for Phase Calibration in Liquid Crystal Spatial Light Modulator Using a Self-Generated Diffraction Grating. *Opt Express* (2016) 24(13):14159–71. doi:10.1364/OE.24.014159
17. Marco D, Vargas A, Sánchez-López Md. M, Moreno I. Measuring the Spatial Deformation of a Liquid-Crystal on Silicon Display with a Self-Interference Effect. *Opt Lett* (2020) 45(16):4480–3. doi:10.1364/ol.396105
18. Huang S, Miao Z, He C, Pang F, Li Y, Wang T. Composite Vortex Beams by Coaxial Superposition of Laguerre-Gaussian Beams. *Opt Lasers Eng* (2016) 78: 132–9. doi:10.1016/j.optlaseng.2015.10.008
19. Moreno I, Sánchez-López MDM, Davis JA, Cottrell DM. Simple Method to Evaluate the Pixel Crosstalk Caused by Fringing Field Effect in Liquid-Crystal Spatial Light Modulators. *J Eur Opt Soc.-Rapid Publ* (2021) 17:27. doi:10.1186/s41476-021-00174-7
20. Moreno I, Davis JA, Klein FA, Mitry MJ. Polarization-Splitting Common-Path Interferometer Based on a Zero-Twist Liquid Crystal Display. *Appl Opt* (2008) 47(11):1797–801. doi:10.1364/ao.47.001797

21. Goodman J. *Introduction to Fourier Optics*. 2nd ed.. New York: McGraw-Hill (1996).
22. García-Martínez P, Marco D, Martínez-Fuentes JL, Sánchez-López MM, Moreno I. Efficient on-Axis SLM Engineering of Optical Vector Modes. *Opt Lasers Eng* (2020) 125:105859. doi:10.1016/j.optlaseng.2019.105859
23. Sánchez-López MM, Davis JA, Moreno I, Cofré A, Cottrell DM. Gouy Phase Effects on Propagation of Pure and Hybrid Vector Beams. *Opt Express* (2019) 27(3):2374–86. doi:10.1364/OE.27.002374

Conflict of Interest: The authors declare that the research was conducted in the absence of any commercial or financial relationships that could be construed as a potential conflict of interest.

Publisher's Note: All claims expressed in this article are solely those of the authors and do not necessarily represent those of their affiliated organizations, or those of the publisher, the editors and the reviewers. Any product that may be evaluated in this article, or claim that may be made by its manufacturer, is not guaranteed or endorsed by the publisher.

Retrieving the phase of diffraction orders generated with tailored gratings

ESTHER NABADDA[1], MARÍA DEL MAR SÁNCHEZ-LÓPEZ[1,2], PASCUALA GARCÍA-MARTÍNEZ[3] AND IGNACIO MORENO[1,4,*]

[1]*Instituto de Bioingeniería, Universidad Miguel Hernández de Elche, 03202 Elche, Spain*
[2]*Departamento de Física Aplicada, Universidad Miguel Hernández de Elche, 03202 Elche, Spain*
[3]*Departamento de Óptica y Optometría y Ciencias de la Visión. Facultat de Física. Universitat de València, 46100 Burjassot, Spain*
[4]*Departamento de Ciencia de Materiales, Óptica y Tecnología Electrónica, Universidad Miguel Hernández de Elche, 03202 Elche, Spain*
**Corresponding author: i.moreno@umh.es*

Received XX Month XXXX; revised XX Month, XXXX; accepted XX Month XXXX; posted XX Month XXXX (Doc. ID XXXXX); published XX Month XXXX

A technique is performed to quantitatively evaluate the intensity and phase of the diffraction orders generated by tailored phase gratings displayed onto a liquid-crystal spatial light modulator (LC-SLM). The SLM displays the grating together with a lens to obtain the Fourier transform. The setup is converted into a polarization common-path interferometer by simply rotating a polarizer. This configuration allows applying a phase-shifting interferometry algorithm to retrieve the phase of the diffraction orders. The quadratic phase arising in the system, which must be subtracted, is calibrated using triplicator gratings of varying periods. Various tailored designs with controlled phase shift between diffraction orders are experimentally tested to prove the advantage and simplicity of the technique. © 2022 Optica

OCIS codes: *(050.0050) Diffraction and gratings; (050.5080) Phase shift; (070.6120) Spatial light modulators; (090.1995) Digital holography.*

http://dx.doi.org/10.1364/OL.99.099999

Diffraction gratings are classical optical elements traditionally used in spectroscopy. The development of optical lithography in the 70's changed their fabrication, offering highly precise control over very large scales, leading to other applications like laser tuning [1] and interferometers [2]. Binary-phase and multilevel gratings were developed in the 90's for laser beam splitting [3]. Later, gratings with continuous phase profiles were designed to produce orders with arbitrary intensity and phase [4]. However, the physical realization of such continuous phase profiles was complicated. They were later demonstrated using the continuous phase modulation provided by a liquid-crystal (LC) spatial light modulator (SLM) [5].

Although these design techniques allow a full control of the complex values at the diffraction orders, most of the research was devoted to control their intensities, and the interest in the phase content was limited to some applications in interferometry [6]. However, polarization diffraction gratings (PDG), gratings that produce diffraction orders with different polarizations, have nowadays become popular. They use continuous phase designs for two orthogonal polarizations, and they can be implemented with LC-SLMs [7], with geometric phase elements [8] or with metamaterials [9]. In all cases, the relative phase between diffraction orders is the key parameter to control the polarization. Therefore, a method for quantitatively measuring the complex-amplitude values of the diffraction orders is of great interest when evaluating the designs of such tailored gratings.

For this purpose, we apply a common-path self-interferometric arrangement of the LC-SLM recently demonstrated with structured light [10]. The system changes from a standard intensity configuration to an interferometer configuration simply by rotating a polarizer. The interferometer configuration implies an additional quadratic phase in the Fourier plane that must be compensated, especially if the observed field is large. Therefore, we here improve the previous system by implementing a calibration procedure based on the optimal triplicator grating design [11].

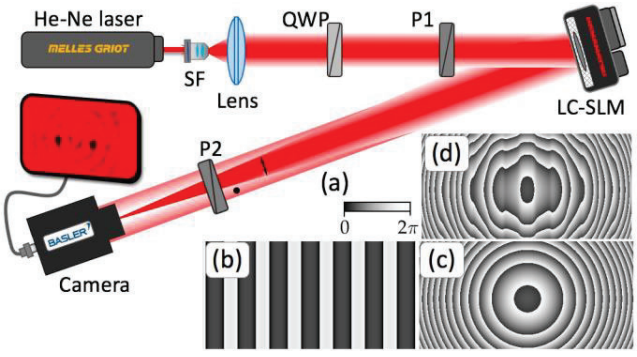

Fig. 1. (a) Scheme of the optical system. SF: spatial filter; QWP: quarter-wave plate; P: linear polarizer. Phase functions displayed on the LC-SLM: (b) Diffraction grating (c) Lens (d) Combined hologram.

Figure 1 shows the experimental setup. A linearly polarized He-Ne laser (Melles-Griot 05-LHP-991, with wavelength $\lambda = 633\ nm$) is spatially filtered and collimated. A quarter-wave plate (QWP) converts it into circularly polarized, so a first linear polarizer (P1) can be rotated without changing the input intensity. The beam illuminates a reflective parallel-aligned LC-SLM (Hamamatsu X10468-01, with 800×600 square pixels, $20\ \mu m$ pixel pitch and 98% fill factor). The reflected beam is directed to a camera detector (Basler scA1390-17fc, with 1390×1038 square pixels of $4.65\ \mu m$ size). A second polarizer (P2) oriented at 45º with respect to the LC director axis is placed in this reflection path.

The SLM displays a phase-only computer-generated hologram (CGH) $\phi_{CGH}(\mathbf{r}) = \phi_G + \phi_L$, $\mathbf{r} = (x, y)$, that combines a grating $g(\mathbf{r}) = \exp[i\phi_G(\mathbf{r})]$ and a converging lens $\phi_L(\mathbf{r}) = \pi r^2 / \lambda f$, where r is the radial coordinate and f is the encoded focal length. The input polarization component parallel to the LC-SLM director axis focuses at the plane located a distance f from the SLM and the field takes the form $G(\mathbf{u}) = \Im[g(\mathbf{r})]$, where $\Im[\cdot]$ denotes the Fourier transform (FT), and $\mathbf{u} = (u, v)$ are the horizontal/vertical spatial frequencies. The spatial coordinates $\mathbf{r}' = (x', y')$ at the Fourier plane are related as $\mathbf{u} = \mathbf{r}' / \lambda f$. Figures 1(b), 1(c) and 1(d) show an example of a grating, the lens and the CGH, where the phases are visualized as the gray levels addressed to the LC-SLM.

In the standard configuration, P1 is aligned parallel to the LC director axis and, consequently, the input beam is fully focused. However, by rotating P1, the system is transformed into a polarization common path interferometer [10]. The polarization component perpendicular to the SLM director axis is unaffected and remains collimated. The second polarizer (P2) makes the two components interfere. The collimated beam acts as the reference, while the focused beam is the test beam. A constant phase can be added to the displayed CGH in order to change the interference condition, thus allowing the application of PSI algorithms to retrieve the phase at the FT plane. Let us note that the employed SLM is free of flicker. Nevertheless, if this were not the case, the related phase fluctuation would yield an additional DC component in the displayed hologram. Since it would not be focused, it would simply add to the background, slightly reducing the interference contrast.

However, since the grating and the lens are both located in the same plane, the optical FT is not exact [12,13] and there is an additional quadratic phase $\phi_Q(r') = -\pi r'^2 / \lambda f$, r' being the radial coordinate at the FT plane. This phase cannot be ignored, especially for measurements far away from the center. In our previous work [10], this phase was simply compensated on the basis of the f value encoded on the CGH. Here, this is quantitatively verified using the optimum phase triplicator grating [11], an analytical design defined by the continuous phase profile:

$$\phi_G(x) = \arctan[a\cos(2\pi x / p)], \qquad (1)$$

where $a = 2.65718\ldots$ and p is the grating period. This grating generates three equally intense zero and ±1 diffraction orders, with a total efficiency that exceeds $\eta = 93\%$. In [14] it was demonstrated that the ±1 orders have a phase shift $\phi_{\pm 1} = \pi / 2$ relative to the zero order. Therefore, the triplicator transmission can be written as

$$g(x) = \exp[i\phi_G(x)] \cong c_0(1 + ie^{+i2\pi x/p} + ie^{-i2\pi x/p}), \qquad (2)$$

with $c_0 \cong \sqrt{0.31}$. Its Fourier transform takes the form

$$G(u) = \Im[g(x)] = c_0[\delta(u) + i\delta(u - u_0) + i\delta(u + u_0)], \qquad (3)$$

with $u_0 = 1/p$. Figure 2 shows experimental results when the SLM displays CGHs with an encoded triplicator of periods $p = n\Delta$, where $\Delta = 20\ \mu m$ (the SLM pixel pitch). We use images of 1024×1024 pixels to calculate the holograms and crop the central 800×600 area to display them on the SLM. Here $n = 1024 / T$ is the period expressed in pixels (px) and we use parameter T to describe the spatial frequency of the gratings. Figure 2 shows results for $T = 8$ and $T = 24$, corresponding to periods of $n = 128\ px$ and $n \simeq 42.7\ px$ respectively. Such large periods ensure that the gratings are not affected by phase quantization. Also, a large focal length $f = 1500\ mm$ is selected to avoid aliasing in the lens function.

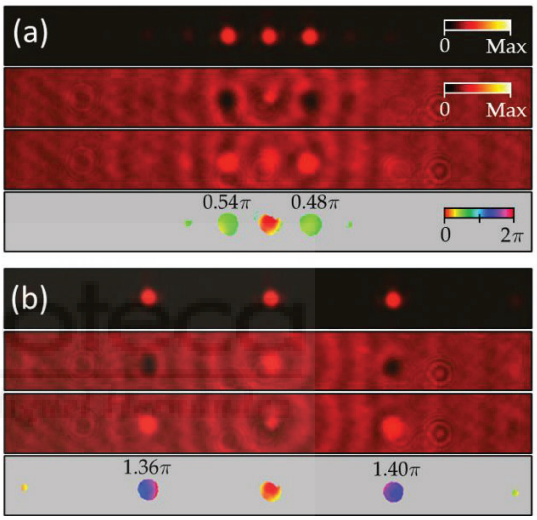

Fig. 2. Intensity (first row), two interferograms with a relative π phase shift (second and third rows) and measured phase (fourth row) for triplicator gratings with different frequency: (a) $T = 8$, (b) $T = 24$.

Each case in Fig. 2 shows four images. The top one is the intensity captured in the standard configuration achieved when P1 is aligned with the SLM director axis. These images verify the generation of three equally intense diffraction orders, with a separation that increases with T. The second and third rows show two interferograms obtained when P1 is rotated. Now the camera shows a background due to the unfocused beam, and the interference is observed at the location of the diffraction orders. Before applying the PSI algorithm, two adjustments are necessary: 1) a constant phase is added to the CGH to put the reference beam in phase with the diffracted field, and 2) P1 is rotated to match the amplitudes of the reference and the diffracted beam, to get a high contrast. The two interferograms shown in each case in Fig. 2 are obtained by adjusting the constant phase to provide destructive and constructive interference in the ±1 orders respectively, as viewed in the corresponding dark and bright spots.

By applying additional constant phase steps, the phase difference between orders can be retrieved using classical PSI algorithms [10]. The result is displayed on the fourth row in each case, where a color code enables to distinguish these phases from the CGHs. The

experimentally measured phases are presented in the range $[0, 2\pi)$ and only on the pixels where the intensity is significative, with values over 5% of the maximum. The phase indicated on each order is the average value over the significative pixels, relative to the phase of the zero order, which is taken as the reference. These averaged values show a standard deviation below 0.03π in most of the measured diffraction orders. According to [14], the phase between the zero order and the ±1 orders must be $\pi/2$. However, the interference condition shown in the interferograms in Fig. 2 is observed to change with T, thus denoting an extra phase. Namely, the quadratic phase caused by the non-perfect FT configuration.

The procedure was repeated for different T values, and for triplicators diffracting in vertical direction and the difference with respect the theoretical value $\pi/2$ was calculated. The graph in Fig. 3 shows the result as a function of the radial coordinate, expressed in pixels of the camera, where the phase function was unwrapped. The curve matches the expected quadratic profile with a correlation coefficient of $R^2 = 0.9987$. The inset shows $\phi_Q(\mathbf{r}')$ on the complete area of the camera, reaching around 20π at the corners. Figure 3(b) shows the intensity when a horizontal and a vertical triplicators are combined, thus yielding nine equally intense diffraction orders. However, their phase content is different, as shown in the interferogram in Fig. 3(c). While the ±1 orders along horizontal and vertical directions are $\pi/2$ phase-shifted with respect to the central order, the four diagonal orders are π phase-shifted, a situation that was indirectly verified in [14] with a geometric phase grating regarding the polarization changes. Here, the experimental phase (Fig. 3(d)) retrieved from PSI (after compensating the quadratic phase) provides a direct measurement that agrees very well with the expected result.

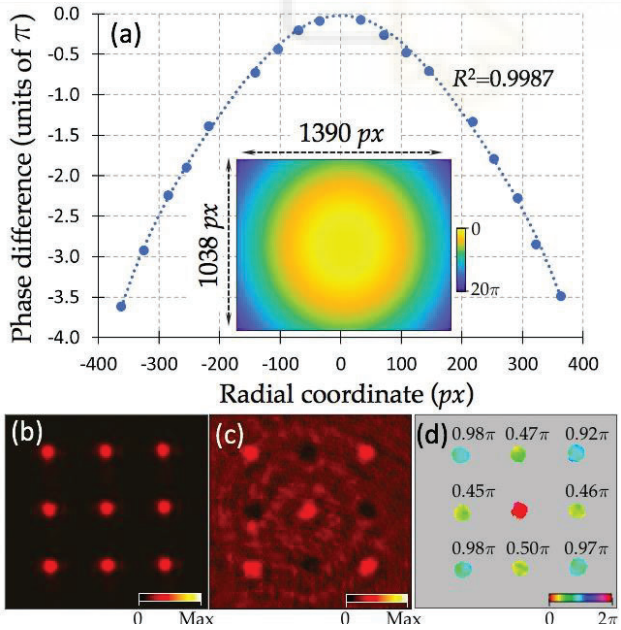

Fig. 3. (a) Experimental quadratic phase profile measured at the FT plane. The inset shows its values at the complete area of the camera array. Nine diffraction orders generated by two crossed triplicators with $T = 12$: (b) intensity, (c) interferogram and (d) phase.

Once the quadratic phase is determined, the procedure can be applied to other gratings. As a first example the detour phase caused by a lateral shifting of the grating is visualized. If the grating $g(x)$ is displaced with respect to the lens by Λp, the FT is transformed to $\Im\{g(x-\Lambda p)\} = G(u)\exp(i2\pi u\Lambda p)$. This additional linear phase changes the phase of the triplicator ±1 orders $(u = \pm 1/p)$, so their phases relative to the zero order become $\phi_{\pm 1} = (\pi/2) \pm 2\pi\Lambda$.

Figure 4 shows the results for gratings with $T = 16$. Figure 4(a) illustrates the CGH functions when the triplicator grating already presented in Fig. 1(d) is displaced by $\Lambda = 1/4$, $\Lambda = 1/2$ and $\Lambda = 3/4$. The intensity distribution (Fig. 4(b)) does not change with Λ. However, the measured phases do change. Figure 4(c) shows the result for the centered grating $(\Lambda = 0)$, where values very close to those expected $\phi_{\pm 1} = \pi/2$ are retrieved. For $\Lambda = 1/4$, phases should change to $\phi_{+1} = \pi$ and $\phi_{-1} = 0$. The experimental values confirm this result, where now the -1 order is in phase with the zero order. On the contrary, for a half-period displacement $(\Lambda = 1/2)$ there is an additional $\pm\pi$ phase-shift at the ±1 orders, thus $\phi_{\pm 1} = 3\pi/2$. Finally, for $\Lambda = 3/4$, the situation is inverted with respect to $\Lambda = 1/4$. In all cases, the measured phases agree well with the expected values.

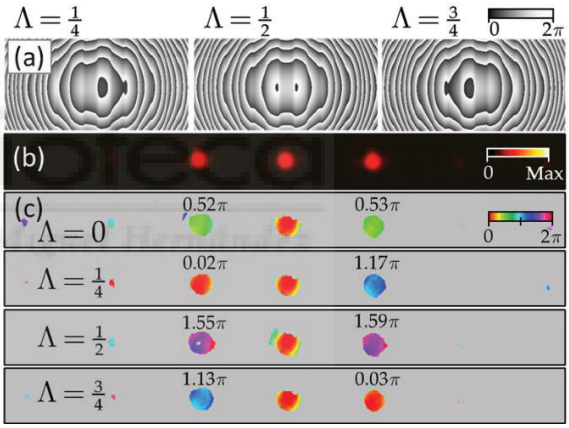

Fig. 4. (a) CGH displayed onto the SLM for triplicator gratings with $T = 16$ and lateral displacements $\Lambda = 0$, $\Lambda = 1/4$, $\Lambda = 1/2$ and $\Lambda = 3/4$. Experimental distributions (b) intensity, and (c) phase.

Finally, two continuous phase gratings are designed to provide a relative intensity and phase shift between orders. The design follows the procedure described in [5] based on the theory of optimum laser beam-splitting gratings [4]. This procedure consists of determining a continuous phase function $\varphi(x)$ that generates a desired pattern of diffraction orders, whose complex amplitude is defined by the Fourier series coefficient:

$$c_k = \sqrt{i_k}\exp(i\beta_k) = \frac{1}{2\pi}\int_{-\pi}^{+\pi}\exp[i\varphi(x)]\exp(-ikx)dx, \qquad (4)$$

k denoting each of the target orders. The design procedure consists in selecting the N desired target orders and defining the desired relative (i_k, β_k) values. Then a function $s(x)$ is defined as

$$s(x) = \sum_{k\in N}\mu_k\exp(i\alpha_k)\exp(i2\pi kx/p), \qquad (5)$$

where (μ_k, α_k) are numerical values of the amplitude and phase of each harmonic component of $s(x)$. These values are determined such that the phase-only function $\exp[i\varphi(x)] = s(x)/|s(x)|$ fulfills the conditions imposed on (i_k, β_k) with the highest possible diffraction efficiency η, defined as the ratio between the sum of intensities at the target diffraction orders relative to the total intensity. More details about can be found in [4,5].

We designed two gratings: Grating 1 is asymmetric with three target orders $k = +2$ and $k = \pm 1$, with intensities $i_{+2} = 2i_{+1} = 2i_{-1}$ and phase shifts $\pi/2$ and π of the second and negative first orders with respect to the first order. Grating 2 has target orders $k = \pm 3$ and $k = \pm 1$, all with the same intensity, and where orders $+3$ and -1 are in phase with the first order, while order -3 has a π phase-shift. Table 1 gives the numerical values of the imposed restrictions relative to the first order, the (μ_k, α_k) parameters and the nominal efficiency. Figure 5(a) shows one period of the continuous phase profiles $\varphi(x)$ for these gratings.

Table 1. Parameters of tailored gratings

GRATING 1			$\eta = 85.3\%$
Target orders	$k = -1$	$k = +1$	$k = +2$
i_k / i_{+1}	1	1	2
$\beta_k - \beta_{+1}$	π	0	$\pi/2$
μ_k	0.9633	0.8189	1.2160
α_k	5.4613	2.3491	3.8993

GRATING 2				$\eta = 86.4\%$
Target orders	$k = -3$	$k = -1$	$k = +1$	$k = +3$
i_k / i_{+1}	1	1	1	1
$\beta_k - \beta_{+1}$	π	0	0	0
μ_k	1.5705	3.4063	5.1173	4.5725
α_k	4.8551	1.7143	1.7136	1.7141

Figure 5 shows the results of Grating 1 and Grating 2. For the first design we also display the complex-conjugated version (Grating 1CC). The intensity and phase of the diffraction orders were measured for gratings with $T = 16$. They show the generation of the target diffraction orders with the desired restrictions. For instance, Grating 1 shows a second order more intense that two equally intense ±1 orders (a weak zero order is also visible). The phase values are presented relative to the first order for Grating 1 and 2 and also bear a very good agreement with the design values. Figure 5(c) shows the result for Grating 1CC which shows the reversed intensity pattern and opposite phases as that in Fig. 5(b). In this case the phase is presented relative to the minus first order.

In summary, we applied a simple experimental technique to experimentally retrieve the phase of diffraction orders generated with tailored diffraction gratings. The technique is based on a self-interferometer configuration of a LC-SLM, where the display is used simultaneously to implement the grating, a lens, and the phase-shift bias required in PSI algorithms. The experimental results confirm the designs and proves the usefulness of the technique to test tailored diffraction gratings before their fabrication with other advanced methods. This can be of particular interest in geometric-phase gratings, where the phase-shift between orders is of great relevance for their polarization-diffraction properties.

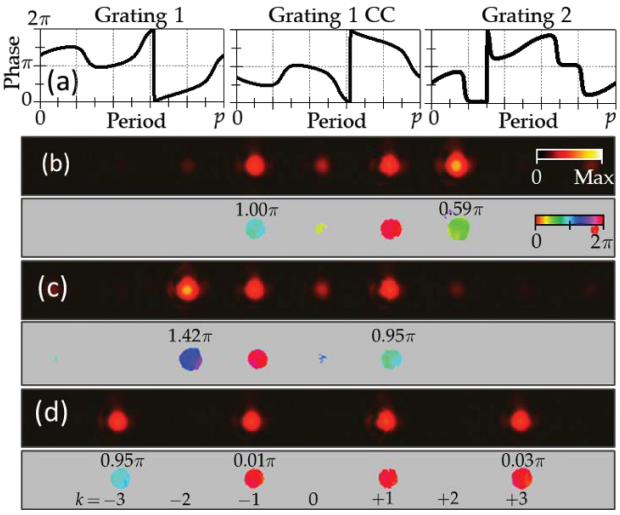

Fig. 5. (a) Phase profiles for three grating designs. (b) Experimental intensity and phase for: (b) Grating 1. (c) Grating 1CC. (d) Grating 2.

Funding. This work received financial support from Ministerio de Ciencia e Innovación, Spain (ref.: PID2021-126509OB-C22) and Generalitat Valenciana (ref. CIAICO/2021/276). EN acknowledges a grant from Generalitat Valenciana (ref. GRISOLIAP/2020/004).

Disclosures. The authors declare no conflicts of interest.

Data availability. Data underlying the results presented in this paper are not publicly available at this time but may be obtained from the authors upon reasonable request.

References

1. N. Bonod and J. Neauport, Adv. Opt. Photon. **8**, 156 (2016).
2. F. Cheng and K. Fan, Appl. Opt. **50**, 4550 (2011).
3. J. N. Mait, J. Opt. Soc. Am. A **7**, 1514 (1990).
4. L. A. Romero and F. M. Dickey, Prog. Optics **54**, 319 (2010).
5. J. Albero, J. A. Davis, D. M. Cottrel, C. E. Granger, K. R. McCormick and I. Moreno, Appl. Opt. **52**, 3637 (2013).
6. C. M. B. Cordeiro, L. Cescato, A. A. Freschi and L. Li, Opt. Lett. **28**, 683 (2003).
7. J. A. Davis, I. Moreno, M. M. Sánchez-López, K. Badham, J. Albero and D. M. Cottrell, Opt. Express **24**, 907 (2016).
8. J. Kim, Y. Li, M. N. Miskiewicz, C. Oh, M. W. Kudenov and M. J. Escuti, Optica **2**, 958 (2015).
9. N. Rubin, A. Zaidi, M. Juhl, R. P. Li, J. P. B. Mueller, R. C. Devlin, K. Leósson and F. Capasso, Opt. Express **26**, 21455 (2018).
10. E. Nabadda, P. García-Martínez, M. M. Sánchez-López and I. Moreno, Front. Phys. **10**, 920111 (2022).
11. F. Gori, M. Santarsiero, S. Vicalvi, R. Borghi, G. Cincotti, E. Di Fabrizio, M. Gentili, Opt. Commun. **157**, 13 (1998).
12. J. W. Goodman, *Introduction to Fourier optics*, 3rd edt. Robert & Company Publishers (2004).
13. I. Moreno, M. M. Sánchez-López, C. Ferreira, J. A. Davis and F. Mateos, Eur. J. Phys. **26**, 261-271 (2005).
14. D. Marco, M. M. Sánchez-López, A. Cofré, A. Vargas and I. Moreno, Opt. Express **27**, 14472 (2019).

J. Eur. Opt. Society-Rapid Publ. 2024, **20**, 5

https://doi.org/10.1051/jeos/2024003
Available online at: https://jeos.edpsciences.org

Journal of the European Optical Society-Rapid Publications

EOSAM 2023
Guest editors: Patricia Segonds, Guy Millot and Bertrand Kibler

RESEARCH ARTICLE

OPEN ACCESS

Mueller matrix imaging polarimeter with polarization camera self-calibration applied to structured light components

Esther Nabadda[1], María del Mar Sánchez-López[1,2,*], Asticio Vargas[3], Angel Lizana[4], Juan Campos[4], and Ignacio Moreno[1,5]

[1] Instituto de Bioingeniería, Universidad Miguel Hernández de Elche, 03202 Elche, Spain
[2] Departamento de Física Aplicada, Universidad Miguel Hernández de Elche, 03202 Elche, Spain
[3] Departamento de Ciencias Físicas, Universidad de La Frontera, Temuco, Chile
[4] Departament de Física, Universitat Autònoma de Barcelona, 08193 Bellaterra, Barcelona, Spain
[5] Departamento de Ciencia de Materiales, Óptica y Tecnología Electrónica, Universidad Miguel Hernández de Elche, 03202 Elche, Spain

Received 8 August 2023 / Accepted 25 January 2024

Abstract. This work presents a complete Mueller matrix imaging polarimeter that uses three liquid-crystal retarders and a pixelated polarization camera. The polarimeter is characterized and optimized with a standard correction procedure here adapted to be performed fully in-situ, without any additional element, based on considering the polarization camera as the reference. The accuracy limit caused by the extinction ratio in the camera micro-polarizers is analyzed. Finally, the imaging polarimeter is tested experimentally by analyzing well-known samples for structured light applications such as patterned retarders, a patterned polarizer, and a liquid-crystal depolarizer. The work is presented in a tutorial style useful to reproduce the procedure by non-experts in polarimetry.

Keywords: Polarimetry, Liquid-Crystals Retarders, Structured Light, Polarization Camera.

1 Introduction

Among the different properties of light, polarization has been demonstrated to provide extremely useful information [1]. This is becoming especially relevant in bioimaging, where several techniques harnessing biological and clinical research are based on the vectorial properties of light [2, 3]. In the last decades, important technological advances related to the generation and measurement of polarized light have been produced, that provide tools and devices like liquid-crystal variable retarders, spatial light modulators (SLM) or polarization cameras that have become common in optics laboratories, leading to the development of precise imaging polarimeters [4, 5].

Another field developed in parallel is the generation and detection of structured light. This denomination was introduced to describe light beams with a spatial and temporal control of their amplitude, phase and state of polarization [6]. Light beams with non-uniform polarization, known as vector beams, are prompting important advances in areas such as microscopy, materials processing, metrology, or optical communications [7, 8]. Structured light is typically produced with patterned polarization elements [9, 10]. SLM devices show the advantage of being reconfigurable, although requiring bulk optical systems [11, 12]. Alternatively, flat patterned polarization components can be fabricated with metamaterials [13] or with liquid-crystal (LC) geometric-phase elements [14, 15]. Patterned polarizers with arbitrary spatial distributions of the transmission axis are of great interest especially for developing micro-polarizers in polarization cameras [16].

Research in patterned polarization elements and research in polarimetric imaging are closely related [17]. While patterned polarization elements are providing new tools for advanced polarization imaging [18, 19], polarimetric imaging relying on the Mueller matrix has proven very worthy to evaluate the quality of the fabricated components [20, 21]. Although Mueller matrix imaging polarimetry has been employed for almost three decades [22], it is a technique in constant evolution, where multiple variants have been introduced over the years [23, 24]. In this context, this work presents the realization of a complete Mueller matrix (MM) imaging polarimeter whose performance is tested on polarization elements commonly applied to generate structured light. This polarimeter is based on our previous system [21], but here we provide the following

* Corresponding author: mar.sanchez@umh.es

improvements: (1) the use of a multiwavelength LED light source to avoid interference and speckle noise, (2) the realization of a setup on a rotatable breadboard to easily change the polarimeter from a transmission to a back-reflection configuration, (3) the use of spectrally calibrated liquid-crystal retarders (LCR), both in the polarization state generator (PSG) and in the polarization state analyzer (PSA), and (4) the application of a well-stablished sequential polarimeter calibration and optimization method [25], here adapted to consider the polarization camera as the reference for polarization measurements (self-calibration). This way, the method can be applied without any additional elements simply by properly tuning the LCR devices in the system. These improvements allow us to present a multifunctional complete MM imaging polarimeter that can be applied to a variety of samples.

The paper is organized as follows: after this introduction, Section 2 describes the polarimeter components. Then, Section 3 presents the calibration steps required to correctly operate the system, including the correct tuning of the LCR devices and the calibration and compensation procedure of the PSG and the PSA systems. Finally, in Section 4 we discuss the results obtained to evaluate different elements used in structured light like spatially patterned retarders and polarizers, and a liquid-crystal depolarizer.

2 Description of the imaging polarimeter

The developed imaging polarimeter system is shown in Figure 1. As mentioned, it represents an upgraded version of our previous system [21] with larger potential for sample imaging and quality control applications. The light source is a multiwavelength RGB LED (Thorlabs LED4D067) with controllable intensity level. A light guide (Thorlabs LLG05-4H) directs the light to the polarimeter entrance. A 50 mm photographic objective lens is used to image the lightguide output onto the sample. A diffuser (Edmund Holo 30 deg) is added to improve the intensity uniformity on the sample plane. The PSG is composed by a vertically oriented linear polarizer, and two liquid-crystal variable retarders (LCR1 and LCR2) from ARCOptix. LCR1 is oriented at 45° while LCR2 is oriented vertically, such that upon adjusting their retardances, an arbitrary fully-polarized state of polarization (SOP) can be generated.

The polarized light illuminates the sample and after light-matter interaction the output is analyzed with a PSA. A circular iris diaphragm of variable diameter is placed just in front of the sample plane and kept in the calibration procedure. The PSA is an imaging detector that comprises a polarization camera and another variable retarder (LCR3), also from ARCOptix. The sample and the PSA are positioned on a rotating breadboard (Thorlabs RBB300A/M), so the detection system can be rotated an angle θ, changing from a transmission configuration (Fig. 1e) to a reflection configuration (Fig. 1f). The transmission configuration is used in the calibration process, and it is useful for analyzing highly transparent samples. The reflection configuration is suitable for samples with high scattering and for reflective devices.

The polarization camera (Thorlabs CS505MUP Kiralux) is a monochrome sensor with 12 bit resolution (4096 intensity digital levels) and with 2448 × 2048 square pixels of 3.45 μm side. The sensor includes an integrated micro-polarizer array attached to the pixel detectors. Thus, images for horizontal (H), vertical (V), diagonal (D) and antidiagonal (A) linear analyzers can be captured in a single shot (Fig. 1c). An objective macro zoom lens (Computar MLH 10X) is attached to the polarization camera; thus, the sample can be imaged with relatively large magnification at distances around 20 cm. If larger magnification is required, an extension tube is added.

The three RGB LEDs of the light source have central wavelengths at 660 nm (red light), 565 nm (green light) and 470 nm (blue light) respectively. Figure 1d shows the spectra of the three LEDs, measured with a spectrometer (Stellar-Net, STN-BLK-C-SR) in the spectral range from 400 to 700 nm, with 2 nm resolution). A spectral filter (SF) filters each of these LED spectra, resulting in filtered spectra with full width at half maximum (FWHM) of about 10 nm, as the measured narrow RGB bands shown in Figure 1d. The SF is useful to reduce depolarization values that might have been artificially added to the final measurements due to the LCRs wavelength retardance dependence.

3 Calibration procedure

This section presents the calibration procedures required to accurately operate the MM imaging polarimeter. First, we review the method for calibrating the LCR devices. Then, the following subsection describes the calibration and optimization of the polarimeter.

3.1 Calibration of the LCR devices

The first step to properly operate the polarimeter is to calibrate the retardance of the LCR devices that will be used to provide the required SOPs, both in the PSG and in the PSA. For that purpose, we follow a simple yet accurate enough procedure that consists in placing the LCR device between crossed/parallel polarizers, oriented at 45° with respect to the LC director axis [26, 27]. The normalized transmission for crossed polarizers is given by

$$T_{\perp}(\lambda,\ V) = \cos^2\left[\frac{1}{2}\varphi(\lambda,\ V)\right], \tag{1}$$

where the LC retardance $\varphi(\lambda,\ V) = (2\pi/\lambda)\cdot\Delta n\cdot t$ depends on the thickness of the LC layer (t), $\Delta n(V)$ is the voltage-dependent birefringence, λ is the wavelength and V is the applied voltage. This relation shows the expected oscillatory behavior of $T_{\perp}\ (\lambda,\ V)$ both as a function of λ and V.

We measured the LCRs retardance versus the applied voltage for the three wavelength bands. As an example, Figure 2 shows the results obtained for LCR1. Figure 2a illustrates the normalized transmission curves $T_{\perp}\ (V)$ for the three wavelength bands centered at λ_R = 660 nm,

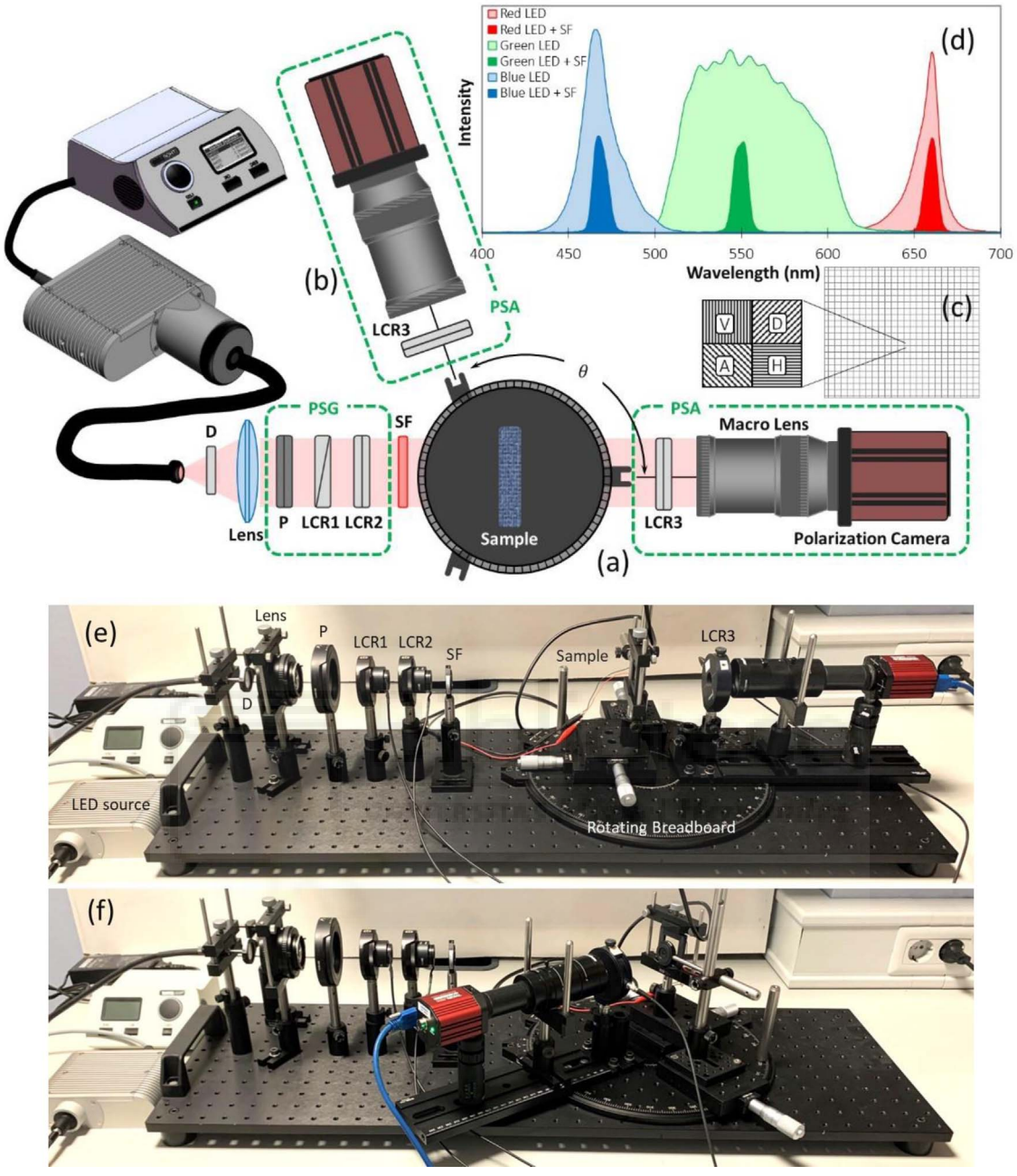

Fig. 1. Scheme of the Mueller matrix imaging polarimeter. D: diffuser. SF: Spectral filter. P: linear polarizer. LCR: liquid-crystal retarders. (a) Transmission geometry. (b) Reflection geometry. (c) Scheme of the micro-polarizers pattern on a macro-pixel of the polarization camera. (d) Spectra of the three LED sources with central wavelengths of 470 nm, 565 nm and 660 nm, and after being filtered by the corresponding spectral filter (SF). Pictures of the system in (e) the transmission configuration and (f) the reflection configuration.

λ_G = 565 nm and λ_B = 470 nm. The curves feature the typical oscillatory behavior, with more oscillations for the shortest blue wavelength. Figure 2b shows the retrieved retardance function $\varphi(V)$ for the three wavelengths. For the longer wavelength λ_R = 660 nm the retardance variation is slightly greater than 2π, while it almost reaches 3π and 3.5π for the green and blue bands respectively.

3.2 Calibration of the PSG

We operate the polarimeter to generate and detect the well-known polarimetric basis consisting of six standard SOP: namely horizontal (H), vertical (V), diagonal (D) and antidiagonal (A) linear states, and right (R) and left (L) circular states. These six SOP define an octahedron in the

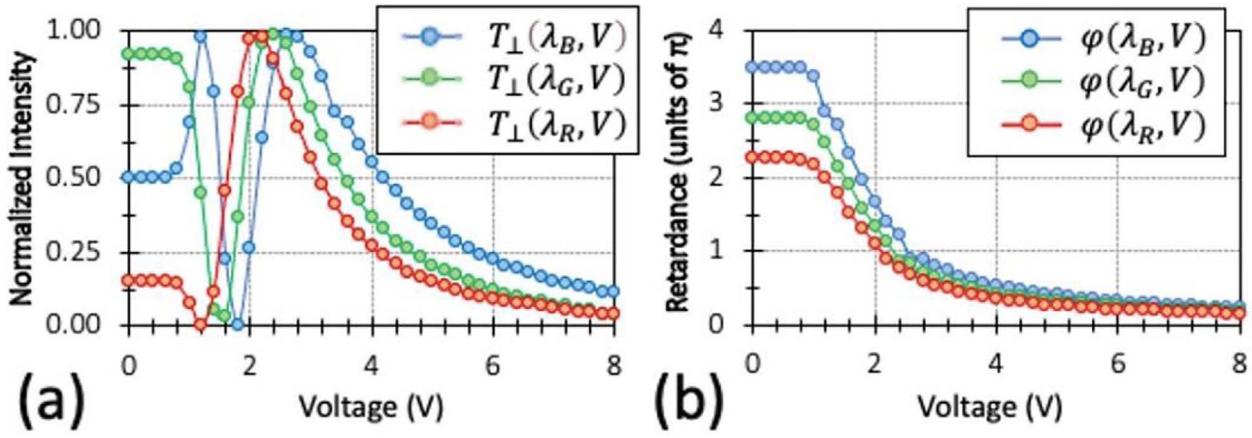

Fig. 2. Example of calibration of an LCR device in the MM imaging polarimeter. (a) Transmission $T_\perp(V)$ between crossed polarizers oriented at 45° with respect to the LC director. (b) LCR retardance $\varphi(V)$. Both graphs show the results for the three bands, with central wavelengths 470 nm (B), 565 nm (G) and 660 nm (R).

Table 1. Retardances required on LCR1 and LCR2 to provide SOP in the PSG.

SOP generated with PSG	H	V	D	A	R	L
LCR1 Retardance	HW	FW	QW	QW	QW	3QW
LCR2 Retardance	FW	FW	QW	3QW	FW	FW

QW: quarter-wave; HW: half-wave; 3QW: three quarter-wave; FW: full-wave.

Poincaré sphere and provide the polarimeter ideal conditional number (CN = 1.732) [25], thus ensuring an optimal performance in terms of noise amplification minimization from intensity measurements to polarimetric measurements. The LCR calibration provides the required voltages; typically, the quarter-wave retardance, the half-wave retardance or the full-wave retardance. Considering that the PSG polarizer (P) is oriented vertically, LCR1 is at 45° and LCR2 is vertical, Table 1 provides the retardances required to achieve the input SOPs.

However, variable LCRs feature effects that might introduce inaccuracy in the polarimeter, being the most relevant the non-uniform retardance on the clear aperture [26], the retardance temperature dependance, and multiple reflection interference effects that cause intensity variations coupled to the retardance modulation [28]. These effects must be compensated to achieve accurate polarimetric values. Among the different methods [29–31], here we propose and apply a modification of a well-stablished sequential calibration and optimization method [32, 33]. In the typical procedure, a calibrated polarimeter serves as the reference to measure the SOP of the PSG states, and the results are compared to those measured with the developed polarimeter. Here the technique is adapted to consider the polarization camera as the reference. This way, a self-reference procedure is applied that does not require any additional external element. Of course, the accuracy of this self-calibration depends on the quality of the micro-polarizers in the polarization camera. To this goal Appendix A includes an analysis of the limits of this procedure considering the extinction ratio of the micro-polarizers in the camera. We measured extinction ratios over 120:1. Although other sources of error have been identified [34] (such as spatial variations of the extinction ratio or misalignments in the orientation of the micro-polarizers), here we assume this simplified model with a limited but uniform extinction ratio. According to the approach described in the Appendix, the self-calibration procedure leads to an error in the measured MM elements below 1.7%.

Figure 3 shows the intensity captured for the circular iris diaphragm under red light illumination. The polarization camera provides a four-quadrant image where quadrants i, ii, iii and iv correspond to the detection of the V, D, A and H linear states. The input intensity is adjusted to ensure the non-saturation of the camera and it is maintained in the sample characterization. Each picture in Figure 3 corresponds to one of the six standard input SOP generated with the PSG (H, V, D, A, R, L). In each case, the voltage values derived from the LCR1 and LCR2 calibrations are taken as the starting point, but a fine adjustment must be then performed to provide images like those in Figure 3. The successful generation of the linear states H, V, A and D is verified when the following conditions are simultaneously fulfilled: the image quadrant of the orthogonal detector becomes the darkest, the image quadrant corresponding to the given input state is the brightest, and the other two quadrants feature the same intensity. On the contrary, the generation of the circular R and L states is verified when the four quadrants appear with equal weight. The information provided by the LCR calibration in Figure 2 allows differentiating

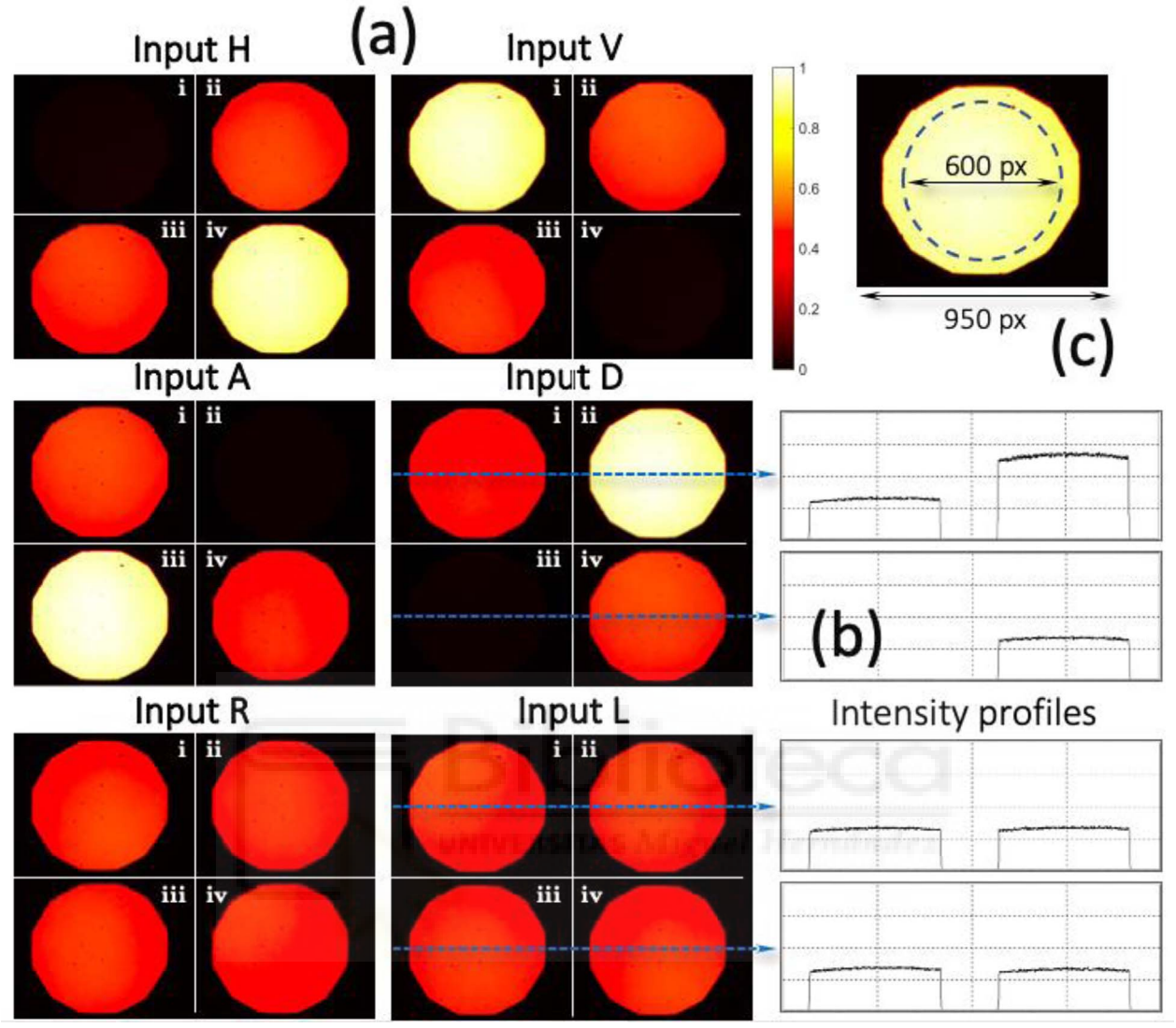

Fig. 3. (a) Calibration of the PSG system: experimental four-quadrant images captured by the polarization camera under the red channel illumination for input SOPs as linear horizontal (H), vertical (V), antidiagonal (A), diagonal (D), circular left (R) and circular right (L). (b) The intensity profiles for inputs D and L. (c) Calculations of average values are performed in the central circle with diameter of 600 pixels.

R and L states. On the right, the intensity profiles of the four quadrants for inputs D and L are shown.

The polarization camera is an incomplete polarimeter, since only the linear polarization components are measured. The first three Stokes parameters S_0, S_1, S_2 can be retrieved from the intensity images $I_i(x,\ y)$, $I_{ii}(x,\ y)$, $I_{iii}(x,\ y)$, and $I_{iv}(x,\ y)$ captured in quadrants *i*, *ii*, *iii*, and *iv* as

$$S_0(x,y) = \frac{1}{2}[I_i(x,y) + I_{ii}(x,y) + I_{iii}(x,y) + I_{iv}(x,y)], \quad (2a)$$

$$S_1(x,y) = I_{iv}(x,y) - I_i(x,y), \quad (2b)$$

$$S_2(x,y) = I_{ii}(x,y) - I_{iii}(x,y). \quad (2c)$$

To retrieve S_3, a quarter-wave plate must be placed in front of the polarization camera, to measure the circular polarization components. However, since LCR2 is oriented vertical, a quarter-wave retardance can be added to this retarder to achieve an equivalent situation and make quadrants *ii* and *iii* behave as equivalent R and L circular analyzers. Therefore, the PSG calibration can be completed with

$$S_3(x,y) = I'_{ii}(x,y) - I'_{iii}(x,y), \quad (2d)$$

where now I' indicates that the additional quarter-wave retardance is added to LCR2. Note that LCR1 and LCR2 devices remain within the PSG system in all measurements, and they simply change voltage, so there are not differences due to reflection or absorption losses.

Table 2. Average intensity values and standard deviation of the images shown in Figure 3.

Input H		Input V	
$\langle I_i \rangle = 0.014 \pm 0.002$	$\langle I_{ii} \rangle = 0.496 \pm 0.013$	$\langle I_i \rangle = 0.938 \pm 0.021$	$\langle I_{ii} \rangle = 0.498 \pm 0.013$
$\langle I_{iii} \rangle = 0.493 \pm 0.012$	$\langle I_{iv} \rangle = 0.923 \pm 0.021$	$\langle I_{iii} \rangle = 0.494 \pm 0.014$	$\langle I_{iv} \rangle = 0.017 \pm 0.002$
Input A		Input D	
$\langle I_i \rangle = 0.497 \pm 0.012$	$\langle I_{ii} \rangle = 0.016 \pm 0.002$	$\langle I_i \rangle = 0.448 \pm 0.012$	$\langle I_{ii} \rangle = 0.954 \pm 0.021$
$\langle I_{iii} \rangle = 0.957 \pm 0.021$	$\langle I_{iv} \rangle = 0.490 \pm 0.013$	$\langle I_{iii} \rangle = 0.018 \pm 0.002$	$\langle I_{iv} \rangle = 0.504 \pm 0.013$
Input R		Input L	
$\langle I_i \rangle = 0.501 \pm 0.024$	$\langle I_{ii} \rangle = 0.501 \pm 0.017$	$\langle I_i \rangle = 0.497 \pm 0.020$	$\langle I_{ii} \rangle = 0.511 \pm 0.014$
$\langle I_{iii} \rangle = 0.495 \pm 0.015$	$\langle I_{iv} \rangle = 0.496 \pm 0.022$	$\langle I_{iii} \rangle = 0.508 \pm 0.014$	$\langle I_{iv} \rangle = 0.523 \pm 0.023$

Table 2 presents the average value of the intensity measured for each of the 6 × 4 images shown in Figure 3. The error is given by the standard deviation. These values are calculated in a circle centered on the image and with diameter 600 pixels, as indicated in Figure 3c. These error values are also affected by noise in the detector. The camera was calibrated following a standard procedure [35] and it was operated in the regime limited by shot noise. The impact of this noise can be reduced by averaging several captures of each image, at the cost of increasing the time required for acquisition. Since we are using relatively high levels of intensity and samples with high transmission, we take single captures.

The measurement of the Stokes parameters for each PSG input state defines the **S** matrix, whose columns are given by images S_{ig} where index $i = 0, 1, 2, 3$ indicates the Stokes parameter, and index g denotes the state generated by the PSG (in our case. g = H, V, D, A, R, L). Thus, **S** is a 4 × 6 matrix defined as:

$$\mathbf{S} = \begin{pmatrix} S_{0H} & S_{0V} & S_{0D} & S_{0A} & S_{0R} & S_{0L} \\ S_{1H} & S_{1V} & S_{1D} & S_{1A} & S_{1R} & S_{1L} \\ S_{2H} & S_{2V} & S_{2D} & S_{2A} & S_{2R} & S_{2L} \\ S_{3H} & S_{3V} & S_{3D} & S_{3A} & S_{3R} & S_{3L} \end{pmatrix} = \begin{pmatrix} 1 & 1 & 1 & 1 & 1 & 1 \\ 1 & -1 & 0 & 0 & 0 & 0 \\ 0 & 0 & 1 & -1 & 0 & 0 \\ 0 & 0 & 0 & 0 & 1 & -1 \end{pmatrix}, \quad (3)$$

where the second part of equation (3) denotes the ideal values. Since **S** is not a square matrix, its pseudo-inverse matrix is a 6 × 4 matrix given by:

$$\mathbf{S^{-1}} = \mathbf{S}^T \left[\mathbf{S} \cdot \mathbf{S}^T\right]^{-1} = \begin{pmatrix} 1/6 & 1/2 & 0 & 0 \\ 1/6 & -1/2 & 0 & 0 \\ 1/6 & 0 & 1/2 & 0 \\ 1/6 & 0 & -1/2 & 0 \\ 1/6 & 0 & 0 & 1/2 \\ 1/6 & 0 & 0 & -1/2 \end{pmatrix}, \quad (4)$$

where superindex T indicates the transposed matrix and where the matrix on the right corresponds again to the ideal values. This expression of the pseudo-inverse matrix is valid when it is considered to multiply a matrix on the right.

Figure 4 shows matrices $\mathbf{S}(x,y)$ and $\mathbf{S^{-1}}(x,y)$ retrieved from the data in Figure 3. We use a color map to represent values from +1 to −1. To avoid presenting calculations in pixels where the input light is blocked by the iris diaphragm, we calculated the average $I_{\text{mean}}(x, y)$ of the 24 images in Figure 3a and searched for its maximum value $M = \max[I_{\text{mean}}(x, y)]$. Then, polarimetric matrices and parameters are calculated at pixels (x, y) where $I_{\text{mean}}(x, y) > 0.2M$, while pixels not fulfilling this threshold are represented in black. The value 0.2 was tested to provide a visualization of the polarimetric parameters within the iris aperture, while the outside region, which otherwise would appear with random values, appears pitch black. The average values of each element in matrices $\mathbf{S}(x, y)$ and $\mathbf{S^{-1}}(x, y)$ were also calculated, together with its corresponding standard deviation, again within the circle defined in Figure 3c, leading to the results indicated in Table 3. These numerical results agree well with the expected theoretical values in equations (3) and (4).

3.3 Calibration of the PSA

Once the PSG has been calibrated, the polarimeter calibration is completed by adding the variable retarder LCR3 to the PSA and measuring again for each input SOP generated with the PSG. LCR3 is set with its axes oriented at 45°. LCR3 retardance is switched between zero or full-wave retardance, where the polarization camera measures H, V, D and A states, and a quarter-wave retardance, where circular R and L states can be measured at the micropixels with vertical and horizontal polarizers. This way, the PSA operates within an octahedron and it thus corresponds to the optimal solution named "T" in [36].

Setting the PSA to detect different SOPs yields the intensity matrix **I** defined by the images $I_{ag}(x, y)$, where a denotes the analyzer in the PSA and g denotes the input state at the PSG. We also select the six standard SOP for the PSA. Hence, **I** is a 6 × 6 matrix where each element I_{ag} is the intensity measured for each input state g = H, V, D, A, R, L when being detected through analyzer a = H, V, D, A, R, L, i.e.:

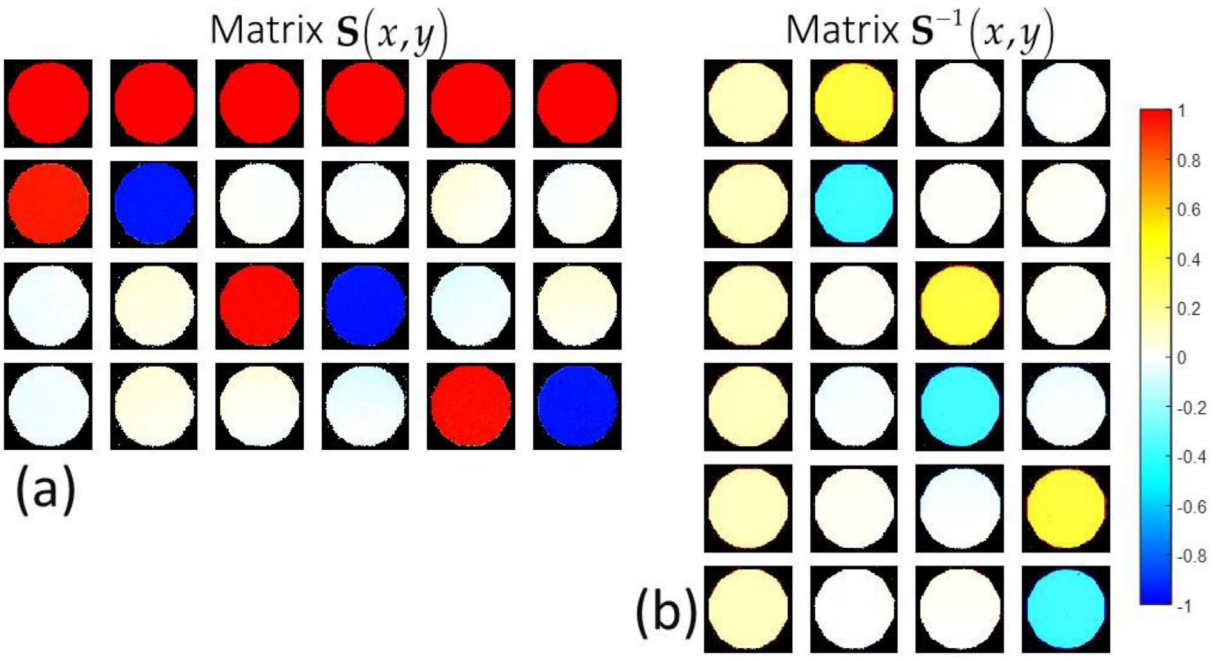

Fig. 4. Experimental images for the PSG polarimeter calibration under the red channel illumination. (a) $\mathbf{S}(x, y)$ matrix and (b) its pseudo-inverse matrix $\mathbf{S}^{-1}(x, y)$.

Table 3a. Average values of the matrix $\langle \mathbf{S}(x, y) \rangle_{\text{exp}}$.

1	1	1	1	1	1
+0.948±0.010	−0.960±0.010	−0.005±0.014	−0.015±0.014	+0.038±0.018	+0.006±0.016
−0.023±0.014	+0.034±0.016	+0.996±0.010	−0.965±0.010	−0.061±0.017	+0.075±0.020
+0.030±0.014	+0.025±0.017	+0.044±0.020	−0.057±0.022	+0.978±0.017	−0.962±0.017

$$\mathbf{I} = \begin{pmatrix} I_{HH} & I_{HV} & I_{HD} & I_{HA} & I_{HL} \\ I_{VH} & I_{VV} & I_{VD} & I_{VA} & I_{VL} \\ I_{DH} & I_{DV} & I_{DD} & I_{VA} & I_{DL} \\ I_{AH} & I_{AV} & I_{AD} & I_{AA} & I_{AL} \\ I_{RH} & I_{RV} & I_{RD} & I_{RA} & I_{RL} \\ I_{LH} & I_{LV} & I_{LD} & I_{LA} & I_{LL} \end{pmatrix}$$

$$= \begin{pmatrix} 1 & 0 & 1/2 & 1/2 & 1/2 & 1/2 \\ 0 & 1 & 1/2 & 1/2 & 1/2 & 1/2 \\ 1/2 & 1/2 & 1 & 0 & 1/2 & 1/2 \\ 1/2 & 1/2 & 0 & 1 & 1/2 & 1/2 \\ 1/2 & 1/2 & 1/2 & 1/2 & 1 & 0 \\ 1/2 & 1/2 & 1/2 & 1/2 & 0 & 1 \end{pmatrix}, \qquad (5)$$

where again the matrix values on the right stand for the ideal case.

Let us emphasize that matrix $\mathbf{I}$ is formed by images so each element $I_{ag}(x, y)$ depends on the pixel location. Also, note that the polarization camera only requires two shots to capture the six images per input SOP. Thus the 36 images required in matrix $\mathbf{I}$ are acquired after only 12 shots corresponding to 6 PSG configurations by 2 PSA configurations. Figure 5a shows the experimental result obtained for $\mathbf{I}(x, y)$ under the red channel illumination. For each input SOP, the images were normalized to the image where the analyzer matches the input polarization. The results bear good agreement with the ideal values in equation (6) despite slight variations along the diaphragm aperture. These variations are due to lighting non-uniformities (as shown in the intensity profiles in Fig. 3b), but also to the insertion of the LCR3 device in the PSA. Again, we calculated the average values and standard deviation of the intensity images in Figure 5a characterizing the intensity matrix. The result given in Table 4, although approximates reasonably well the expected values indicated in equation (5), shows significant differences that suggest the necessity of performing the compensation procedure to achieve accurate results.

Matrices $\mathbf{I}$ in equation (5) and $\mathbf{S}$ in equation (3) are related as $\mathbf{I} = \mathbf{A}\cdot\mathbf{S}$, where for simplicity we omit the pixel dependence. Here $\mathbf{A}$ is the detector matrix that characterizes the PSA. For the selected SOP, $\mathbf{A}$ is a 6×4 matrix that can be calculated as:

Table 3b. Average values of the matrix $\langle \mathbf{S}^{-1}(x, y) \rangle_{\text{exp.}}$

$+0.159 \pm 0.004$	$+0.497 \pm 0.009$	-0.004 ± 0.006	-0.009 ± 0.007
$+0.159 \pm 0.004$	-0.504 ± 0.009	0.000 ± 0.006	$+0.008 \pm 0.007$
$+0.156 \pm 0.004$	$+0.012 \pm 0.006$	$+0.487 \pm 0.009$	$+0.031 \pm 0.007$
$+0.164 \pm 0.004$	-0.020 ± 0.007	-0.484 ± 0.009	-0.036 ± 0.008
$+0.160 \pm 0.004$	$+0.026 \pm 0.007$	-0.026 ± 0.008	$+0.495 \pm 0.009$
$+0.158 \pm 0.004$	0.000 ± 0.007	$+0.024 \pm 0.008$	-0.487 ± 0.009

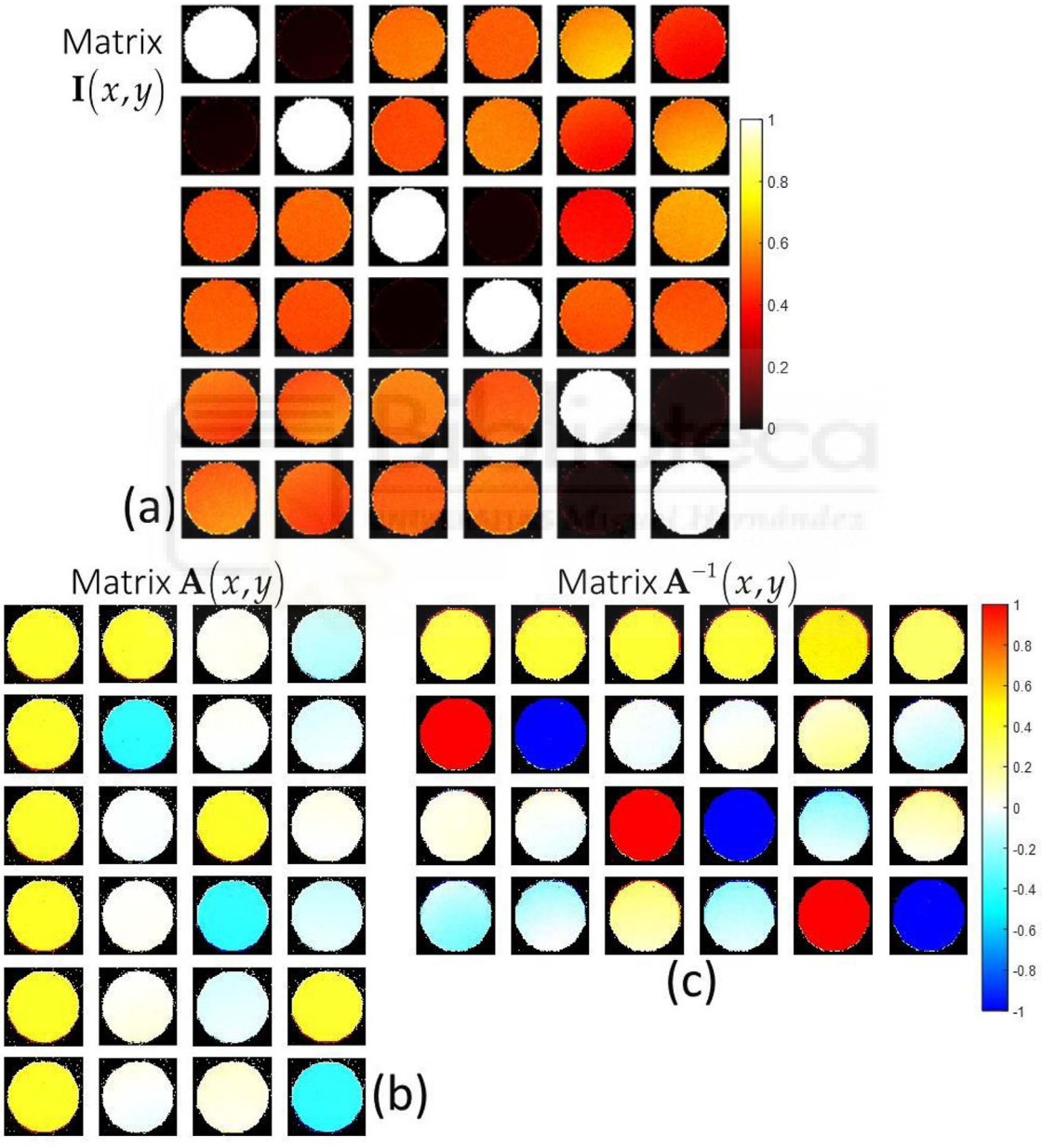

Fig. 5. Experimental images for the polarimeter PSA calibration under the red channel illumination. (a) Intensity matrix $\mathbf{I}(x, y)$. (b) Detector matrix $\mathbf{A}(x, y)$. (c) Pseudo-inverse detector matrix $\mathbf{A}^{-1}(x, y)$.

Table 4. Average values of the matrix $\langle \mathbf{I}(x, y)\rangle_{\text{exp}}$.

1	0.023 ± 0.004	0.544 ± 0.015	0.499 ± 0.014	0.395 ± 0.018	0.628 ± 0.025
0.035 ± 0.006	1	0.512 ± 0.017	0.537 ± 0.014	0.410 ± 0.020	0.617 ± 0.025
0.461 ± 0.012	0.527 ± 0.014	1	0.018 ± 0.002	0.498 ± 0.018	0.490 ± 0.017
0.532 ± 0.014	0.475 ± 0.013	0.029 ± 0.003	1	0.426 ± 0.016	0.581 ± 0.018
0.497 ± 0.022	0.525 ± 0.023	0.464 ± 0.014	0.579 ± 0.016	1	0.023 ± 0.002
0.541 ± 0.024	0.473 ± 0.023	0.580 ± 0.017	0.456 ± 0.014	0.023 ± 0.002	1

Table 5a. Average values of the matrix $\langle \mathbf{A}(x, y)\rangle_{\text{exp}}$.

+0.393 ± 0.008	+0.393 ± 0.010	+0.019 ± 0.008	−0.096 ± 0.012
+0.398 ± 0.009	−0.389 ± 0.012	−0.005 ± 0.011	−0.075 ± 0.013
+0.395 ± 0.009	−0.011 ± 0.008	+0.398 ± 0.011	+0.032 ± 0.015
+0.403 ± 0.008	+0.013 ± 0.008	−0.387 ± 0.011	−0.090 ± 0.015
+0.398 ± 0.008	0.001 ± 0.016	−0.066 ± 0.012	+0.384 ± 0.010
+0.398 ± 0.008	+0.022 ± 0.016	+0.068 ± 0.014	−0.387 ± 0.011

Table 5b. Average values of the matrix $\langle \mathbf{A}^{-1}(x, y)\rangle_{\text{exp.}}$

+0.39 ± 0.02	−0.41 ± 0.02	+0.43 ± 0.02	+0.42 ± 0.02	+0.55 ± 0.02	+0.310 ± 0.013
+0.96 ± 0.03	−0.99 ± 0.03	−0.04 ± 0.02	+0.02 ± 0.03	+0.07 ± 0.04	0.00 ± 0.04
+0.04 ± 0.02	−0.02 ± 0.03	+0.94 ± 0.03	−0.93 ± 0.03	−0.20 ± 0.05	+0.19 ± 0.05
−0.11 ± 0.05	−0.19 ± 0.05	+0.24 ± 0.04	−0.18 ± 0.04	+0.95 ± 0.03	−0.91 ± 0.03

$$\mathbf{A} = \mathbf{I} \cdot \mathbf{S}^{-1} = \begin{pmatrix} 1/2 & 1/2 & 0 & 0 \\ 1/2 & -1/2 & 0 & 0 \\ 1/2 & 0 & 1/2 & 0 \\ 1/2 & 0 & -1/2 & 0 \\ 1/2 & 0 & 0 & 1/2 \\ 1/2 & 0 & 0 & -1/2 \end{pmatrix}, \quad (6)$$

where the pseudo-inverse matrix $\mathbf{S}^{-1}$ in equation (4) was applied. The corresponding pseudo-inverse matrix $\mathbf{A}^{-1}$ is a 4 × 6 matrix given by

$$\mathbf{A}^{-1} = \left[\mathbf{A}^T \cdot \mathbf{A}\right]^{-1} \cdot \mathbf{A}^T = \begin{pmatrix} 1/3 & 1/3 & 1/3 & 1/3 & 1/3 & 1/3 \\ 1 & -1 & 0 & 0 & 0 & 0 \\ 0 & 0 & 1 & -1 & 0 & 0 \\ 0 & 0 & 0 & 0 & 1 & -1 \end{pmatrix}, \quad (7)$$

where the matrices on the right in equations (6) and (7) correspond to the ideal values. This expression in equation (7) is valid when it is considered to multiply a matrix on the left.

Figures 5b and 5c show the experimental images of $\mathbf{A}(x, y)$ and $\mathbf{A}^{-1}(x, y)$, which again bear a good agreement with the expected values in equations (6) and (7). However, note some elements of $\mathbf{A}^{-1}$ in Figure 5c appreciably differ from the ideal zero value in equation (7), indicating the correction that the PSA experimental matrix requires. Let us remark that these matrices are calculated at every pixel, thus providing a PSA calibration at pixel level. Again, for each element on these matrices, we calculated the average value and its standard deviation on the circle defined in Figure 3c. The results are given in Table 5. These values differ appreciably from the ideal values in equations (6) and (7) since they account for the non-ideal behaviour of the components involved in the PSG and the PSA.

4 Mueller matrix imaging

Once the PSG and PSA matrices, $\mathbf{S}(x, y)$ and $\mathbf{A}(x, y)$, have been determined, the sample can be introduced in the polarimeter. For each input SOP generated by the PSG, the images given by the PSA are captured. As a result, a new set of 36 images are obtained that define a new intensity matrix $\mathbf{I}_S(x, y)$, like in equation (5), now related to the sample Mueller matrix $\mathbf{M}_S(x, y)$ as

$$\mathbf{I}_S(x, y) = \mathbf{A}(x, y) \cdot \mathbf{M}_S(x, y) \cdot \mathbf{S}(x, y). \quad (8)$$

$\mathbf{M}_S(x, y)$ is then obtained with the aid of the pseudo-inverse matrices $\mathbf{A}^{-1}$ and $\mathbf{S}^{-1}$ as:

$$\mathbf{M}_S(x, y) = \mathbf{A}^{-1} \cdot \mathbf{I}_S \cdot \mathbf{S}^{-1} = \left\{\left[\mathbf{A}^T \cdot \mathbf{A}\right]^{-1} \cdot \mathbf{A}^T\right\} \cdot \mathbf{I}_S \cdot \left\{\mathbf{S}^T \cdot \left[\mathbf{S} \cdot \mathbf{S}^T\right]^{-1}\right\}. \quad (9)$$

We illustrate the procedure by considering different polarization devices that modify the input SOP by three distinct physical mechanisms: a pure retarder, a pure diattenuator,

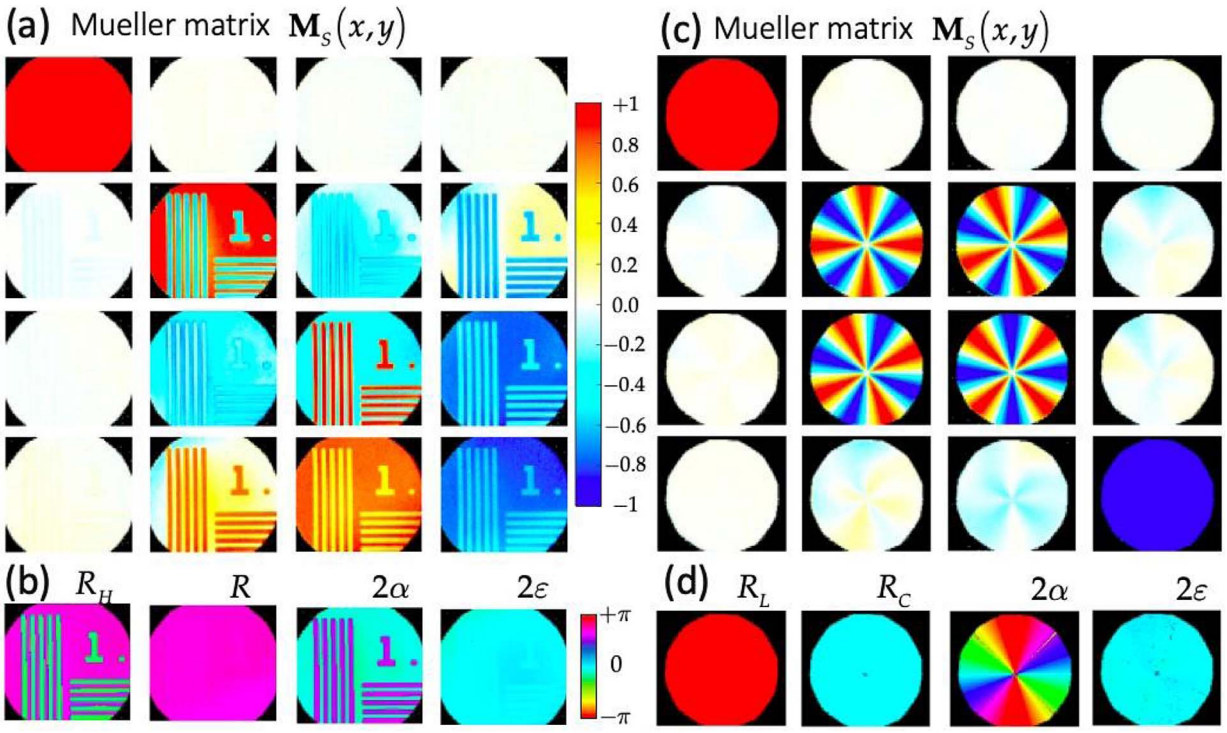

Fig. 6. (a) Experimental MM of the birefringent resolution test under red light channel illumination. (b) Retrieved horizontal linear retardance (R_L) and total retardance (R), and azimuth (α) and ellipticity (ε) of fast eigenstates. (c) and (d) show equivalent results for the q-plate element under red channel illumination.

and a pure depolarizer. These samples of well-defined properties thus serve as validation tests to probe the accuracy of the imaging polarimeter. For each sample, the experimental MM was retrieved following equation (9) and the Lu–Chipman decomposition $\mathbf{M}_S = \mathbf{M}_\Delta \cdot \mathbf{M}_R \cdot \mathbf{M}_D$ [37] was applied to calculate relevant polarimetric parameters using standard formulas [21]. We applied the very well-known Lu–Chipman decomposition because these samples, each of distinct physical mechanism, imply relatively simple Mueller matrices. Note that more complex Mueller matrices, simultaneously dealing with retardance, depolarization and diattenuation responses could require other decompositions, like for instance the inverse decomposition, the arrow form decomposition or the symmetric decomposition, among others [38].

As a first example, Figure 6 shows the results for two patterned retarders: a birefringent NBS 1963A resolution test (Thorlabs R2L2S1B), and a q-plate device (Thorlabs WPV10-633), both under the red channel illumination. Figures 6a and 6c show the retrieved MM normalized to m_{00}. They show the expected result for a retarder, where $m_{0j} = m_{j0} \approx 0$, for $j = 1, 2, 3$, indicating null polarizance and null diattenuation. The retarder information is contained in the 3×3 bottom right submatrix. The retardance vector [21, 37] is calculated and some representative parameters of the retarder are shown in each case.

Figures 6a and 6b show the results for the birefringent resolution test. This is a linear retarder designed to have a uniform retardance but a different orientation in the patterns compared to the background. The total retardance $R(x, y)$ appears uniform all over the image, with average value $\langle R \rangle = 131° \pm 1°$ (the value is obtained by averaging over the significant pixels and the error is given by its standard deviation, where again, the significant pixels are those comprised within a circle as defined in Fig. 3c). However, the horizontal component of the retardance vector $R_H(x, y)$ clearly shows a difference between the patterns and the background. The azimuth $\alpha(x, y)$ of the fast eigenstate confirms the two regions, with the background oriented approximately horizontal, $\langle \alpha_b \rangle = -8.5° \pm 0.5°$, and the resolution test pattern oriented at $\langle \alpha_t \rangle = -55.8° \pm 1.0°$. The ellipticity image $\varepsilon(x, y)$ of the fast eigenstate remains uniform over the entire image, with a very small value, $\langle \varepsilon \rangle = 2.6° \pm 1.2°$ as expected for a linear retarder.

Figures 6c and 6d show equivalent results for the q-plate component, a patterned retarder widely used to generate orbital angular momentum (OAM) beams and vector beams [39]. This is a linear retarder with fixed retardance and whose axes orientation changes azimuthally. This q-plate was designed as a half-wave retarder for the 633 nm wavelength and with value $q = 1$, so the retarder axes make a complete azimuthal rotation. In this case, since the retarder is very close to the half-wave condition, the most relevant information in the MM is in the m_{11}, m_{12}, m_{21}, and m_{22} elements, which show an azimuthal variation in the complete range from -1 to $+1$, and in the m_{33} element, which

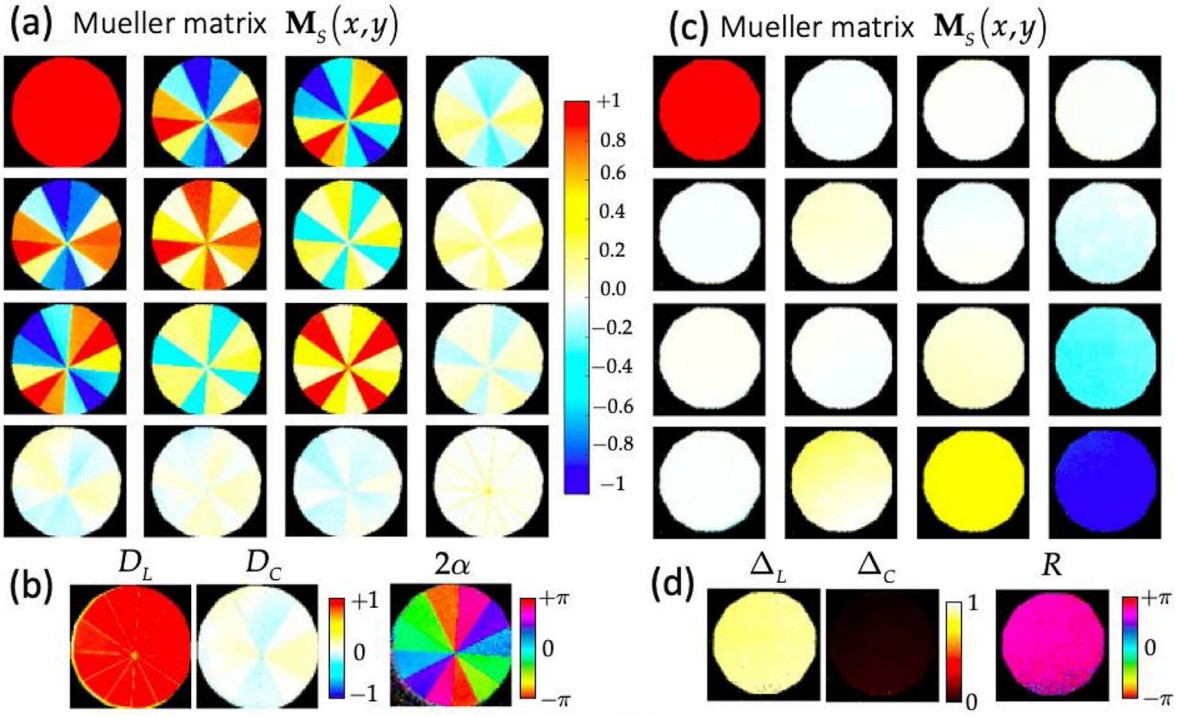

Fig. 7. (a) Experimental MM of a radial polarizer under red channel illumination. (b) Linear diattenuation (D_L), circular diattenuation (D_C), and azimuth (α) of the transmission axis. (c) Experimental MM for a depolarizing FLC modulator under the green channel illumination. (d) Linear depolarizance (Δ_L), circular depolarizance (Δ_C), and total effective retardance (R).

appears uniform with a value around −1. In this case Figure 6d illustrates the linear R_L and circular R_C components of the retardance vector, which confirm the linear retarder condition of this component. The total retardance is uniform with an average value $\langle R \rangle = 178° \pm 1.1°$ in agreement with the half-wave retardance design of this q-plate for red light. The azimuth of the fast eigenstate orientation $\alpha(x, y)$ shows a continuous azimuthal variation, as corresponding to a q-plate with $q = 1$ and the eigenstate ellipticity $\varepsilon(x, y)$ shows a null constant value with an average value $\langle \varepsilon \rangle = 1° \pm 3°$, as expected for a linear retarder.

The second type of structured polarization sample is a pure diattenuator: a radial polarizer from the company Codixx (ColorPol VIS500 BC3), consisting of 12 segments where the transmission axis is aligned radially, thus being shifted 30° between adjacent segments. Figure 7a shows the corresponding MM, again using the red channel. In this case the last row and column become null, $m_{3j} = m_{j3} \approx 0$ with $j = 0, 1, 2$. The other MM elements clearly show the segmentation of the polarizer. Figure 7b shows as parameters of interest the linear and circular components of the diattenuation, $D_L(x, y)$ and $D_C(x, y)$. The average total diattenuation is $\langle D \rangle = 0.85 \pm 0.13$, where again the value is averaged over the significant pixels and the error is given by its standard deviation. We also calculate the polarizer transmission angle $\alpha(x, y)$, which confirms the expected rotation.

Finally, as a pure depolarizing sample we consider a ferroelectric liquid–crystal (FLC) modulator. This type of modulator behaves as a linear retarder whose director axis switches between two stable orientations within the modulator plane [40]. When operated at a high frequency compared to the detector integration time, FLC modulators have proven to be useful to generate an effective depolarization [41]. In this work, we use a FLC modulator (CRL Opto LCS2-G) showing a switching angle of 45° and a retardance of 180° for green light [40]. We operate the device at a switching frequency of 500 Hz, much higher than the frame rate of the polarization camera. Therefore, each measurement with the camera corresponds to the incoherent superposition of the two states emerging from the FLC [42]. The measured MM can be regarded as the average of $\mathbf{M}_\mathrm{A}$ and $\mathbf{M}_\mathrm{B}$ the two matrices corresponding to the two stable states of the modulator.

The MM of a retarder with retardance φ and orientation α, corresponding to the first FLC stable position is given by [1]:

$$\mathbf{M}_\mathrm{A} = \begin{pmatrix} 1 & 0 & 0 & 0 \\ 0 & c_{2\alpha}^2 + c_\varphi s_{2\alpha}^2 & (1 - c_\varphi) s_{2\alpha} c_{2\alpha} & -s_\varphi s_{2\alpha} \\ 0 & (1 - c_\varphi) s_{2\alpha} c_{2\alpha} & s_{2\alpha}^2 + c_\varphi c_{2\alpha}^2 & s_\varphi c_{2\alpha} \\ 0 & s_\varphi s_{2\alpha} & -s_\varphi c_{2\alpha} & c_\varphi \end{pmatrix}, \tag{10}$$

where $c_x = \cos(x)$ and $s_x = \sin(x)$. The second FLC stable position is given by $\mathbf{M}_B = (-45°) \cdot \mathbf{M}_A \cdot \mathbf{R}(+45°)$ where $\mathbf{R}$ stands for the Mueller rotation matrix. Then, the average MM given by $\langle \mathbf{M}_\mathrm{FLC} \rangle = \frac{1}{2}(\mathbf{M}_A + \mathbf{M}_B)$ results in

$$\langle \mathbf{M}_{\mathrm{FLC}} \rangle = \begin{bmatrix} 1 & 0 & 0 & 0 \\ 0 & c_{2\varphi}^2 & 0 & -\frac{1}{2} s_\varphi (c_{2\alpha} + s_{2\alpha}) \\ 0 & 0 & c_{2\varphi}^2 & \frac{1}{2} s_\varphi (c_{2\alpha} + s_{2\alpha}) \\ 0 & \frac{1}{2} s_\varphi (c_{2\alpha} + s_{2\alpha}) & -\frac{1}{2} s_\varphi (c_{2\alpha} + s_{2\alpha}) & c_\varphi \end{bmatrix}. \tag{11}$$

In the case of a half-wave retardance, $\varphi = 180°$, this average matrix $\langle \mathbf{M}_{\mathrm{FLC}} \rangle$ becomes:

$$\langle \mathbf{M}_{\mathrm{FLC}} \rangle = \begin{pmatrix} 1 & 0 & 0 & 0 \\ 0 & 0 & 0 & 0 \\ 0 & 0 & 0 & 0 \\ 0 & 0 & 0 & -1 \end{pmatrix}. \tag{12}$$

This result can be regarded as a perfect depolarizer for input linear polarizations, whereas circular polarizations retain the full degree of polarization but change handedness.

Figure 7c shows the experimental MM results obtained with the polarimeter. In this case we use the green channel where the FLC layer behaves closely to the half-wave retardance condition [40]. Now the experimental MM elements are uniform images since the FLC modulator is a single-pixel element. The retrieved MM matches quite well the expected ideal result in equation (12). All the elements are close to zero, except $m_{00} \approx 1$ and $m_{33} \approx -1$. Elements m_{32} and m_{23} slightly differ from zero, due to the nonperfect half-wave retardance of the FLC layer. Figure 7d shows images of the depolarization and retardance parameters are calculated. The linear depolarizance $\Delta_L(x, y)$ shows high values, with an average value $\langle \Delta_L \rangle = 0.88 \pm 0.03$, while the circular depolarization $\Delta_C(x, y)$ has very low values, with $\langle \Delta_C \rangle = 0.04 \pm 0.03$. This confirms the ability of the FLC modulator to depolarize linearly polarized input light. Finally, the effective retardance $R(x, y)$ shows an average value $\langle R \rangle = 158° \pm 3°$, not far but non-perfect half-wave retardance. Again, the error given in these average values is calculated as the standard deviation of the values in all pixels in the aperture.

5 Conclusion

In summary, this work presents an imaging complete MM polarimeter comprised of a polarization camera and three LCRs. The use of polarization cameras in imaging systems is quite recent and it is arising high interest in a wide range of applications. The presented polarimeter is an improved version of our previous system [21] with significant advances. First, a multiwavelength LED light source replaced the laser source, thus avoiding interference and speckle derived from the coherent source. A rotatable breadboard is added to allow changing from the transmission configuration to a configuration useful for reflective or back-scattering samples. The system incorporates two LCRs in the PSG and another one in the PSA, to allow fully automated measurements without any moving element. All LCR devices were calibrated for the three spectral bands of the LED source.

The polarimeter was calibrated and compensated by modifying the time sequential method [25, 32]. The procedure has been illustrated step by step. The novelty here is that the polarization camera included in the polarimeter is itself the calibration reference. This way no additional external elements are required and the polarimeter can be fully optimized in situ. Furthermore, the procedure is applied at pixel level, therefore compensating the residual non-uniformities in the illumination and in the PSA system, because of the pixelwise calculation of the normalized Mueller matrix.

This approach of course relies on the quality of the polarization camera. To this aim, the Appendix incorporates a calculation of the error in the measurement of the MM elements caused by the limited extinction ratio (ER) of the micro-polarizers, which shows an error lower than 1.7% for the minimum value of ER = 120 measured in our camera. The calibration and compensation procedure has been illustrated step by step by displaying the $\mathbf{S}(x, y)$ and $\mathbf{A}(x, y)$ images that define the PSG and the PSA. They are compared with the theoretical expected values, showing a very good agreement in all cases.

Finally, three different samples used in structured light applications with well-known polarization properties were evaluated to verify the accuracy of the polarimeter: (1) two patterned pure retarders with constant retardance but different orientation of the optical axis (a birefringent resolution test and a q-plate), (2) a radial linear polarizer, and 3) a linear depolarizer based on a fast-switching FLC modulator with 45° switching angle. The retrieved experimental MM agree very well with the expected results and, after performing the Lu–Chipman decomposition, the polarization parameters of interest (retardance, diattenuation and depolarization) were derived in each case.

Funding

This work was financed by Ministerio de Ciencia e Innovación, Spain (refs.: PID2021-126509OB-C22, -C21 and PDC2022-133332-C22) and Generalitat Valenciana (ref. CIAICO/2021/276). EN acknowledges Generalitat Valenciana (ref. GRISOLIAP/2020/004). AV acknowledges Fondecyt N° 1191811.

Conflicts of Interest

This work has no financial or non-financial competing interests.

Data availability statement

Data will be made available on request.

Author contribution statement

All coauthors contributed to the paper. EN and AV contributed with the realization of the experiments. EN and IM contributed with the computer calculations. MMSL, AL, JC and IM contributed to the conceptualization, design of the experiments, and analysis of the results. MMSL contributed to writing the manuscript, and all authors contributed to the revision of the manuscript.

References

1 Goldstein D.H. (2010) *Polarized Light*, Marcel Dekker, New York, NY, USA.
2 Ramella-Roman J.C., Saytashev I., Piccini M. (2020) A review of polarization-based imaging technologies for clinical and preclinical applications, *J. Opt.* **22**, 123001. https://doi.org/10.1088/2040-8986/abbf8a.
3 He C., He H., Chang J., Chen B., Ma H., Booth M.J. (2021) Polarisation optics for biomedical and clinical applications: a review, *Light: Sci Appl.* **10**, 194. https://doi.org/10.1038/s41377-021-00639-x.
4 Gottlieb D., Arteaga O. (2021) Mueller matrix imaging with a polarization camera: application to microscopy, *Opt. Express* **29**, 21, 34723–34374. https://doi.org/10.1364/OE.439529.
5 Van Eeckhout A., Garcia-Caurel E., Garnatje T., Escalera J.C., Durfort M., Vidal J., Gil J.J., Campos J., Lizana A. (2021) Polarimetric imaging microscopy for advanced inspection of vegetal tissues, *Sci. Rep.* **11**, 3913. https://doi.org/10.1038/s41598-021-83421-8.
6 Rubinsztein-Dunlop H., Forbes A., Berry M.V., Dennis M.R., Andrews D.L., Mansuripur M., Denz C., Alpmann C., Banzer P., Bauer T., Karimi E., Marrucci L., Padgett M., Ritsch-Marte M., Litchinitser N.M., Bigelow N.P., Rosales-Guzmán C., Belmonte A., Torres J.P., Neely T.W., Baker M., Gordon R., Stilgoe A.B., Romero J., White A.G., Fickler R., Willner A.E., Xie G., McMorran B., Weiner A.M. (2017) Roadmap on structured light, *J. Opt.* **19**, 013001. https://doi.org/10.1088/2040-8978/19/1/013001.
7 Piquero G., Martínez-Herrero R., de Sande J.C.G., Santarsiero M. (2020) Synthesis and characterization of non-uniformly totally polarized light beams: tutorial, *J. Opt. Soc. Am. A* **37**, 4, 591. https://doi.org/10.1364/JOSAA.379439.
8 Rosales-Guzmán C., Ndagano B., Forbes A. (2018) A review of complex vector light fields and their applications, *J. Opt.* **20**, 123001. https://doi.org/10.1088/2040-8986/aaeb7d.
9 Devrinkas R., Kazansky P.G. (2017) High-performance geometric phase elements in silica glass, *APL Photon.* **2**, 066104. https://doi.org/10.1063/1.4984066.
10 Liu G.-G., Lee Y.-H., Huang Y., Zhu Z., Tan G., Cai M.-Q., Li P.-P., Wang D., Li Y., Pang S., Tu C., Wu S.-T., Wang H.-T. (2017) Dielectric broadband meta-vector-polarizers based on nematic liquid crystal, *APL Photon.* **2**, 066104. https://doi.org/10.1063/1.5006016.
11 Davis J.A., McNamara D.E., Cottrell D.M., Sonehara T. (2000) Two-dimensional polarization encoding with a phase-only liquid-crystal spatial light modulator, *Appl. Opt.* **39**, 10, 1549–1554. https://doi.org/10.1364/AO.39.001549.
12 Kenny F., Lara D., Rodríguez-Herrera O.G., Dainty C. (2012) Complete polarization and phase control for focus-shaping in high-NA microscopy, *Opt. Exp.* **20**, 13, 14015–14029. https://doi.org/10.1364/OE.20.014015.
13 Wen D., Croizier K.B. (2021) Metasurfaces 2.0: Laser-integrated and with vector field control, *APL Photon.* **6**, 080902. https://doi.org/10.1063/5.0057904.
14 De Sio L., Roberts D.E., Liao Z., Nersisyan S., Uskova O., Wickboldt L., Tabiryan N., Steeves D.M., Kimball B.R. (2016) Digital polarization holography advancing geometrical phase optics, *Opt. Exp.* **24**, 16, 18297–18306. https://doi.org/10.1364/OE.24.018297.
15 Curcio V., Alemán-Castañeda L.A., Brown T.G., Brasselet S., Alonso M.A. (2020) Birefringent Fourier filtering for single molecule coordinate and height super-resolution imaging with dithering and orientation, *Nature Commun.* **11**, 5307. https://doi.org/10.1038/s41467-020-19064-6.
16 Zhang Z., Dong F., Cheng T., Qiu K., Zhang Q., Chu W., Wu X. (2014) Nano-fabricated pixelated micropolarizer array for visible imaging polarimetry, *Rev. Sci. Instrum.* **85**, 105002. https://doi.org/10.1063/1.4897270.
17 Singh K., Tabebordbar N., Forbes A., Dudley A. (2020) Digital Stokes polarimetry and its application to structured light: tutorial, *J. Opt. Soc. Am. A* **37**, C33–C44. https://doi.org/10.1364/JOSAA.397912.
18 Angelo J.P., Germer T.A., Litorja M. (2019) Structured illumination Mueller matrix imaging, *Biomed. Opt. Exp.* **10**, 6, 2861–2868. https://doi.org/10.1364/BOE.10.002861.
19 Rubin N.A., D'Aversa G., Chevalier P., Shi Z., Chen W.T., Capasso F. (2019) Matrix Fourier optics enables a compact full-Stokes polarization camera, *Science* **365**, eaax1839. https://doi.org/10.1126/science.aax18.
20 Arteaga O., Bendada H. (2020) Geometrical phase optical components: Measuring geometric phase without interferometry, *Crystals* **10**, 880. https://doi.org/10.3390/cryst10100880.
21 López-Morales G., Sánchez-López M.M., Lizana A., Moreno I., Campos J. (2020) Mueller matrix polarimetric imaging analysis of optical components for the generation of cylindrical vector beams, *Crystals* **10**, 1155. https://doi.org/10.3390/cryst10121155.
22 Pezzaniti J.L., Chipman R.A. (1995) Mueller matrix imaging polarimetry, *Opt. Eng.* **34**, 6, 1558–1568. https://doi.org/10.1117/12.206161.
23 Kudenov M.W., Escuti M.J., Hagen N., Dereniak E.L., Oka K. (2012) Snapshot imaging Mueller matrix polarimeter using polarization gratings, *Opt. Lett.* **37**, 8, 1367–1369. https://doi.org/10.1364/OL.37.001367.
24 Carnicer A., Bosch S., Javidi B. (2019) Mueller matrix polarimetry with 3D integral imaging, *Opt. Exp.* **27**, 8, 11525–11536. https://doi.org/10.1364/OE.27.011525.
25 Garcia-Caurel E., Ossikovski R., Foldyna M., Pierangelo A., Drévillon B., De Martino A. (2013) Advanced Mueller ellipsometry instrumentation and data analysis (Chapter 2), in *Ellipsometry at the nanoscale*, M. Losurdo, K. Hingerl (eds.), Springer Verlag, Berlin.
26 Vargas A., Donoso R., Ramírez M., Carrión J., Sánchez-López M.M., Moreno I. (2013) Liquid crystal retarder spectral retardance characterization based on a Cauchy dispersion relation and a voltage transfer function, *Opt. Rev.* **20**, 5, 378–384. https://doi.org/10.1007/s10043-013-0068-4.
27 Messaadi A., Sánchez-López M.M., García-Martínez P., Vargas A., Moreno I. (2016) Optical system for measuring the spectral retardance function in an extended range, *J. Eur. Opt. Soc. – Rapid Pub.* **12**, 12, 21. https://doi.org/10.1186/s41476-016-0023-7.
28 Vargas A., Sánchez-López M.M., García-Martínez P., Arias J., Moreno I. (2014) Highly accurate spectral retardance characterization of a liquid crystal retarder including Fabry-Perot interference effects, *J. Appl. Phys.* **115**, 3, 033101. https://doi.org/10.1063/1.4861635.
29 Chipman R.A. (1995) Polarimetry, in *Handbook of Optics*, 2nd edn., McGraw-Hill, New York.
30 Twietmeyer K.M., Chipman R.A. (2008) Optimization of Mueller matrix polarimeters in the presence of error sources, *Opt. Exp.* **16**, 15, 11589–11603. https://doi.org/10.1364/OE.16.011589.
31 Peña-Gutiérrez S., Royo S. (2023) Polarization calibration assessment for a broadband imaging polarimeter based on a division of aperture architecture, *Opt. Exp.* **31**, 3, 3839–3856. https://doi.org/10.1364/OE.472070.
32 Peinado A., Lizana A., Vidal J., Iemmi C., Campos J. (2010) Optimization and performance criteria of a Stokes polarimeter based on two variable retarders, *Opt. Exp.* **18**, 8, 9815. https://doi.org/10.1364/OE.18.009815.
33 Cofré A., Vargas A., Torres-Ruiz F.A., Campos J., Lizana A., Sánchez-López M.M., Moreno I. (2017) Quantitative performance of a polarization diffraction grating polarimeter encoded onto two liquid-crystal-on-silicon displays, *Opt. Laser Technol.* **96**, 219–226. https://doi.org/10.1016/j.optlastec.2017.05.027.
34 Roussel S., Boffety M., Goudail F. (2018) Polarimetric precision of micropolarizer grid-based camera in the presence of additive and

Poisson shot noise, *Opt. Exp.* **26**, 23, 29968–29982. https://doi.org/10.1364/OE.26.029968.
35 Janesick J. (1997) CCD transfer method – standard for absolute performance of CCDs and digital CCD camera systems, *Proc. SPIE* **3019**, 70–102. https://doi.org/10.1117/12.275190.
36 Roussel S., Boffety M., Goudail F. (2019) On the optimal ways to perform full Stokes measurements with a linear division-of-focal plane polarimetric imager and a retarder, *Opt. Lett.* **44**, 11, 2927–2930. https://doi.org/10.1364/OL.44.002927.
37 Lu S.-Y., Chipman R.A. (1996) Interpretation of Mueller matrices based on polar decomposition, *J. Opt. Soc. Am. A* **13**, 5, 1106–1113. https://doi.org/10.1364/JOSAA.13.001106.
38 Gil J.J., Ossikovski R. (2022) *Polarized light and the mueller matrix approach*, CRC Press, New York. https://doi.org/10.1201/9780367815578.
39 Rubano A., Cardano F., Piccirillo B., Marrucci L. (2019) Q-plate technology: A progress review, *J. Opt. Soc. Am. B* **36**, 5, D70–D87. https://doi.org/10.1364/JOSAB.36.000D70.
40 Martínez A., Beaudoin N., Moreno I., Sánchez-López M.M., Velásquez P. (2006) Optimization of the contrast ratio of a ferroelectric liquid crystal optical modulator, *J. Opt. A: Pure Appl. Opt.* **8**, 11, 1013–1018. https://doi.org/10.1088/1464-4258/8/11/013.
41 Lizana A., Estévez I., Torres-Ruiz F.A., Peinado A., Ramirez C., Campos J. (2015) Arbitrary state of polarization with customized degree of polarization generator, *Opt. Lett.* **40**, 16, 3790–3793. https://doi.org/10.1364/OL.40.003790.
42 Marco D., López-Morales G., Sánchez-López M.M., Lizana A., Moreno I., Campos J. (2021) Customized depolarization spatial patterns with dynamic retardance functions, *Sci. Rep.* **11**, 9415. https://doi.org/10.1038/s41598-021-88515-x.

Appendix

A1 Evaluation of the micro-polarizers limited extinction ratio

The polarization camera has wire-grid micro-polarizers attached to the pixels of the CMOS detector. In this appendix we evaluate the accuracy of the polarimeter self-calibration procedure in terms of their extinction ratio. Since the polarization camera is used as the reference, the accuracy of the polarimeter calibration is dictated by the quality of its polarizers. Although other sources of errors have been identified (such as the spatial variation of the extinction ratio, or spatial variations in the orientation angle of the micro-polarizers transmission axes) [34], here we assume a simplified model where we consider the micro-polarizers perfectly oriented (horizontal, vertical, diagonal and antidiagonal), but having a limited and spatially uniform extinction ratio ER $= T_{\|}/T_{\perp}$ where $T_{\|}$ and $T_{\perp}$ are the transmission for parallel and crossed polarizers respectively. Information about this main source of error in the polarization camera is provided by the supplier, indicating in our case values ER $>$ 120:1 in the three colour bands. To take this into account, the MM of these four linear polarizers with limited ER is calculated analytically. The MM of a polarizer aligned horizontal and with limited extinction ratio is given by [1]:

$$\mathbf{P}_0 = \frac{T_{\|}}{2}\begin{pmatrix} 1+e & 1-e & 0 & 0 \\ 1-e & 1+e & 0 & 0 \\ 0 & 0 & 2\sqrt{e} & 0 \\ 0 & 0 & 0 & 2\sqrt{e} \end{pmatrix}, \tag{A1a}$$

where $e \equiv 1/\mathrm{ER} = T_{\perp}/T_{\|}$. The limit $e \to 0$ leads to the ideal polarizer with normalized MM:

$$\mathbf{P}_0(e=0) = \frac{T_{\|}}{2}\begin{pmatrix} 1 & 1 & 0 & 0 \\ 1 & 1 & 0 & 0 \\ 0 & 0 & 0 & 0 \\ 0 & 0 & 0 & 0 \end{pmatrix}. \tag{A1b}$$

We measured values ER $>$ 120:1 for our camera polarizers in the three spectral bands, in agreement with the manufacturer data. The MM of the micro-polarizers oriented vertical and at $\pm 45°$ are simply obtained by applying the corresponding rotation transformation [1].

Assuming ideal input states (ideal values in the **S** matrix in Eq. (3)), and that the circular components R and L are measured using an ideal QWP in front of the camera, the intensity measured for each input state when being analyzed with these limited linear micro-polarizers can be calculated analytically, leading to an intensity matrix as in equation (5) which now takes the following form:

See the equation (A2) bottom of the page

where the ideal matrix in equation (5) is recovered for the limit $e \to 0$ and $T_{\|} \to 1$. Hence, equation (A2) is the intensity matrix of the polarimeter calibration, which contains the errors induced by the limited ER of the micro-polarizers. The analytical expression of the calibrated PSA matrix that compensates the limited ER is thus obtained as $\mathbf{A}(e) = \mathbf{I}_{\mathrm{air}}(e) \cdot \mathbf{S}^{-1}$) using equation (A2) and the ideal $\mathbf{S}^{-1}$ matrix in equation (4). Its pseudo-inverse is given by:

$$\mathbf{A}^{-1}(e) = \frac{1}{T_{\|}}\begin{pmatrix} \frac{1}{3(1+e)} & \frac{1}{3(1+e)} & \frac{1}{3(1+e)} & \frac{1}{3(1+e)} & \frac{1}{3(1+e)} & \frac{1}{3(1+e)} \\ \frac{1}{1-e} & \frac{1}{1-e} & 0 & 0 & 0 & 0 \\ 0 & 0 & \frac{1}{1-e} & \frac{1}{1-e} & 0 & 0 \\ 0 & 0 & 0 & 0 & \frac{1}{1-e} & \frac{1}{1-e} \end{pmatrix}. \tag{A3}$$

$$\mathbf{I}_{\mathrm{air}}(e) = T_{\|}\begin{pmatrix} 1 & e & \frac{1}{2}(1+e) & \frac{1}{2}(1+e) & \frac{1}{2}(1+e) & \frac{1}{2}(1+e) \\ e & 1 & \frac{1}{2}(1+e) & \frac{1}{2}(1+e) & \frac{1}{2}(1+e) & \frac{1}{2}(1+e) \\ \frac{1}{2}(1+e) & \frac{1}{2}(1+e) & 1 & e & \frac{1}{2}(1+e) & \frac{1}{2}(1+e) \\ \frac{1}{2}(1+e) & \frac{1}{2}(1+e) & e & 1 & \frac{1}{2}(1+e) & \frac{1}{2}(1+e) \\ \frac{1}{2}(1+e) & \frac{1}{2}(1+e) & \frac{1}{2}(1+e) & \frac{1}{2}(1+e) & 1 & e \\ \frac{1}{2}(1+e) & \frac{1}{2}(1+e) & \frac{1}{2}(1+e) & \frac{1}{2}(1+e) & e & 1 \end{pmatrix}, \tag{A2}$$

This matrix recovers the ideal case in the right part of equation (7) in the limit when $e \to 0$ and $T_{\parallel} \to 1$.

To evaluate analytically the impact of the limited extinction ratio on the polarimeter measurement, we first consider as sample the air and apply equation (9), $\mathbf{M} = \mathbf{A}^{-1}\,\mathbf{I}\,\mathbf{S}^{-1}$, to obtain the MM of air. Here we use the non-ideal intensity matrix $\mathbf{I}_{\text{air}}$ in equation (A2), but we consider the ideal values of the matrices $\mathbf{S}^{-1}$ and $\mathbf{A}^{-1}$ given in the right part of equation (4) and equation (7) respectively. This way we assume that the polarizers extinction ratio error is present in the experiment, but it is ignored in the polarimetric calculation. The analytical calculation leads to a MM matrix affected by the error e given by:

$$\mathbf{M}_{\text{air}}(e) = \mathbf{A}^{-1} \cdot \mathbf{I}_{\text{air}}(e) \cdot \mathbf{S}^{-1} = T_{\parallel} \begin{pmatrix} 1+e & 0 & 0 & 0 \\ 0 & 1-e & 0 & 0 \\ 0 & 0 & 1-e & 0 \\ 0 & 0 & 0 & 1-e \end{pmatrix}, \tag{A4}$$

which recovers the expected identity matrix of air when $e \to 0$ and $T_{\parallel} \to 1$. The MM in equation (A4) can be rewritten as

$$\mathbf{M}_{\text{air}}(e) = T_{\parallel}(1+e) \begin{pmatrix} 1 & 0 & 0 & 0 \\ 0 & 1-\delta & 0 & 0 \\ 0 & 0 & 1-\delta & 0 \\ 0 & 0 & 0 & 1-\delta \end{pmatrix}, \tag{A5}$$

which shows that the MM normalized to m_{00} has diagonal elements $m_{11} = m_{22} = m_{33} = (1-e)/(1+e) \equiv 1-\delta$. This result reflects that the limited extinction ratio of the camera micro-polarizers induces an error δ in the diagonal elements of the normalized MM for air given by:

$$\delta = 1 - \frac{1-e}{1+e} = \frac{2e}{1+e} = \frac{2}{1+ER} \simeq \frac{2}{ER}, \tag{A6}$$

where we used that $e = 1/ER$ and $ER \gg 1$ in the final approximation. Figure A1 shows the evolution of this error parameter as a function of the extinction ratio. Since ER > 120:1 in our polarization camera, the deviation expected from this problem is $\delta < 1.7\%$.

Obviously, the identity MM of air is also recovered when the PSA calibration compensates for the limited ER i.e., when using the PSA pseudo-inverse matrix $\mathbf{A}^{-1}(e)$ in equation (A3). Then equation (9) results directly on the identity matrix since $\mathbf{A}^{-1}(e) \cdot \mathbf{I}_{\text{air}}(e) \cdot \mathbf{S}^{-1} = \mathbf{A}^{-1}(e) \cdot \mathbf{A}(e)$.

We can now analytically show that, for any other sample, the procedure described in Section 4 compensates the limited ER of the micro-polarizers if the PSA pseudo-inverse matrix $\mathbf{A}^{-1}(e)$ in equation (A3) is the one employed to retrieve the Mueller matrix. To illustrate this, we consider as sample an ideal linear polarizer with horizontal transmission axis, whose MM is given by equation (A1b). The 6 × 6 elements of the intensity matrix $\mathbf{I}_{\text{p}}(e)$ of this polarizer sample are analytically obtained by calculating the intensity I_{ag} expected for each input state, g = H, V, D, A, R, L (assumed ideal), when being detected through analyzers a = H, V, D, A, R, L affected by a limited extinction ratio ($e \neq 0$). In this case, the obtained intensity matrix is:

See the equation (A7) bottom of the page

The MM of this polarizer sample is then obtained from equation (9). If the calculation is made ignoring the error in the micro-polarizers, i.e., using the ideal $\mathbf{A}^{-1}$ matrix defined equation (7), the analytical expression of such non-compensated MM is:

$$\mathbf{M}_p(e) = \mathbf{A}^{-1} \cdot \mathbf{I}_p(e) \cdot \mathbf{S}^{-1} = \frac{T_{\parallel}}{2}(1+e) \begin{pmatrix} 1 & 1 & 0 & 0 \\ 1-\delta & 1-\delta & 0 & 0 \\ 0 & 0 & 0 & 0 \\ 0 & 0 & 0 & 0 \end{pmatrix}. \tag{A8}$$

Thus, the the normalized MM contains errors in the m_{10} and m_{11} elements. These errors are completely compensated by using the pseudo-inverse matrix $\mathbf{A}^{-1}(e)$ of equation (A3). A simple calculation shows that the matrix product $\mathbf{A}^{-1}(e)\ \mathbf{I}_p(e)\ \mathbf{S}^{-1}$ results in the expected MM in equation (A1b).

Finally, the same kind of calculation can be generalized to an arbitrary sample described by a generic MM:

$$\mathbf{M}_s = \begin{pmatrix} m_{00} & m_{01} & m_{02} & m_{03} \\ m_{10} & m_{11} & m_{12} & m_{13} \\ m_{20} & m_{21} & m_{22} & m_{23} \\ m_{30} & m_{31} & m_{32} & m_{33} \end{pmatrix}. \tag{A9}$$

We again evaluate analytically the intensity matrix $I_{\text{s}}(e)$ when the sample is introduced in the polarimeter affected by the error e. We calculate the intensity I_{ag} expected for each input state g = H, V, D, A, R, L (assumed ideal), when

$$I_p(e) = T_{\parallel} \begin{pmatrix} 1 & e & \frac{1}{2} & \frac{1}{2} & \frac{1}{2} & \frac{1}{2} \\ e & 1 & \frac{1}{2}e & \frac{1}{2}e & \frac{1}{2}e & \frac{1}{2}e \\ \frac{1}{2}(1+e) & 0 & \frac{1}{4}(1+e) & \frac{1}{4}(1+e) & \frac{1}{4}(1+e) & \frac{1}{4}(1+e) \\ \frac{1}{2}(1+e) & 0 & \frac{1}{4}(1+e) & \frac{1}{4}(1+e) & \frac{1}{4}(1+e) & \frac{1}{4}(1+e) \\ \frac{1}{2}(1+e) & 0 & \frac{1}{4}(1+e) & \frac{1}{4}(1+e) & \frac{1}{4}(1+e) & \frac{1}{4}(1+e) \\ \frac{1}{2}(1+e) & 0 & \frac{1}{4}(1+e) & \frac{1}{4}(1+e) & \frac{1}{4}(1+e) & \frac{1}{4}(1+e) \end{pmatrix} \tag{A7}$$

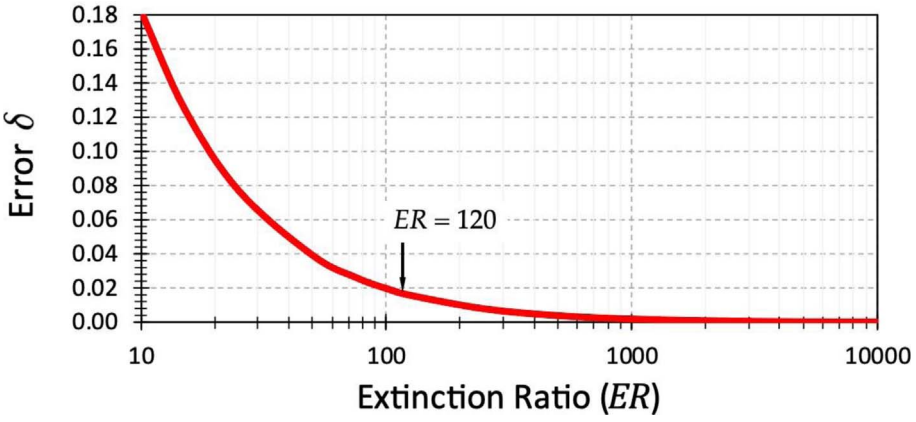

Fig. A1. Evolution of the error parameter δ as a function of the polarizers extinction ratio ER. The arrow indicates the limit value $ER = 120$ measured for our polarization camera.

$$M_s(e) = T_{\parallel}(1+e)\begin{pmatrix} m_{00} & m_{01} & m_{02} & m_{03} \\ m_{10}(1-\delta) & m_{11}(1-\delta) & m_{12}(1-\delta) & m_{13}(1-\delta) \\ m_{20}(1-\delta) & m_{21}(1-\delta) & m_{22}(1-\delta) & m_{23}(1-\delta) \\ m_{30}(1-\delta) & m_{31}(1-\delta) & m_{32}(1-\delta) & m_{33}(1-\delta) \end{pmatrix}, \tag{A10}$$

being detected through analyzers a = H, V, D, A, R, L affected by a limited extinction ratio ($e \neq 0$). Again, the impact of the limited extinction ratio on the polarimeter measurement can be analytically evaluated by considering equation (9), $\mathbf{M}_S(e) = \mathbf{A}^{-1} \cdot \mathbf{I}_S(e) \cdot \mathbf{S}^{-1}$, where the ideal $\mathbf{A}^{-1}$ is applied (thus ignoring the error in the micro-polarizers). It is a long but straightforward calculation to obtain that the retrieved MM reads:

See the equation (A10) top of the page

which recovers the ideal matrix in equation (A9) in the limit $e \to 0$ ($\delta \to 0$) and $T_{\parallel} \to 1$. This shows that all elements in the normalized MM except those in the first row are affected by the same factor $1 - \delta$.

However, it can also be demonstrated that the sample matrix in equation (A10) is recovered when using the PSA matrix in equation (A3) to calculate $\mathbf{A}^{-1}(e) \cdot \mathbf{I}_s(e) \cdot \mathbf{S}^{-1} = \mathbf{M}_s$, i.e., the ER error of the micro-polarizers is completely compensated.

Finally, let us note that we are applying this compensation method to a simplified model where only a uniform limited extinction ratio of the micro-polarizers is considered. The effect of spatial variations of the extinction ratio or errors in the orientation of the micro-polarizers can be considered as indicated in [34].